MAX-PLANCK INSTIUTE FOR POLYMER RESEARCH

Graphene Based Electrode Materials for Solar Cell and Electrochemical Oxygen Reduction

Ph.D. Dissertation

zur Erlangung des Grades

“Doktor der Naturwissenschaften”

dem Fachbereich Chemie und Pharmazie der

Johannes Gutenberg-Universität Mainz

vorgelegt von

Qi Su

2/4/2012

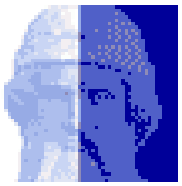

Abstract:

This work has explored many unprecedented synthetic approaches towards novel graphene composites and nitrogen containing graphitic materials. The resulting materials were applied as the transparent electrodes of solar cells, the free-standing electrodes with enhanced mechanical strength, and the cathodes of fuel cells for oxygen reduction.

All the results have clearly demonstrated the great potential of graphene based materials and nitrogen containing graphitic carbons as novel electrode materials for new energy devices.

Decan: _____

1. Berichterstatter: _____

2. Berichterstatter: _____

Tag der mündlichen Prüfung: _____

Table of Contents

Chapter 1. Introduction

Carbon materials, during the last couple of decades, have drawn particular attention in scientific research due to their unique properties as electrodes and electrolytes in a range of new energy devices, including photovoltaic cells, lithium batteries, fuel cells and supercapacitors. Most recently, the discovery of graphene and its composites has revealed a whole new area with numerous opportunities. In this thesis, different types of graphene based composites and nitrogen doped graphitic materials have been developed for the purpose of novel carbon electrodes. This introduction aims to describe the related backgrounds and brief the general motivations of the research works in this dissertation.

1.1 Graphene-based materials for electrochemical application

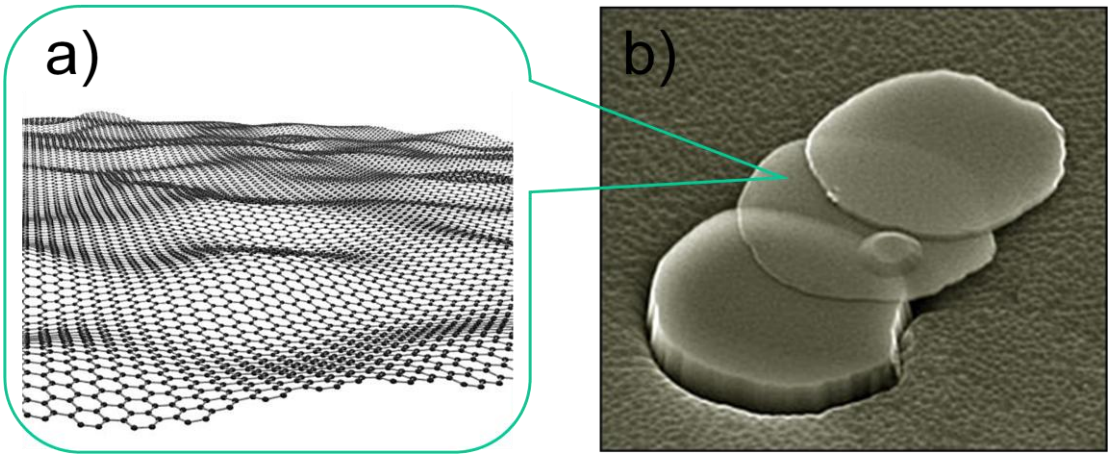

Figure 1.1 a) A structural model of a graphene membrane: as a infinite large polyaromatic hydrocarbon; b) Scanning electron microscopy (SEM) image of graphene

Graphene is a flat monolayer of carbon atoms tightly packed into a two-dimensional (2D) honeycomb lattice. It is a basic building block for graphitic materials of all other dimensionalities including graphite, charcoal, carbon nanotubes and fullerenes.[1] It can be wrapped up into 0D fullerenes, rolled into 1D nanotubes or stacked into 3D graphite.[2] It can also be considered as an infinitely

large polycyclic aromatic hydrocarbon (as illustrated in Figure 1.1a).

1.1.1 Unique properties of graphene:

One of the most important reasons that graphene has attracted tremendous attention lies in its remarkable properties, such as:

a) Electronic properties

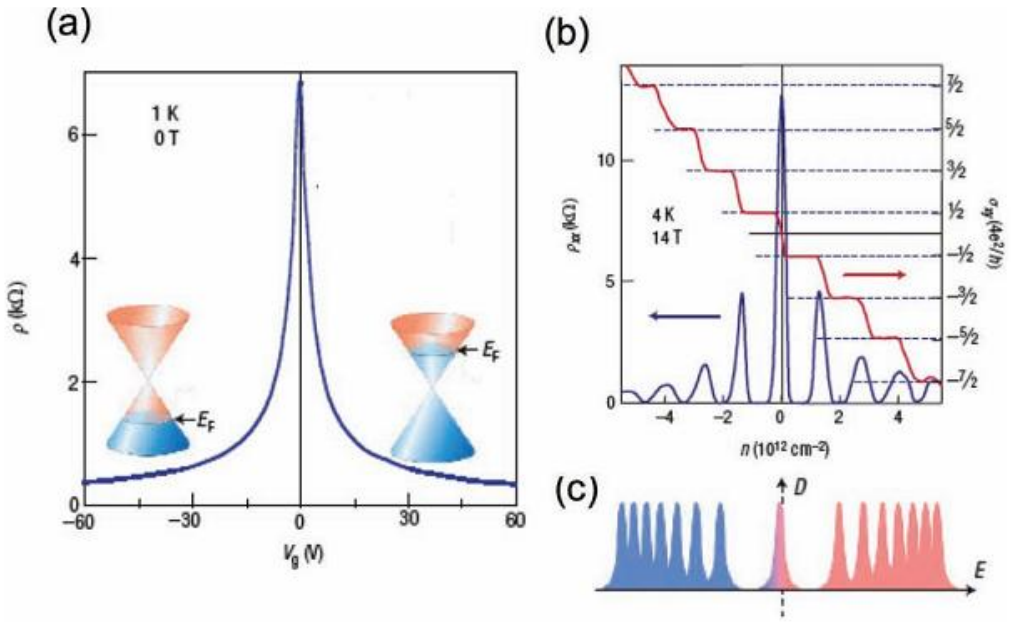

Figure 1.2 a) Ambipolar electric field effect in monolayer graphene. The insets show the changes in the position of the Fermi energy EF with changing gate voltage Vg; b) the hallmark of massless Dirac fermions is QHE plateau in σ_{xy} at half integers of $4e^2/h$; c) Landau levels in the density of states D in graphene are described by equation En for massless Dirac fermions. [3]

Graphene differs from most conventional three-dimensional materials. Intrinsic graphene has an ambipolar electric field effect (Figure 1.2a) for which charge carriers can be tuned continuously between electrons and holes in concentration as high as 10^{13} cm^{-2}. The mobility is nearly independent of temperature between 10 K and 100

K,[3,4] which implies that the dominant scattering mechanism is defect scattering. Experimental results from transport measurements show that graphene has a remarkably high electron mobility μ exceeding 15,000 $cm^2V^{-1}s^{-1}$ even under ambient conditions.[1,3,5,6] The corresponding resistivity of the graphene sheet would be 10^{-6} Ω·cm, which is less than the resistivity of silver, the lowest resistivity substance known at room temperature.[7,8] The μ remains high even at the highest electric-field-induced concentrations, and seems to be little affected by chemical doping, translates into ballistic transport on the sub-micrometer scale.[1] A further indication of the extreme electronic property is the quantum Hall effect (QHE) that can be observed in graphene even at room temperature, extending the previous temperature range for the QHE by a factor of 10 (Figure 1.2b).[9]

Another unique nature of graphene lies in its charge carriers. Due to the linear (or “conical") dispersion relation at low energies, electrons and holes in graphene have a zero effective mass, and the charge carriers of graphene mimic relativistic particles and are more easily and naturally described starting with the Dirac equation rather than the Schrödinger equation. [1,3,10-17]

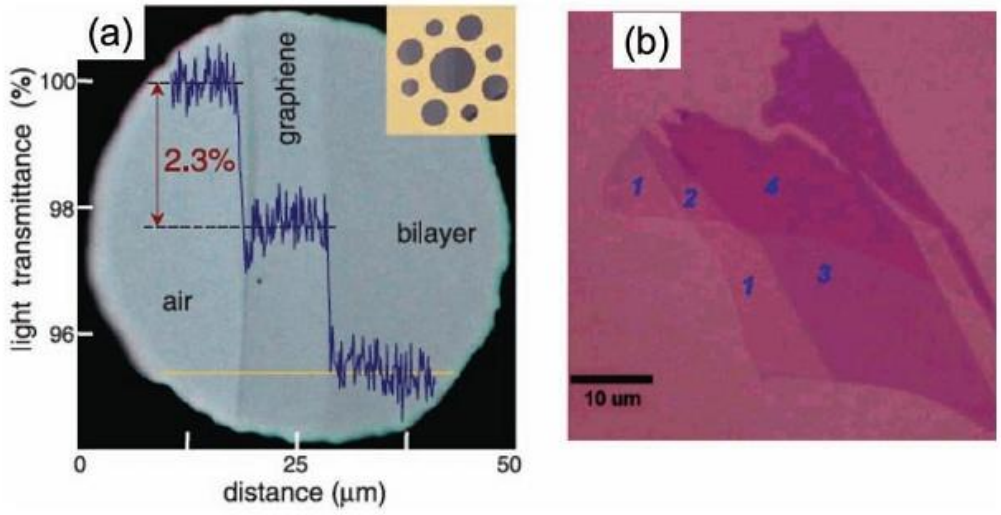

Figure 1.3 (a) Photograph of an aperture partially covered by graphene and its bilayer. The line scan profile shows the intensity of transmitted white light along the yellow line;[18] (b) Optical image of graphene flakes with one, two, three, and four layers.[19]

b) Optical properties

Graphene's unique electronic properties produce an unexpectedly high transparency for an atomic monolayer. As shown in Figure 1.3a the constant transparency (~97.7%) has been experimentally observed for graphene in the visible range and the transmittance linearly decreases with the number of layers for n-layer graphene.[18]

c) Thermal properties

The near-room temperature thermal conductivity of suspended graphene was recently measured to be between 5 $\times 10^3$ $Wm^{-1}K^{-1}$.[20] These values are in excess of those measured for carbon nanotubes or diamond. A thermal conductivity of ~2500 $Wm^{-1}K^{-1}$ (at 350 K) was obtained from chemical vapor deposition (CVD) grown graphene deposited onto a thin silicon nitride membrane.[21] Recently it has been measured that the thermal conductivity of mechanically exfoliated graphene deposited on a SiO_2 substrate is ~600 $Wm^{-1}K^{-1}$, higher than those of metals such as Cu.[22,23]

d) Mechanical properties

The mechanical properties of monolayer graphene including the Young's modulus and fracture strength have been investigated by simulations.[24,25] The Young's modulus of few-layer graphene was experimentally investigated with force-displacement measurements by atomic force microscopy (AFM) on a strip of graphene suspended over trenches.[26] The elastic properties and intrinsic breaking strength of free-standing monolayer graphene were measured by nanoindentation using an AFM (Figure 1.4a and b). It was reported that defect-free graphene has a Young's modulus of 1.0 TPa and a fracture strength of 130 GPa.[27] The graphene oxide

reduced by hydrogen plasma exhibited a mean elastic modulus of 0.25 TPa with a standard deviation of 0.15 TPa.[28]

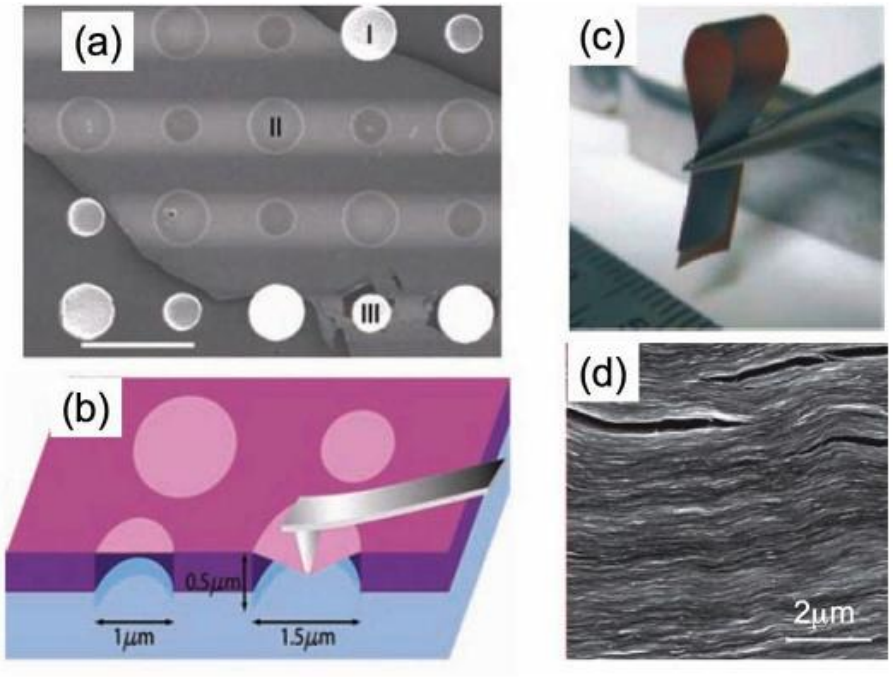

Figure 1.4 a) SEM image of a graphene flake spanning an array of circular holes and b) Schematic illustration of nanoindentation on membranes; c) and (d) show graphene oxide paper and its cross-section in SEM.[27,29]

1.1.2 Preparation of graphene

As graphene presents so many unique physical properties, how to produce such material has become a critical issue. Currently, graphene has mainly been made by three different methods. The first is micromechanical exfoliation. In essence, graphene is an isolated atomic plane of graphite. From this perspective, Novoselov *et al*. first used cohesive tape to repeatedly split graphite crystals into increasingly thinner pieces, and finally peeled off individual graphene planes from graphite in 2004 (Figure 1.2a, b).[3] This technique provides crystals of high structural and electronic quality.[30] However, only small samples in extremely limited production scale can be made though this method that is only useful for fundamental study.[31] Instead of manually cleaving graphite, it is also possible to make the process

automatically by using, for example, ultrasonication in suitable solution.[32] It leads to semi-stable suspensions of submicrometer graphene crystallites (Figure 1.5 c, d), which can then be used to make polycrystalline films and composite materials.[29,32]

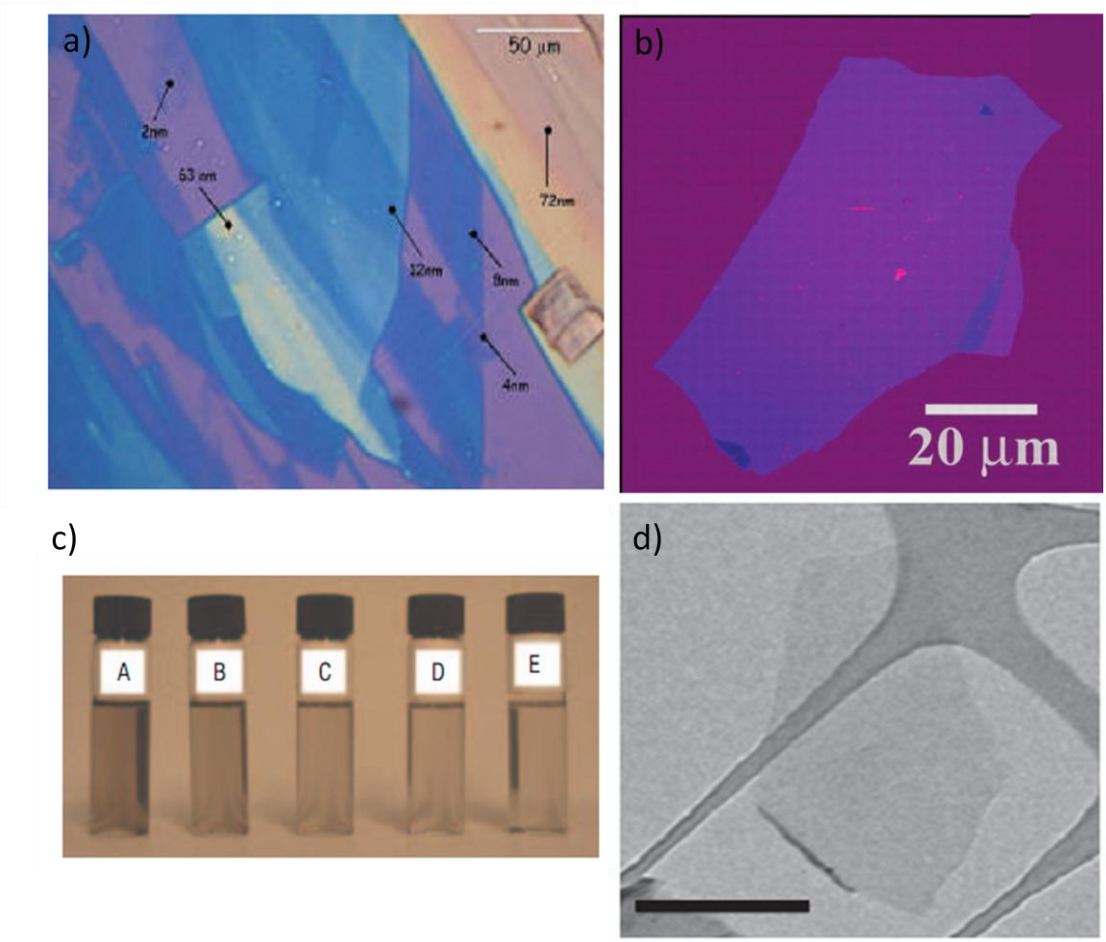

Figure 1.5 a) Photograph of graphene flake with various thickness on top of an Si wafer; b) Photograph of a relatively large multilayer graphene flake with thickness ~3 nm on top of an oxidized Si wafer.[5] c) Dispersions of graphite flakes in NMP; d) Bright-field TEM images of monolayer graphene flakes deposited from GBL[32]

The second method of producing graphene is epitaxial growth on various substrates. The first substrate that has been discovered is silicon carbide (SiC). That means to heat silicon carbide (SiC) at high temperatures (>1100 °C) to reduce it to graphene.[33,34] The dimensions of epitaxial graphene produced in this process depend upon the size of the SiC substrate (wafer). As the alternative, graphitic layers can grow epitaxially on top of metal crystals, including Ruthenium,[35] Iridium,[36]

Nickel[37-39] and Copper.[40-42] This method uses the atomic structure of a metal substrate to seed the growth of graphene. It is the 3D growth during which epitaxial layers remain bound to the underlying substrate and the bond-breaking fluctuations are suppressed. After the epitaxial structure is cooled down, one can remove the metal substrate by chemical etching.[30] Subsequently the graphene sheets are transferred to various substrates, demonstrating viability for numerous electronic applications.[39] However, epitaxial growth requires extreme conditions, such as high vacuum (10^{-6} Torr), high temperature (>1000 °C), crystalline surface and complicated etching&transfer process, which makes it far away from large scale production with low cost.

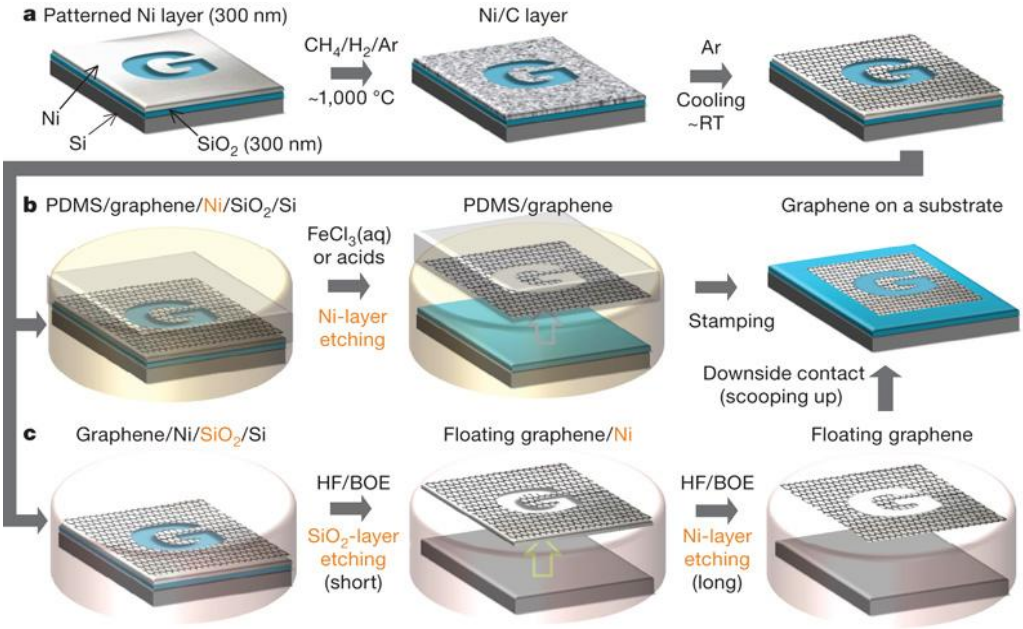

Figure 1.6 A) Synthesis of patterned graphene films on thin nickel substrate. b) Etching using $FeCl_3$ (or acids) and transfer of graphene films using a PDMS stamp. C) Etching using BOE or hydrogen fluoride (HF) solution and transfer of graphene films. RT, room temperature (approx25 °C).[39]

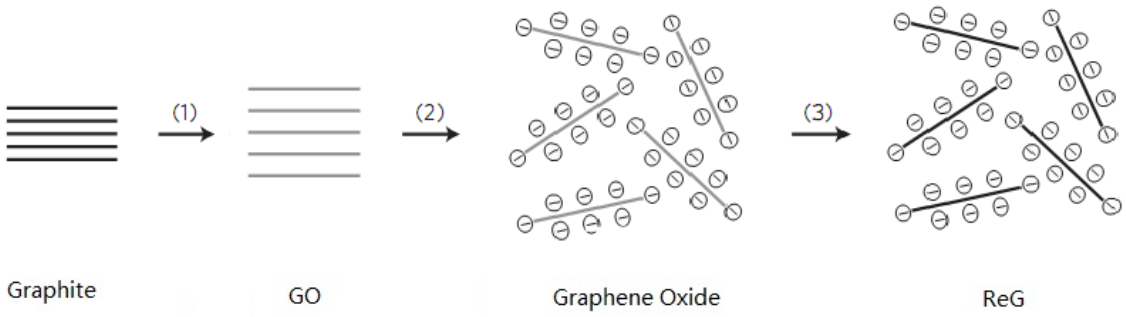

Figure 1.7 Scheme showing the chemical route to the synthesis of aqueous graphene dispersions. 1) Oxidation of graphite to graphite oxide; 2) Exfoliation of graphite oxide in water by sonication to obtain graphene oxide colloids; 3) Controlled conversion of graphene oxide to graphene through deoxygenation by reduction.[43]

The third method to obtain graphene is to reduce exfoliated graphite oxide (GO). In this method, graphite is firstly oxidized to provide GO. By different exfoliation approaches, a single layer of GO, which is referred as "graphene oxide" was generated.[44] Such graphene oxide can be reduced under various conditions to produce graphene in a large quantity. Graphene produced by this way has been given a variety of names, including: reduced graphene oxide (ReG), chemically-reduced graphene oxide (CRG), and graphene.[45] For the sake of clarity, the product is here referred as ''reduced graphene oxide (ReG)'' though the distinction with pristine graphene will be made apparently. The two are often confused but the quality of graphene produced by graphite oxide reduction is much lower than e.g. scotch tape graphene due to incomplete removal of various functional groups.

Even though simply reducing GO is not able to provide graphene with perfect structure, it offers incomparable advantages in large scale production of solution processable single graphene (or GO) layer with low cost. Therefore, extensive studies have been done to reveal the chemical structure of GO in aim to find out possible approaches to retrieve the honeycomb structure of graphene.

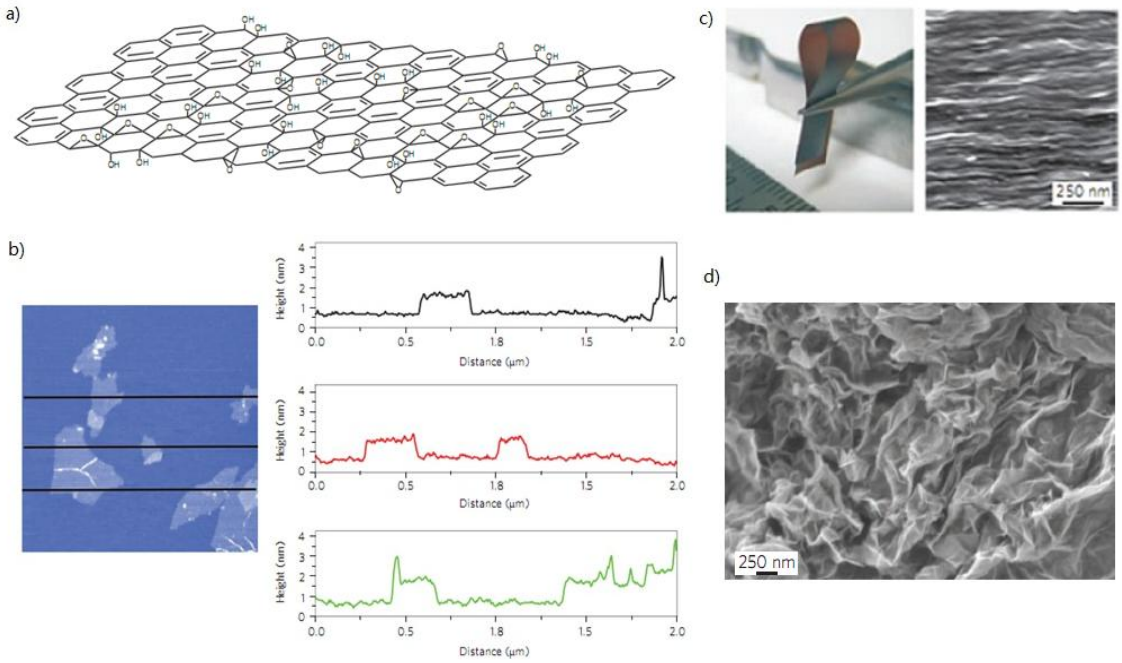

Figure 1.8 a) Chemical structure of GO; b) An AFM image of exfoliated graphene oxide sheets[46]; the sheets are ~1 nm thick; c) Photograph of folded graphene oxide paper; d) A SEM image of the cross-section of the graphene oxide paper, showing layered structure.[29]

GO has been mainly oxidized from graphite via Hummer's method in which graphite reacts with a mixture of potassium permanganate ($KMnO_4$), concentrated nitric acid (HNO_3) and sulfuric acid (H_2SO_4). Investigation by solid-state ^{13}C-NMR spectroscopy of GO and recently of ^{13}C-labelled GO proposed the model of GO structure as shown in Figure 1.5a.[31,47]. The sp^2-bonded carbon network of graphene oxide is strongly disrupted and a significant fraction of this carbon network is bonded to hydroxyl groups or epoxide groups.[47-50] Minor components of carboxylic or carbonyl groups are abundant at the edges of the layers in GO. As a result, graphene oxide sheets are hydrophilic, so that water molecules can readily intercalate between the layers. The interlayer distance between the graphene oxide sheets increases reversibly from 6 to 12 Å with increasing relative humidity.[44] The surface functionality (particularly in basic media) greatly weakens the layer-layer interactions. Therefore, a variety of thermal and mechanical methods can be used to

exfoliate GO to graphene oxide.[45,46,51]

The measurement of the surface charge (zeta potential) of graphene oxide sheets[43] shows that there is negative charged nature in GO dispersion in water. This suggests that electrostatic repulsion between graphene oxide sheets could generate a stable aqueous suspension of them. The maximum dispersibility of graphene oxide in solution, which is important for processing and further functionalization, depends both on the solvent and the extent of surface functionalization imparted during oxidation.[46]

Both GO and graphene oxide are electrically insulating materials due to their disrupted sp^2 bonding networks. On the other hand, the reduction of the GO (and graphene oxide) can recover the π-network and restore the electrical conductivity of graphene. Thus, graphene oxide sheets became one of the most promising starting materials in the mass production of solution processable graphene sheets through various chemical reduction approaches, e.g. by chemical reduction (using reductants such as hydrazine[46,52-54] dimethylhydrazine[55], hydroquinone[56] and $NaBH_4$[57,58]), by thermal reduction (annealing in argon/hydrogen)[59,60] or by electrochemical reduction.[61]

The reduction of aqueous graphene oxide dispersion by hydrazine at the pH of the dispersion as made results in agglomerated graphene-based nanosheets. When dried, it forms a black powder which is electrically conductive (powder conductivity, ~2×10^2 S m^{-1}).[46] Elemental analysis (atomic C/O ratio, ~10) of the reduced graphene oxides measured by combustion revealed the existence of a significant amount of oxygen, indicating that reduced graphene oxide is not the same as pristine graphene.[45] Theoretical calculations of the reduction of graphene oxide (graphene oxide used in the model was decorated with hydroxyl and epoxide groups) suggest that reduction below 6.25% of the area of the graphene oxide (C/O = 16 in atomic

ratio) may be difficult in terms of removing the remaining hydroxyl groups.[62]

Thermal treatment of GO is another route used to obtain reduced graphene oxide. Rapid heating (>2,000°C min^{-1}) up to 1,050°C exfoliates as well as reduces GO, yielding a black powder.[60,63] The platelets have similar oxygen content to that of hydrazine-reduced graphene oxide, and powder conductivity has been reported in the range of (1 - 2.3) × 10^3 S m^{-1}.[60,63] Although thermal reduction is able to eliminate oxygen-containing groups, the corruption of sp^2 carbon network during the graphite oxidation strongly hampers the properties of ReG. How to mend the defects left on ReG is a key and open question for producing high quality graphene by reducing exfoliated graphite oxide.

1.1.3 Graphene functionalization and composite

For better tuning the properties of graphene and to make it a more versatile precursor for a wide range of applications, one possible route is to functionalize graphene and incorporate graphene sheets into various composite materials.[64] The manufacturing of such materials requires not only that graphene sheets must be produced on a sufficient scale but that they also be homogeneously distributed into various reaction media.[55] Compared with exfoliation of graphite and epitaxial growth on silicon carbide, chemical reduction appears to be more feasible in the large scale production of ReG. This is one of the most important reasons that the majority of work on graphene nanocomposites has been based on ReG.[31]

As for making a homogeneous dispersion, the chemical functionalization of ReG has been widely explored and demonstrated as a useful tool to improve their dispersibility in various media as well as the compatibility with various matrices. As a consequence, the incorporation of graphene has brought significant enhancements of properties at much lower volume loadings (0.1–5 vol%) when compared to other

lamellar clays,[65,66], and thus led us to a wide variety of graphene-base composite materials polymers, nanoparticles in polymer matrices.

a) Covalent functionalization of graphene

Currently, there are two main approaches to functionalize graphene, namely covalent and non-covalent functionalization. Covalent functionalization is to "graft" functional species onto graphene surface or periphery by covalent bonds. These functional species as delicate morphological organization bring the fine interface control, uniform dispersion, and ease of processing, which are essential to the performance of the graphene composites. Compared to chemically inert surface of graphene sheets, ReG acts as a far more reactive platform for covalent functionalization.[45] Firstly, ReG has a better dispersibility in many hydrophilic media which give functional groups access to the graphene surface. Secondly, ReG has chemically reactive oxygen functionality, such as carboxylic acid groups at their edges. A wide range of reactions utilizing carboxylic acids has been developed over the course of the development of small molecule organic chemistry, and many of these reactions can be and have been applied to graphene.[67-71] The products from covalent functionalization are mostly characterized by X-ray photoelectron spectroscope (XPS), Fourier transform infrared (FT-IR), and NMR spectroscope.

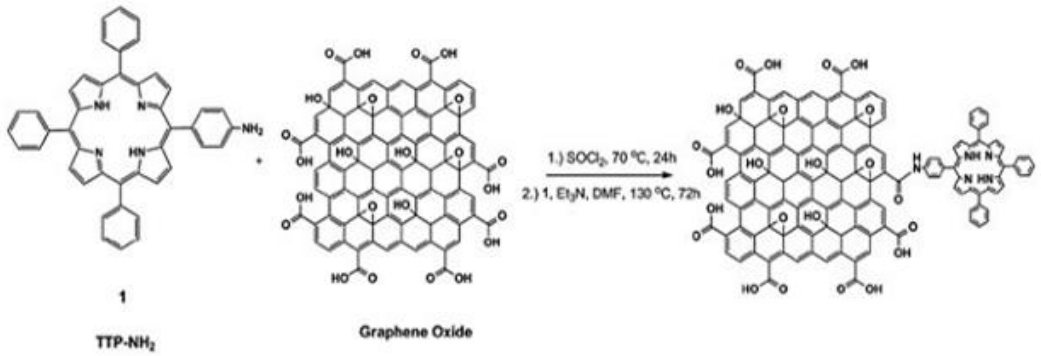

Figure 1.9 Functionalization of the carboxylic acid groups of graphene oxide showing the covalent attachment of porphyrins.[70]

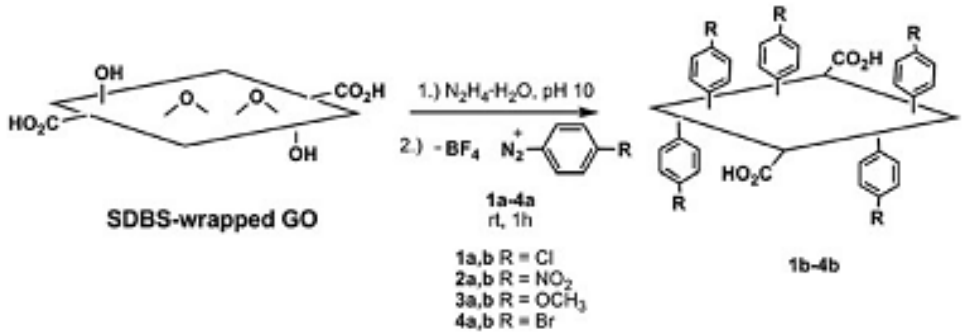

Figure 1.10 Covalent functionalization of reduced graphene oxide platelets with diazonium salts (SDBS, sodium dodecylbenzenesulfonate).[52]

Another type of covalent functionalization is to graft functional groups directly on the basal plane of graphene. Tour *et al.* first described this type of bonding by reacting ReG with aryl salts (Figure 1.10).[52,72] The resulting ReG has a moderate dispersibility in polar aprotic solvents such as dimethylformamide (DMF). In addition, 1,3-dipolar addition was found to be effective to attach functional groups, namely azomethine ylide, on graphene basal plane.[73] Such functionalized graphene was dispersed in organic solvents, such as ethanol.

b) Non-covalent functionalization of graphene

In addition to covalent functionalization, graphene also exhibits non-covalent binding via π-π stacking, cation-π or van der Waals interactions on the sp^2 networks (where present) that are not oxidized or engaged in hydrogen bonding. Via these non-covalent bindings, functional species can be anchored on the surface of graphene sheets without chemical bonding, but able to render external forces to disperse graphene in various media. Moreover, the non-covalent functionalization, comparing to covalent functionalization, is considered to have less impact on the structure and properties of graphene. Ruoff *et al*. first used poly(sodium 4-styrenesulfonate) (PSS), a ionic polymer with abundant aromatic structures, to stabilize ReG solution in water.[51] The strong π-π interaction between graphene plane

and PSS prevents ReG from reaggregation during the reduction step and therefore, form a very stable aqueous dispersion of ReG with concentration up to 1 mg/mL. Similar effect was also observed when aromatic molecules or polymers were applied as surfactant (such as Phospholipid-PEG,[74] pyrene salts,[75] TCNQ,[76] pyrlene diimide salts[64] and sulfonated polyaniline[77] etc.).

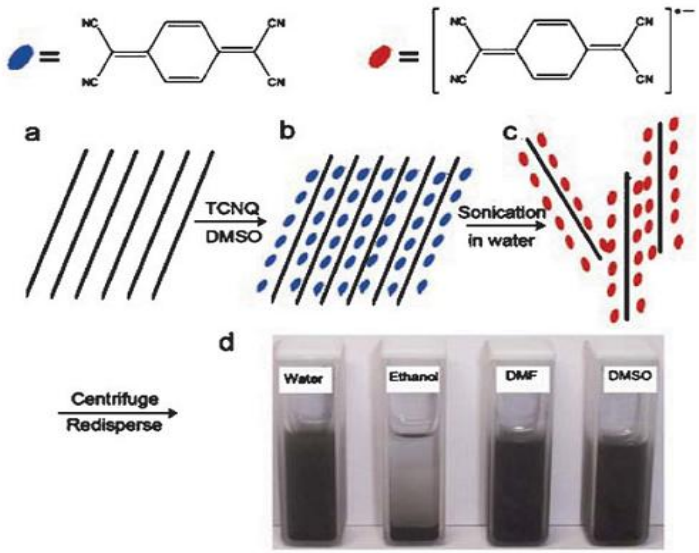

Figure 1.11 Schematic illustration of aqueous graphene dispersions stabilized with TCNQ anion. a) pristine expanded graphite; b) TCNQ insertion into graphite by the aid of DMSO; c) after durative sonication, TCNQ-anion-stabilized graphene in water; d) photograph of TCNQ anion adsorbed graphene dispersed in different solvents: water, ethanol, DMF, DMSO.[76]

Later on, it has been discovered that carboxylic acids were not affected by chemical reduction of GO, and these groups would remain intact on the edge of graphene sheets after hydrazine reduction and, if deprotonated, would provide sufficient electrostatic repulsion (zeta potential is about –30mV) to overcome the aforementioned van der Waals attraction.[43] By adding ammonia to raise the pH of the suspension to ~10 during the hydrazine reduction of graphene oxide, a stable aqueous dispersion of graphene was obtained. Unfortunately, this suspension was fairly sensitive to both pH and the presence of ‘‘hard’’ electrolytes such as sodium chloride. Furthermore, graphene sheets were successfully transferred into organic

solution (such as chloroform) via ionic interaction with the assistance of amphiphilic alkyl ammonia salt (NR_4^+).[78]

Although functionalization of ReG has been extensively studied and demonstrated as a useful tool to improve its compatibility, quite a few works pay enough attention to the quality of ReG sheets after functionalization. The properties of ReG in graphene-based composite materials are greatly limited by the functionalization processes and the defects left during the processes. How to increase the electrical/thermal conductivity as well as the mechanical strength of graphene-based composite materials remains a big challenge. In chapter 2 and 3 we will present two different methods to improve the quality of ReG sheets as well their electrical and mechanical properties, for better applying such materials as electrodes in new energy devices.

1.1.4 Graphene-based electrode materials

a) Graphene-based transparent electrode for solar cell

Polymer solar cells have attracted considerable attention in the past few years owing to their potential of providing environmentally safe, flexible, lightweight, inexpensive and efficient solar cells. Especially, bulk-heterojunction solar cells consisting of a mixture of ~~a~~ conjugated donor and acceptor polymer is considered as a promising approach.

Various architectures for organic solar cells have been investigated in recent years. In general, for a successful organic photovoltaic cell four important processes have to be optimized to obtain a high conversion efficiency of solar energy into electrical energy:

(i) Absorption of light;

(ii) Charge transfer and separation of the opposite charges;

(iii) Charge transport;

(iv) Charge collection.

To assure an efficient light absorption and charge transport, a window electrode should be transparent with good conductivity. Currently, Indium tin oxide (ITO) and fluorine doped tin oxide (FTO) have been widely used as window electrodes in optoelectronic devices. These metal oxides, however, appear to be increasingly problematic due to (i) the limited availability of the element indium on earth, (ii) their instability in the presence of acid or base, (iii) their susceptibility to ion diffusion into polymer layers, (iv) their limited transparency in the near-infrared region, and (v) the current leakage of FTO devices caused by FTO structure defects. The search for novel electrode materials with good stability, high transparency and excellent conductivity is therefore a crucial goal for optoelectronics.

With high electrical conductivity, high carrier mobility, and high optical transmittance in the visible range of the spectrum, graphene materials have become a great candidate of transparent conductive films (TCFs) in photovoltaic devices.[22] In particular, graphene's mechanical strength and flexibility are advantageous compared with ITO and FTO. Moreover, graphene films can be deposited from solution over large areas. In particular, the scalability of production and convenient processing of GO has led to its emergence as an important precursor for the fabrication of TCFs.

The most frequently used film formation techniques of graphene oxide platelets have been reported including spin-coating,[79,80] dip-coating,[59] vacuum filtration,[81] and Langmuir-Blodgett (LB) assembly,[82] followed by chemical reduction and/or thermal annealing. Researchers have also developed various methods to obtain graphene or reduced graphene oxide suspensions for the preparation of TCFs.[31] For example,

spray-coated TCFs from aqueous dispersions of reduced graphene oxide nanoplatelets were obtained by changing the pH to about 10 prior to reduction with hydrazine.[43,64] LB-assembled films consisting of overlapped and stacked ReG platelets yielded a sheet resistance of 8 kΩ/square at a transparency of 83% (at a wavelength of 1000 nm).[74] Liquid-liquid assembly, occurring at the H_2O-chloroform interface, has been used to prepare films consisting of multilayer graphene platelets, from which a sheet resistance of 100 Ω/square was obtained with a light transmittance of 70% at 500 nm.[83] Disordered films of randomly stacked few-layer graphene platelets, made by directly sonicating graphite in organic solvents followed by vacuum filtration,[32] have shown a sheet resistance of ~3 kΩ/square at a transmittance of ~ 75% (at 550 nm).[84] Recently, the chemical reduction of graphene oxide platelets in a liquid dispersion and their assembly were achieved in one step in the fabrication of graphene based TCFs, from which a sheet resistance of 11.3 kΩ/square with a transmittance of 87% at 550 nm was obtained.[85] Graphene TCFs have been used as electrodes for dye-sensitized solar cells,[59] liquid crystal devices,[86] and organic light-emitting diodes.[87] The sheet resistance reported for ReG TCFs varies over a wide range due to the variety of surface functionalities and defects introduced.

On the other hand, CVD on metals offers the possibility of growing large area graphene films of reasonably high quality.[37,39,40] The graphene films prepared by this way have yielded lower sheet resistances for similar transparency values. Stretchable transparent electrodes were produced by transferring graphene grown on Ni onto polydimethylsiloxane (PDMS) substrates.[39] By this method, a minimum sheet resistance of ~ 280 Ω/square at a transparency of ~ 76% (at 550 nm) was achieved. In another work, the dependence of the sheet resistance on the transmittance of few-layer graphene films grown on Ni or Cu followed by a transfer onto cover glass was studied.[88] Considering the argument that the intrinsic sheet resistance of graphene is about 30 Ω/square,[89] there is still potential for improving the quality of

graphene for use in TCF devices. Meanwhile, the lack of large scale production is also a very important limitation of CVD growth of such graphene-based TCFs.

b) Graphene-based electrode in other electrochemical application

Graphene is also a promising electrode material for lithium ion batteries (LIBs), due to its high theoretical surface area of 2630 m^2g^{-1} and ability to facilitate electron- or hole-transfer along its two-dimensional surface.[22] monolayer graphene in disordered carbon has been proposed to have a Li_2C_6 stoichiometry, twice as much as graphite(LiC_6),[89] since lithium ions could bind on both sides of its surfaces.[90] When silicon nanoparticles were mixed with reduced graphene oxide platelets in a paper-like material, a storage capacity > 2200 $mAhg^{-1}$ after 50 cycles and > 1500 $mAhg^{-1}$ after 200 cycles was obtained recently.[91] It was believed that the uniform dispersion of silicon particles in the composites and the reconstitution of graphene platelets to form a continuous, highly conducting 3D network are important for the high storage capacities. Other graphene hybrid nanostructures (such as TiO_2/graphene,[92] SnO_2/graphene,[93,94] and ceramic/graphene[95] composites), have attracted special attention as high capacity anode materials in LIBs as well, owing to their excellent lithium storage properties.

Supercapacitors represent another important class of energy storage devices where graphene-based electrodes have been employed.[96] In the last few years, it has been proposed that graphene should be a competitive electrode material for supercapacitor applications due to its superb characteristics of chemical stability, high electrical conductivity, and large surface area. Several groups have reported graphene-based supercapacitors using metal oxide/graphene,[97,98] CNTs,[99] and polymer/graphene composites as electrodes.[100-103] Capacitance values as high as 190 Fg^{-1} in aqueous and 120 Fg^{-1} in organic electrolytes have been achieved.[104]

Besides, graphene materials have also been used in studies of hydrogen storage,

fuel cells, and other electrochemical devices. For example, ReG made by reduction of graphene oxide with hydrazine and with a Brunauer-Emmett-Teller (BET) specific surface area of 640 m^2g^{-1} (when dried down), has shown a hydrogen adsorption capacity of 0.68 wt% at 77K and 1 bar.[105] This value was expected to be increased by further increasing the surface area of graphene materials. Besides, graphene has been identified as a catalyst support for oxygen reduction and methanol oxidation in a fuel cell configuration.[106-110] Conductive graphene scaffolds for platinum nanoparticles facilitated efficient collection and transfer of electrons to the electrode surface. All of these efforts have not only outlined the great potential of graphene composite materials for electrochemical application, but also urge people to futher engage in discovering better approaches to produce and modify graphene (or ReG).

1.2 N-containing macrocycles and N-containing graphitic materials for ORR in fuel cell

Enlightened by the great opportunity of applying graphene composite materials in electrochemical application, researchers turn their eyes to other forms of graphene derivatives, such as heteroatom doped graphene/graphitic materials. Among them, nitrogen containing graphitic materials has attracted a lot interests specifically due to its promising application as cathode materials in fuel cells.

1.2.1 The basic principle of fuel cells

A fuel cell is an electrochemical cell that converts energy from a fuel into electrical energy. In general, it is made up of three segments which are sandwiched together: the anode, the electrolyte, and the cathode (as shown in Figure 1.12). The fuel flows into the cell, and two chemical reactions occur at the interfaces of the three different segments. In such a way, fuel is consumed, water or carbon dioxide is

created, and an electric current is created, which can be used to power electrical devices.

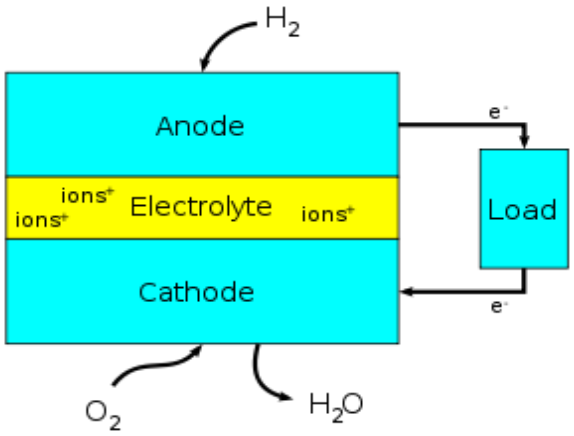

Figure 1.12 Schematic illustration of basic working principle of fuel cells[111]

$$H_2 \rightarrow 2\,H^+ + 2\,e^- \;;\; E^o = 0.0\ V \qquad \textbf{(At Anode)}$$

$$\tfrac{1}{2}\,O_2 + 2\,H^+ + 2\,e^- \rightarrow H_2O;\; E^o = 1.23\ V \qquad \textbf{(At Cathode)}$$

$$H_2 + \tfrac{1}{2}\,O_2 \rightarrow H_2O;\; E^o = 1.23\ V$$

Equation 1.1 The principle reaction in a hydrogen fuel cell

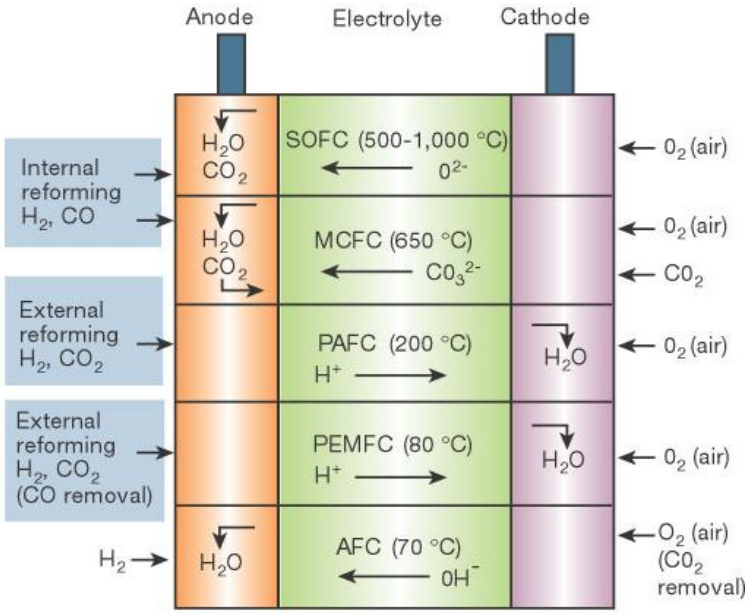

Figure 1.13 Schematic summary of fuel-cell types [112]

As can be seen in the general electrochemical mechanism of a fuel cell described in Equation 1.1: the oxidation reaction takes place at the anode (+) and involves the liberation of electrons. These electrons travel round the external circuit producing electrical energy, and arrive at the cathode (-) to participate in the reduction reaction (for example, $1/2O_2 + 2e^- = O^{2-}$ or $1/2O_2 + 2H^+ + 2e^- = H_2O$). Heat is also produced in addition to producing electrical energy and the reaction products (for example, H_2O and CO_2).

1.2.2 Oxygen reduction reaction in fuel cell

Fuel cell reactions invariably involve oxygen reduction at the cathode. Normally the investigation of a fuel cell focuses on the anode materials since it is involved in the combustion of the fuel and hence directly involved in the performance of the fuel cell. However, it should be noted from Equation 1.1 that oxygen reduction reaction (ORR), in regards of energy, is the demanding reaction in fuel cell operation. Actually, splitting oxygen molecules into oxygen atoms and the subsequent formation of water are currently the rate limiting steps in the process of getting energy from fuel cells, the reaction that restricts overall power production. Till now, the sluggish oxygen reduction is still the main reason for losing efficiency and power density at cathode.[113]

In principle, there are two overall electrochemical pathways to reduce oxygen to water in aqueous electrolytes (as illustrated in Figure 1.14): *Path A* -- direct pathway which needs four electrons to reduce O_2 to water with the rate constant k_1; *Path B* -- H_2O_2 may be produced as intermediate with a rate constant k_2 along the sequential pathway. Subsequently, hydrogen peroxide can be electrochemically reduced to water with the rate constant k_3, desorbed (k_5), or catalytically decomposed on the electrode surface (k_4). In *Path-B*, each step needs 2 electron transfer process.[114,115]

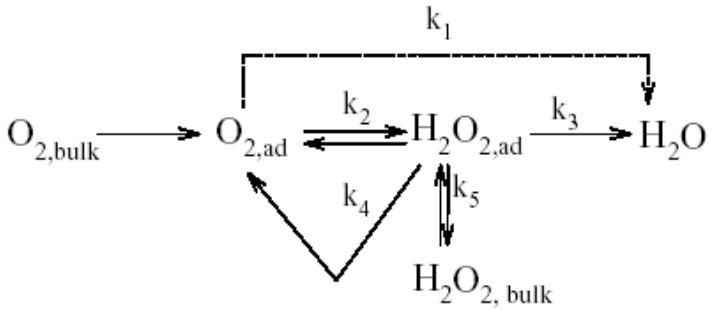

Figure 1.14 Kinetic pathway of reduction from O_2 to water[114]

At high potentials K_1/K_2 is constant with $K_1>k_3$ indicating a direct reduction of oxygen to water than to peroxide. At intermediate potentials, the decrease of k_1/k_2 indicates an increase in the reduction to peroxide. At lower potentials k_1/k_2 becomes less than 1. However, K_3 increases, resulting in further reduction of peroxide to water before it escapes into solution.[114]

On the other hand, the oxygen reduction reactions proceed quite differently from each other when acid or alkaline electrolyte is used in fuel cell. The reactions are listed as follow:

Path A – direct pathway, involves **four-electron reduction**

Acid $O_2 + 4\,H^+ + 4\,e^- \rightarrow 2\,H_2O$; $E^o = 1.229$ V

Base $O_2 + 2\,H_2O + 4\,e^- \rightarrow 4\,HO^-$; $E^o = 0.401$ V

Path B – indirect pathway, involves **two-electron reduction** followed by further two-electron reduction

Acid $O_2 + 2\,H^+ + 2\,e^- \rightarrow H_2O_2$; $E^o = 0.695$ V

$H_2O_2 + 2\,H^+ + 2\,e^- \rightarrow 2\,H_2O$; $E^o = 1.77$ V

Base $O_2 + H_2O + 2\,e^- \rightarrow HO_2^- + HO^-$; $E^o = -0.065$ V

$HO_2^- + H_2O + 2\,e^- \rightarrow 3\,HO^-$; $E^o = 0.867$ V

The thermodynamic equilibrium potential of the reduction of oxygen to H_2O_2 is, in acidic condition for instance, 0.695 V vs. normal hydrogen electrode (NHE).[116,117] Therefore, a mixed potential obtained in an ORR will be about 2.47 V.[118-120]

Compared with the direct four-electron pathway, the stepwise reduction of oxygen (first to hydrogen peroxide and, subsequently, to water) is not favorable for two reasons. One is the kinetic barrier. At the operating potential of the cathode (~1.23V), the equilibrium concentration of H_2O_2 is only ca. 10^{-8} M; so to pass desirable current densities (~1.0 A cm^{-2}) via a stepwise reduction would require a standard heterogeneous rate constant for the reduction of H_2O_2 to H_2O greater than 10^{12} cm s^{-1}. This value far exceeds the collision-limited rate (~10^4 cm s^{-1}). If H_2O_2 were to be consumed by disproportionation to dioxygen and water, the rate constant for this reaction should be near 10^{22} M^{-1} s^{-1}. Clearly, the intermediacy of H_2O_2 in an overall four-electron reduction of oxygen is impractical for fuel cell applications.[121] Another drawback of hydrogen peroxide is that it can attack (oxidize) the active site of metal complexes and thus, causes loss of activity.[122]

However, for most electrocatalysts, oxygen reduction takes place by the formation of a higher energy intermediate, H_2O_2 followed by further reduction to H_2O. It is probably a consequence of the high stability of the O-O bond of oxygen, which has a dissociation energy of 492 kJ/mol.[123] Therefore, finding suitable electrocatalysts that can promote direct four-electron reduction of oxygen molecules is of the greatest interest in fuel cell research.

The essential criteria for better oxygen reduction electrocatalysts are: i) good electronic conductivity; ii) chemical and structural stability during oxygen adsorption and reduction in electrolyte medium; iii) operating temperature; iv) high uptake of oxygen and electrolyte; v) ability to decompose the intermediate H_2O_2 species formed during the reduction process; vi) chemical and thermomechanical

compatibility to electrolyte and interconnector materials; vii) tolerant to contaminants (e.g., halide ions, methanol, NOx, COx, Sox) and viii) low cost.[124-127]

It has been always advocated that platinum (Pt) supported on carbon or alloys of Pt are the best known cathodes for fuel cell applications, since they exhibit good activity and chemical stability under the operating conditions. However, Pt is found to be very sensitive to the contaminants, including organic (benzene, propane) and inorganic (CO, NO_2, SO_2, NH_3, dust strongly adsorbing halides Cl^-, Br^-, I^-) species.[128] In particular, alcohols (–OH) are usually formed at operation voltage (~0.8 V) from the water oxidation as well as corrosion under acidic conditions on the Pt surface which significantly reduces the activity of Pt catalysts.[129] The high cost of Pt is another main hurdle for the commercialization of the Pt electrocatalysts. Due to the five-orders-of-magnitude slower kinetics of the oxygen reduction reaction compared to that of the hydrogen oxidation reaction, most Pt is located at the cathode side.[130] The latter usually contains ten times more Pt than the anode.[131] To reduce the amount of Pt loading at the cathode side, thereby reducing cost, various synthetic approaches are adopted to disperse Pt on suitable support. Among the various supporting materials, carbon is the most attractive one because of its unique features like good electronic conductivity, chemical stability, surface area, mechanical stability, abundance and low cost.[132-135]

Nevertheless, using the most common platinum loadings (0.4 mg/cm^2) on carbon still leads to fuel cell costs that are too high by at least an order of magnitude (two orders of magnitude for transportation applications) to permit commercialization.[136]

In aim of replacing Pt as well as other noble metal electrocatalysts, a series of non-noble metal electrocatalysts were invented including transition metal chalcogenides and transition metal macrocyclic compounds.[122,137-140] More recently,

metal-free catalysts[141-150] for ORR have attracted enormous attention as the alternative electrocatalyst. In particular, nitrogen-doped carbon materials exhibit excellent electrocatalytic activity for ORR as a result of their unique electronic properties derived from the conjugation between the nitrogen lone-pair electrons and the π-system of graphene units in carbon.[116,151-153]

1.2.3 Metal complex of N-containing macrocycles as cathodic catalyses in ORR

As mention above, a great deal of research has focused on cathode electrocatalyst development for the ORR. Metal–N4 macrocycles, such as Fe- and Co-macrocycles, are important non-noble catalysts which have attracted attention due to their reasonable activity and remarkable selectivity towards the ORR.[122,154] In 1964, Jasinski reported the first ORR catalysts with the macrocyclic structure containing nitrogen–metal coordination, the Co-phthalocyanine, adsorbed on carbon.[140] Shortly thereafter, the desires for a low cost, catalytic oxygen electrode for fuel cells have accelerated the examination of various transition metal macrocycles as potential catalysts. Metal phthalocyanines, porphyrines, Schiff bases and related derivatives are frequently investigated. All these materials display an activity for the reduction of oxygen.[122]

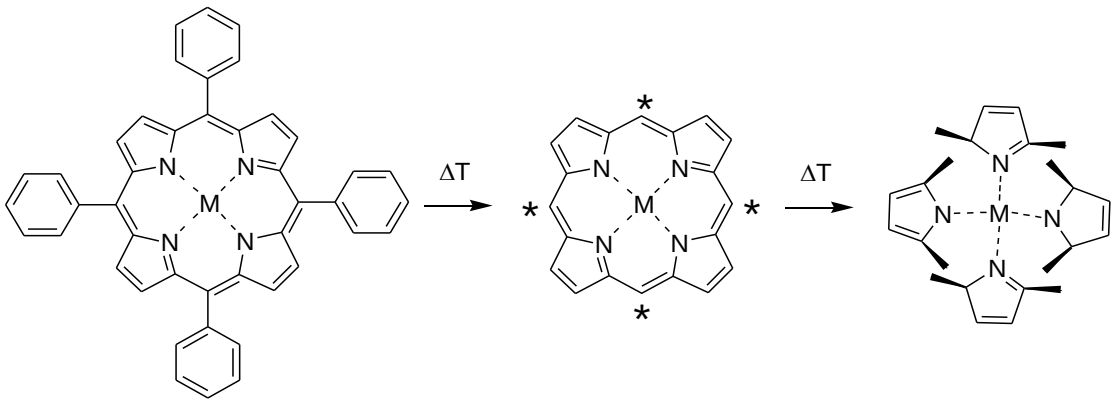

Figure 1.15 A structural scheme of metal–N4 macrocycles and the structure changes during thermolysis

As shown in Figure 1.15, these molecules, in general, have square planar structures with the metal atom symmetrically surrounded by four nitrogen atoms. The nitrogen atoms lie in each ring systems, which are connected by carbon atoms (porphyrins) or nitrogen atoms (phthalocyanines). Catalytic activity for oxygen reduction is found only when metal atoms are bounded with the ligand, which has a cyclic conjugation of 'π' electrons.[123]

In addition, this class of catalysts usually shows inertness to alcohol oxidation, and many of them can catalyze the ORR to water through a four-electron process without significant production of peroxide.[155] A major drawback of this kind of catalyst is its general low stability in acidic media (or in the PEM fuel cell operation environment).[139,156] It has been suggested that this can be attributed primarily to the loss of the active site caused by the attack of hydrogen peroxide generated during the O_2 reduction.[155,157]

Macrocyclic M-N4 complexes of a great variety of metals have been tested first to evaluate the critical influence of the nature of the metallic centers on the catalytic activity. With the experimental evidences accumulated over the years, it has been demonstrated that macrocyclic complexes of Fe and Co exhibit the highest activity towards the ORR. In some particular ligands, Fe shows better activity, while Co is better for other ligands.[158] Oxygen reduction on most Co chelates gives hydrogen peroxide as the main product of the reaction[123] which indicates a two-electron transfer pathway in ORR. The activity of Fe phthalocyanine is lower than that of Co phthalocyanines, whereas the activity of Fe porphyrins is better than that of Co porphyrins. However, they suffer from low electrochemical stability, and they decompose either via hydrolysis in the electrolyte or attack of the macrocycle ring by peroxy intermediates generated during oxygen reduction.[122,124,132,158]

It has been found that the nature of the ligand is also an important role. A

relation exists between an increasing hydrogen peroxide decomposition rate constant and increasing oxygen reduction activity in acid solution. All the experimental results show that metal porphyrins and phthalocyanines have the advantage, in comparison to Schiff bases, that their chemical properties can be manipulated through substitution in the β- or meso-positions. Also, electrocatalytic activity and stability in acidic media appear to be enhanced for metal porphyrins and metallo- phthalocyanines with respect to the Schiff bases.[122,158]

Earlier studies have also demonstrated that the carbon support plays an important role in improving the activity and stability of metal macrocycles.[159,160] In addition to increase the conductivity of the electrodes, the surface properties of the carbon support have a significant effect on the degree of catalyst dispersion. The most commonly used carbon supports, including carbon black, active carbon, and graphite, which have been specifically employed in M–N/C catalyst systems. The most popular carbon supports are Vulcan XC 72 and Black Pearls.

It was also discovered that heat treatment of the M-macrocycles in an inert atmosphere can significantly improve ORR activity as well as stability.[161] Van Veen et al.[162] discussed four models in an effort to explain this effect: i) improving the dispersion of the supported chelate; ii) catalyzing the formation of a special type of carbon, which is actually the active phase; iii) generating the M–N species; and iv) promoting a reaction between chelate and subjacent carbon in such a way as to modify the electronic structure of the central metal ion with retention of its N_4 coordinated environment. After heat treatment, the stability of those catalysts improved significantly and the corresponding oxygen reduction is better suited to a four-electron pathway.[154] However, this improvement is still not enough for practical applications.[139]

On the other hand, the multiple metal center-N4 macrocycles were invented as

a new class of electrocatalysts of ORR. Collman [121] and Steiger *et al.*[163] investigated the oxygen reduction activity of dicobalt face-to-face porphyrins, other binuclear and polynuclear Co phthalocyanines and found the direct reduction to water in acidic medium.

For a theoretic explanation of the activity of transition metal complexes of N-containing macrocycles, different concepts were developed. The well-accepted explanation is the redox catalysis concept. In this concept the redox potential of the central metal ion is crucial. The interaction of O_2 molecules with the metal center in the macrocycle causes a partial electron transfer from the frontier orbitals of the metal to the frontier orbitals of the O_2 molecules. The precursor or adduct formed, undergoes further reduction to give intermediate species like peroxide which can be the product or decomposed/reduced further to give water. The crucial steps in the catalytic cycle are given as follows:

$$M\text{-}N4(III)OH + e^- \rightarrow M\text{-}N4(II) + OH^-$$

$$M\text{-}N4(II) + O_2 \rightarrow M\text{-}N4(III)\text{-}O^{2-}$$

$$M\text{-}N4(III)\text{-}O^{2-} + e^- \rightarrow M\text{-}N4(II) + \text{intermediates}$$

According to this redox mechanism, the redox potential of M(III)/M(II) must be located within an appropriate, rather narrow window of potential values to obtain maximum activity. However, recent studies of different substituted phthalocyanines have revealed that the lower the electron density on the metal center, the higher the catalytic activity for O_2 reduction. For studies conducted with substituted Co phthalocyanines (CoPc), it was also found that the greater reducing power a CoPc has, the less active it shows in O_2 reduction. This was explained in terms of the chemical intermolecular hardness of the system, i.e., the more the separation between the energy of the frontier orbitals of the donor (Co-Pc) and the acceptor (O_2), the less the reactivity. These studies reveal that questions still remain open on the role of the redox potential in determining the catalytic activity. However, most

works agree that the redox mechanism requires the stability of the 3^+ and 2^+ oxidation states of the metal, needed for oxygen activation in the potential region of interest for O_2 reduction. It has been found that Co and Fe porphyrins are active as long as the 3^+ oxidation state is accessible at a given potential. However, for some Co complexes, O_2 reduction takes place at potentials far below the potential of the Co(III)/Co(II).[121] Most works also demonstrate that the Fe(II)/Fe(I) redox couple is the one that plays the crucial role in the activation of the O_2 molecule.[123] On the other hand, there were a large number of works trying to explain the 4-electron mechanism of pyrolyzed metal–N4 macrocycles. Unfortunately however, since the structure of MN_4Cx species generated by the pyrolysis was not known, mechanism was not well established yet.

In general, the catalytic activity and stability of metal complex of N-containing macrocycles (both pyrolyzed and non-pyrolyzed) are still below the performance of Pt-based catalyst. Therefore, there is still a long way to get breakthrough in the ORR catalytic activity and stability of these non-noble catalysts. It is believed that under the strong driving force of fuel cell commercialization, Pt-free cathode catalysts with methanol tolerance, such as Fe– and Co–N/C, are attractive candidates for addressing the cost issue of fuel cell catalysts.[122,132,158]

1.2.4 N-containing graphitic materials as cathodic catalyses in ORR

As discussed in chapter 1.2.1, carbon is an ideal support for electrocatalysts in fuel cell. In order to further improve the catalytic properties, nitrogen was doped into porous carbon nanostructure materials.[143] As is known, nitrogen-doped carbon nanotubes/nanofibers (N-CNT/N-CNF) loaded with metal catalyst have shown enhanced catalytic activity toward oxygen reduction reaction (ORR).[116,142,164] Moreover, nitrogen-doped carbon supports are also expected to improve the

durability of the resultant catalysts, because of the enhanced π bonding [165-167], the basic property,[168] and the strong electron donor behavior of nitrogen.[169-172]

Other than only working as catalyst support, N-carbon itself without incorporation of metal species also shows catalytic activity towards ORR. Some researchers argued that the metal (e.g., Pt, Fe, Co) is not required for ORR in nitrogen-doped carbon,[173] even though only lower activity was achieved via N-carbon catalysts without metals.[174] It has been shown[166] that N-doped CNF electrodes exhibited improved electrocatalytic activity towards ORR. In both neutral and alkaline conditions, the N-doped CNFs demonstrate over a 100-fold increase in catalytic activity for H_2O_2 decomposition.[166,175] Such values (of catalytic reaction rates) are within an order of magnitude of decomposition rates reported for most active catalysts, e.g., Pt/C.[176] The authors attributed the enhanced activity to the presence of edge plane defects (the defects appearing at the edge of graphitic plane) and nitrogen functionalities within the CNF structure.[177] It is observed that the sidewalls of the N-doped CNFs contain more dislocations and disruptions (irregular curvature) in the graphene stacking, which is due to the propensity of incorporated nitrogen to form pentagonal defects in the graphene layer.[178] The catalytic activity of N-CNFs toward ORR and H_2O_2 decomposition is a direct result of such nitrogen doping.[166]

Thereafter, nitrogen doping has repeatedly been reported to increase the basic nature and catalytic activity of the graphitic carbon towards oxygen reduction reaction. In 2009, Dai et al firstly synthesized vertically aligned nitrogen- containing carbon nanotubes (VA-NCNTs) by using by pyrolyzing iron(II) phthalocyanine (FePc) at 800-1100°C with additional NH_3. Such N-doped CNT could act as a metal-free electrode with a much better electrocatalytic activity, long-term operation stability, and tolerance to crossover effect than platinum for oxygen reduction in alkaline fuel cells.[148] This work has brought N-doped CNT into the scope as electrocatalysts for

ORR.[179,180] Later on, with the fast booming of graphene-base materials, N-doped graphene has become the newest materials extensively investigated for ORR. Nitrogen-doped graphene (N-graphene) could be produced by chemical vapor deposition of methane in the presence of ammonia. The resultant N-graphene was demonstrated to act as a metal-free electrode also with an improved electrocatalytic activity via a four-electron pathway, long-term operation stability and tolerance to crossover effect than platinum for oxygen reduction in alkaline fuel cells.[149] Besides, several other types of N-doped graphitic carbon with large surface area were created, mainly by precursor-defined pyrolysis with the help of silicon based porous hard templates.[146,147,150]

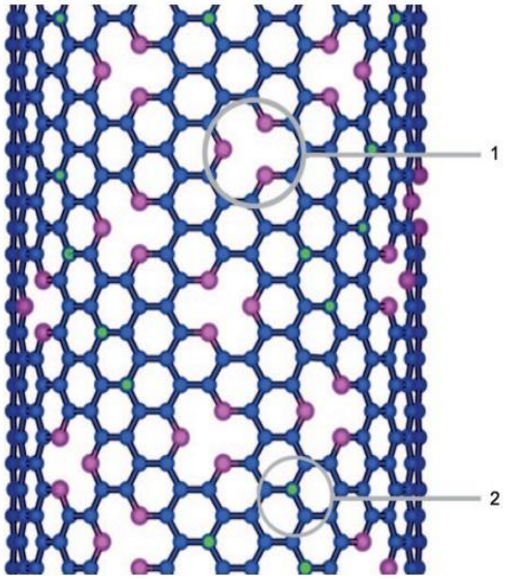

Figure 1.16 N-doped CNTs exhibiting two types of nitrogen: 1) pyridine-type in which each N atom is bonded to two C atoms; responsible for creating cavities and corrugation in the structure, and 2) substitutional N atoms, which are bonded to three C atoms.[181]

Nitrogen-doping into carbon can be performed either directly during synthesis or by post-synthetic treatment.[182] However, post-treatment often yields a nitrogen

doping just on the surface of carbon materials,[116,183-185] and thus does not change the bulk material properties. In contrast, doping of carbons during solid synthesis by using nitrogen containing precursors can lead to a homogeneous incorporation of nitrogen into the entire carbon material. Indeed, several N-doped carbons have been prepared using this method. For instance, high surface area porous carbons with high nitrogen content can be produced by pyrolysis of defined organic precursors such as melamine,[171,181] benzylamine,[186] acetonitrile,[187,188] N-heterocycles,[189-191], perylene diimides or phthalocyanines.[192] Besides, N-doped CNTs and CNFs have been synthesized by methods similar to the synthesis of pristine CNTs but with a nitrogen containing source as precursor.

In nitrogen-doped carbon, it is inferred that the performance of these materials crucially depends on the amount of nitrogen in the carbon host as well as its local structure.[182] Either pyridinic or pyrrol/pyridone type nitrogen was responsible for the ORR activity of carbon.[193] However there are still controversies over this topic: Ozkan et al.[142] believed that, even though a significantly higher amount of pyridinic nitrogen results in a better activity of catalyst, pyridinic nitrogen itself may not be the active site for ORR, but a activator for edge plane exposure (the plane in which pyridinic nitrogen is found). At such edge position many electrocatalytic reactions show increased kinetics. Oxygen could not only be reduced to peroxide when it reacted on the basal plane of nitrogen-doped carbon,[169,172] but could potentially be reduced further to H_2O when it reacted at the edge.[116,169,172,194] Furthermore, the samples that expose more edge planes with pyridinic nitrogen were found to be more selective towards 4-electron transfer process. Some of the modeling simulation could propose that a high nitrogen content and an edge plane exposure of N-doped graphitic nanostructures lead to high catalytic reactivity.[116,195] The selectivity of the catalysts for complete oxygen reduction to water followed a trend similar to the activity.

1.3 General motivation

As previously discussed, graphene, as a new wonder land in new carbon electrode materials and composite materials, has revealed numerous unknown possibilities as well as open questions. As chemical reduction of GO seems to be, till now, the only approach to produce graphene (ReG) on a sufficient scale, one of the key issues is how to mend the defects remaining in ReG and to increase its properties (conductivity, mechanical strengths etc.) as much as possible. In this dissertation, we will address this issue with our new approaches in creating novel graphene-based composite materials.

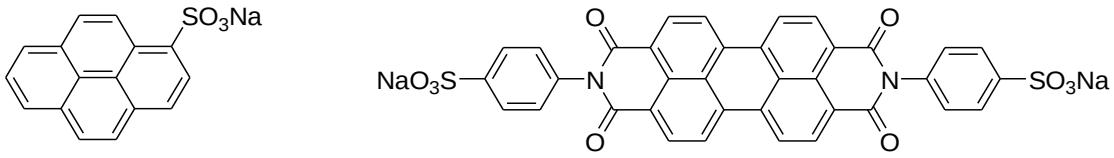

Figure 1.17 pyrene-1-sulfonic acid sodium salt (PyS) and diasodium salt of 3,4,9,10-perylenetetracarboxylic diimide bisbenzenesulfonic acid (PDI)

In chapter 2 we will present a novel approach to produce graphene composites with two well-known organic hole and electron semiconducting materials, pyrene-1-sulfonic acid sodium salt (PyS) as an electronic donor, and the diasodium salt of 3,4,9,10-perylenetetracarboxylic diimide bisbenzenesulfonic acid (PDI) as an electronic acceptor (as shown in Figure 1.17). They are intentionally selected, in that they are polyaromatic molecules decorated with water-soluble moieties. The noncovalent functionalization of graphene by these two aromatic molecules greatly enhances the aqueous processability of ReG sheets in water, and the further thermal annealing successfully mends the defects and improves the conductivity of the ReG film. To test the electronic and optical properties, the as-made ReG film is applied as

TGF in polymer solar cells and provides a comparable total efficiency to that of ITO TGFs

In chapter 3 we try to further improve the conductivity and mechanical strength of the ReG films by composite graphene with its 1D analogue – carbon nanotubes (CNT). Other than using physical mixing, covalent functionalization is applied as an effective method to ensure a close interaction between graphene and CNTs. We firstly present an unprecedented graphene-cobalt complex (**ReG-Co**), which possesses the advantages of homogenous distribution and covalent functionalization of organocobalt moieties [$C_2Co_2(CO)_6$] on chemically reduced graphene oxide sheets (**ReG**). The covalent functionalization of ReG via organic reaction results in **ReG-Co** precursor with good solution processability in organic solvents. It allows a ready fabrication of free-standing films with tunable dimension. Moreover, the organometallic species of Co ([$C_2Co_2(CO)_6$]) covalently anchored on the **ReG** plane can serve as catalytic spots for CNT growth. In this way, highly conductive free-standing graphene/CNT composite films can be created based on an acetylene-assisted thermolysis approach. Both the mechanical flexibility and electrical conductivity of graphene/CNT composite films are superior to those of thermally treated pristine graphene films.

Rather than only investigating new graphene-based electrode materials, we also make our attempts to create nitrogen-doped graphitic electrode materials, which are hoped to enable a combination of bulk and surface properties of such materials to the overall behavior in fuel cells. For such purposes two different kinds of precursors, namely transition metal macrocycles and nitrogen containing polyaromatic cations, were used to build up N-doped graphitic cathode materials as electrochemical catalyst for oxygen reduction reaction.

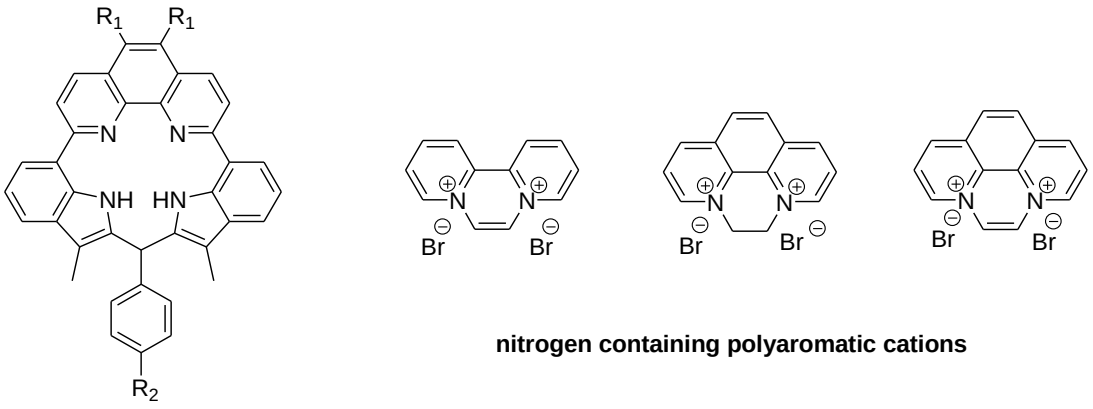

Figure 1.18 Schematic illusions of transition metal macrocycles and nitrogen containing polyaromatic cations (NPCs)

In chapter 4, we develop a series of novel N-containing macrocycles (NHM) base on 1,10-phenanthroline and indole. As mentioned previously, a large number of macrocyclic transition metal complexes have been developed as oxygen reduction catalysts, but most seem to perform only at rather negative potentials and to effect only a two-electron reduction of dioxygen to hydrogen peroxide. Therefore, NHM-Co was synthesized as novel Co-macrocycles in attempt to achieve 4-electron transfer in ORR.

Consequently, even if NHMs could be aromatized into fully conjugated structures; Zn and Co can still be successfully complexed into these macrocycles. The Co complexes of NHM (NHM-Co) were applied as transition metal catalyst for ORR in fuel cells which exhibited unfortunately only a 2-eletron kinetic reduction of oxygen. To further improve the electrocatalytic activity, NHM-Co was pyrolyzed at 700 ^{o}C in argon. As a consequence, the oxygen reduction activity of NHM-Co after pyrolysis was greatly enhanced to a 4-eletron transfer kinetics.

In chapter 5, we will demonstrate the fabrication of nitrogen-doped ordered mesoporous graphitic carbon arrays (NMGCAs) based on N-containing polyaromatic

cations (**NPC**). This approach involves a metal-free nanocasting technology which is simple, cost-effective, and readily reproducible by using ordered mesoporous silica SBA-15 as template. The resulting nitrogen-doped carbon materials could serve as true metal-free catalysts which exhibited good electrocatalytic activity towards ORR.

Most importantly, we have compared the electrocatalytic performance of NMGCA electrodes produced via different casting procedures, at various pyrolysis temperatures and from different precursors to infer how these parameters could influence the final catalytic properties for ORR. The utmost goal is to build up a system panel for a rational design of precursor and conditions for producing highly active NMGCA cathode in fuel cell.

Reference:

(1) Geim, A. K.; Novoselov, K. S. *Nature Materials* **2007**, *6*, 183.

(2) Allen, M. J.; Tung, V. C.; Kaner, R. B. *Chemical Reviews* **2010**, *110*, 132.

(3) Novoselov, K. S.; Geim, A. K.; Morozov, S. V.; Jiang, D.; Katsnelson, M. I.; Grigorieva, I. V.; Dubonos, S. V.; Firsov, A. A. *Nature* **2005**, *438*, 197.

(4) Chen, J. H.; Jang, C.; Xiao, S. D.; Ishigami, M.; Fuhrer, M. S. *Nature Nanotechnology* **2008**, *3*, 206.

(5) Novoselov, K. S.; Geim, A. K.; Morozov, S. V.; Jiang, D.; Zhang, Y.; Dubonos, S. V.; Grigorieva, I. V.; Firsov, A. A. *Science* **2004**, *306*, 666.

(6) Zhang, Y. B.; Tan, Y. W.; Stormer, H. L.; Kim, P. *Nature* **2005**, *438*, 201.

(7) http://en.wikipedia.org/wiki/Graphene.

(8) Morozov, S. V.; Novoselov, K. S.; Katsnelson, M. I.; Schedin, F.; Elias, D. C.; Jaszczak, J. A.; Geim, A. K. *Physical Review Letters* **2008**, *100*.

(9) Novoselov, K. S.; Jiang, Z.; Zhang, Y.; Morozov, S. V.; Stormer, H. L.; Zeitler, U.; Maan, J. C.; Boebinger, G. S.; Kim, P.; Geim, A. K. *Science* **2007**, *315*, 1379.

(10) Gonzalez, J.; Guinea, F.; Vozmediano, M. A. H. *Physical Review Letters* **1996**, *77*, 3589.

(11) Gorbar, E. V.; Gusynin, V. P.; Miransky, V. A.; Shovkovy, I. A. *Physical Review B* **2002**, *66*.

(12) Katsnelson, M. I.; Novoselov, K. S.; Geim, A. K. *Nature Physics* **2006**, *2*, 620.

(13) Katsnelson, M. I. *European Physical Journal B* **2006**, *51*, 157.

(14) Schakel, A. M. J. *Physical Review D* **1991**, *43*, 1428.

(15) Semenoff, G. W. *Physical Review Letters* **1984**, *53*, 2449.

(16) Fradkin, E. *Physical Review B* **1986**, *33*, 3263.

(17) Haldane, F. D. M. *Physical Review Letters* **1988**, *61*, 2015.

(18) Nair, R. R.; Blake, P.; Grigorenko, A. N.; Novoselov, K. S.; Booth, T. J.; Stauber, T.; Peres, N. M. R.; Geim, A. K. *Science* **2008**, *320*, 1308.

(19) Ni, Z. H.; Wang, H. M.; Kasim, J.; Fan, H. M.; Yu, T.; Wu, Y. H.; Feng, Y. P.; Shen, Z. X. *Nano Letters* **2007**, *7*, 2758.

(20) Balandin, A. A.; Ghosh, S.; Bao, W. Z.; Calizo, I.; Teweldebrhan, D.; Miao, F.; Lau, C. N. *Nano Letters* **2008**, *8*, 902.

(21) Cai, W. W.; Moore, A. L.; Zhu, Y. W.; Li, X. S.; Chen, S. S.; Shi, L.; Ruoff, R. S. *Nano Letters* **2010**, *10*, 1645.

(22) Zhu, Y. W.; Murali, S.; Cai, W. W.; Li, X. S.; Suk, J. W.; Potts, J. R.; Ruoff, R. S. *Adv. Mater.* **2010**, *22*, 3906.

(23) Seol, J. H.; Jo, I.; Moore, A. L.; Lindsay, L.; Aitken, Z. H.; Pettes, M. T.; Li, X. S.; Yao, Z.; Huang, R.; Broido, D.; Mingo, N.; Ruoff, R. S.; Shi, L. *Science* **2010**, *328*, 213.

(24) Kudin, K. N.; Scuseria, G. E.; Yakobson, B. I. *Physical Review B* **2001**, *64*.

(25) Van Lier, G.; Van Alsenoy, C.; Van Doren, V.; Geerlings, P. *Chemical Physics Letters* **2000**, *326*, 181.

(26) Frank, I. W.; Tanenbaum, D. M.; Van der Zande, A. M.; McEuen, P. L. *Journal of Vacuum Science & Technology B* **2007**, *25*, 2558.

(27) Lee, C.; Wei, X. D.; Kysar, J. W.; Hone, J. *Science* **2008**, *321*, 385.

(28) Gomez-Navarro, C.; Burghard, M.; Kern, K. *Nano Letters* **2008**, *8*, 2045.

(29) Dikin, D. A.; Stankovich, S.; Zimney, E. J.; Piner, R. D.; Dommett, G. H. B.; Evmenenko, G.;

Nguyen, S. T.; Ruoff, R. S. *Nature* **2007**, *448*, 457.

(30) Geim, A. K. *Science* **2009**, *324*, 1530.

(31) Park, S.; Ruoff, R. S. *Nature Nanotechnology* **2009**, *4*, 217.

(32) Hernandez, Y.; Nicolosi, V.; Lotya, M.; Blighe, F. M.; Sun, Z. Y.; De, S.; McGovern, I. T.; Holland, B.; Byrne, M.; Gun'ko, Y. K.; Boland, J. J.; Niraj, P.; Duesberg, G.; Krishnamurthy, S.; Goodhue, R.; Hutchison, J.; Scardaci, V.; Ferrari, A. C.; Coleman, J. N. *Nature Nanotechnology* **2008**, *3*, 563.

(33) Sutter, P. *Nature Materials* **2009**, *8*, 171.

(34) Berger, C.; Song, Z. M.; Li, X. B.; Wu, X. S.; Brown, N.; Naud, C.; Mayou, D.; Li, T. B.; Hass, J.; Marchenkov, A. N.; Conrad, E. H.; First, P. N.; de Heer, W. A. *Science* **2006**, *312*, 1191.

(35) Sutter, P. W.; Flege, J. I.; Sutter, E. A. *Nature Materials* **2008**, *7*, 406.

(36) Coraux, J.; N'Diaye, A. T.; Busse, C.; Michely, T. *Nano Letters* **2008**, *8*, 565.

(37) Reina, A.; Jia, X. T.; Ho, J.; Nezich, D.; Son, H. B.; Bulovic, V.; Dresselhaus, M. S.; Kong, J. *Nano Letters* **2009**, *9*, 30.

(38) Yu, Q. K.; Lian, J.; Siriponglert, S.; Li, H.; Chen, Y. P.; Pei, S. S. *Applied Physics Letters* **2008**, *93*.

(39) Kim, K. S.; Zhao, Y.; Jang, H.; Lee, S. Y.; Kim, J. M.; Ahn, J. H.; Kim, P.; Choi, J. Y.; Hong, B. H. *Nature* **2009**, *457*, 706.

(40) Li, X. S.; Cai, W. W.; An, J. H.; Kim, S.; Nah, J.; Yang, D. X.; Piner, R.; Velamakanni, A.; Jung, I.; Tutuc, E.; Banerjee, S. K.; Colombo, L.; Ruoff, R. S. *Science* **2009**, *324*, 1312.

(41) Oshima, C.; Nagashima, A. *Journal of Physics-Condensed Matter* **1997**, *9*, 1.

(42) Bae, S.; Kim, H.; Lee, Y.; Xu, X. F.; Park, J. S.; Zheng, Y.; Balakrishnan, J.; Lei, T.; Kim, H. R.; Song, Y. I.; Kim, Y. J.; Kim, K. S.; Ozyilmaz, B.; Ahn, J. H.; Hong, B. H.; Iijima, S. *Nature Nanotechnology* **2010**, *5*, 574.

(43) Li, D.; Muller, M. B.; Gilje, S.; Kaner, R. B.; Wallace, G. G. *Nature Nanotechnology* **2008**, *3*, 101.

(44) Buchsteiner, A.; Lerf, A.; Pieper, J. *J. Phys. Chem. B* **2006**, *110*, 22328.

(45) Dreyer, D. R.; Park, S.; Bielawski, C. W.; Ruoff, R. S. *Chemical Society Reviews* **2010**, *39*, 228.

(46) Stankovich, S.; Dikin, D. A.; Piner, R. D.; Kohlhaas, K. A.; Kleinhammes, A.; Jia, Y.; Wu, Y.; Nguyen, S. T.; Ruoff, R. S. *Carbon* **2007**, *45*, 1558.

(47) Cai, W. W.; Piner, R. D.; Stadermann, F. J.; Park, S.; Shaibat, M. A.; Ishii, Y.; Yang, D. X.; Velamakanni, A.; An, S. J.; Stoller, M.; An, J. H.; Chen, D. M.; Ruoff, R. S. *Science* **2008**, *321*, 1815.

(48) Lerf, A.; He, H. Y.; Forster, M.; Klinowski, J. *J. Phys. Chem. B* **1998**, *102*, 4477.

(49) He, H. Y.; Klinowski, J.; Forster, M.; Lerf, A. *Chemical Physics Letters* **1998**, *287*, 53.

(50) He, H. Y.; Riedl, T.; Lerf, A.; Klinowski, J. *Journal of Physical Chemistry* **1996**, *100*, 19954.

(51) Stankovich, S.; Piner, R. D.; Chen, X. Q.; Wu, N. Q.; Nguyen, S. T.; Ruoff, R. S. *Journal of Materials Chemistry* **2006**, *16*, 155.

(52) Lomeda, J. R.; Doyle, C. D.; Kosynkin, D. V.; Hwang, W. F.; Tour, J. M. *Journal of the American Chemical Society* **2008**, *130*, 16201.

(53) Tung, V. C.; Allen, M. J.; Yang, Y.; Kaner, R. B. *Nature Nanotechnology* **2009**, *4*, 25.

(54) Gilje, S.; Han, S.; Wang, M.; Wang, K. L.; Kaner, R. B. *Nano Letters* **2007**, *7*, 3394.

(55) Stankovich, S.; Dikin, D. A.; Dommett, G. H. B.; Kohlhaas, K. M.; Zimney, E. J.; Stach, E. A.; Piner, R. D.; Nguyen, S. T.; Ruoff, R. S. *Nature* **2006**, *442*, 282.

(56) Wang, G. X.; Yang, J.; Park, J.; Gou, X. L.; Wang, B.; Liu, H.; Yao, J. *J. Phys. Chem. C* **2008**, *112*,

8192.

(57) Si, Y.; Samulski, E. T. *Nano Letters* **2008**, *8*, 1679.

(58) Muszynski, R.; Seger, B.; Kamat, P. V. *J. Phys. Chem. C* **2008**, *112*, 5263.

(59) Wang, X.; Zhi, L. J.; Mullen, K. *Nano Letters* **2008**, *8*, 323.

(60) Schniepp, H. C.; Li, J. L.; McAllister, M. J.; Sai, H.; Herrera-Alonso, M.; Adamson, D. H.; Prud'homme, R. K.; Car, R.; Saville, D. A.; Aksay, I. A. *J. Phys. Chem. B* **2006**, *110*, 8535.

(61) Liu, N.; Luo, F.; Wu, H. X.; Liu, Y. H.; Zhang, C.; Chen, J. *Advanced Functional Materials* **2008**, *18*, 1518.

(62) Boukhvalov, D. W.; Katsnelson, M. I. *Journal of the American Chemical Society* **2008**, *130*, 10697.

(63) McAllister, M. J.; Li, J. L.; Adamson, D. H.; Schniepp, H. C.; Abdala, A. A.; Liu, J.; Herrera-Alonso, M.; Milius, D. L.; Car, R.; Prud'homme, R. K.; Aksay, I. A. *Chem. Mat.* **2007**, *19*, 4396.

(64) Su, Q.; Pang, S. P.; Alijani, V.; Li, C.; Feng, X. L.; Mullen, K. *Adv. Mater.* **2009**, *21*, 3191.

(65) Paul, D. R.; Robeson, L. M. *Polymer* **2008**, *49*, 3187.

(66) Compton, O. C.; Nguyen, S. T. *Small* **2010**, *6*, 711.

(67) Veca, L. M.; Lu, F. S.; Meziani, M. J.; Cao, L.; Zhang, P. Y.; Qi, G.; Qu, L. W.; Shrestha, M.; Sun, Y. P. *Chemical Communications* **2009**, 2565.

(68) Liu, Z.; Robinson, J. T.; Sun, X. M.; Dai, H. J. *Journal of the American Chemical Society* **2008**, *130*, 10876.

(69) Zhang, L.; Liang, J. J.; Huang, Y.; Ma, Y. F.; Wang, Y.; Chen, Y. S. *Carbon* **2009**, *47*, 3365.

(70) Liu, Z. B.; Xu, Y. F.; Zhang, X. Y.; Zhang, X. L.; Chen, Y. S.; Tian, J. G. *J. Phys. Chem. B* **2009**, *113*, 9681.

(71) Niyogi, S.; Bekyarova, E.; Itkis, M. E.; McWilliams, J. L.; Hamon, M. A.; Haddon, R. C. *Journal of the American Chemical Society* **2006**, *128*, 7720.

(72) Sinitskii, A.; Dimiev, A.; Corley, D. A.; Fursina, A. A.; Kosynkin, D. V.; Tour, J. M. *ACS Nano* **2010**, *4*, 1949.

(73) Georgakilas, V.; Bourlinos, A. B.; Zboril, R.; Steriotis, T. A.; Dallas, P.; Stubos, A. K.; Trapalis, C. *Chemical Communications* **2010**, *46*, 1766.

(74) Li, X. L.; Zhang, G. Y.; Bai, X. D.; Sun, X. M.; Wang, X. R.; Wang, E.; Dai, H. J. *Nature Nanotechnology* **2008**, *3*, 538.

(75) Xu, Y. X.; Bai, H.; Lu, G. W.; Li, C.; Shi, G. Q. *Journal of the American Chemical Society* **2008**, *130*, 5856.

(76) Hao, R.; Qian, W.; Zhang, L.; Hou, Y. *Chemical Communications* **2008**, 6576.

(77) Bai, H.; Xu, Y.; Zhao, L.; Li, C.; Shi, G. *Chemical Communications* **2009**, 1667.

(78) Liang, Y. Y.; Wu, D. Q.; Feng, X. L.; Mullen, K. *Adv. Mater.* **2009**, *21*, 1679.

(79) Becerril, H. A.; Mao, J.; Liu, Z.; Stoltenberg, R. M.; Bao, Z.; Chen, Y. *ACS Nano* **2008**, *2*, 463.

(80) Watcharotone, S.; Dikin, D. A.; Stankovich, S.; Piner, R.; Jung, I.; Dommett, G. H. B.; Evmenenko, G.; Wu, S. E.; Chen, S. F.; Liu, C. P.; Nguyen, S. T.; Ruoff, R. S. *Nano Letters* **2007**, *7*, 1888.

(81) Eda, G.; Fanchini, G.; Chhowalla, M. *Nature Nanotechnology* **2008**, *3*, 270.

(82) Cote, L. J.; Kim, F.; Huang, J. X. *Journal of the American Chemical Society* **2009**, *131*, 1043.

(83) Biswas, S.; Drzal, L. T. *Nano Letters* **2009**, *9*, 167.

(84) De, S.; King, P. J.; Lotya, M.; O'Neill, A.; Doherty, E. M.; Hernandez, Y.; Duesberg, G. S.; Coleman, J. N. *Small* **2010**, *6*, 458.

(85) Zhu, Y. W.; Cai, W. W.; Piner, R. D.; Velamakanni, A.; Ruoff, R. S. *Applied Physics Letters* **2009**,

95.

(86) Blake, P.; Brimicombe, P. D.; Nair, R. R.; Booth, T. J.; Jiang, D.; Schedin, F.; Ponomarenko, L. A.; Morozov, S. V.; Gleeson, H. F.; Hill, E. W.; Geim, A. K.; Novoselov, K. S. *Nano Letters* **2008**, *8*, 1704.

(87) Wu, J. B.; Agrawal, M.; Becerril, H. A.; Bao, Z. N.; Liu, Z. F.; Chen, Y. S.; Peumans, P. *ACS Nano* **2010**, *4*, 43.

(88) Cai, W. W.; Zhu, Y. W.; Li, X. S.; Piner, R. D.; Ruoff, R. S. *Applied Physics Letters* **2009**, *95*.

(89) Winter, M.; Besenhard, J. O.; Spahr, M. E.; Novak, P. *Adv. Mater.* **1998**, *10*, 725.

(90) Liu, Y. H.; Xue, J. S.; Zheng, T.; Dahn, J. R. *Carbon* **1996**, *34*, 193.

(91) Lee, J. K.; Smith, K. B.; Hayner, C. M.; Kung, H. H. *Chemical Communications* **2010**, *46*, 2025.

(92) Wang, D. H.; Choi, D. W.; Li, J.; Yang, Z. G.; Nie, Z. M.; Kou, R.; Hu, D. H.; Wang, C. M.; Saraf, L. V.; Zhang, J. G.; Aksay, I. A.; Liu, J. *ACS Nano* **2009**, *3*, 907.

(93) Yao, J.; Shen, X. P.; Wang, B.; Liu, H. K.; Wang, G. X. *Electrochemistry Communications* **2009**, *11*, 1849.

(94) Paek, S. M.; Yoo, E.; Honma, I. *Nano Letters* **2009**, *9*, 72.

(95) Ji, F.; Li, Y. L.; Feng, J. M.; Su, D.; Wen, Y. Y.; Feng, Y.; Hou, F. *Journal of Materials Chemistry* **2009**, *19*, 9063.

(96) Chen, D.; Tang, L. H.; Li, J. H. *Chemical Society Reviews* **2010**, *39*, 3157.

(97) Chen, S.; Zhu, J. W.; Wu, X. D.; Han, Q. F.; Wang, X. *ACS Nano* **2010**, *4*, 2822.

(98) Zhang, Y. P.; Li, H. B.; Pan, L. K.; Lu, T.; Sun, Z. *Journal of Electroanalytical Chemistry* **2009**, *634*, 68.

(99) Yu, D. S.; Dai, L. M. *Journal of Physical Chemistry Letters* **2010**, *1*, 467.

(100) Wu, Q.; Xu, Y. X.; Yao, Z. Y.; Liu, A. R.; Shi, G. Q. *ACS Nano* **2010**, *4*, 1963.

(101) Wang, H. L.; Hao, Q. L.; Yang, X. J.; Lu, L. D.; Wang, X. *Electrochemistry Communications* **2009**, *11*, 1158.

(102) Murugan, A. V.; Muraliganth, T.; Manthiram, A. *Chem. Mat.* **2009**, *21*, 5004.

(103) Wang, D. W.; Li, F.; Zhao, J. P.; Ren, W. C.; Chen, Z. G.; Tan, J.; Wu, Z. S.; Gentle, I.; Lu, G. Q.; Cheng, H. M. *ACS Nano* **2009**, *3*, 1745.

(104) Zhu, Y. W.; Stoller, M. D.; Cai, W. W.; Velamakanni, A.; Piner, R. D.; Chen, D.; Ruoff, R. S. *ACS Nano* **2010**, *4*, 1227.

(105) Srinivas, G.; Zhu, Y. W.; Piner, R.; Skipper, N.; Ellerby, M.; Ruoff, R. *Carbon* **2010**, *48*, 630.

(106) Kou, R.; Shao, Y. Y.; Wang, D. H.; Engelhard, M. H.; Kwak, J. H.; Wang, J.; Viswanathan, V. V.; Wang, C. M.; Lin, Y. H.; Wang, Y.; Aksay, I. A.; Liu, J. *Electrochemistry Communications* **2009**, *11*, 954.

(107) Yoo, E.; Okata, T.; Akita, T.; Kohyama, M.; Nakamura, J.; Honma, I. *Nano Letters* **2009**, *9*, 2255.

(108) Xu, C.; Wang, X.; Zhu, J. W. *J. Phys. Chem. C* **2008**, *112*, 19841.

(109) Seger, B.; Kamat, P. V. *J. Phys. Chem. C* **2009**, *113*, 7990.

(110) Li, Y. M.; Tang, L. H.; Li, J. H. *Electrochemistry Communications* **2009**, *11*, 846.

(111) http://en.wikipedia.org/wiki/File:Fuel_Cell_Block_Diagram.svg.

(112) Steele, B. C. H.; Heinzel, A. *Nature* **2001**, *414*, 345.

(113) Jaouen, F.; Proietti, E.; Lefevre, M.; Chenitz, R.; Dodelet, J.-P.; Wu, G.; Chung, H. T.; Johnston, C. M.; Zelenay, P. *Energy & Environmental Science* **2011**, *4*, 114.

(114) Wroblowa, H. S.; Pan, Y. C.; Razumney, G. *Journal of Electroanalytical Chemistry* **1976**, *69*, 195.

(115) Damjanov.A; Dey, A.; Bockris, J. O. M. *Journal of the Electrochemical Society* **1966**, *113*, 739.

(116) Sidik, R. A.; Anderson, A. B.; Subramanian, N. P.; Kumaraguru, S. P.; Popov, B. N. *J. Phys. Chem. B* **2006**, *110*, 1787.

(117) Buvet, R.; Sechaud, P.; Darolles, J.; Leport, L.; Sechaud, F. *Bioelectrochemistry and Bioenergetics* **1987**, *18*, 13.

(118) Kobayashi, N.; Janda, P.; Lever, A. B. P. *Inorganic Chemistry* **1992**, *31*, 5172.

(119) Dong, S. J.; Liu, B. F.; Liu, J. L.; Tabard, A.; Guilard, R. *Electroanalysis* **1995**, *7*, 537.

(120) Brito, P. S. D.; Sequeira, C. A. C. *Journal of Power Sources* **1994**, *52*, 1.

(121) Collman, J. P.; Denisevich, P.; Konai, Y.; Marrocco, M.; Koval, C.; Anson, F. C. *Journal of the American Chemical Society* **1980**, *102*, 6027.

(122) Bezerra, C. W. B.; Zhang, L.; Lee, K. C.; Liu, H. S.; Marques, A. L. B.; Marques, E. P.; Wang, H. J.; Zhang, J. J. *Electrochimica Acta* **2008**, *53*, 4937.

(123) Zagal, J. H. *Coordination Chemistry Reviews* **1992**, *119*, 89.

(124) Zhang, L.; Zhang, J. J.; Wilkinson, D. P.; Wang, H. J. *Journal of Power Sources* **2006**, *156*, 171.

(125) Smotkin, E. S.; Diaz-Morales, R. R. *Annual Review of Materials Research* **2003**, *33*, 557.

(126) Lee, K.; Zhang, J. J.; Wang, H. J.; Wilkinson, D. P. *Journal of Applied Electrochemistry* **2006**, *36*, 507.

(127) Antolini, E. *Applied Catalysis B-Environmental* **2009**, *88*, 1.

(128) Schmidt, T. J.; Paulus, U. A.; Gasteiger, H. A.; Behm, R. J. *Journal of Electroanalytical Chemistry* **2001**, *508*, 41.

(129) Zamel, N.; Li, X. G. *Prog. Energy Combust. Sci.* **2011**, *37*, 292.

(130) J. Larminie, A. L. D. **2003**, 51.

(131) Gasteiger, H. A.; Panels, J. E.; Yan, S. G. *Journal of Power Sources* **2004**, *127*, 162.

(132) Liu, H. S.; Song, C. J.; Zhang, L.; Zhang, J. J.; Wang, H. J.; Wilkinson, D. P. *Journal of Power Sources* **2006**, *155*, 95.

(133) Wang, C.; Waje, M.; Wang, X.; Tang, J. M.; Haddon, R. C.; Yan, Y. S. *Nano Letters* **2004**, *4*, 345.

(134) Dyer, C. K. *Journal of Power Sources* **2002**, *106*, 31.

(135) Li, W. Z.; Liang, C. H.; Zhou, W. J.; Qiu, J. S.; Zhou, Z. H.; Sun, G. Q.; Xin, Q. *J. Phys. Chem. B* **2003**, *107*, 6292.

(136) Ramani, V. *The Electrochemical Society's Interface* **2006**

(137) Jaouen, F.; Herranz, J.; Lefevre, M.; Dodelet, J. P.; Kramm, U. I.; Herrmann, I.; Bogdanoff, P.; Maruyama, J.; Nagaoka, T.; Garsuch, A.; Dahn, J. R.; Olson, T.; Pylypenko, S.; Atanassov, P.; Ustinov, E. A. *Acs Applied Materials & Interfaces* **2009**, *1*, 1623.

(138) Lefevre, M.; Proietti, E.; Jaouen, F.; Dodelet, J. P. *Science* **2009**, *324*, 71.

(139) Bashyam, R.; Zelenay, P. *Nature* **2006**, *443*, 63.

(140) Jasinski, R. *Nature* **1964**, *201*, 1212.

(141) Biddinger, E. J.; von Deak, D.; Ozkan, U. S. *Topics in Catalysis* **2009**, *52*, 1566.

(142) Matter, P. H.; Zhang, L.; Ozkan, U. S. *Journal of Catalysis* **2006**, *239*, 83.

(143) Shao, Y. Y.; Sui, J. H.; Yin, G. P.; Gao, Y. Z. *Applied Catalysis B-Environmental* **2008**, *79*,

89.

(144) Iwazaki, T.; Obinata, R.; Sugimoto, W.; Takasu, Y. *Electrochemistry Communications* **2009**, *11*, 376.

(145) Niwa, H.; Horiba, K.; Harada, Y.; Oshima, M.; Ikeda, T.; Terakura, K.; Ozaki, J.; Miyata, S. *Journal of Power Sources* **2009**, *187*, 93.

(146) Yang, W.; Fellinger, T. P.; Antonietti, M. *Journal of the American Chemical Society* **2011**, *133*, 206.

(147) Paraknowitsch, J. P.; Zhang, J.; Su, D. S.; Thomas, A.; Antonietti, M. *Adv. Mater.* **2010**, *22*, 87.

(148) Gong, K. P.; Du, F.; Xia, Z. H.; Durstock, M.; Dai, L. M. *Science* **2009**, *323*, 760.

(149) Qu, L. T.; Liu, Y.; Baek, J. B.; Dai, L. M. *ACS Nano* **2010**, *4*, 1321.

(150) Liu, R. L.; Wu, D. Q.; Feng, X. L.; Mullen, K. *Angewandte Chemie-International Edition* **2010**, *49*, 2565.

(151) Kurak, K. A.; Anderson, A. B. *J. Phys. Chem. C* **2009**, *113*, 6730.

(152) Ikeda, T.; Boero, M.; Huang, S. F.; Terakura, K.; Oshima, M.; Ozaki, J. *J. Phys. Chem. C* **2008**, *112*, 14706.

(153) Panchakarla, L. S.; Govindaraj, A.; Rao, C. N. R. *Inorganica Chimica Acta* **2010**, *363*, 4163.

(154) Wang, B. *Journal of Power Sources* **2005**, *152*, 1.

(155) Fierro, C.; Anderson, A. B.; Scherson, D. A. *Journal of Physical Chemistry* **1988**, *92*, 6902.

(156) Bezerra, C. W. B.; Zhang, L.; Liu, H. S.; Lee, K. C.; Marques, A. L. B.; Marques, E. P.; Wang, H. J.; Zhang, J. J. *Journal of Power Sources* **2007**, *173*, 891.

(157) Liu, H. S.; Song, C. J.; Tang, Y. H.; Zhang, J. L.; Zhang, H. J. *Electrochimica Acta* **2007**, *52*, 4532.

(158) Vasudevan, P.; Santosh; Mann, N.; Tyagi, S. *Transition Metal Chemistry* **1990**, *15*, 81.

(159) Wei, G.; Wainright, J. S.; Savinell, R. F. *Journal of New Materials for Electrochemical Systems* **2000**, *3*, 121.

(160) Widelov, A.; Larsson, R. *Electrochimica Acta* **1992**, *37*, 187.

(161) Alt, H.; Binder, H.; Sandsted.G *Journal of Catalysis* **1973**, *28*, 8.

(162) Vanveen, J. A. R.; Colijn, H. A.; Vanbaar, J. F. *Electrochimica Acta* **1988**, *33*, 801.

(163) Steiger, B.; Anson, F. C. *Inorganic Chemistry* **1994**, *33*, 5767.

(164) Sun, C. L.; Chen, L. C.; Su, M. C.; Hong, L. S.; Chyan, O.; Hsu, C. Y.; Chen, K. H.; Chang, T. F.; Chang, L. *Chem. Mat.* **2005**, *17*, 3749.

(165) Coloma, F.; Sepulvedaescribano, A.; Rodriguezreinoso, F. *Journal of Catalysis* **1995**, *154*, 299.

(166) Maldonado, S.; Stevenson, K. J. *J. Phys. Chem. B* **2005**, *109*, 4707.

(167) Shao, Y. Y.; Yin, G. P.; Gao, Y. Z.; Shi, P. F. *Journal of the Electrochemical Society* **2006**, *153*, A1093.

(168) van Dommele, S.; de Jong, K. P.; Bitter, J. H. *Chemical Communications* **2006**, 4859.

(169) Strelko, V. V.; Kartel, N. T.; Dukhno, I. N.; Kuts, V. S.; Clarkson, R. B.; Odintsov, B. M. *Surface Science* **2004**, *548*, 281.

(170) Czerw, R.; Terrones, M.; Charlier, J. C.; Blase, X.; Foley, B.; Kamalakaran, R.; Grobert, N.;

Terrones, H.; Tekleab, D.; Ajayan, P. M.; Blau, W.; Ruhle, M.; Carroll, D. L. *Nano Letters* **2001**, *1*, 457.

(171) Terrones, M.; Redlich, P.; Grobert, N.; Trasobares, S.; Hsu, W. K.; Terrones, H.; Zhu, Y. Q.; Hare, J. P.; Reeves, C. L.; Cheetham, A. K.; Ruhle, M.; Kroto, H. W.; Walton, D. R. M. *Adv. Mater.* **1999**, *11*, 655.

(172) Strelko, V. V.; Kuts, V. S.; Thrower, P. A. *Carbon* **2000**, *38*, 1499.

(173) Matter, P. H.; Ozkan, U. S. *Catalysis Letters* **2006**, *109*, 115.

(174) Matter, P. H.; Wang, E.; Arias, M.; Biddinger, E. J.; Ozkan, U. S. *J. Phys. Chem. B* **2006**, *110*, 18374.

(175) Biniak, S.; Walczyk, M.; Szymanski, G. S. *Fuel Processing Technology* **2002**, *79*, 251.

(176) Venkatachalapathy, R.; Davila, G. P.; Prakash, J. *Electrochemistry Communications* **1999**, *1*, 614.

(177) Maldonado, S.; Stevenson, K. J. *J. Phys. Chem. B* **2004**, *108*, 11375.

(178) Sjostrom, H.; Stafstrom, S.; Boman, M.; Sundgren, J. E. *Physical Review Letters* **1995**, *75*, 1336.

(179) Zhu, C.; Higgins, D.; Haisheng, T.; Hsu, R. S.; Zhongwei, C. *J. Phys. Chem. C* **2009**, 21008.

(180) Jafri, R. I.; Rajalakshmi, N.; Ramaprabhu, S. *Journal of Materials Chemistry* **2010**, *20*, 7114.

(181) Terrones, M.; Terrones, H.; Grobert, N.; Hsu, W. K.; Zhu, Y. Q.; Hare, J. P.; Kroto, H. W.; Walton, D. R. M.; Kohler-Redlich, P.; Ruhle, M.; Zhang, J. P.; Cheetham, A. K. *Applied Physics Letters* **1999**, *75*, 3932.

(182) Su, D. S.; Zhang, J.; Frank, B.; Thomas, A.; Wang, X. C.; Paraknowitsch, J.; Schlogl, R. *Chemsuschem* **2010**, *3*, 169.

(183) Roy, S. C.; Harding, A. W.; Russell, A. E.; Thomas, K. M. *Journal of the Electrochemical Society* **1997**, *144*, 2323.

(184) Titirici, M. M.; Thomas, A.; Antonietti, M. *Journal of Materials Chemistry* **2007**, *17*, 3412.

(185) Jiang, L. Q.; Gao, L. *Carbon* **2003**, *41*, 2923.

(186) Terrones, M.; Kamalakaran, R.; Seeger, T.; Ruhle, M. *Chemical Communications* **2000**, 2335.

(187) Kudashov, A. G.; Okotrub, A. V.; Bulusheva, L. G.; Asanov, L. P.; Shubin, Y. V.; Yudanov, N. F.; Yudanova, L. I.; Danilovich, V. S.; Abrosimov, O. G. *J. Phys. Chem. B* **2004**, *108*, 9048.

(188) Glerup, M.; Castignolles, M.; Holzinger, M.; Hug, G.; Loiseau, A.; Bernier, P. *Chemical Communications* **2003**, 2542.

(189) Sen, R.; Satishkumar, B. C.; Govindaraj, S.; Harikumar, K. R.; Renganathan, M. K.; Rao, C. N. R. *Journal of Materials Chemistry* **1997**, *7*, 2335.

(190) Kim, D. P.; Lin, C. L.; Mihalisin, T.; Heiney, P.; Labes, M. M. *Chem. Mat.* **1991**, *3*, 686.

(191) Liu, J.; Czerw, R.; Carroll, D. L. *Journal of Materials Research* **2005**, *20*, 538.

(192) Zhi, L. J.; Gorelik, T.; Friedlein, R.; Wu, J. S.; Kolb, U.; Salaneck, W. R.; Mullen, K. *Small* **2005**, *1*, 798.

(193) Ozaki, J. I.; Tanifuji, S. I.; Kimura, N.; Furuichi, A.; Oya, A. *Carbon* **2006**, *44*, 1324.

(194) Khomenko, V. G.; Barsukov, V. Z.; Katashinskii, A. S. *Electrochimica Acta* **2005**, *50*, 1675.

(195) Zhong, H. X.; Zhang, H. M.; Liu, G.; Liang, Y. M.; Hu, J. W.; Yi, B. L. *Electrochemistry*

Communications **2006**, *8*, 707.

Chapter 2. Transparent graphene films as window electrodes in organic solar cell

2.1 Introduction

As illustrated in Figure 2.1, to assure an efficient light absorption and charge transport in a solar cell, a window electrode should be transparent with good conductivity.

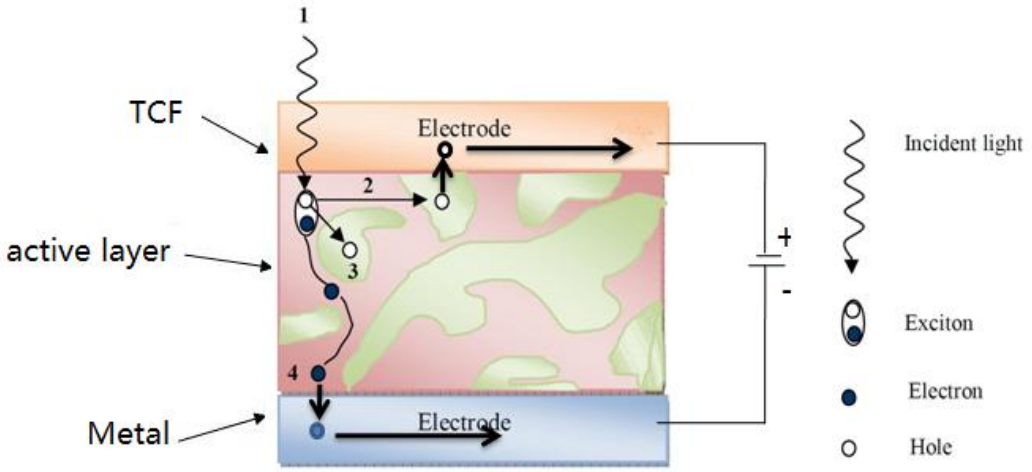

Figure 2.1 The basic working principle of Hetero-junction solar cell

With high electrical conductivity and high optical transmittance, graphene-based materials have become great candidates for transparent conductive films (TCFs) in photovoltaic devices. Nevertheless, two central challenges remain in the practical applications of graphene as transparent electrodes. The first problem is the large scale production of solution processable graphene. For the commercial manufacturing of photovoltaic devices, they often require large-area film fabrication from solution via simple coating techniques such as spin-coating, dip-coating, vacuum filtration, or Langmuir-Blodgett assembly. The second barrier for graphene

being used as TCFs is how to tailor the electronic properties of graphene films at the solid state.[1]

To overcome the first obstacle, the scalability of production and convenient processing of reduced graphene oxide (ReG), compared to micromechanical exfoliation, epitaxial growth, have led to its emergence as an important precursor for the fabrication of graphene-based TCFs.[2] To further increase the dispersibility of ReG in solution (as well as the concentration of graphene in solution), noncovalent functionalization, as introduced in carbon nanotubes (CNTs),[14-15] is particularly attractive. Without destroying the electronic π-system, it can attach chemical handles through van der Waals forces or π-π interactions to render extra force to stable graphene sheets in solution.

As for the second and more critical issue of tailoring electronic properties, great efforts have been made to improve the electrical conductivities of ReG sheets by optimizing the reductive conditions.[9-11, 13, 17-18] Molecular doping by various gases[19] and electrochemical doping by using gate voltage[20] were also found to be effective means of modifying the electronic structure of graphene. In addition, the fabrication of graphene composites with aromatic molecules, by analogy with graphite and carbon nanotubes (CNTs),[21-24] is also supposed to exert a rational control over the electronic properties of graphene sheets because they may involve a serious modification of the electronic structures of graphene sheets due to the charge transfer between the two components.

On the other hand, the oxidation of graphite into GO sheets during the preparation of ReG could cause initial structural defects on the graphene sheets, which is one of the main reasons of low conductivity of ReG after reduction from GO. The previous works in our group have discovered that a bottom-up approach by thermal annealing of nanographene molecules could result in a conductive graphene

film,[25] suggesting that large aromatic molecules may heal the defective vacancies in the graphene sheets under high temperature, and thus increase the conductivity of ReG. Accordingly, it is reasonable to assume that the composite of graphene sheets with large aromatic molecules provides an opportunity to not only fabricate graphene sheets in a feasible way but also tailor their electronic properties in a desired manner.

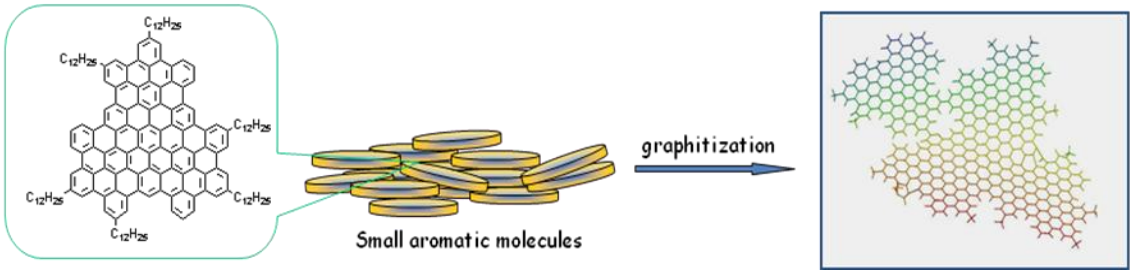

Figure 2.2 Schematic illustration of thermal fusion of polyaromatic hydrocarbons into carbon films

In this chapter an unprecedented approach is presented to noncovalently functionalize graphene with large aromatic donor and acceptor molecules, which gives rise to a novel class of graphene composites with tunable electronic properties. Two well-known organic hole and electron semiconducting materials, namely pyrene and perylenediimide[26-27] with nanographene units, are decorated with water-soluble moieties (as shown in Figure 2.3). Pyrene-1-sulfonic acid sodium salt (PyS) as an electronic donor, and the diasodium salt of 3,4,9,10-perylenetetracarboxylic diimide bisbenzenesulfonic acid (PDI) as an electronic acceptor, are hence intentionally selected (Figure 2.3). Both PyS and PDI have large planar aromatic structures which can strongly anchor them on the hydrophobic surface of graphene sheets via π-interactions without disruption of the electronic conjugation of graphene.[14] In

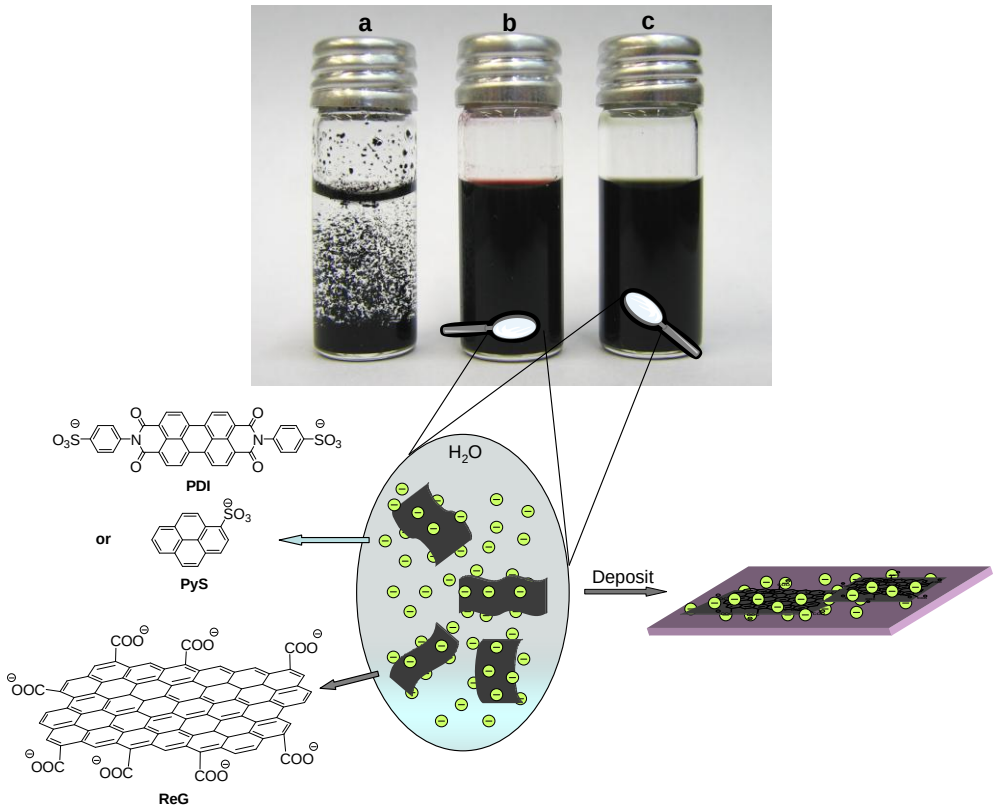

Figure 2.3 Schematic illustration and images of aqueous dispersions of graphene sheets (0.25 mg/mL) and composites on the surface: a) ReG aqueous dispersion, black precipitate after reduction; b) ReG-PDI aqueous dispersion, without precipitate after centrifugation (5000 rps/30 min); c) ReG-PyS aqueous dispersion, without precipitate after centrifugation (5000 rps/30 min).

addition, the negative charges in both dispersant molecules can act as stabilizing species to maintain a strong static repulsion force between the negatively charged reduced graphene sheets in solution.[28-29] As a result, the stability of the aqueous dispersion of graphene sheets was greatly enhanced (Figure 2.3) and a large number of monolayer and double-layer graphene sheets could be easily fabricated on the substrates. The upshift/downshift of the G-band in Raman spectra and sp^2 carbon peaks in X-ray photoelectron spectra (XPS) obviously demonstrated the different

charge transfer effects between the graphene sheets and PyS/PDI molecules. Remarkably, the composite of PDI with graphene sheets resulted in a significant conductivity increase for ReG-PDI (13.9 S/cm) compared to pristine ReG (3.0 S/cm), whereas a 30% decrease in conductivity was observed for ReG-PyS (1.9 S/cm). Thermal annealing of ReG-PDI and ReG-PyS at high temperatures led to further thermal reduction of ReG sheets accompanied with additional thermal reaction of large aromatic molecules. As a consequence, the conductivities of both ReG-PDI and ReG-PyS were dramatically increased to >1100 S/cm at 1000 ^{o}C, about twice as high as that of pristine ReG (517 S/cm), indicating an improved π-conjugation upon the "doping" of graphene sheets with nanographene molecules. Moreover, a remarkable improvement of the overall power efficiency from 0.78% to 1.12% was hence achieved by using ReG-PyS as anode electrode in bulk heterojunction solar cell instead of pristine ReG film.

2.2 Preparation of Graphene nanocomposites

In a typical experimental procedure to prepare graphene nanocomposites in solution, aqueous dispersion of graphite oxide (GO), as starting materials, was made from natural graphite flakes by a modified Hummer's method.[30] The resulting GO formed a homogeneous golden brown dispersion.

20 mL of as-prepared GO dispersion (0.25 mg / mL) was reduced by 125 μL of hydrazine monohydrate (98 wt% aqueous solution) at 90 ^{o}C for 24 h. PDI or Pys was added here as surfactant to increase the stability of the resulting ReG dispersion. Such ReG dispersion can be kept stable for weeks without any aggregation and precipitation.

Comparing with previous works, which had described the reduction of GO in

solution, it can be found that a stable ReG dispersion had never been achieved under such a harsh reduction condition. The original work done by Stankovich *et al* [3] in 2006 has described the gradual precipitation of ReG agglomerate under the same reduction condition. In the later work reported by Li *et al*[4], GO dispersion was reduced by 0.25 μL of hydrazine (35 wt% aqueous solution) at 90 ^{o}C for only 1 h. Under such a mild reduction condition, minor precipitation was still inevitable. When a typical surfactant, e.g. PSS (poly sodium 4-styrenesulfonate)[5], was added, a stable yet very diluted ReG dispersion was obtained (up to 0.1 mg/mL). In contrast, using PDI and Pys as large aromatic stabilizer greatly enhance the dispersability of ReG in aqueous solvent even after a very harsh reduction. Such a good stability of ReG dispersion with enough concentration is critical for the further processing of ReG films.

2.3 Characterization of Graphene nanocomposites

2.3.1 π–π interaction between graphene and aromatic molecules

As mentioned in chapter 2.1, PyS and PDI were intentionally chosen to confer extra electrostatic repulsion on graphene surface. It is assumed that the large planar aromatic structures of both PyS and PDI could strongly anchor them on surface of graphene sheets via π–π interactions. By this way, the extra charge repulsion force could increase the stability of ReG dispersion in water.

The visual evidence of this assumption firstly comes from the experimental observation described in chapter 2.2. Under certain concentration (0.25 mg/mL) and reductive condition (hydrazine, 90 ^{o}C for 24 h), ReG sheets severely aggregated, while the ReG-PDI and ReG-PyS composite remained stable for weeks. Therefore, the ReG dispersion referenced below was obtained from the reduction of 0.1 mg/mL GO

solution, which was still unstable after several days.

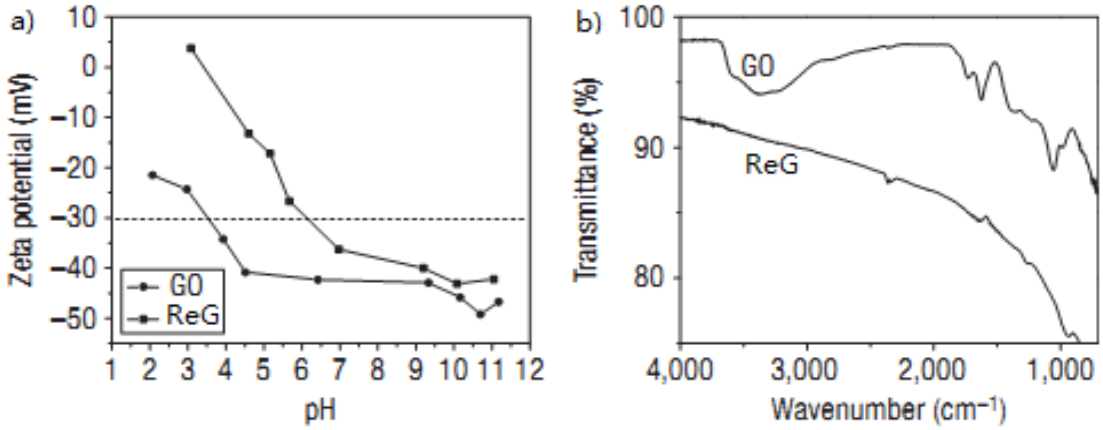

Figure 2.4 Surface properties of GO and ReG. (a) Zeta potential of GO and ReG as a function of pH, in aqueous dispersions at a concentration of 0.05 mg/ml; (b) FT-IR spectra of GO and ReG. The absorption band at around 1,700 cm^{-1} is attributed to carboxyl groups.[4]

It is well known that exfoliated graphite oxide (or GO) can form well-dispersed aqueous dispersions with high concentration.[6-8] The study of the surface charge (zeta potential) of GO sheets by Li *et al.* shows that these sheets are highly negatively charged when dispersed in water, apparently as a result of ionization of the carboxylic acid and phenolic hydroxyl groups on the GO sheets.[4] It suggests that the stability of GO dispersion can be attributed to electrostatic repulsion, rather than just the hydrophilicity of GO as previously presumed.[3] Given that carboxylic acid groups are unlikely to be totally reduced by hydrazine under the given reaction conditions, [3] these groups should therefore remain in the reduced product as confirmed by FT-IR analysis. Nevertheless, it is assumed that the electrostatic repulsion mechanism that makes GO colloids stable could also enable the formation of dispersed ReG in water. However, the loss of phenolic hydroxyl groups and some of the carboxylic acid still leads to a drop of the zeta-potential of a ReG dispersion (as shown in Figure 2.4a). This could explain the aggregation of ReG after reduction as described in chapter

2.2.6.

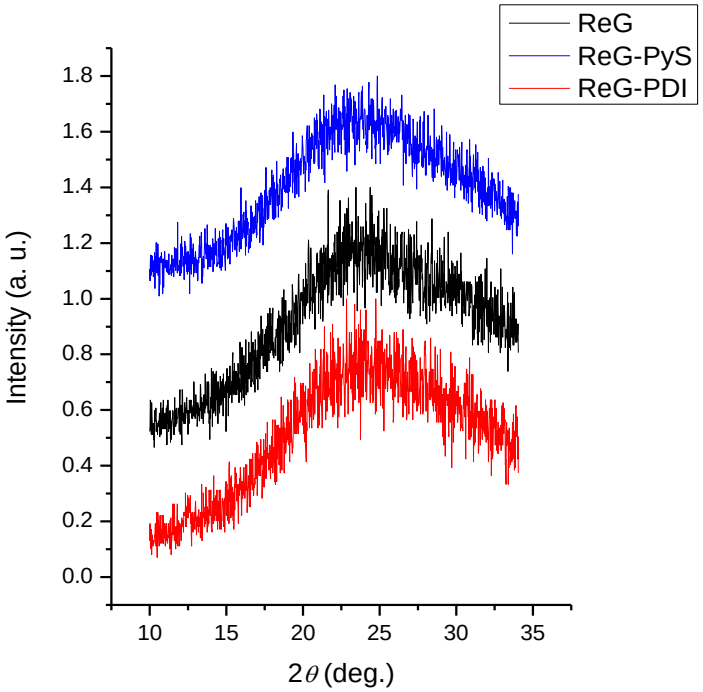

Figure 2.5 XRD pattern of ReG, ReG-Pys and ReG-PDI dispersion drop-casted on glass slides.

The characteristic peak (2θ) in the XRD pattern of ReG, ReG-Pys and ReG-PDI (Figure 2.5) appeared at ~25^{o}, corresponding to the layer-to-layer distance (d-spacing) of ~0.35 nm. The values are close to the d-spacing (0.335 nm) of natural graphite. These results corroborate the AFM observation that the PyS and PDI molecules are well packed on both sides of graphene basal plane in a face-on manner.

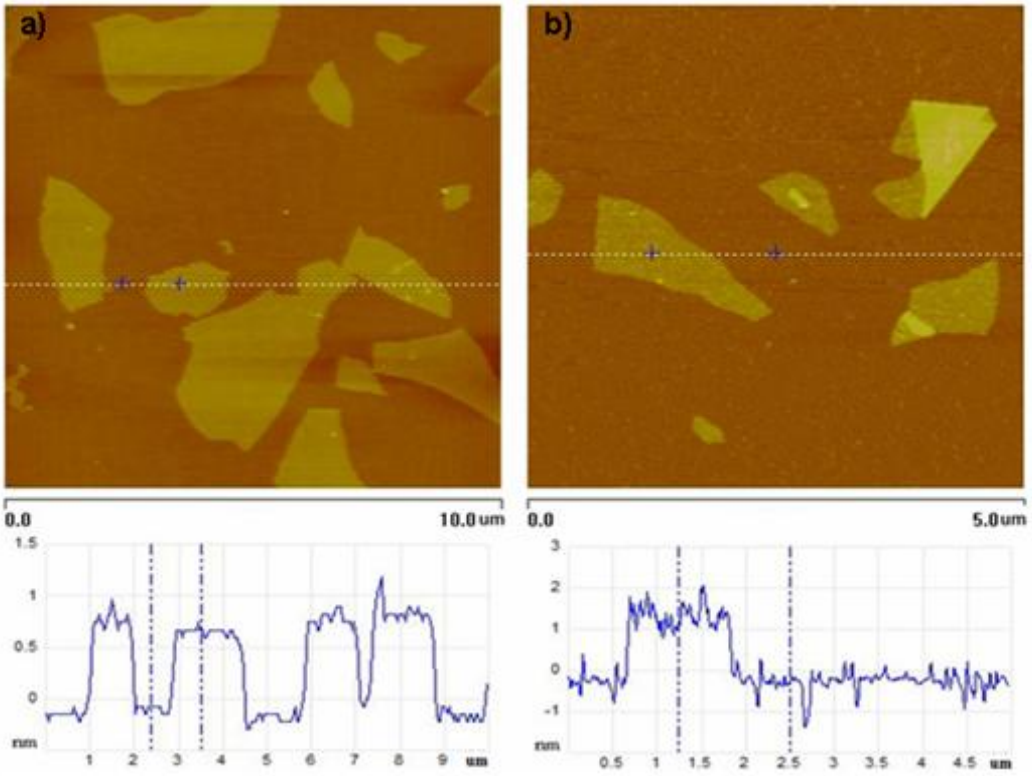

Figure 2.6 Tapping mode AFM images and cross-section graphs of a) GO and b) ReG dispersion dip-coated on mica.

AFM images (Figure 2.6 and 2.7) provide more detailed information on the π-interactions between graphene sheets and aromatic donor or acceptor molecules in solid state. Dip-coating of much diluted dispersions (less than 0.01 mg/mL) on freshly-cleaved mica enables us to observe morphology details of individual graphene sheet and graphene composite sheets without interference of sheet overlapping. In Figure 2.6a, a typical cross-section image of a single-layer exfoliated GO indicates an average thickness of 0.8 nm, consistent with the characteristic value of GO reported in the literature.[9,10] An average thickness of ReG around 1.0 nm is observed (Figure 2.6b), which is in agreement with the result reported by Li *et al*.[11]

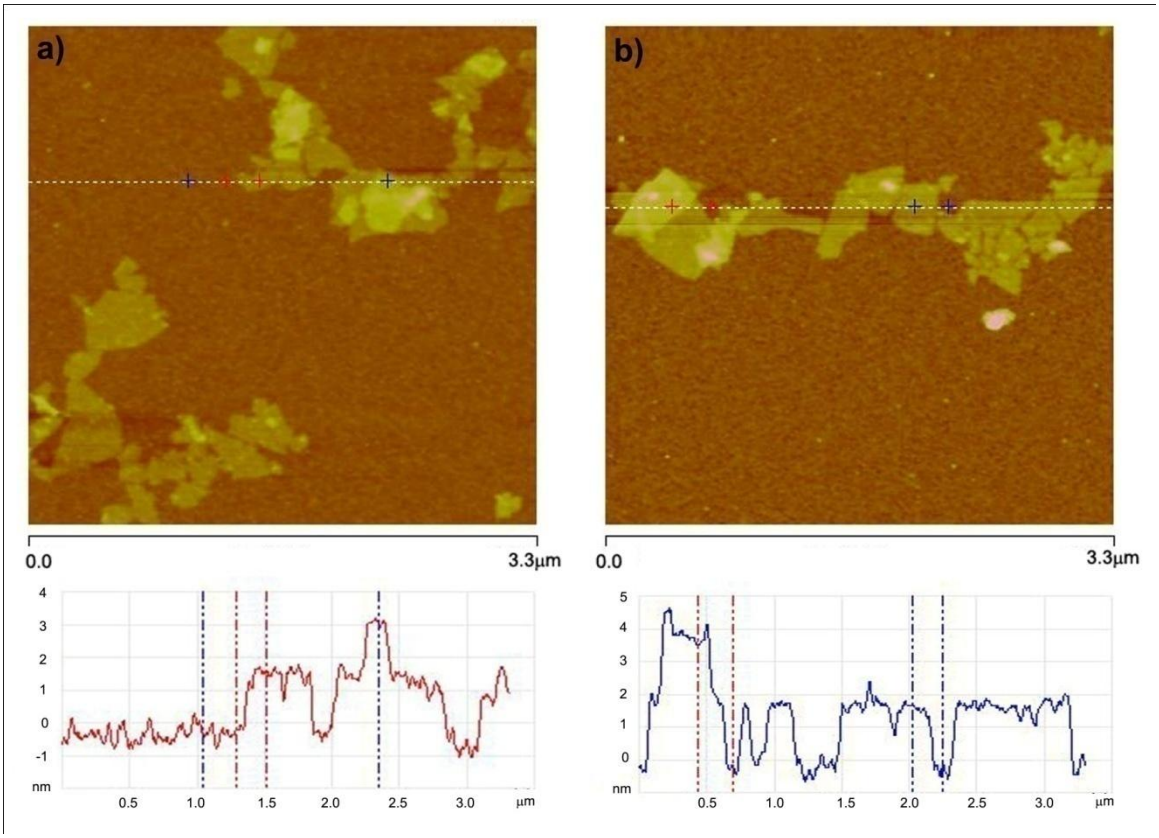

Figure 2.7 Tapping mode AFM images and cross-section graphs of a) ReG-Pys and b) ReG-PDI dispersion dip-coated on mica.

As shown in Figure 2.7a, the red cross-section line indicates that the thickness of a single layer ReG-PyS is ~ 1.7 nm. The interlayer distance between PyS (or PDI) layer and graphene sheets, as estimated from X-ray diffraction spectra (XRD), is ~ 0.35 nm (Figure 2.5), which agrees with the characteristic distance of π–π stacking. Taking into account that the thickness of a single- layer ReG is ~ 1 nm, it is reasonable to deduce that the PyS molecules are mainly arranged face-on on both sides of ReG sheet in a sandwich-like manner (as illustrated in Figure 2.8). Besides the large quantities of single layer graphene observed on the surface, the blue cross-section also illustrates the presence of a double-layer ReG-PyS with a thickness of ~ 3.4 nm, corresponding to the tandem sandwich structures. The same conclusion can be drawn from the

AFM images of ReG-PDI (Figure 2.7b), in which a single layer of ReG-PDI with a thickness of ~ 1.7 nm (blue cross-section) and a double layer with ~ 3.4 nm (red cross-section) are observed. These results again confirm that the dispersant molecules with large aromatic structures and extra negative charges are able to be noncovalently immobilized on the basal plane of graphene sheets via strong π-π interactions. This not only increases the inter-sheet static repulsion forces in solution, but also prevents graphene sheets from re-aggregation once deposited on the surface.

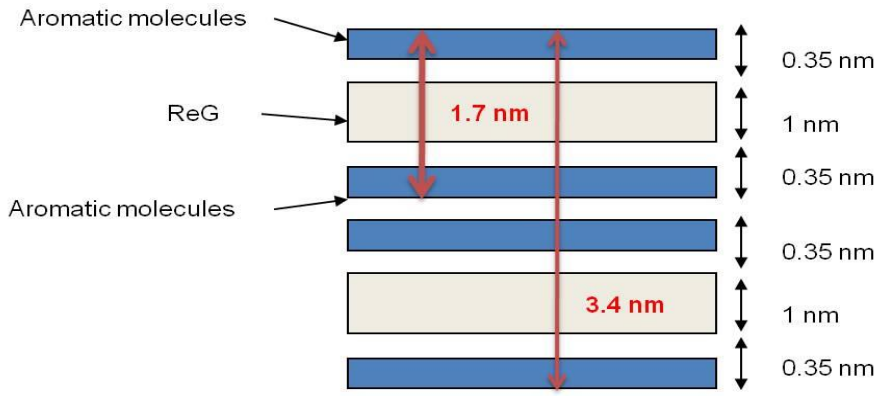

Figure 2.8 Schematic illustration of thickness increase of ReG-PyS and ReG-PDI

2.3.2 Charge transfer interaction between graphene and aromatic molecules

The Fermi energy (E_F) in graphene is found to be related to the square root of the carrier concentration in the plane of the sheet. It is shifted by the doping effect due to stiffening or softening of phonons and other effects which modify the phonon dispersion by changing the carrier concentration and mobility.[11-13] Significant changes in the properties of graphene, in particular its phonon spectrum and electronic structure, are reported to occur when electrons or holes are introduced by electrochemical or chemical methods.[12,13] At the same time, it has been shown in

recent years that organic molecules which act as electron-donors or –acceptors can modify the electronic structure of SWCNTs, the 1-D analogue of graphene, giving rise to significant changes in the electronic structure as well as electrical properties.[14-16]

As illustrated in chapter 2.3.1, strong π-interactions between PDI/PyS and graphene sheets were achieved. On the other hand, PDI is known as an electron acceptor and PyS, an electron donor. Many recent investigations have revealed that graphene (as well as single-walled carbon nanotubes) compositing with electron donor /acceptor molecules often induces charge transfer effects and impacts on the electronic structure of the graphene (or the nanotubes).[12,17-20] Prompted by the results obtained in these works, we assume that the significant π-interactions between PDI/PyS molecules and the graphene basal plane could also produce charge transfer effects, and in this way, affect the electronic structure of graphene sheets.

To prove this assumption, graphene-base composite samples (ReG, ReG-PDI and ReG-PyS) have been prepared by drop-casting on quartz wafers, and their electronic structures were studied by means of Raman spectroscopy, X-ray photoelectron spectroscopy (XPS), fluorescence spectroscopy and electrical conductivity measurements.

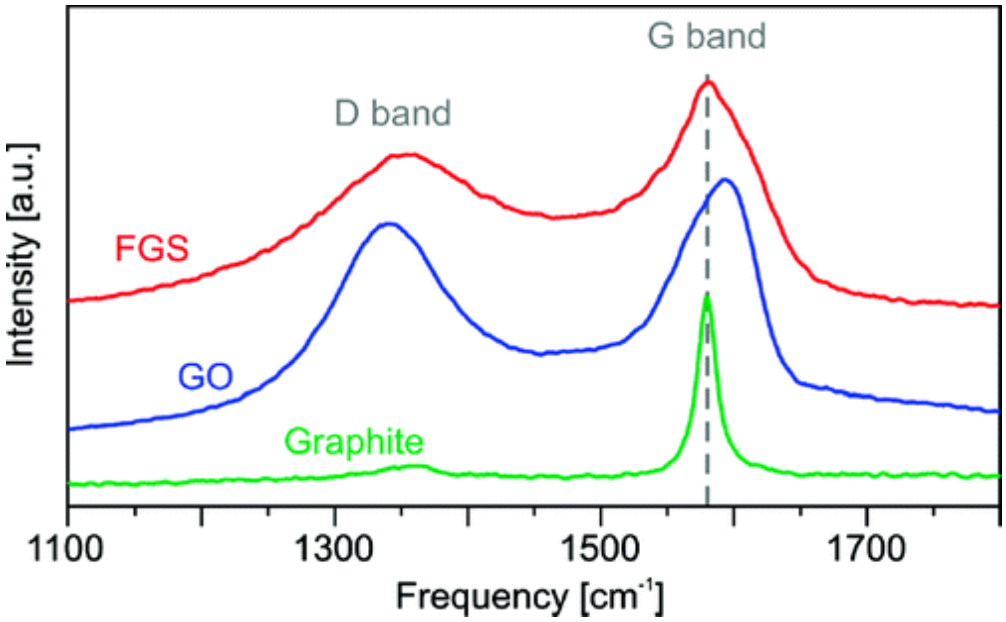

Figure 2.9 Evolution of the Raman spectra during the oxidation and exfoliation processes for graphite, GO, and FGS. (exciting laser wavelength = 514.5 nm) [17]

Raman spectroscopy is a powerful non-destructive technique for identifying the electronic structure and doping effect of graphene.[11,18-20] Typical Raman spectra of graphite, graphite oxide (GO) and functionalized graphene sheets (FGS) were discussed by Kudin et al. as shown in Figure 2.9.[17]

In particular, the D (~1300 cm^{-1}), G (~1600 cm^{-1}) and 2D (~2700 cm^{-1}) bands are useful in understanding the number of layers, structure, doping and disorder of graphene. Note that the 2D band is prominent in the Raman spectrum while the D band is absent in single-layer graphene. In the presence of more than one layer both the D and 2D bands are found in the spectrum.[12,13,17,20,21] For examining the changes brought about in the electronic structure of graphene, G bands are particularly useful as a fingerprint to understand the effects of electron- and hole-doping. Specifically, the G-band is shifted to lower frequency by electron donors and to higher frequency by acceptors.[15,22]

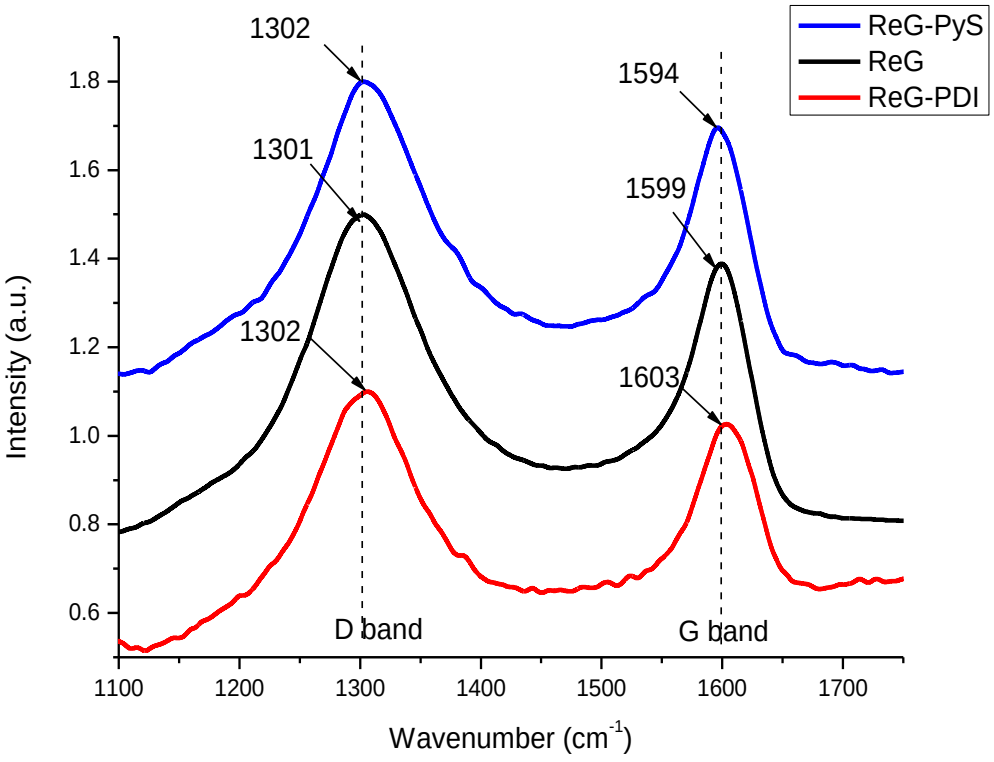

Figure 2.10 Raman spectra of ReG, ReG-PyS and ReG-PDI film drop-cast on quartz

By comparing the G-bands of ReG, ReG-PyS and ReG-PDI films drop-cast on quartz (Figure 2.10), it is clear that when the electron-donor PyS is applied, the G-band of graphene sheets occurs at 1594 cm^{-1}, which is downshifted by 5 cm^{-1} compared to that of ReG. In contrast, using PDI as dispersant, the G-band of graphene sheets is upshifted from 1599 to 1603 cm^{-1}. The G band in the Raman spectrum of graphene is known to be shifted to lower frequencies (softening) by electron-donor molecules and to higher frequencies (stiffening) by electron-acceptor molecules. [15,22,23] The softening and stiffening values of the G-band observed here are lower than those of the electrochemical doping of graphene[13] (which are usually up to 15~20 cm^{-1}), but in the range of the chemical doping of graphene (which was reported between 2 cm^{-1} to 10 cm^{-1} for dopants such as halogen,[24] aniline, nitrobenzene,[23,25,26] 5-naphthalenediamine, 9,10-dimethyl- anthracene,

9,10-dibromoanthracene, tetrasodium 1,3,6,8-pyrenetetrasulfonic acid,[27] coronene tetracarboxylic acid[23] and so on). The additional charge carriers brought by dispersant aromatic molecules change the carrier concentration in the plane of graphene and lead to the shift of the Fermi level.[13,16,28] Meanwhile, it is interesting to notice that the D band position is not sensitive to the interaction with either PDI or PyS, which is in agreement with the results of electrochemical doping[13] and chemical doping on graphene.[12] The same D band position also excludes the possibility that the shifts of the G band are due to the experimental error. Therefore, the Raman shifts of the G-band provide reliable evidence for the charge transfer between the graphene sheets and PyS (or PDI).

X-ray photoelectron spectroscopy (XPS) as a quantitative spectroscopic technique that measures the elemental composition, empirical formula, chemical state and electronic state of the elements that exist within a material, is another useful method to investigate the charge transfer interaction between graphene and aromatic molecules. The samples were prepared by drop-casting the dispersions of GO, ReG, ReG-PDI and ReG-PyS on a Si wafers (~30 nm thick).

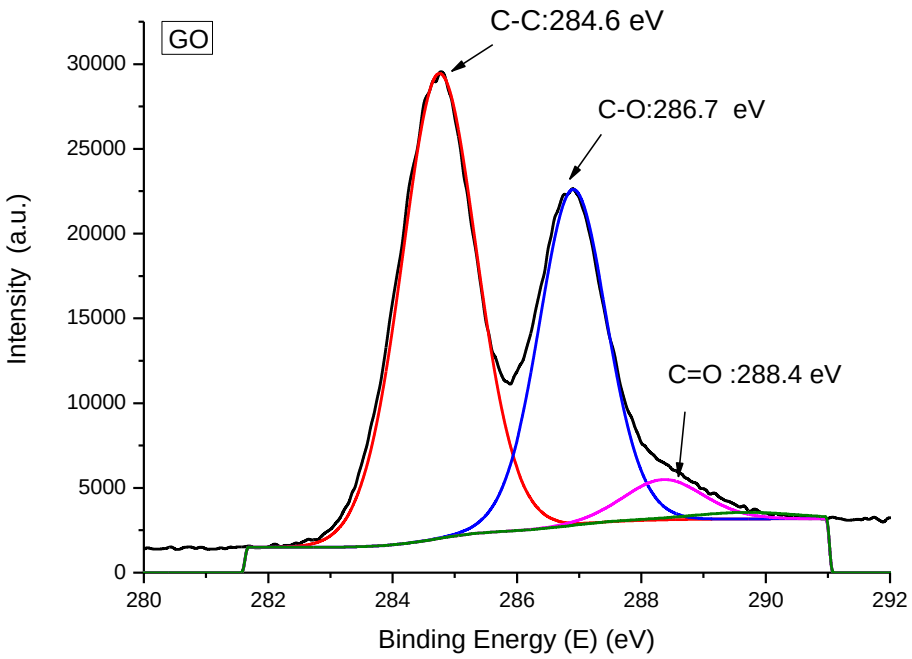

Figure 2.11 C1s XPS peaks of graphite oxide (GO)

The deconvolution of C1s XPS spectra is firstly used to monitor the elimination of oxygen containing groups (such as carboxylic acid and phenolic hydroxyl groups) during reduction process. In brief, the C1s XPS spectrum of GO (Figure 2.11) clearly indicates a considerable degree of oxidation that correspond to carbon atoms in different functional groups: the non-oxygenated ring C-C (284.6 eV), the C in C–O bonds (286.7 eV), and the carbonyl C (288.4 eV). Although the C1s XPS spectrum of the reduced graphene oxide (Figure 2.12) also exhibits these same oxygen functionalities, their peak intensities are much smaller than those in GO. These observations indicate a considerable de-oxygenation by the chemical reduction process.

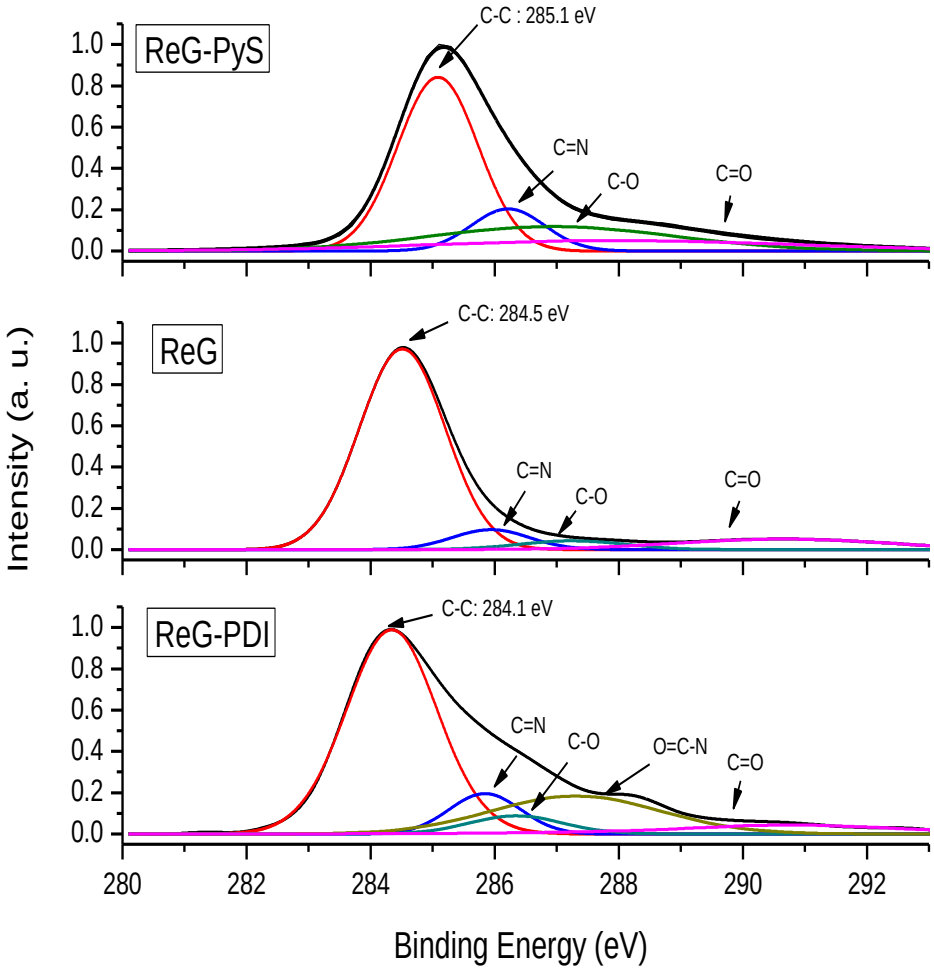

Figure 2.12 C1s XPS peaks of ReG, ReG-PyS and ReG-PDI film drop-cast on Si wafer

More importantly, the modification of the Fermi level of graphene induced by donor/acceptor molecules is emphasized by the shift of the C1s XPS peak. Compared to Raman spectroscopy, XPS affords great sensitivity and allows one to quantitatively establish the occurrence of charge-transfer interaction.[29] As shown in Figure 2.12, the deconvolution reveals mainly four components presented in both the ReG and ReG-PyS films: C-C (~284.5 eV) of sp^2 carbon in the basal plane of graphene sheets; C-O (286.6 eV) and C=O (289.3 eV) coming from carboxylic groups; and C=N (285.8 eV) resulting from the bond formation by hydrazine[5,30] An extra species of ReG-PDI

appearing at 288.4 eV is assigned to the C of O=C-N groups brought by PDI. The Fermi level of graphene is represented by the main sp^2 peak position.[15,28,31] Obviously, the PDI as electronic acceptor results in the C-C peak for ReG-PDI at 284.1 eV, which is downshifted by 0.4 eV compared to that of pristine ReG. In contrast, the C-C peak for ReG-Pys at 285.1 eV is upshifted by 0.6 eV. These two values are in the range of shifts (from 0.3~0.5 eV) observed for single-walled carbon nanotubes composited with halogen and NO_2,[32] and other aromatic donor/ acceptor molecules.[15,29] Furthermore, the shifts in XPS peaks of sp^2 carbon corroborate the results of the Raman spectra mentioned above that there is a charge transfer between large aromatic molecules and the graphene sheets. By this means, the electronic structure of graphene sheets can be rationally modified as a function of the electron-donating or electron–accepting characteristics of the dispersants.

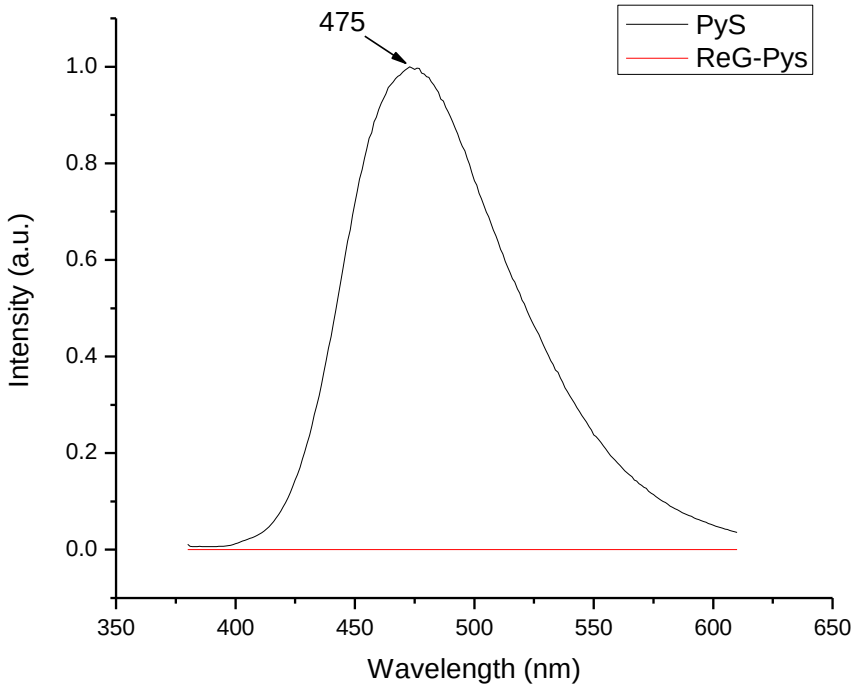

Figure 2.13 Fluorescence spectra (λ=363 nm) of ReG-PyS and Pys drop-casted on quartz plates.

In addition to Raman spectra and XPS, fluorescence spectra of ReG-PyS and Pys were also measured to demonstrate the charge transfer between graphene sheets and Pys. As shown in figure 2.13, the characteristic emission of pyrene at 475 nm is completely quenched, further indicating a strong electronic interaction at the pyrene/graphene interface.[33] However, the electronic interactions between PDI and graphene sheets do not reveal a distinct influence on the absorption spectra of ReG-PDI.

2.3.3 Conductivity measurement of ReG, ReG-PyS and ReG-PDI

The conductivities of the graphene sheets composited with PyS or PDI were measured taking into consideration that the charge transfer effects of donor and acceptor would influence them in different ways.[12,13,31] The thin films were fabricated by spray-coating the dispersions of ReG, ReG-PDI and ReG-PyS on Si wafer with a thickness around 10 nm. A 4-point resistivity probe was used to measure the sheet resistance (*Rs*) of the films. The conductivity can be calculated the following equation:

$$C = \frac{1 \times 10^7}{4.532 \times h \times Rs}$$

in which *C* is the conductivity (S/cm), *h* is the thickness of the film (nm) and *Rs* is the sheet resistance (Ω/sq) read from the probe.

As shown in Figure 2.17, the conductivity of ReG film was calculated to be 3.0 S/cm at room temperature, whereas the conductivity of ReG-PyS (1.9 S/cm) was 30% less than that of pristine ReG. Remarkably, the conductivity of ReG-PDI was 13.9 S/cm, almost four times higher than that of ReG. These results undoubtedly indicate

that the conductivity can be rationally adjusted by the composition of graphene with large aromatic donor or acceptor molecules, comparable to the phenomena observed recently when carbon nanotubes interact with electron-donor or acceptor solvents,[12] as well as when graphene is electrochemically doped by the change of gate voltages.[13]

2.4 Transparent graphene composite film

In previous studies of our group it is found that large polyaromatic hydrocarbons (PAHs) were suitable units for the bottom-up construction of graphene sheets by thermal fusion at high temperatures by stepwise heat treatment.[34-36] Considering the fact that pyrene and PDI are large aromatic molecules as well, it is reasonable to assume that they would also serve as nanographene building blocks. They may fuse not only with each other but also with ReG sheets in a similar manner as in bottom-up approach, and by this way, to heal the defects of ReG sheets and reconstruct graphene films at high temperatures.

Therefore, the thermal reduction of ReG-PDI and ReG-PyS is expected to further increase the conductivity of graphene films due to the deoxygenation,[37] better graphitization[37,38] and additional thermal reactions of nanographene units within the graphene sheets.[36]

2.4.1. Preparation of transparent graphene composite film

All the samples for the thermal reduction of graphene composites were prepared by spray-coating corresponding dispersion of ReG, ReG-PDI and ReG-PyS. The wafers were pre-heated at 95 ^{o}C and set perpendicular to the ground. The spray

head was adjusted in an angle of ~45^{o} to the wafer and spray in a one-shot manner for several times.

The thermal reduction was carried out under a reductive atmosphere of argon (100 sccm/min) and hydrogen (5 sccm/min) at 400 ^{o}C, 800 ^{o}C and 1000 ^{o}C, respectively.

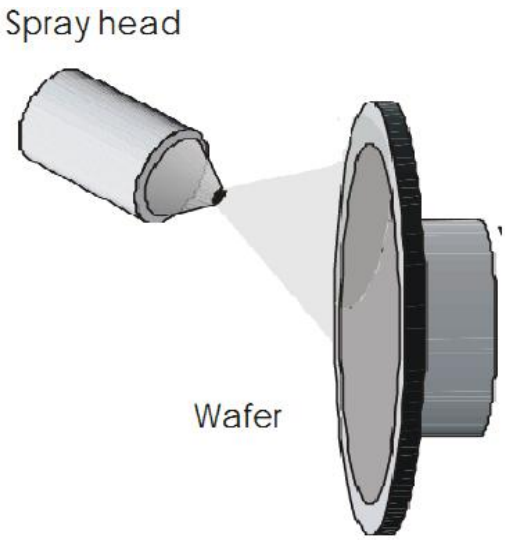

Figure 2.14 Schematic illustration of spray coating of ReG composite dispersion on substrates

2.4.2. Characterization of transparent graphene composite films

The effect of additional thermal reduction on the micro-structure of graphene composite films was evaluated by Raman spectroscopy (figure 2.15). By comparing the D band and G band of ReG with those of ReG further reduced at 1000 ^{o}C (ReG-1000), a slight increase of D/G intensity ratio is observed while the G band downshifts to lower frequency. This slight downshift of G band could be attributed to a graphitic "self-healing" similar to what was observed from the chemical reduction

of graphite oxide to ReG.[17] At the same time, the increased D/G intensity ratio indicates that new graphitic domains created during the further thermal reduction are smaller in size to the ones presented in ReG, but more numerous in number.[3] Apart from the intrinsic structural defects of ReG, the release of carbon dioxide or carbon oxide under high temperature also renders typical 5 or 5–8–5 defects on the carbon frameworks of graphene during thermal reduction (Figure 2.16).[39] Therefore, both the shift of the G band and the increasing D/G intensity ratio imply a further deoxygenation of ReG sheets and a slight fragmentation of graphitic network during the thermal reduction, which is in agreement with the report by Chen *et al*.[40]

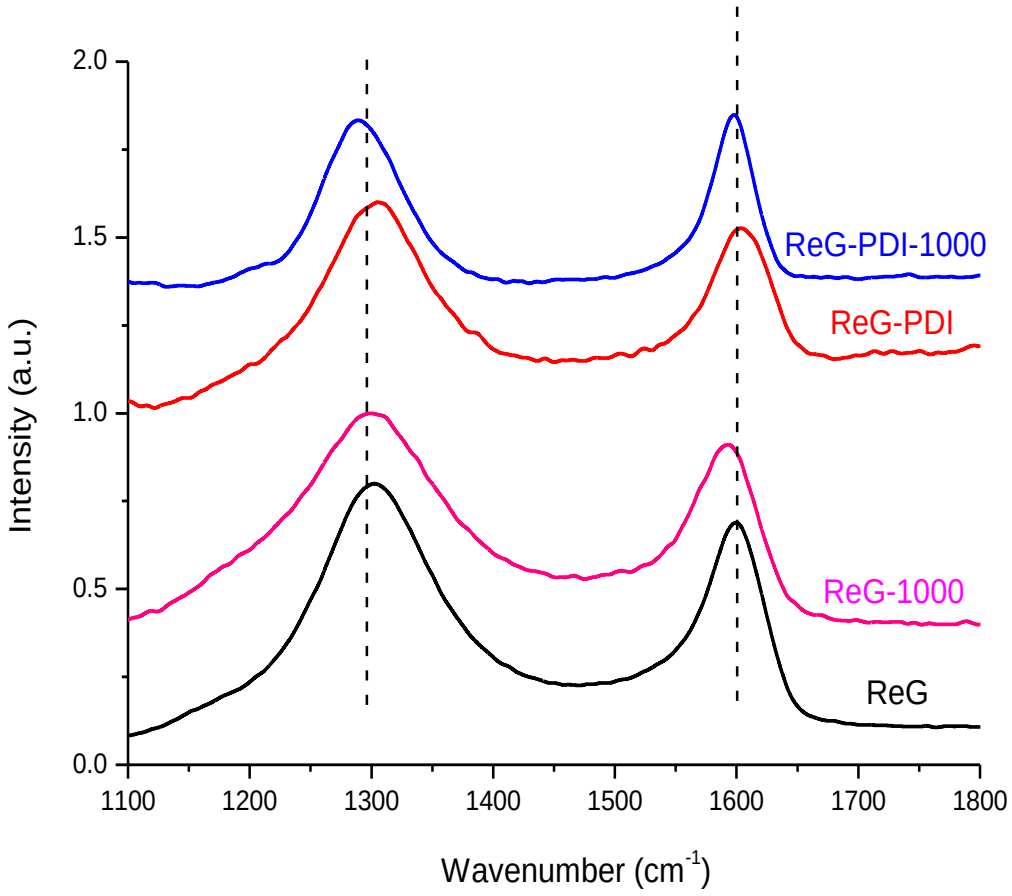

Figure 2.15 Raman spectra of ReG, ReG-PyS and ReG-PDI film drop-cast on quartz

On the other hand, the thermal reduction of ReG-PDI and ReG-PyS is expected to heal the graphene films by additional thermal reactions of nanographene units within the graphene sheets. This is indeed observed in Raman spectra. Taking ReG-PDI as an example, it is remarkable that the G band of ReG-PDI sharpens after thermal reduction at 1000 ^{o}C compared to G bands of ReG-PDI and ReG-1000. Even though both G and D bands (at 1599 cm^{-1} and 1301 cm^{-1}, respectively) remain prominent, it should be noted that the thermal reduction of ReG-PDI diminished the D/G intensity ratio of graphene sheets. As previously stated, thermal reduction of ReG should increase of the D/G intensity ratio due to new defects and the fragmentation of carbon frameworks of the graphene basal plane under high temperature. In contrast, the decrease of the D/G intensity ratio and the sharpened G-band of ReG-PDI-1000 evidently demonstrate that PDI (or PyS), as a nanographene building block, is actually able to fuse some of the structural defects on the intrinsic 2D framework of graphene plane, and hence render a better π-conjugation via thermal reaction.

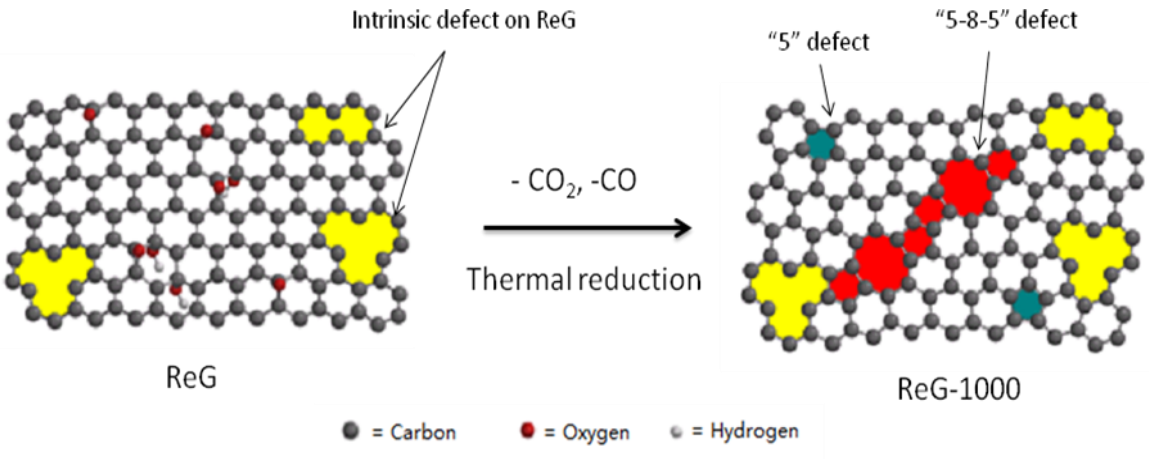

Figure 2.16 Atomistic model of the ReG to ReG-1000: the structural defects caused by oxidation treatment are labeled in yellow, 5 or 5–8–5 defects labeled in blue or red, respectively.[39]

Considering that a better π-conjugation ensures a higher conductivity along graphene sheets, the conductivity measurement was carried out for ReG, ReG-PDI and ReG-PyS thermally reduced at different temperature, aiming to further confirm the influence of aromatic molecules upon graphene sheet during thermal treatment.

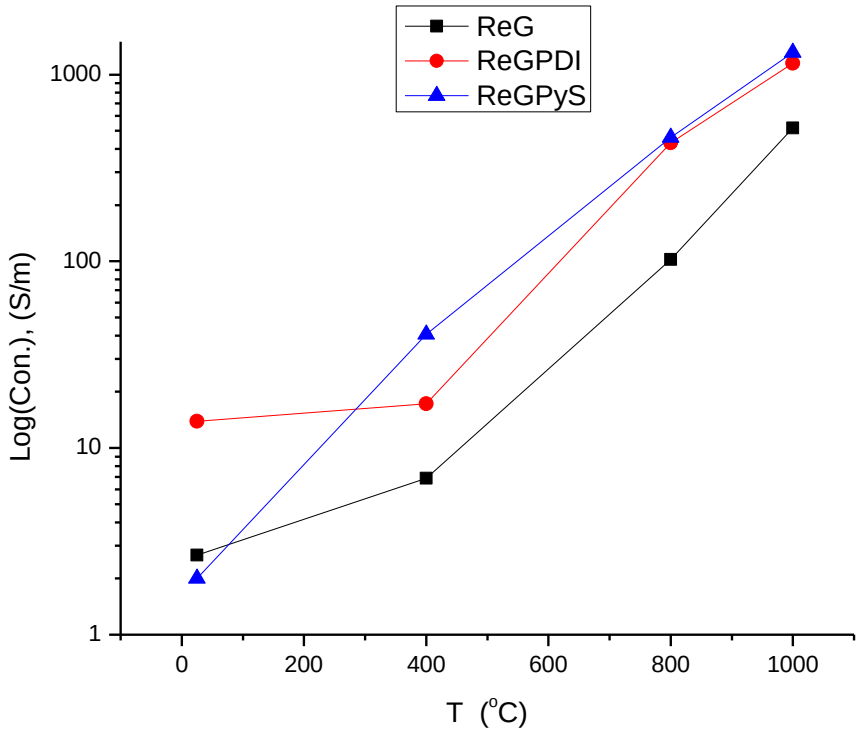

Figure 2.17 The conductivity of ReG, ReG-PDI and ReG-PyS film spray-coated on Si wafer with/without thermal reduction at high temperatures.

As demonstrated in Figure 2.17, thermal annealing at 400 °C increased the conductivity of ReG, ReG-PDI and ReG-PyS to 6.9 S/cm, 17.2 S/cm and 40.6 S/cm respectively. The higher value of ReG-PyS with respect to that of ReG-PDI could be ascribed to the thermal decomposition of pyrene under this condition, which

induced the thermal reaction between pyrene and graphene sheets and resulted in a better π-conjugation. After annealing at 800 ^{o}C, the further thermal reduction of graphene sheets and thermal reaction of pyrene or PDI units led to a comparable conductivity for ReG-PDI (431.0 S/cm) and ReG-Pys (459.8 S/cm), which are more than three times higher than that of ReG (102.2 S/cm). This suggests that the nanographene units could indeed improve the electrical conductivity of pristine graphene sheets. The same trend was also held at 1000 ^{o}C. The further thermal reduction and fusion resulted in better graphitization of graphene sheets, and hence further increased the conductivity to 1149 S/cm and 1314 S/cm for ReG-PyS and ReG-PDI, respectively. It is noteworthy that these are among the highest conductivity values ever achieved for graphene films under the same thermal treatment. On the other hand, however, the ReG only yielded a conductivity of 517 S/cm under the same conditions. This value is comparable with the conductivity (500 S/cm) achieved by our previous work in which GO was reduced by hydrogen at 1100 ^{o}C.[38]. Due to the thermal fusion and surface-mediated reaction[41] of nanographene, it is reasonable to assume that the thermal annealing of the composite films consisting of graphene sheets and large aromatic molecules could heal the defects formed within the plane of ReG. This process would give rise to a better π-conjugation of graphene basal plane, and in this way dramatically increase the conductivity.

2.5 Transparent graphene film as window electrodes of organic solar cell

To investigate how the graphene film with increased conductivity preformed as anode in photovoltaic devices, the bulk heterojunction solar cells were thus fabricated consisting of quartz/graphene/PEDOT:PSS/ (P3HT+PCBM)/ZnO/Al (Figure 2.19). Poly(3-hexyl)thiophene (P3HT) was used as electronic donor and phenyl-C60-butyric acid methyl ester (PCBM) as electronic acceptor, while poly(3,4-ethylenedioxythiophene) : poly(styrenesulfonate) (PEDOT:PSS) acted as

electron blocking layer and ZnO nanoparticles as the hole blocking and optical space layer. The photoactive composite layer was sandwiched between graphene/quartz and an Al electrode. For comparison, graphene films with different thickness were fabricated from ReG or ReG-PyS respectively on the quartz substrates and thermally reduced at 1000 ^{o}C.

2.5.1 Device fabrication

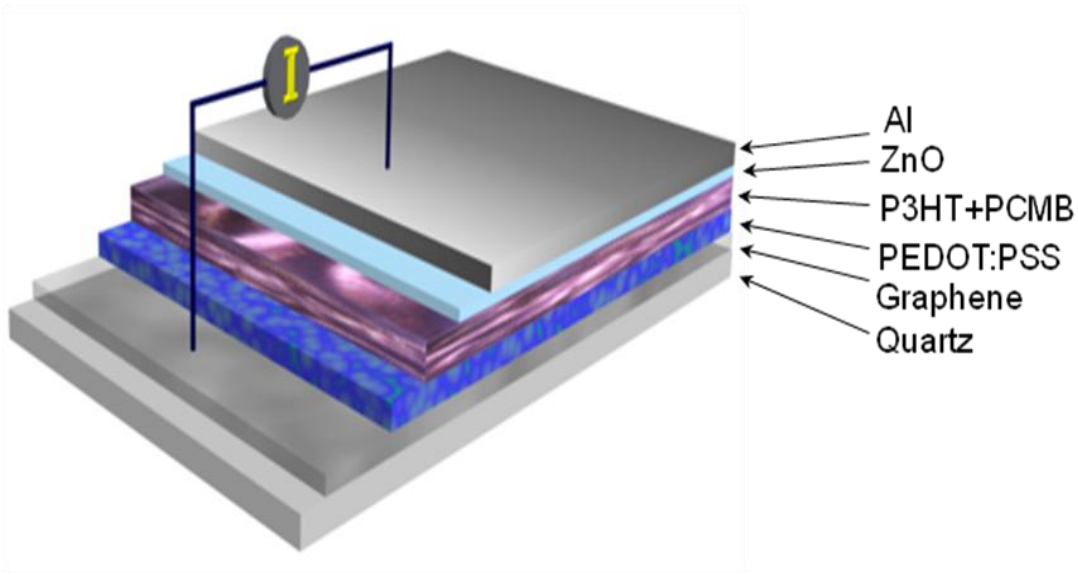

Figure 2.18 Schematic illustration of the solar cell; the five layers from top to bottom are Al, ZnO, a blend of P3HT and PCMB, PEDOT:PSS, graphene film, and quartz, respectively.

Polymer solar cells were fabricated according to the following procedure: Highly conducting PEDOT:PSS was spin-coated (4000 rpm) with a thickness of ~ 40 nm from an aqueous solution (after passing a 0.8 μm filter). The substrate was dried at 140 ^{o}C for 15 min. The dichlorobenzene solution comprising P3HT (10 mg/mL) and PCBM (8 mg/mL) was then spin-coated on the top of PEDOT:PSS layer. Subsequently, 30 nm

thin film of ZnO nanoparticles were spin-coated on the composite layer from 1-butanol after filting a 0.2 μm filter. After the solvent had dried, the substrate was pumped down in a vacuum and then ~100 nm Al film was deposited on the top of ZnO layer. Finally, the substrate was moved into a glove box for the annealing treatment (110 ^{o}C for 10 min) and measurement.

The graphene-based window electrodes were fabricated on quartz substrate by spray-coating of ReG and ReG-PyS dispersion as described in chapter 2.4.1. The thickness of film was controlled by the times of spay-coating. All the samples were thermally reduced under an atmosphere of argon (100 sccm) and hydrogen (5 sccm) at 1000 ^{o}C.

2.5.2 Transparency measurement

As shown in Figure 2.20a, a thin ReG-PyS film on quartz after thermal annealing at 1000 ^{o}C turns out to be transparent to natural solar light.

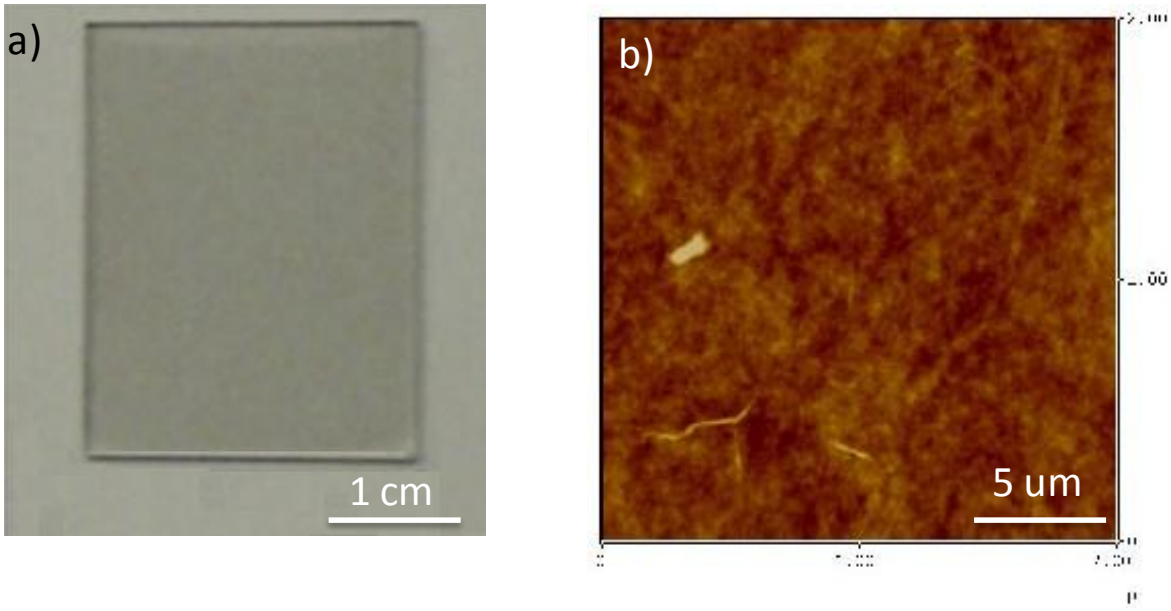

Figure 2.19 a) Photograph of a transparent ReG-PyS film on quartz (2.5x2 cm^2) after thermal annealing; b) AFM image (2 mm x2 mm) of ReG-PyS film on quartz

after thermal annealing.

More detailed information for a ReG-PyS-1000 film on quartz was revealed by AFM image in which the film shows an ultra-smooth surface without large aggregates, pinholes, and cracks (Figure 2.20b). The average surface roughness (Ra) of ReG-PyS-1000 with thicknesses of 10 nm over a 2 x 2 mm^2 area was 0.5 nm. At the same time, the ReG-PyS-1000 films on quartz remained intact after 30 min in bath ultrasonication in common organic solvents, thus revealing the strong adhesion and chemical stability of ReG-PyS-1000 films on substrates. Compared with the relatively rough surface and chemical instability of ITO, ReG-PyS-1000 films have a smoother surface as well as higher mechanical and chemical stability, which are key requirements for electrodes used in optoelectronic devices.

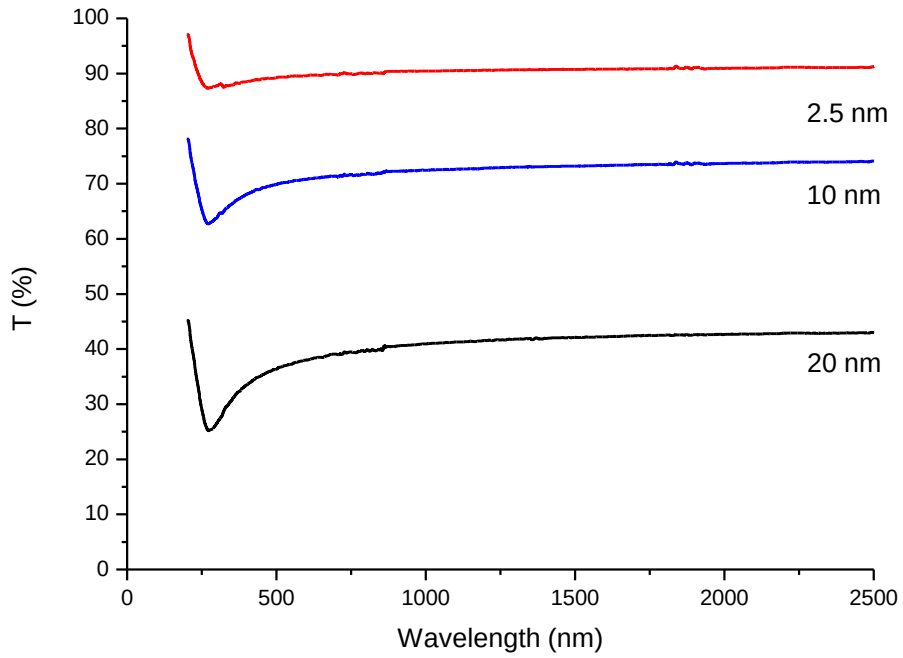

Figure 2.20 Transparency of ReG-PyS-1000 film on quartz with different thickness

The transparency of ReG-PyS-1000 was quantitatively measured by a Perkin-Elmer Lambda 9 spectrometer at room temperature. The transmittance of

ReG-PyS-1000 could be tuned by the film thickness by varying the condition of spary-coating. ReG-PyS-1000 films with thicknesses of 20, 10, and 2.5 nm show transmittance of 47, 70 and 88 %, respectively, at a wavelength of 550 nm (Figure 2.21).

2.5.3 Conductivity measurement

The sheet resistance of the as-prepared ReG-PyS-1000 films with different thickness was evaluated by a four-point probe measurement as mentioned above. As demonstrated in Table 1, a small decrease in the film conductivity is observed as the film thickness decreases. In contrast, the thinner is ReG-PyS-1000 film, the higher the transparency of window electrode can be achieved.

Table 1. Transmittance and Resistance data of ReG-PyS-1000 film on quartz with different thickness

Transmittance (%)	**Sheet resistance (KΩ/square)**	**Thinkness (nm)**	**Conductivity (S/cm)**
88.25	4.92	2.5	813.01
70.24	1.04	10	962.63
47.54	0.48	20	1046.96
14.53	0.23	40	1105.36

2.5.4 Efficiency measurement

To demonstrate how the ReG-PyS-1000 performed as anodes, organic solar cells were fabricated based on ReG-1000 and ReG-PyS-1000 as described in chapter 2.5.1.

The corresponding transmittance and conductivity of ReG were 70 % and ~500 S/cm respectively, while those of ReG-PyS were 70 % and 912 S/cm, respectively.

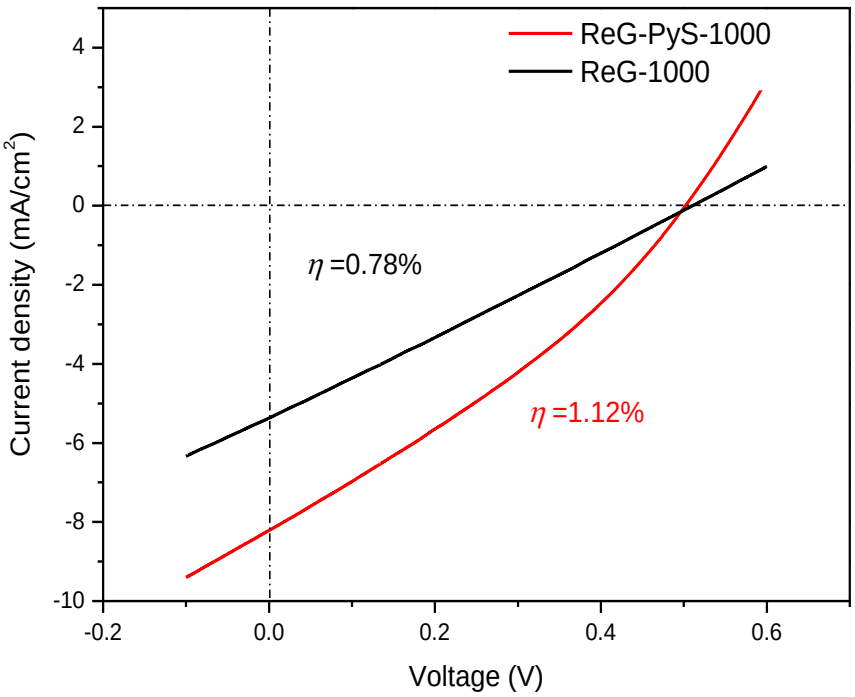

Figure 2.21 Current density-Voltage (I-V) curves of P3HT/PCBM heterojunction solar cells with 10 nm thick thermally reduced ReG and ReG-PyS-1000 film as the transparent electrodes, respectively.

Table 2. Efficiency data of ReG-PyS-1000 film on quartz as TCFs for polymer solar cell

Transparent Electrode	I_{sc} [mA/cm^2]	V_{oc} [V]	FF	PCE
ReG-PyS-1000	8.21	0.51	0.31	1.12 %
ReG-1000	5.37	0.50	0.26	0.78 %
ITO	1.00	0.41	0.48	1.17 %

Table 3. Summary of graphene based TCFs and best PCEs employing them in organic solar cells[42]

Graphene	Sheet resistance	T (%)	Device structures (G = graphene)	PCE
rGO [a)]	17.9 kΩ/sq	69	G/PEDOT:PSS/P3HT:PCBM/LiF/Al	0.13 %
rGO	500 kΩ/sq	85	G/CuPc/C60/BCP/Ag	0.4 %
rGO	1.6 kΩ/sq	55	G/PEDOT:PSS/P3HT:PCBM/TiO_2/Al	0.78 %
rGO	40 kΩ/sq	64	G/PEDOT:PSS/P3HT:PCBM/Al	0.1 %
rGO	1 kΩ/sq	80	G/PEDOT:PSS/P3HT:PCBM/Al	1.01 %
bottom-up synthesis	18 kΩ/sq	85	G/P3HT:PCBM/Ag	0.29 %
CVD	1350 Ω/sq	72	G/PEDOT:PSS/P3HT:PCBM/LiF/Al	1.71 %
CVD	230 Ω/sq	72	G/PEDOT:PSS/CuPc/C60/BCP/Al	1.27 %
CVD	606 Ω/sq	87	G/PEDOT:PSS/P3HT:PCBM/TiO_X/Al	2.58 %
CVD	520 Ω/sq	85	G/WPF-6-oxy-F/P3HT:PCBM/PEDOT:PSS/Al	1.23 %
CVD	80 Ω/sq	90	G/MoO3/PEDOT:PSS/P3HT:PCBM/LiF/Al	2.5 %
CVD-AuCl	300 kΩ/sq	90	G/PEDOT:PSS/CuPc/C60/BCP/Ag	1.63 %

a) rGO = reduced graphene oxide

As demonstrated in Figure 2.21, the ReG-PyS-1000 film with higher conductivity obviously led to a larger short-circuit current and fill factor (8.2 mA cm^{-2}, 0.31) than the values using ReG-1000 as the transparent electrode (5.4 mA cm^{-2}, 0.26). It is remarkable that an overall power converting efficiency (PCE) of 1.12% was achieved using ReG-PyS-1000 as transparent electrode, while ReG-1000 showed a lower efficiency of 0.78%. More importantly, this efficiency is comparable to that of the solar cell where ITO was applied as transparent electrode (Table 2). These results present the first example that the combination of nanographene and graphene sheets could generate desirable electrode materials that qualify for photovoltaic

devices.[30,36-38] The enhanced quality and conductivity of ReG-PyS-1000 film indeed improve the PCE when it is used as transparent electrodes in solar cell. Compared to the best PCEs achieved in the literatures with different graphene base transparent electrodes, it is interesting to note that ReG-PyS-1000 presents the highest PCE among all transparent electrodes based on reduce graphene oxide. Actually, its PCE is in the range of those of the graphene electrodes produced via CVD growth from metal substrates. In other words, ReG-PyS-1000 is able to demonstrate as good performance as pristine graphene does in organic solar cell.

2.6 Conclusion

In conclusion, we have demonstrated an unprecedented approach to functionalize graphene with large aromatic donor and acceptor molecules, resulting in a novel combination of graphene and nanographene building blocks. By this means, one can effectively stabilize the aqueous dispersion of graphene sheets, and hence yield monolayer and double-layer graphene sheets on substrates in large quantities. Our results further disclose that the different electronic characteristics of large aromatic donor and acceptor molecules enable a rational modification of both the electronic structure and conductivity of graphene sheets. Remarkably, the further thermal reduction of graphene sheets at 1000 ^{o}C results in additional thermal reaction of nanographene units and leads to a dramatic increase of the conductivity up to >1000 S/cm. As a consequence, the power efficiency is improved by using graphene composite film as TGF electrodes in heterojunction solar cells. The total efficiency was achieved as 1.12% which is comparable to the solar cells based on ITO TGFs and pristine graphene TGFs.

Refrence:

(1) Su, Q.; Pang, S. P.; Alijani, V.; Li, C.; Feng, X. L.; Mullen, K. *Adv. Mater.* **2009**, *21*, 3191.

(2) Zhu, Y. W.; Murali, S.; Cai, W. W.; Li, X. S.; Suk, J. W.; Potts, J. R.; Ruoff, R. S. *Adv. Mater.* **2010**, *22*, 3906.

(3) Stankovich, S.; Dikin, D. A.; Piner, R. D.; Kohlhaas, K. A.; Kleinhammes, A.; Jia, Y.; Wu, Y.; Nguyen, S. T.; Ruoff, R. S. *Carbon* **2007**, *45*, 1558.

(4) Li, D.; Muller, M. B.; Gilje, S.; Kaner, R. B.; Wallace, G. G. *Nature Nanotechnology* **2008**, *3*, 101.

(5) Stankovich, S.; Piner, R. D.; Chen, X. Q.; Wu, N. Q.; Nguyen, S. T.; Ruoff, R. S. *Journal of Materials Chemistry* **2006**, *16*, 155.

(6) Szabo, T.; Szeri, A.; Dekany, I. *Carbon* **2005**, *43*, 87.

(7) Kovtyukhova, N. I.; Ollivier, P. J.; Martin, B. R.; Mallouk, T. E.; Chizhik, S. A.; Buzaneva, E. V.; Gorchinskiy, A. D. *Chem. Mat.* **1999**, *11*, 771.

(8) Kotov, N. A.; Dekany, I.; Fendler, J. H. *Adv. Mater.* **1996**, *8*, 637.

(9) Gilje, S.; Han, S.; Wang, M.; Wang, K. L.; Kaner, R. B. *Nano Letters* **2007**, *7*, 3394.

(10) Gomez-Navarro, C.; Weitz, R. T.; Bittner, A. M.; Scolari, M.; Mews, A.; Burghard, M.; Kern, K. *Nano Letters* **2007**, *7*, 3499.

(11) Pisana, S.; Lazzeri, M.; Casiraghi, C.; Novoselov, K. S.; Geim, A. K.; Ferrari, A. C.; Mauri, F. *Nature Materials* **2007**, *6*, 198.

(12) Das, B.; Voggu, R.; Rout, C. S.; Rao, C. N. R. *Chemical Communications* **2008**, 5155.

(13) Das, A.; Pisana, S.; Chakraborty, B.; Piscanec, S.; Saha, S. K.; Waghmare, U. V.; Novoselov, K. S.; Krishnamurthy, H. R.; Geim, A. K.; Ferrari, A. C.; Sood, A. K. *Nature Nanotechnology* **2008**, *3*, 210.

(14) Voggu, R.; Rout, C. S.; Franklin, A. D.; Fisher, T. S.; Rao, C. N. R. *J. Phys. Chem. C* **2008**, *112*, 13053.

(15) Shin, H. J.; Kim, S. M.; Yoon, S. M.; Benayad, A.; Kim, K. K.; Kim, S. J.; Park, H. K.; Choi, J. Y.; Lee, Y. H. *Journal of the American Chemical Society* **2008**, *130*, 2062.

(16) Rao, A. M.; Eklund, P. C.; Bandow, S.; Thess, A.; Smalley, R. E. *Nature* **1997**, *388*, 257.

(17) Kudin, K. N.; Ozbas, B.; Schniepp, H. C.; Prud'homme, R. K.; Aksay, I. A.; Car, R. *Nano Letters* **2008**, *8*, 36.

(18) Casiraghi, C.; Pisana, S.; Novoselov, K. S.; Geim, A. K.; Ferrari, A. C. *Applied Physics Letters* **2007**, *91*.

(19) Yan, J.; Zhang, Y. B.; Kim, P.; Pinczuk, A. *Physical Review Letters* **2007**, *98*.

(20) Ferrari, A. C.; Meyer, J. C.; Scardaci, V.; Casiraghi, C.; Lazzeri, M.; Mauri, F.; Piscanec, S.; Jiang, D.; Novoselov, K. S.; Roth, S.; Geim, A. K. *Physical Review Letters* **2006**, *97*.

(21) Ferrari, A. C. *Solid State Communications* **2007**, *143*, 47.

(22) Poenitzsch, V. Z.; Winters, D. C.; Xie, H.; Dieckmann, G. R.; Dalton, A. B.; Musselman, I. H. *Journal of the American Chemical Society* **2007**, *129*, 14724.

(23) Ghosh, A.; Rao, K. V.; George, S. J.; Rao, C. N. R. *Chemistry – A European Journal* **2010**, *16*, 2700.

(24) Jung, N.; Kim, N.; Jockusch, S.; Turro, N. J.; Kim, P.; Brus, L. *Nano Letters* **2009**, *9*, 4133.

(25) Das, B.; Voggu, R.; Rout, C. S.; Rao, C. N. R. *Chem. Commun.* **2008**, 5155.

(26) Varghese, N.; Ghosh, A.; Voggu, R.; Ghosh, S.; Rao, C. N. R. *The Journal of Physical Chemistry C* **2009**, *113*, 16855.

(27) Dong, X.; Fu, D.; Fang, W.; Shi, Y.; Chen, P.; Li, L.-J. *Small* **2009**, *5*, 1422.

(28) Graupner, R.; Abraham, J.; Vencelova, A.; Seyller, T.; Hennrich, F.; Kappes, M. M.; Hirsch, A.; Ley, L. *Physical Chemistry Chemical Physics* **2003**, *5*, 5472.

(29) Choudhury, D.; Das, B.; Sarma, D. D.; Rao, C. N. R. *Chemical Physics Letters* **2010**, *497*, 66.

(30) Becerril, H. A.; Mao, J.; Liu, Z.; Stoltenberg, R. M.; Bao, Z.; Chen, Y. *ACS Nano* **2008**, *2*, 463.

(31) Lee, R. S.; Kim, H. J.; Fischer, J. E.; Thess, A.; Smalley, R. E. *Nature* **1997**, *388*, 255.

(32) Larciprete, R.; Goldoni, A.; Lizzit, S.; Petaccia, L. *Applied Surface Science* **2005**, *248*, 8.

(33) Xu, Y. X.; Bai, H.; Lu, G. W.; Li, C.; Shi, G. Q. *Journal of the American Chemical Society* **2008**, *130*, 5856.

(34) Zhi, L. J.; Wu, J. S.; Li, J. X.; Kolb, U.; Mullen, K. *Angewandte Chemie-International Edition* **2005**, *44*, 2120.

(35) Gherghel, L.; Kubel, C.; Lieser, G.; Rader, H. J.; Mullen, K. *Journal of the American Chemical Society* **2002**, *124*, 13130.

(36) Wang, X.; Zhi, L. J.; Tsao, N.; Tomovic, Z.; Li, J. L.; Mullen, K. *Angewandte Chemie-International Edition* **2008**, *47*, 2990.

(37) Li, X. L.; Zhang, G. Y.; Bai, X. D.; Sun, X. M.; Wang, X. R.; Wang, E.; Dai, H. J. *Nature Nanotechnology* **2008**, *3*, 538.

(38) Wang, X.; Zhi, L. J.; Mullen, K. *Nano Letters* **2008**, *8*, 323.

(39) Liang, Y. Y.; Frisch, J.; Zhi, L. J.; Norouzi-Arasi, H.; Feng, X. L.; Rabe, J. P.; Koch, N.; Mullen, K. *Nanotechnology* **2009**, *20*.

(40) Chen, H.; Muller, M. B.; Gilmore, K. J.; Wallace, G. G.; Li, D. *Adv. Mater.* **2008**, *20*, 3557.

(41) Liu, L.; Rim, K. T.; Eom, D.; Heinz, T. F.; Flynn, G. W. *Nano Letters* **2008**, *8*, 1872.

(42) Wan, X. J.; Long, G. K.; Huang, L.; Chen, Y. S. *Adv. Mater.* **2011**, *23*, 5342.

Chapter 3. Graphene/CNT composite film as free-standing electrode

3.1 Introduction

As we discussed in chapter 1 and 2, the extraordinary thermal, mechanical, and electrical properties of graphene have made it the most discussed topic that brings many new areas of application in modern materials science.[1-4] One possible route to harnessing these properties would be to incorporate graphene sheets in composite materials.[5] By this way, these thermally and electrically conductive reinforced composites generated huge exploration in the possible implementation of graphene-based devices, including electronic transistors, sensors, energy storage devices, transparent electrodes for displays and solar cells.

The manufacturing of such materials requires that graphene sheets not only must be produced on a sufficient scale (in size of micrometers and produced in gram scale) but also should be homogeneously distributed into various reaction media. For making a homogeneous dispersion, the chemical functionalization of graphene has been widely explored as a useful tool to improve their dispersibility in various media as well as the compatibility with various matrices. As a consequence, the favorable incorporation of graphene with other functional materials has brought significant enhancements of properties at much lower volume loadings (0.1–5 vol%), and thus led to a wide variety of graphene-base composite materials.[5]

Among them, composite materials of graphene and carbon nanotubes (CNTs) have been described in recent years[5-7] . Carbon nanotubes (CNTs), as the 1D analogue of graphene, have delivered high axial carrier mobilities, making them an obvious choice for use as electrode materials.[8] Composite materials of graphene and carbon nanotubes (CNTs) is supposed to establish synergistic effects between these two different graphitic nanostructures both having unique electronic, thermal and

mechanical properties.[4,9-11]

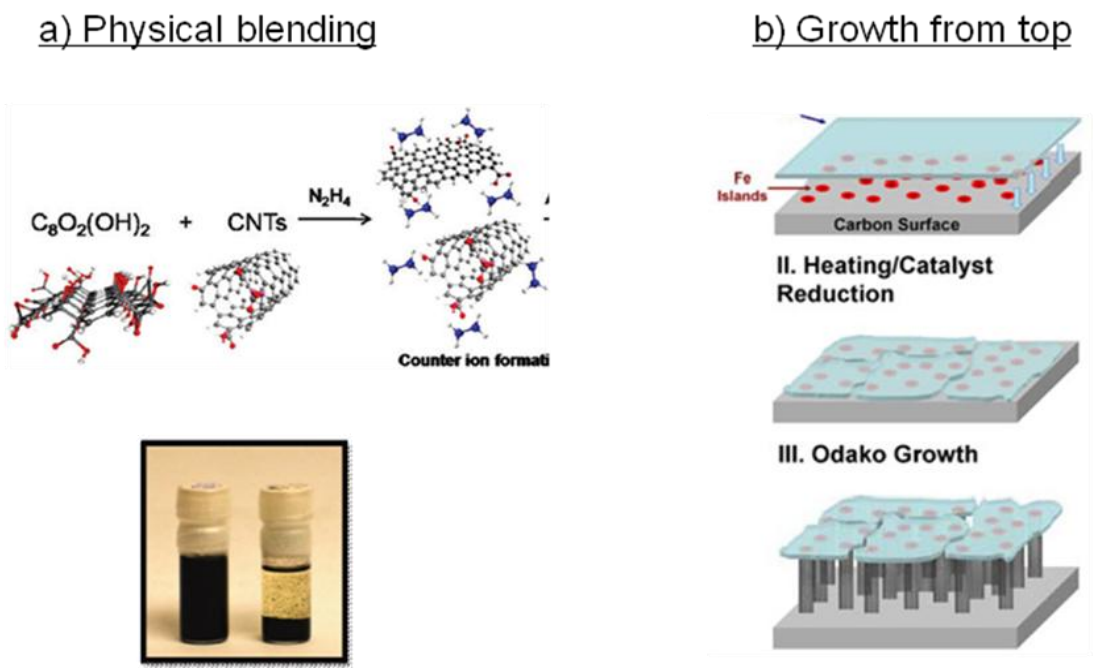

Figure 3.1 Schematic illustration of the so far explored approaches to prepare graphene/CNT nanocomposite materials: a) co-reduction of graphite oxide and CNTs by hydrazine in water;[8] b) CVD growth of CNTs on the top of graphene layers embed with metal catalytic particles[12]

Considering that graphene can provide conductive pathways within a larger area per unit mass than CNTs, *Song et al.*[13] first produced conductive hybrid films consisting of CNTs and graphite oxide nanoplatelets. Later, *Yang et al.*[8] utilized hydrazine to reduce aqueous dispersions of CNTs and graphene oxide (GO) and fabricated graphene/CNT composite films as transparent electrodes. Thereby, the electrical conductivity was greatly improved in comparison with that of pure graphene films. In addition, *Haddon et al.*[14] employed CNT/graphite nanoplatelet hybrids as fillers for epoxy resins, achieving an enhanced thermal conductivity compared to that of pure graphene or CNT fillers. Apparently, all these studies

involved graphene/CNT composite fabrication by mixing graphene sheets and CNTs in dispersions with the aid of sonication. However, this physical blending could hardly ensure a close interaction between CNTs and graphene species.

Until very recently, Kim et al. have reported a method to grow CNTs directly from GONPs decorated with Fe nanoparticles.[12] In this approach, a pattern process on silicon substrate was necessary. After etching the silicon wafer by hydrofluoric acid or by PDMS-infiltrated, a free-standing carbon hybrid films was achieved of which CNTs grew on the top of graphene. Indeed, an efficient synthesis of graphene/CNT composites with precise morphology control has not yet been available.

In this chapter, we will present an unprecedented graphene-cobalt complex (**ReG-Co**), which possesses the advantages of homogenous distribution and covalent functionalization of organocobalt moieties [$C_2Co_2(CO)_6$] on chemically reduced graphene oxide sheets (**ReG)** as illustrated in Figure 3.2. The chemical functionalization of ReG via organic reaction (diazonium grafting reaction, Sonogashira coupling and organometallic complexsion in this case) results in **ReG-Co** precursor with a good solution processability**,** which allows one to fabricate free-standing films with tunable dimensions upon filtration through polytetrafluoroethylene (PTFE) membranes. Moreover, the organometallic species of Co ([$C_2Co_2(CO)_6$]) covalently anchored on the **ReG** plane can serve as catalytic spots for CNT growth. In this way, highly conductive free-standing graphene/CNT composite films can be created based on an acetylene-assisted thermolysis approach. Both the mechanical flexibility and electrical conductivity of graphene/CNT composite films are tested to be superior to those of thermally treated pristine graphene films.

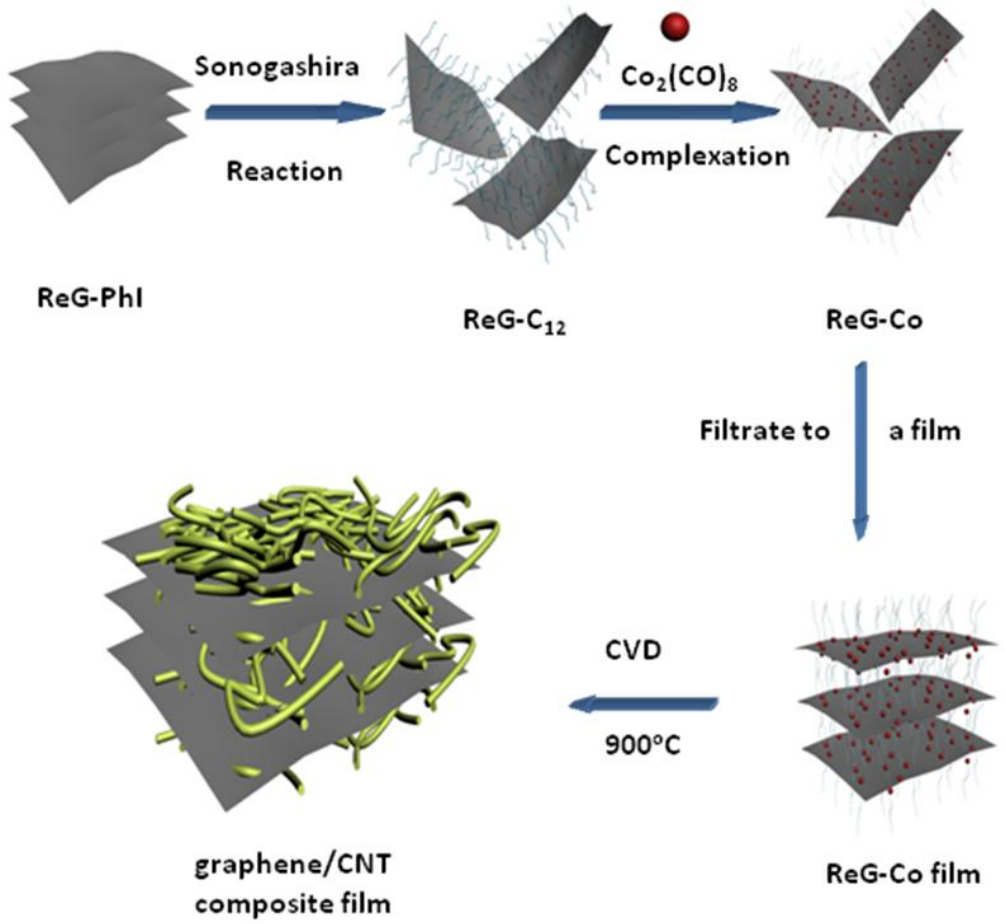

Figure 3.2 Schematic illustration of the synthesis of graphene/CNT composite

3.2 Preparation of Graphene/CNT composite materials

3.2.1 Synthesis of ReG-C_{12} precursor in solution

In a typical experimental procedure, **ReG** was prepared from chemical reduction of graphene oxide (GO) by hydrazine.[15]

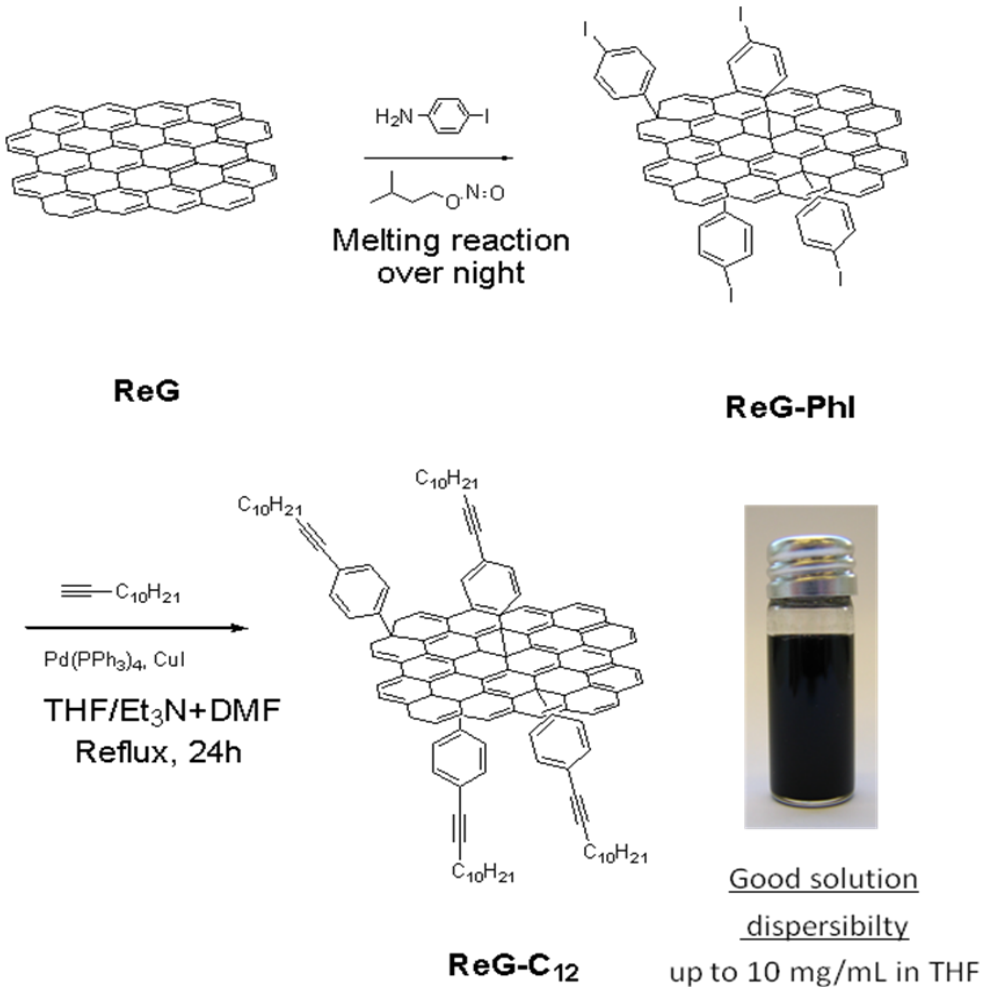

Figure 3.3 Synthesis of **ReG-C_{12}** complex from ReG: i) amyl nitrite, 4-iodoaniline, 60 ^{o}C, overnight, 92 wt% yield; ii) 1-dodecyne, CuI, $Pd(PPh_3)_4$, THF /Et3N/DMF, reflux, 24h, 90 wt% yield.

For the synthesis of the above-mentioned **ReG-Co** complex, the key step is to functionalize graphene with long aliphatic chains (alkylnyl in this case) that could enable a high dispersibility in organic solution. Towards this prerequisite, diazonium reaction of 4-halogen aniline was intentionally chosen in the first step, which has been demonstrated as a reliable method to covalently functionalize graphitic nanostructures, including CNT[16-18] and graphene.[19,20] It allows the attachment of iodophenyl groups to the graphene plane.

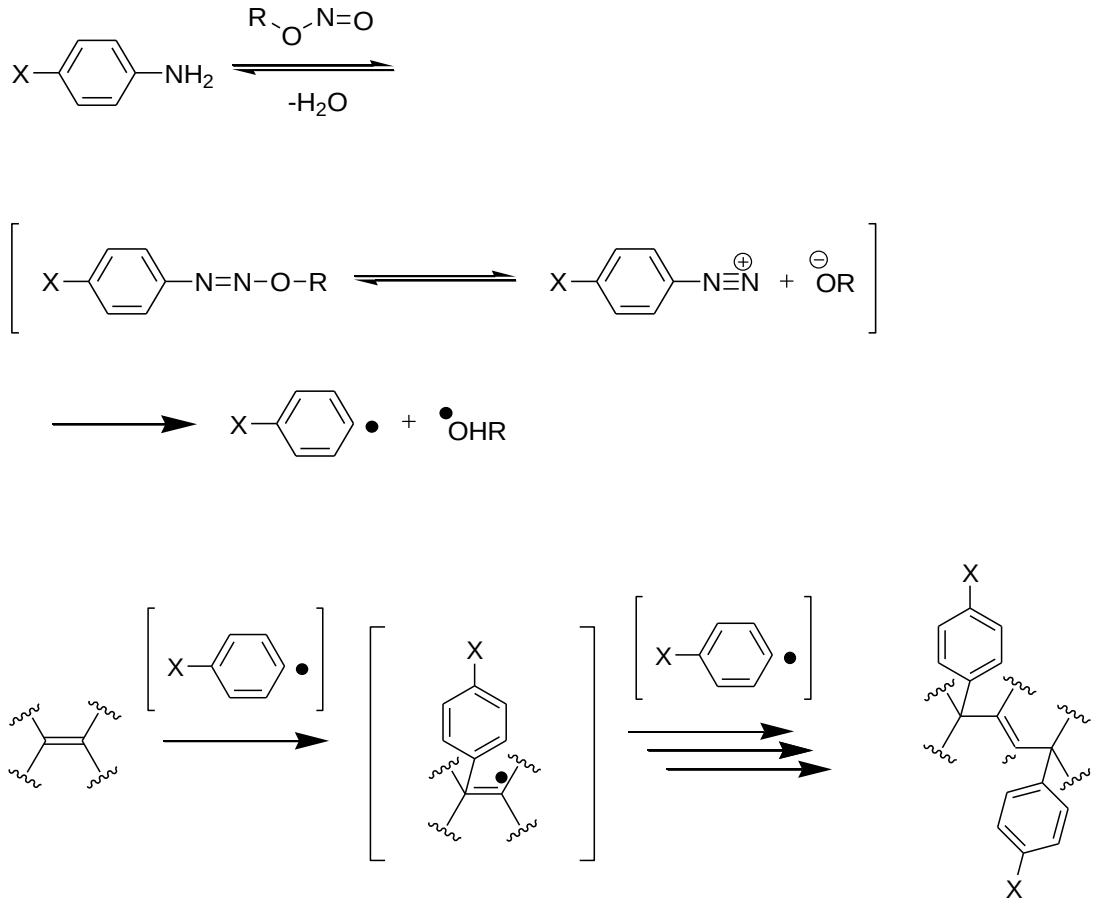

Figure 3.4 Typical arenediazonium salt decomposition pathway and the mechanism of diazonium addition of aryl radical to graphitic aromatic plane.

As illustrated in Figure 3.4, treating 4-iodo-aniline with isoamyl nitrite produces an active diazo entity which further generates 4-iodo-aryl radical in situ.[21] Such a reactive aryl radical is readily to react with the aromatic plane of graphene followed by delocalization and reaction with a second aryl radical.[18] By this means, the para-iodo phenyl substituent, as an active species in several palladium catalyzed aryl-aryl coupling reactions, is linked onto the graphene plane. Moreover, this organic functionalization gives ReG a moderate dispersibility in polar aprotic solvents, such as DMF, which is vital for the next reaction in solution.

Subsequently, the as-prepared iodophenyl-substituted graphene (**ReG-PhI**) was subjected to react with 1-dodecyne via Sonogashira coupling to afford 4-(dodec-1-ynyl)phenyl functionalized graphene (**ReG-C_{12}**) as a black solid. With 4-(dodec-1-ynyl)phenyl substituents as organic solubilizing moieties, **ReG-C_{12}** could be re-dispersed in most common organic solvents, such as dichloromethane (DCM), chloroform and tetrahydrofuran (THF) under a mild sonication condition. For instance, a homogeneous dispersion of **ReG-C_{12}** with a concentration of up to 10 mg/mL in THF could be achieved as shown in Figure 3.3. No indication of precipitation was observed after two weeks in contrast to the poor solubility of **ReG-PhI** in THF.

The experimental details and conditions to synthesize **ReG-C_{12}** in solution are described in experimental part in chapter 6

3.2.2 Synthesis of ReG-Co precursor in solution

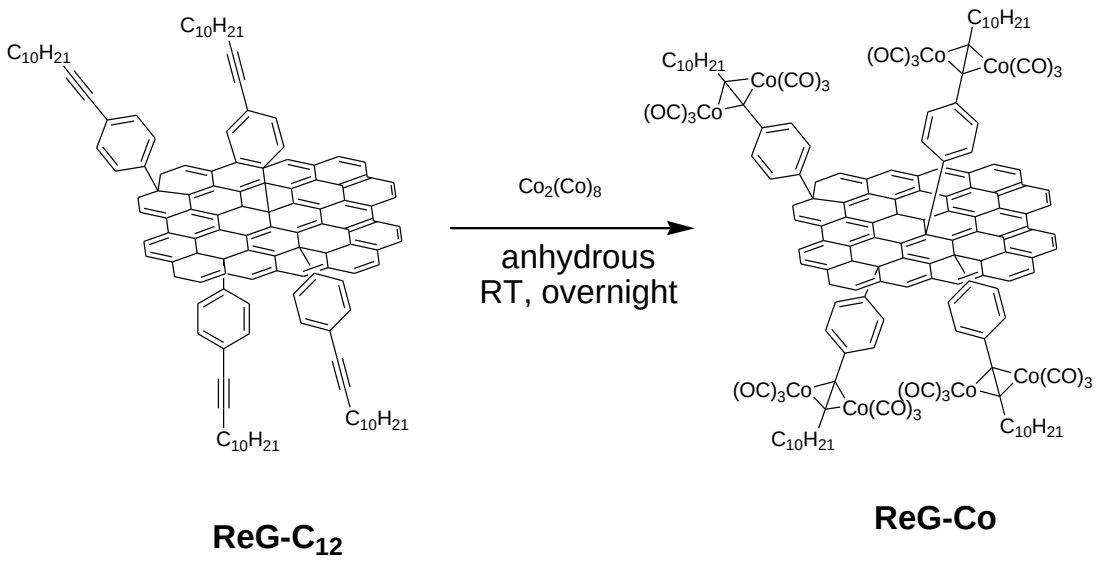

Figure 3.5 Synthesis of **ReG-Co** complex from **ReG-C_{12}**, 95 wt% yield.

The complexation between **ReG-C_{12}** and $Co_2(CO)_8$ was carried out in anhydrous

THF solution at room temperature for 6 h. Since $Co_2(CO)_8$ is sensitive to moisture, oxygen and light, the reaction must be kept under inert atmosphere and absence of light. By this means, $[C_2Co_2(CO)_6]$ complexes could be formed by the addition of $Co_2(CO)_8$ to ethynyl groups, and thus covalently attached to the graphene surface (Figure 3.5).

When the reaction finished, the mixture was filtrated, and the unreacted $Co_2(CO)_8$ residue could be removed by extensive washing with THF. A black solid of functionalized **ReG-Co** complex was finally achieved in 90% yield by weight.

After Co complexation, it was found that **ReG-Co** still had a good dispersibility in THF. It is believed that the decyl substituent remains intact during metal complexation, which could maintain the solution processability of **ReG-Co**. The good solution processability further enables a simple film formation process, which could easily be done by filtration.

3.2.3 Preparation of free-standing **ReG-Co** film

To establish a free-standing precursor film of **ReG-Co** for the build-up of a graphene/CNT composite, a **ReG-Co** dispersion was vacuum-filtrated through a 0.20 μm PTFE membrane (Fig. 5b). The resulting film was further dried at 80 ^{o}C for 24h with PTFE membrane on it. The diameter and thickness of the **ReG-Co** films could be easily adjusted by the size of the PTFE membranes and the volume of the solution before filtration. The covalent functionalization of $[C_2Co_2(CO)_6]$ complexes on graphene ensured that no catalytic sites were lost during the filtration process.

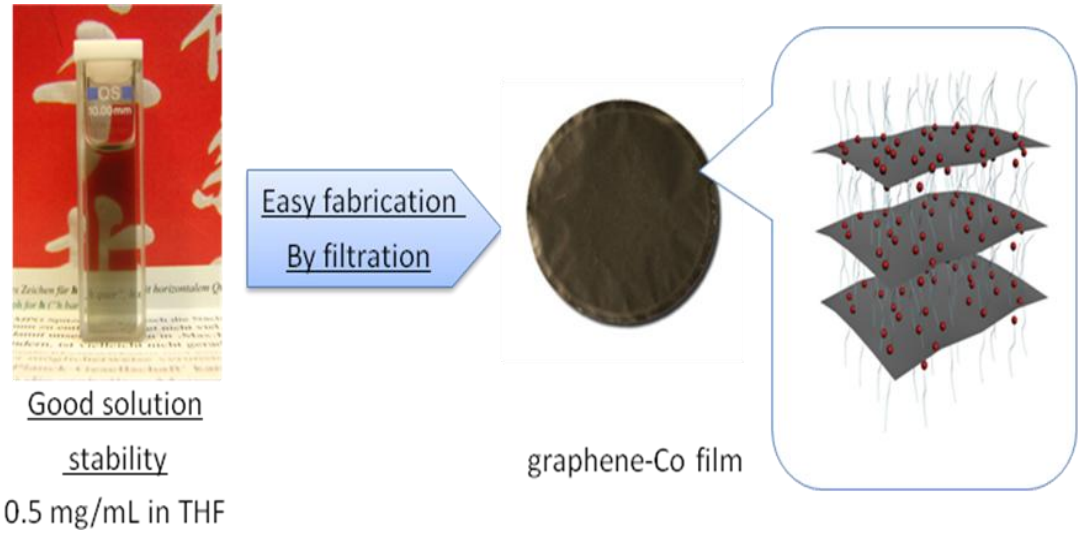

Figure 3.6 Left: Good solution processability of **ReG-Co** in THF; Right: Easy film formation of **ReG-Co**: covalent bonds avoid losing Co species during film processing.

3.2.4 Growth of graphene/CNT composite film

After transferring the fragile, yet free-standing **ReG-Co** precursor film from the PTFE membrane into a chemical vapor deposition (CVD) chamber, the growth of CNTs on graphene sheets was carried out at 900 ^{o}C under a flow of C_2H_2/H_2/Argon (5 sccm/60 sccm/100 sccm) for 5 min. Under this reductive atmosphere, the underlying film composed of overlapping ReG sheets was thermally deoxygenated and reduced.[11] The graphene/CNTs composite film exhibits a shiny metallic luster indicating a high quality of graphitic feature with in this film.

For comparison, a free-standing film of **ReG-C_{12}** was prepared similarly to the preparation of the free-standing **ReG-Co** film described in chapter 3.2.3, and the pyrolysis was carried out under same condition described in chapter 3.2.4.

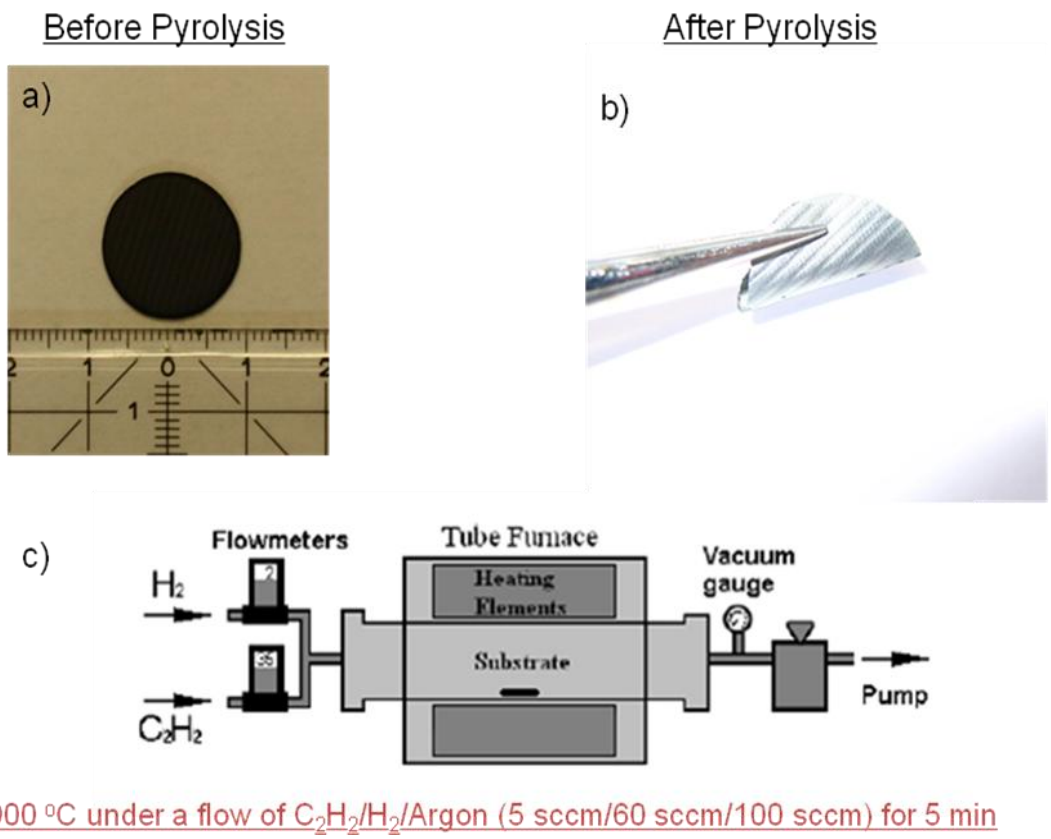

Figure 3.7 a) Photography of **ReG-Co** precursor film: a black fragile film; b) photography of graphene/CNT film pyrolyzed from **ReG-Co** precursor film: The film exhibits a shiny metallic luster.; c) schematic illustration of the instrument for acetylene-assisted CVD growth of CNTs on graphene sheets.

3.3 Structural Characterization

3.3.1 ReG-C_{12} precursor

The good dispersibility allows for further characterization of **ReG-C_{12}** by UV-Vis spectroscopy in organic solvents. Figure 3.8a shows the UV-Vis spectrum of **ReG-C_{12}** in THF at a concentration of 0.1 mg/mL. A typical absorption peak of graphene around 280 nm can be attributed to the extended electronic conjugation of the

graphene plane with respect to that of graphene oxide (230 nm).[22]

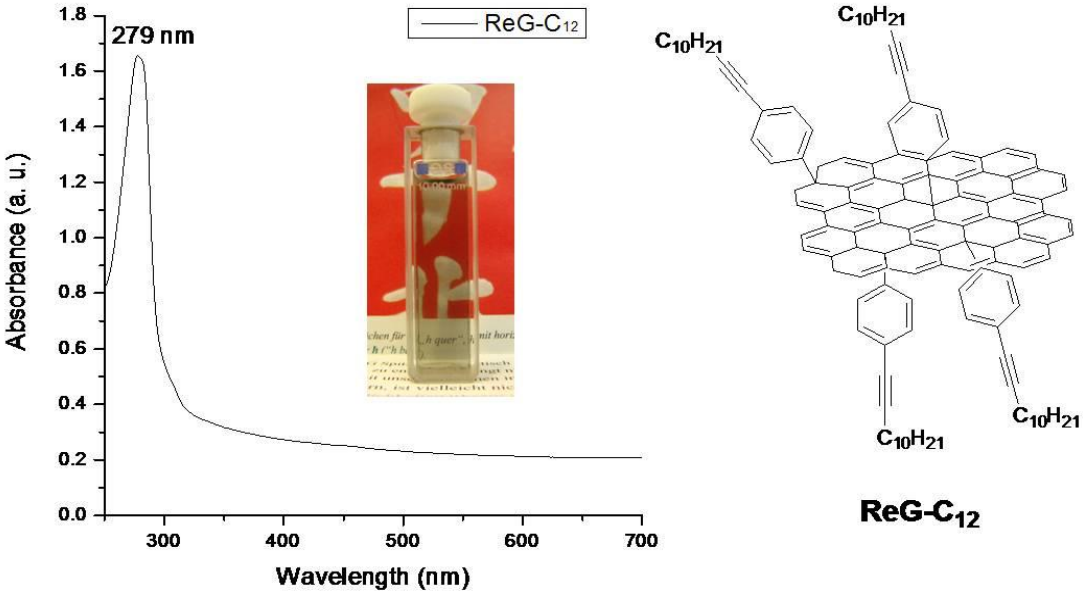

Figure 3.8 UV-Vis spectrum of **ReG-C_{12}** in THF; Inset is the stable dispersion of **ReG-C_{12}** in THF (0.1 mg/mL)

Furthermore, infrared spectroscopy as a useful tool to identify chemical structure and functional groups is utilized to monitor the structure evolution from **ReG** to **ReG-C_{12}**.

The black curve in Figure 3.9 shows the solid state FT-IR spectrum of **ReG-PhI**. All the characteristic peaks of **ReG** can be identified in FT-IR spectrum of **ReG-PhI** too. The weak peak above 3500 cm^{-1} (O-H stretching vibrations) is the evidence of a severe deoxygenation during chemical reduction of GO.[23] Stretching vibrations from C=O at 1720 cm^{-1}, C-OH stretching vibrations at 1220 cm^{-1} and C-O stretching vibrations at 1060 cm^{-1} are almost identical with **ReG**, which are due to the remaining carboxyl groups even after hydrazine reduction.[22] On the other hand, the peak of C-I

stretching vibration at around 600 cm^{-1} should be noted, which confirms that the 4-iodo-phenyl substituent was covalently anchored on ReG sheets.

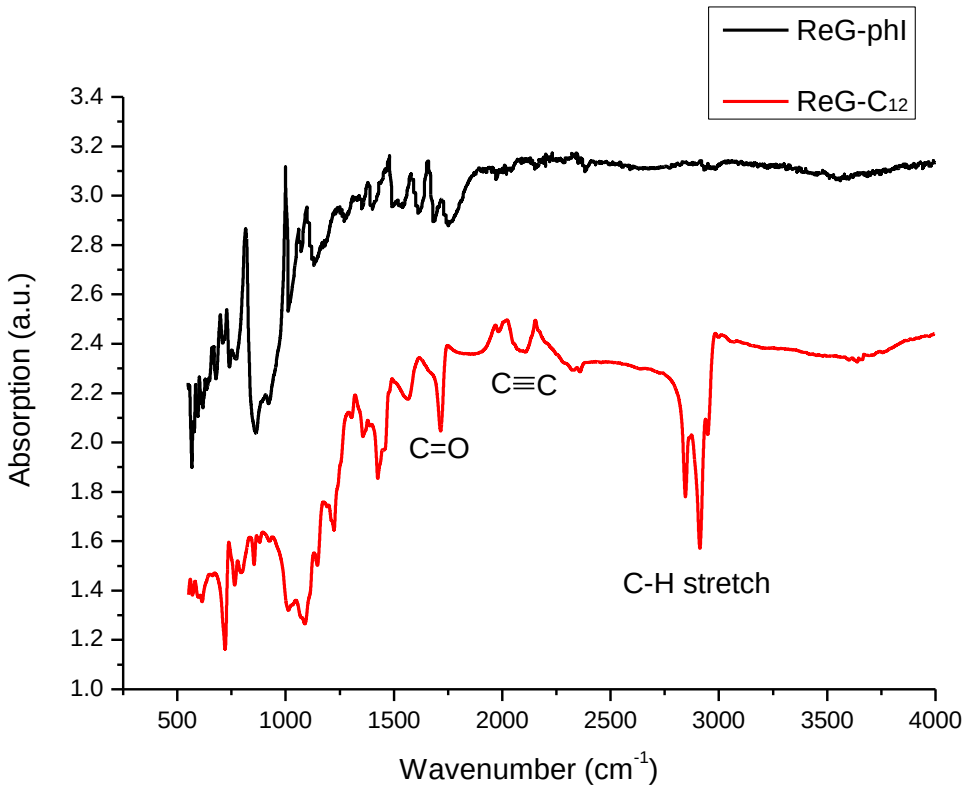

Figure 3.9 Solid state FT-IR spectra of **ReG-PhI** and **ReG-C_{12}** as solid films.

Upon a comparison of the solid state FT-IR spectra between **ReG-PhI** and **ReG-C_{12}** (Figure 3.9), the aromatic C=C stretch (1560 cm^{-1} and 1460 cm^{-1}) and characteristic aromatic C-H bending (800 cm^{-1}) indicate the presence of phenyl groups attached to the graphene basal plane, while the appearance of the sp^3 C-H (2920 cm^{-1} and 2846 cm^{-1}), the CH_3 bending (1380 cm^{-1}) and the skeletal vibration of the methylene group (720 cm^{-1}) can be ascribed to the decyl chains ($-C_{10}H_{21}$). Associated with a broad peak around 2220 cm^{-1} (ethynyl group), the results evidently validate that a large number of 4-(dodec-1-ynyl)phenyl groups have been successfully

anchored on graphene plane via covalent functionalization. Moreover, the disappearance of the peak of C-I stretching vibration at around 600 cm^{-1} implies that most of the iodophenyl substituents have been converted.

As proved by FT-IR spectra, the organic functionalization of **ReG** renders the successful decoration of the basal plane of graphene sheets with a large number of 4-(dodec-1-ynyl)phenyl substituents. This was also observed in the Raman spectra from the increasing amount of sp^3 carbon of **ReG-C_{12}**. Figure 3.10 clearly shows an increased D/G intensity ratio, namely the ratio between sp^3 carbon and sp^2 carbon, of **ReG-C_{12}** comparing with that of **ReG**. As the decyl substituents contain a lot of sp^3 carbons, the increased D/G intensity ratio of **ReG-C_{12}** could be attributed to the addition of solubilising chains on the basal plane of **ReG**.

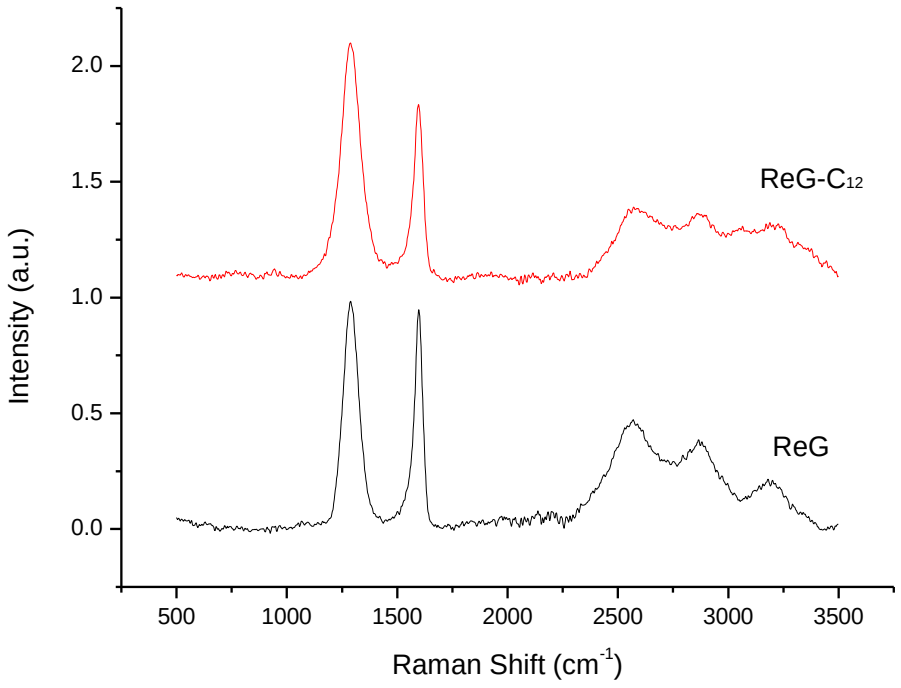

Figure 3.10 Raman spectra of **ReG**, **ReG-C_{12}**

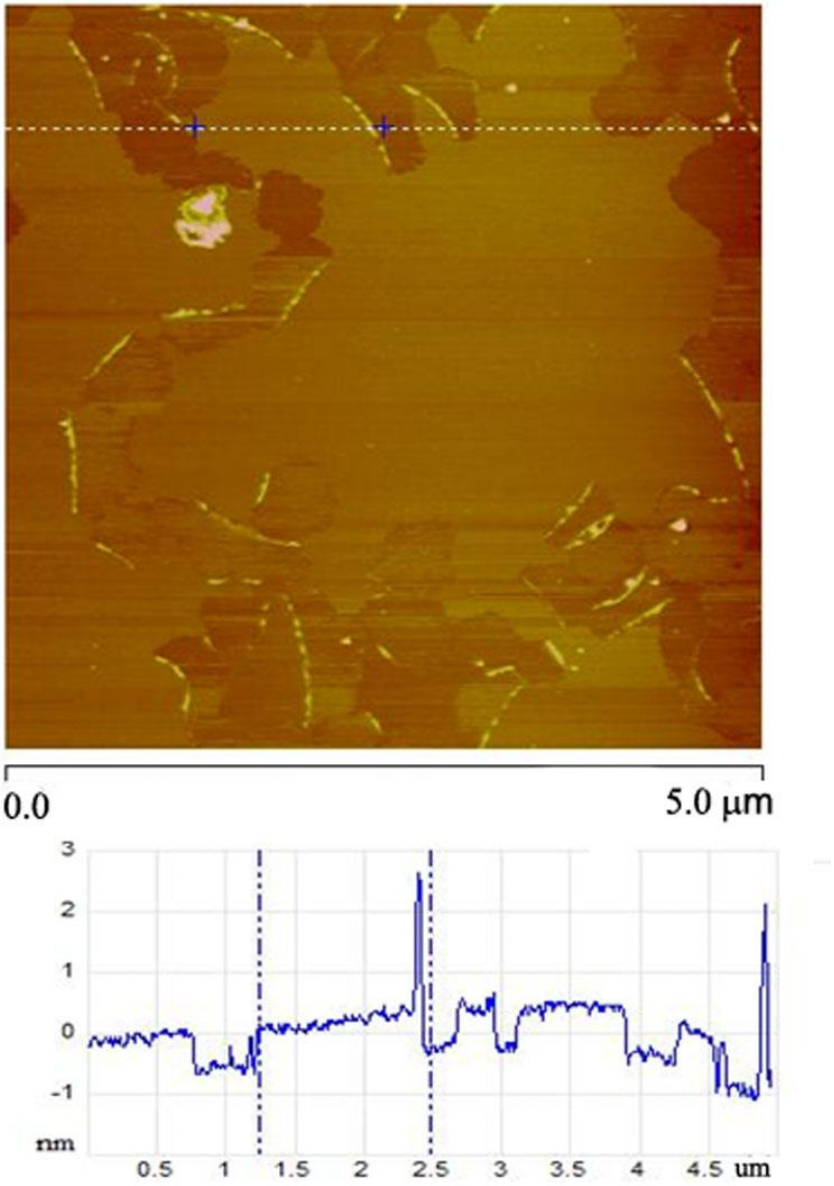

Figure 3.11 AFM image of **ReG-C_{12}** prepared by drop-casting the THF dispersion on silicon wafer

An atomic force microscopy (AFM) image (Figure 3.11) of **ReG-C_{12}** provides the detailed information of its morphology on the surface. The samples were prepared by drop-casting a THF dispersion of **ReG-C_{12}** on SiO_2 substrates. In AFM image, **ReG-C_{12}** monolayers with a lateral size of 2~10 µm can be identified on the surface. A

typical AFM cross-section image (blue curve in Figure 3.11) indicates that the average thickness of a single-layer **ReG-C_{12}** is around 1.2 nm. As mentioned in Chapter 2, the thickness of **ReG** monolayer measured by AFM is generally to be 0.5 – 1.0 nm.[22,23] It is reasonable to deduce that the slight increase of the thickness is caused by the presence of 4-(dodec-1-ynyl)phenyl groups across the graphene basal plane. Meanwhile, no obvious aggregates, pinholes and cracks found on smooth surface of **ReG-C_{12}** suggests that the graphene plane, even after several steps organic functionalization, remains intact without severe defects.

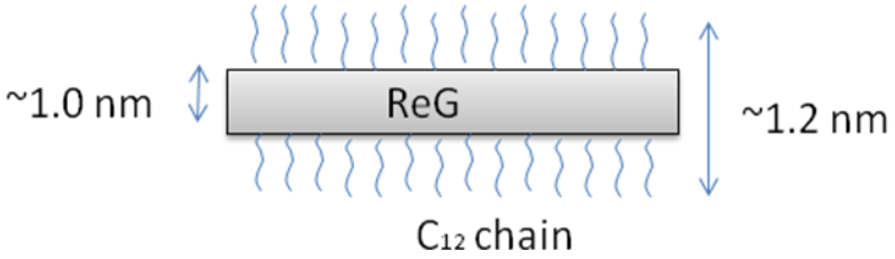

Figure 3.12 Schematic explanation of the increase of the thickness of **ReG-C_{12}** on surface

Further inspection of the TEM images reveals a large number of flat monolayers (as shown in Figure 3.13a), folded (Figure 3.13b) and stacked (Figure 3.13c) **ReG-C_{12}** with lateral dimensions ranging from 1 to 5 μm. These results suggest that the stable THF dispersion of **ReG-C_{12}** mostly consists of exfoliated, functionalized individual graphene sheets with minimum aggregation among them. The good accessibility to interlayers of graphene sheets dispersed in organic solvents makes **ReG-C_{12}** ready to intimately coordinate with $Co_2(CO)_8$ during complexation.

Moreover, electron diffraction (ED) was used to characterize crystal structure of monolayer of **ReG-C_{12}**. As can be seen from Figure 3.13d, the ED pattern of **ReG-C_{12}** shows the typical six fold symmetry that is similar to that of peeled-off graphene. [24,25]

This evidence along with the UV spectrum and AFM images of **ReG-C_{12}** indicate that the well-crystallized, single-layer graphene structures still remained in **ReG-C_{12}** even after multiple step organic functionalizations.

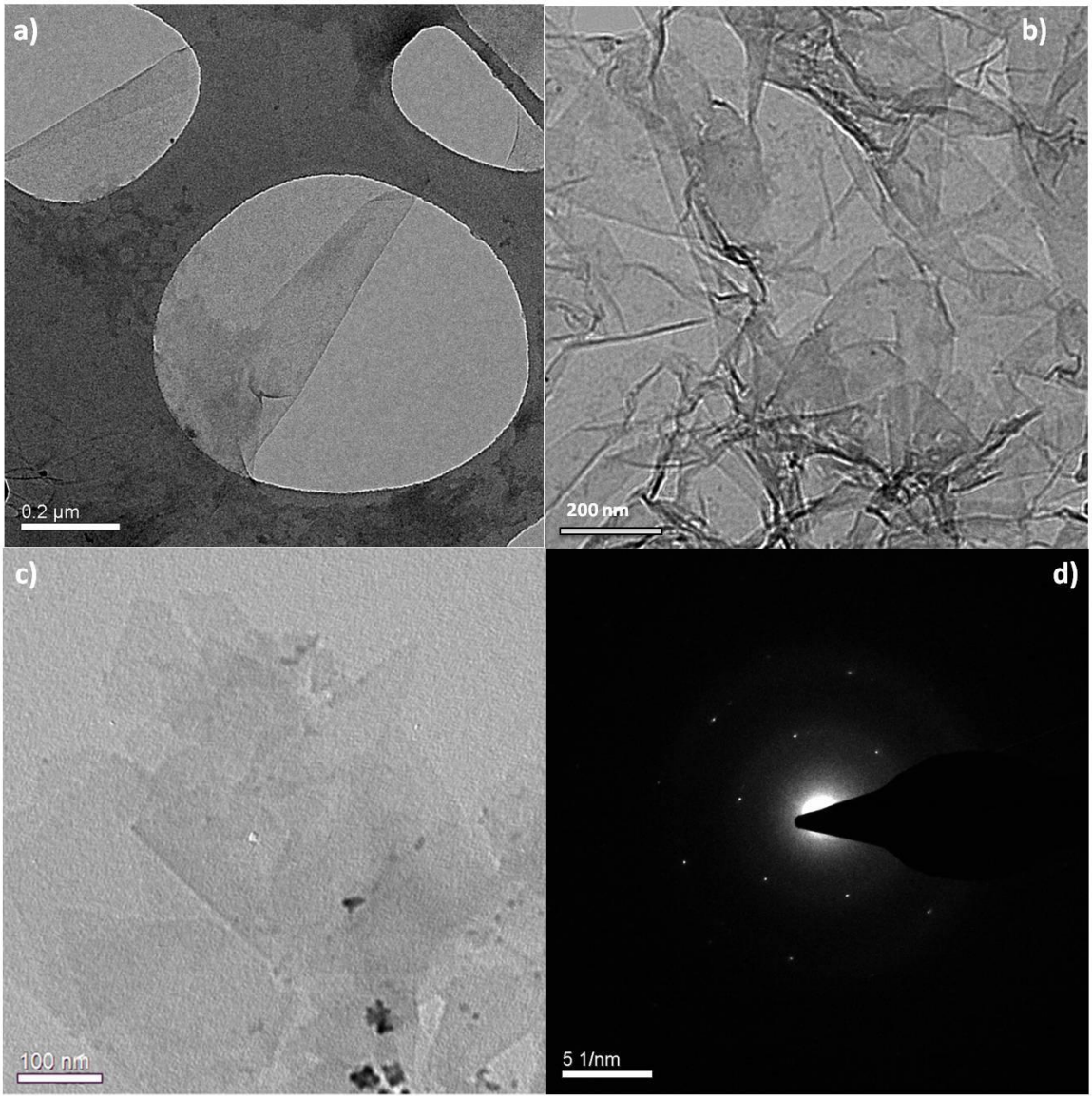

Figure 3.13 TEM image of a) flat monolayer; b) folded monolayer and c) stacked multiple layers of **ReG-C_{12}** prepared by drop-casting the THF dispersion on silicon wafer; d) electron diffraction (ED) pattern of flat monolayer of **ReG-C_{12}**.

3.3.2 Re-Co precursor

The complexation between **ReG-C_{12}** and $Co_2(CO)_8$ was carried out in THF. By this means, $[C_2Co_2(CO)_6]$ complexes could be formed via the addition of $Co_2(CO)_8$ to ethynyl groups, and thus covalently attached to the graphene surface. Compared to **ReG-C_{12}**, the solid state FT-IR spectrum of **ReG-Co** (Fig. 3b) reveals the presence of peaks at 2920 cm^{-1}, 2850 cm^{-1}, 1380 cm^{-1} and 760 cm^{-1}, suggesting that the decyl groups are preserved within graphene after cobalt complexation. Meanwhile, the disappearance of the broad peak ascribed to the ethynyl group at 2200 cm^{-1} along with the appearance of sharp peaks attributable to $[C_2Co_2(CO)_6]$ moieties (around 2100 cm^{-1})[26] imply that all ethynyl groups have been converted. Furthermore, no obvious cobalt nanoparticles can be found in the TEM image of **ReG-Co** (Figure 3.15), suggesting that the $[C_2Co_2(CO)_6]$ complexes are covalently anchored onto the graphene basal plane in a homogeneous manner. This covalent functionalization of $[C_2Co_2(CO)_6]$ complexes on graphene ensured that no catalytic sites were lost during the filtration process.

As investigated by the FT-IR spectrum of **ReG-Co**, complexation of Co onto the graphene plane was carried out in a homogeneous manner. On the other hand, the extensive washing of products over THF is supposed to eliminate any remaining unreacted $Co_2(CO)_8$. Therefore, no aggregates of either $[C_2Co_2(CO)_6]$ or $Co_2(CO)_8$ species could be found on **ReG-Co** sheets. This is actually confirmed by TEM images (Fig. 4a and b), which provide a close view of graphene sheets deposited on Cu grid from a THF dispersion of **ReG-Co**. No obvious cobalt particles can be found even in an enlarged view (Figure 3.15b), suggesting that the $[C_2Co_2(CO)_6]$ complexes are covalently and homogeneously anchored onto the graphene basal plane.

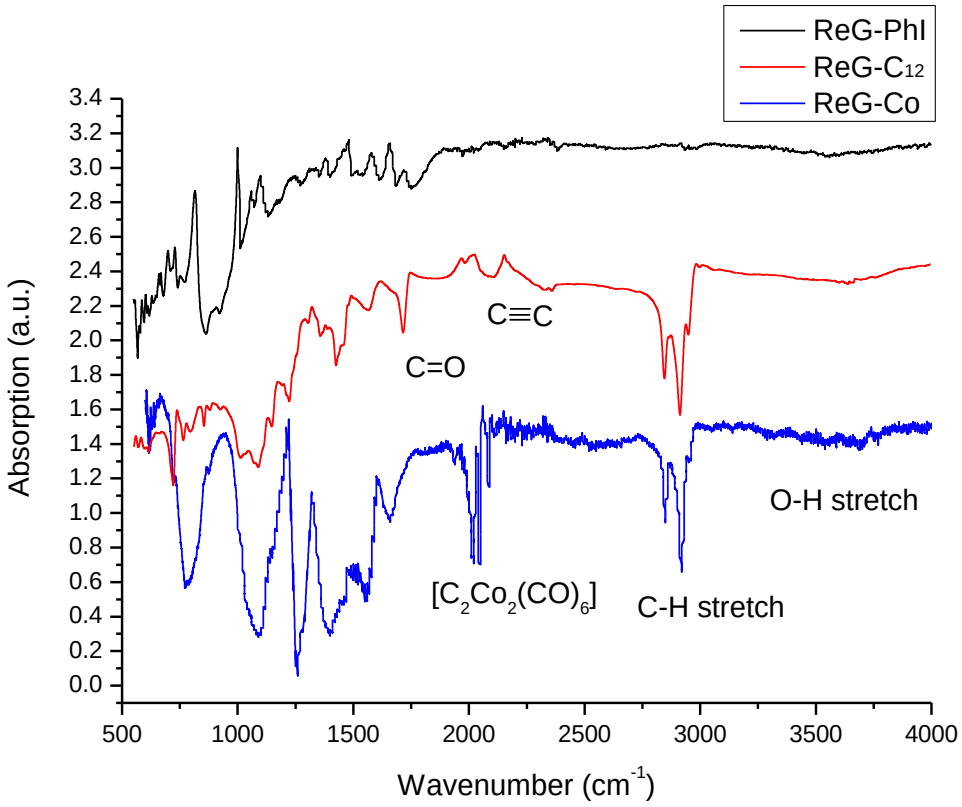

Figure 3.14 Solid state FT-IR spectra of **ReG-PhI**, **ReG-C_{12}** and **ReG-Co** as solid films.

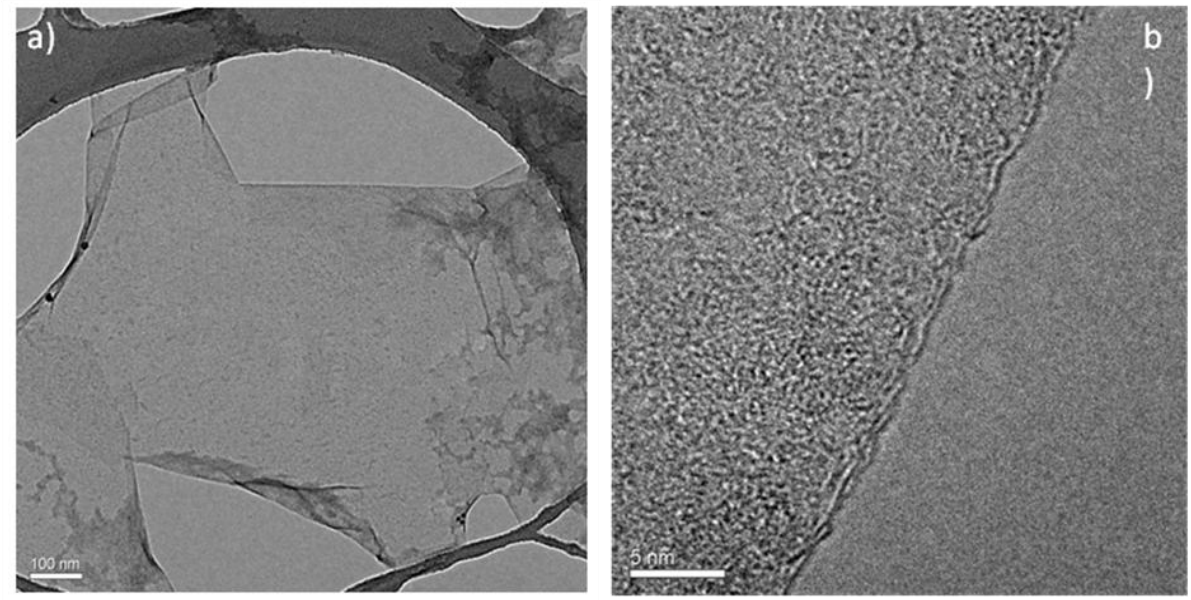

Figure 3.15 a) TEM image and b) HRTEM image of **ReG-Co** prepared by drop-casting the THF dispersion on a silicon wafer.

3.3.3 Graphene/CNT composite

After transferring the **ReG-Co** film from the PTFE membrane into a chemical vapor deposition (CVD) chamber, the growth of CNTs on graphene sheets was carried out at 900 ^{o}C under a flow of C_2H_2/H_2/Argon (5 sccm/ 60 sccm/ 100 sccm) for 5 min. For comparison, pristine **ReG-C_{12}** film was also pyrolyzed upon the same CVD treatment at 900 ^{o}C (**ReG-C_{12}-900**) as reference sample.

Under the reductive atmosphere, the underlying film composed of overlapping graphene sheets should be thermally reduced as literature described.[27,28] On the other hand, Co nanoparticles released from the decomposition of $[C_2Co_2(CO)_6]$ complexes could serve as catalytic nuclei for CNT growth during the CVD treatment.[29,30] Acetylene here acts as the carbon source, which is supposed not only to build up carbon nanotubes under the catalysis of Co particles, but also to repair the defects on graphene surface of ReG. After thermal treatment, the cobalt residues were removed from the resulting film with a 1M HCl solution.

Figure 3.16 shows the Raman spectra of **ReG**, **ReG-C_{12} ReG**, **ReG-C_{12}-900** and graphene/CNT composite films measured at solid states. The significant structural changes occurring during the thermal processing from **ReG-C_{12}** to **ReG-C_{12}-900**, and from **ReG** to graphene/CNT composite are reflected in their Raman spectra.

Comparing the Raman spectrum of **ReG-C_{12}-900** with that of **ReG-C_{12}**, both of them display comparable D bands at ~1300 cm^{-1}, indicating the non-perfect in-plane sp^2 domains along the graphene surface generated during the oxidation process of graphite. However, an exceptional change of G band and D/G intensity ratio of **ReG-C_{12}-900** were observed. As described in literatures, and in Chapter 2.4.2, a further thermal reduction would lead to a slight increase of the D/G ratio, in that new graphitic domains created in thermal reduction have a smaller size than the

ones present in ReG before reduction;[31,32] and also because the appearance of typical 5 or 5–8–5 defects on the carbon frameworks due to the release of CO_2 or CO under high temperature (Figure 2.8).[28]

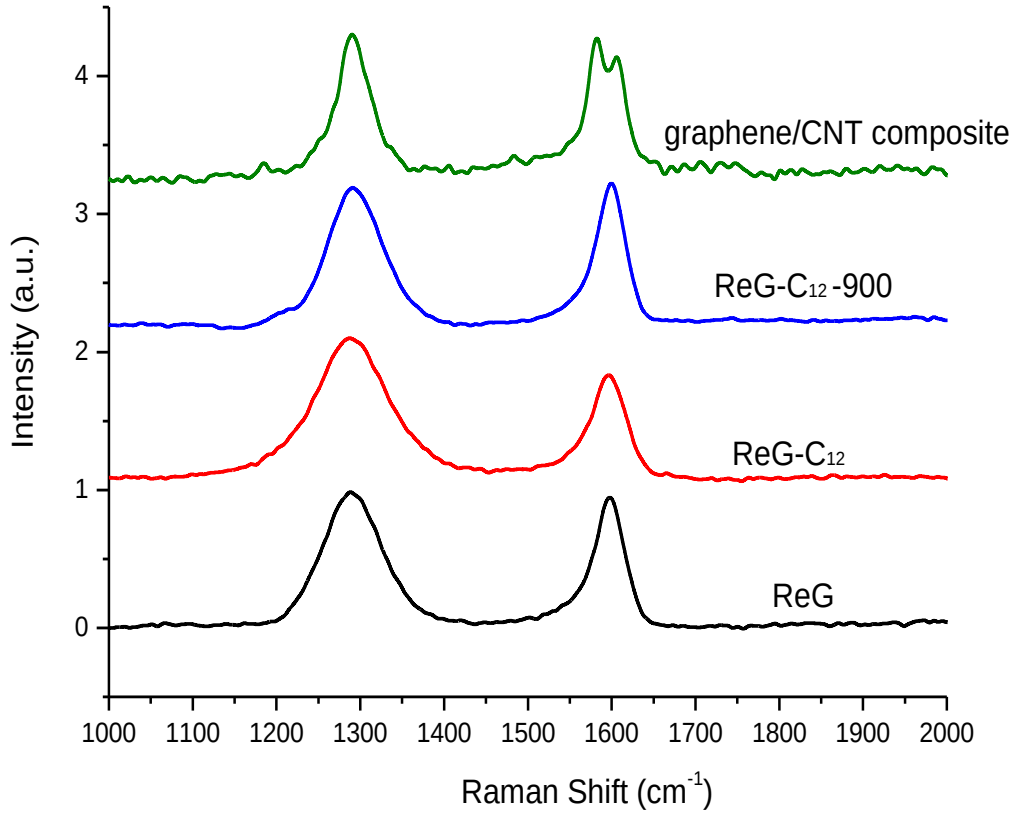

Figure 3.16 Raman spectra of **ReG**, **ReG-C_{12}** **ReG-C_{12}-900** and graphene/CNT composite film

In contrast, the G band of **ReG-C_{12}-900** at 1600 cm^{-1} (Figure 3.16) has a higher intensity than that of **ReG-C_{12}**; and thus the D/G intensity ratio of **ReG-C_{12}-900** is decreased after thermal reduction compared with that of **ReG-C_{12}**, indicating an enlarged in-plane sp^2 domain size of graphene sheets. This could be explained by the

aid of acetylene, which could generate abundant carbons in radical form that may restrain the loss of carbon atoms from the frameworks and the occurrence of defects, while oxygen-containing groups are removed during the thermal treatment.[33] Moreover, dodecynyl-phenyl substituent of **ReG-C_{12}** could act as supplementary carbon source during thermal reduction as well, which establish a carbon-rich atmosphere that may allow for mending the pristine defects in ReG sheets.

In comparison with **ReG-C_{12}**, a splitting G band in the Raman spectrum of the graphene/CNT composite film was identified at 1582 cm^{-1} and 1607 cm^{-1}. A splitting G band of solid state Raman spectra implies a different form of sp^2 carbon structures from pure graphene film. Furthermore, it should be noted that the similar G band splitting is frequently observed in Raman spectrum of multiwalled CNTs, which has been confirmed to be composed of both the G-band modes from the innermost tube and graphite-like mode from the outer cylinders in MWNT.[34] This characteristic observation in Raman spectra indicates that MWNTs have been generated during the thermal reduction of **ReG-C_{12}** film upon an acetylene-assistant CVD treatment.

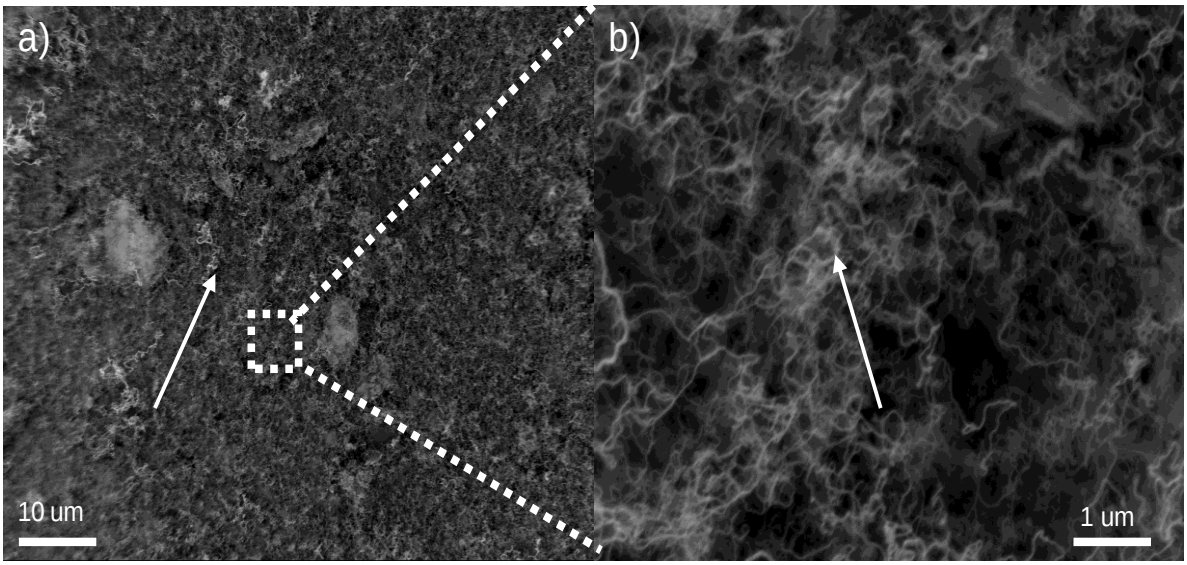

Figure 3.17 a) Top-view of SEM image of graphene/CNT composite film; b) a enlarged view of SEM image of graphene/CNT composite film.

Comparing to spectroscopic results, SEM images obviously provide more direct evidence that the thermal reduction of **ReG-C_{12}** film upon an acetylene-assisted CVD treatment result in the growth of CNTs between graphene layers.

First of all, the top view SEM images of graphene/CNT composite film (SEM) in Figure 3.14a) and b) disclose a massive growth of CNTs on top of graphene layers. Those nanotubes are randomly coiled on graphene surface. The diameter of the as-grown CNTs ranges from 30 to 50 nm, and the tube length is up to 5 µm. These results suggest that the stable THF dispersion of **ReG-C_{12}** mostly consists of exfoliated, functionalized individual graphene, so that CNTs could grow at the interlayer of graphene sheets. The tangled arrangement of CNTs is expectable when non-template or orientation technique was applied during the CVD growth of them.

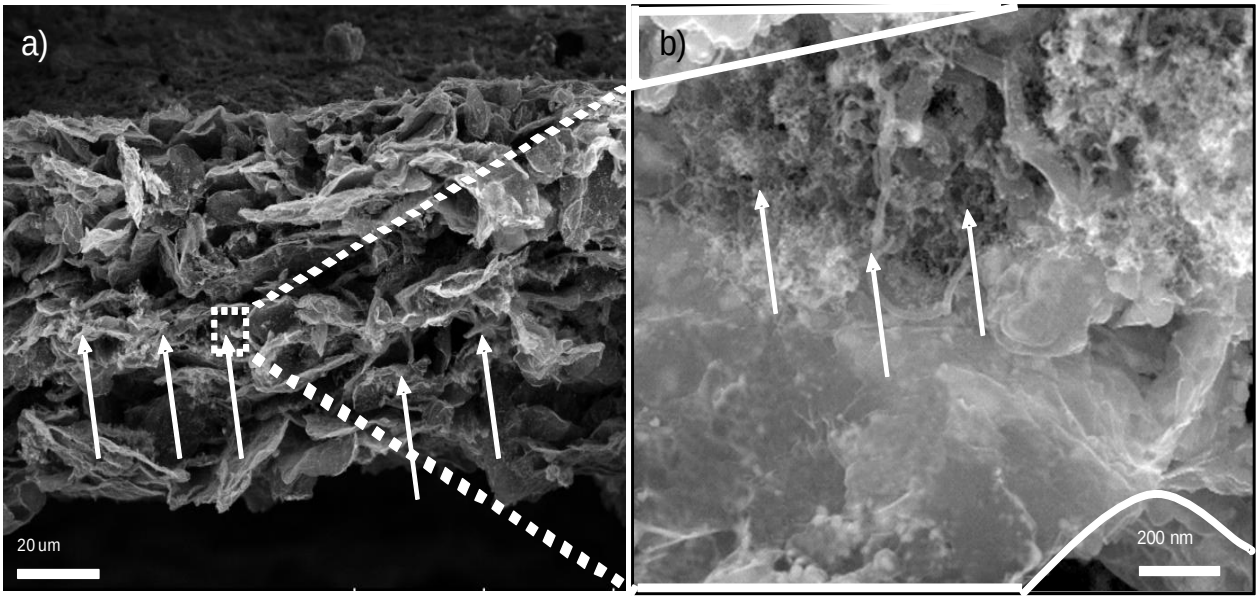

Figure 3.18 a) Cross-sectional SEM image of graphene/CNT composite film; b) a enlarged view of SEM image of graphene/CNT composite film: The white line draw the outline of graphene layers and the white arrows indicate the CNTs between graphene layers.

Moreover, CNTs can be also observed between the graphene layers by the cross-sectional view SEM images of graphene/CNT composite film as shown in Figure 3.15a) and b). At first, the sheet-like structure of graphene layers can be identified (as indicated by the solid white lines). With the increase of voltage applied in SEM, CNTs at the deep space between graphene layers show themselves with a similar diameter of the CNTs growing on the top, but small in their total length. Interestingly, the CNTs between graphene layers are randomly and horizontally stacked between the graphene layers (Figure 3.15). This can be attributed to the restriction of full length extension of the flexible CNTs in the space within the graphene layers, which act as supporting holder to mediate the organization of the CNTs.

In contrast, no CNTs can be identified in the SEM images (Figure 3.16) of the pristine **ReG-C_{12}** film upon the same CVD treatment at 900 ^{o}C (**ReG-C_{12}-900**). This result further confirm that Co critical effect of [$C_2Co_2(CO)_6$] complexes covalently linked on **ReG-Co**. It is the Co particles generated from the organocobalt moieties [$C_2Co_2(CO)_6$] that serve as the catalyst for the growth of CNTs between graphene layers.

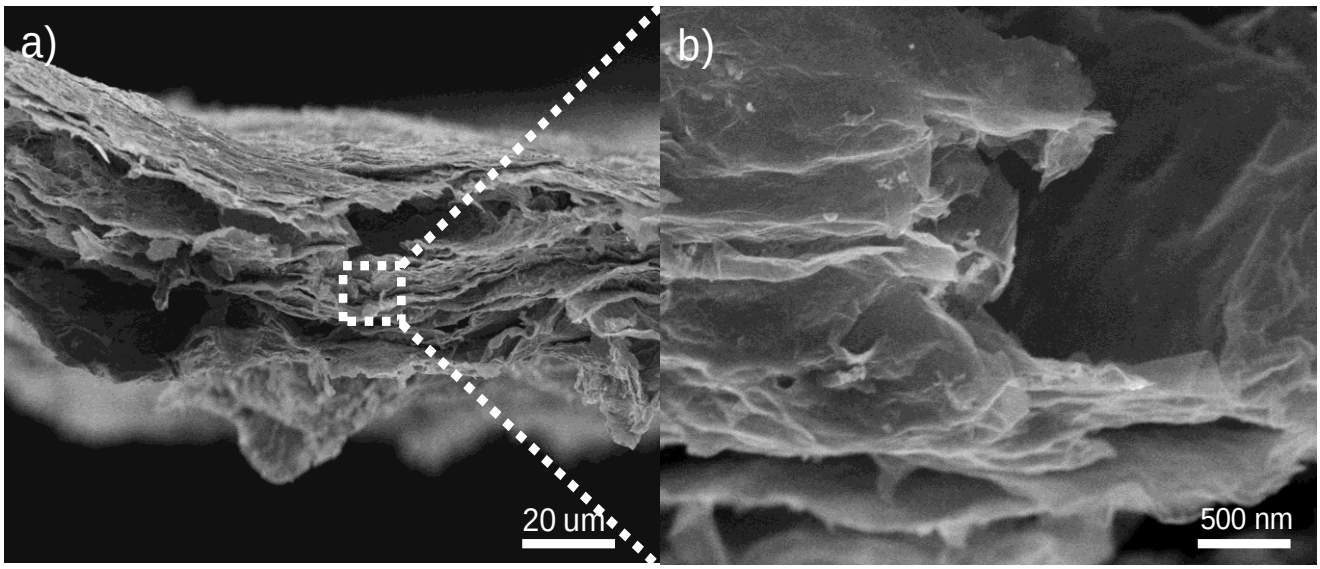

Figure 3.19 Cross-sectional SEM image of **ReG-C_{12}-900** film

Further inspection of TEM images brings more details of the morphology of graphene/CNT composite films. Since the CNTs grew between graphene layers, the materials after thermal treatment can hardly be dispersed in any organic solvents. The thin layered structure of graphene/CNT composite was only obtained by using Cu grids scratching over the surface of the film several times. As can be seen from a clear picture with CNTs stacking on a single layer graphene in Figure 3.17a, the diameter of CNTs is around 30 nm, almost identical to the observation in SEM images. Furthermore, the wall thickness of the CNTs generated in this case ranges from 10~15 nm, a quite narrow distribution. This also indicates that the as-grown CNTs are multiwalled CNTs, which is in agreement with the phenomenon of G band splitting found in its Raman spectra. In addition, a large number of CNTs can be found in Figure 3.17b, which are randomly coiled between graphene layers.

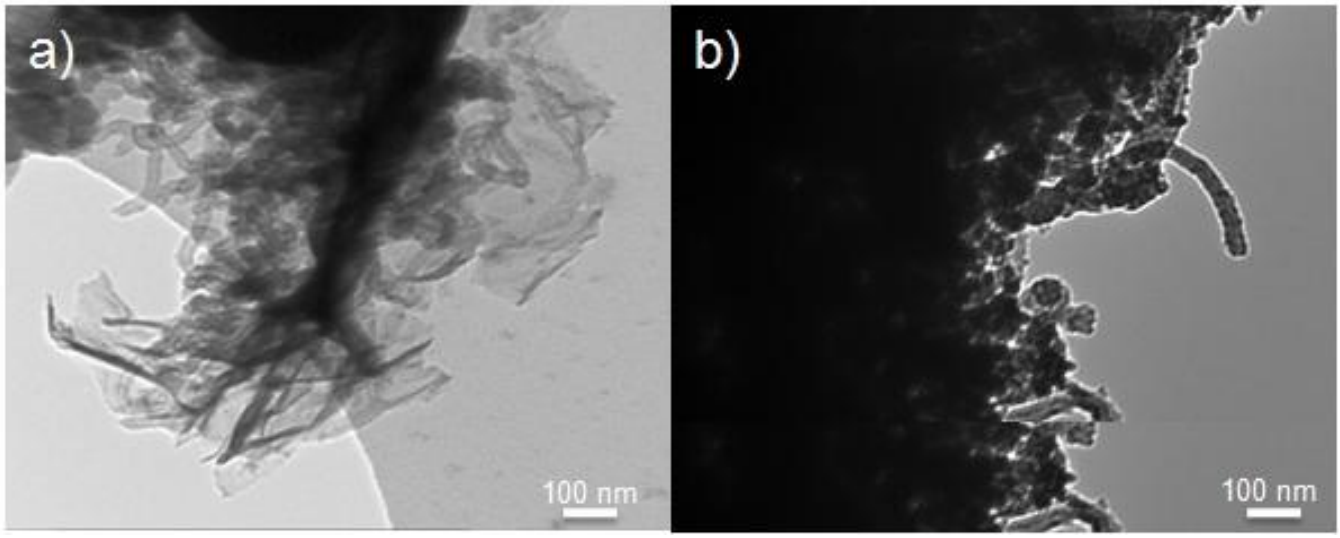

Figure 3.20 TEM image of graphene/CNT composite film, sample was prepared by using grid scratching over the film several times;

3.4 Mechanical and Electrical Properties of graphene/CNT composite film

3.4.1 Tensile measurement of graphene/CNT composite and **ReG-C_{12}-900** films

As demonstrated in chapter 3.3, a composite structure of graphene and CNTs was achieved via an acetylene-assistant thermolysis. The CNTs arise directly from graphene sheets, enabling a close interaction between graphene and CNTs. Since CNT has been used as a mechanical reinforcement in several composite materials, it is reasonable to deduce that graphene/CNT composite film processes a better mechanical property than graphene film itself.

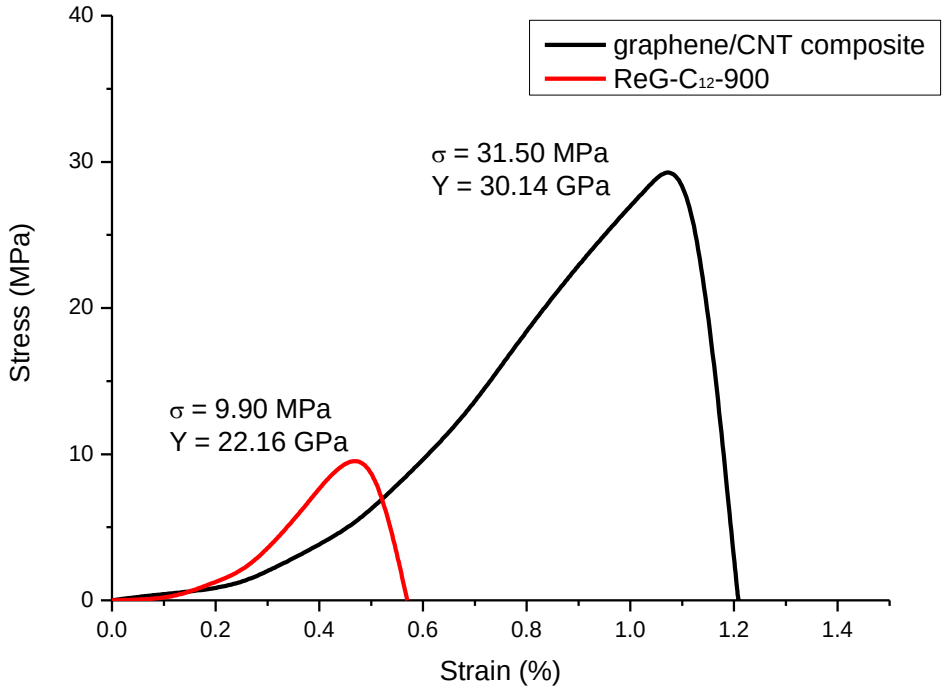

Figure 3.21 Stress-strain curves of graphene/CNT composite film and **ReG-C_{12}-900** film

To demonstrate this assumption, a tensile testing was carried out at room temperature. From the typical stress–strain curves, the Young's modulus (stiffness) and the stress (strength) of **ReG-C_{12}-900** film were measure to be 22.16 GPa and 9.90

MPa. These values are comparable with those reported for graphene oxide film[35]; and higher than those of a reduced graphene oxide film[36] and a flexible graphite foil.[37] Meanwhile, the stiffness and the strength of graphene/CNT composite film were measured to be 30.01 GPa and 31.15 MPa. It is interesting to notice that the stiffness and strength of the graphene/CNT composite film are about 36 % and 218 % higher than **ReG-C_{12}-900** respectively. This phenomenon is similar with the observation of the mechanical reinforcement of CNTs in CNT/polymer composite.[38]

It is usually believed that there are four main requirements for an effective mechanical reinforcement from CNTs in the composite materials. These are a large aspect ratio, good dispersion, interfacial stress and alignment.[39] Aspect ratio must be large enough for the load transfer to the nanotubes.[40] Moreover, CNTs must be uniformly dispersed in the composite materials. This results in a more uniform stress distribution along the composite materials and minimizes the presence of stress-concentration centers. An additional important requirement is the interfacial shear stress between different composites (in our case, CNTs and graphene sheets). This is the strength at the interface (or junctions) where breaks at critical stress. Alignment is somehow less crucial since aligned composites have very anisotropic mechanical properties, which must be avoided in bulk samples.[39]

The SEM and TEM images of the graphene/CNT composite film in figure 3.17, 3.18 and 3.20 suggest a high aspect ratio and a unified dispersion of CNTs between graphene layers. Moreover, as the CNTs are directly raised up from graphene layers, they are linked with each other covalently. Thus, a strong interface stress is expected. All in all, such a graphene/CNT composite film meets the three major criteria for an effective mechanical reinforcement of CNTs in the graphene/CNT composite. Therefore, the significant increase of the stiffness and strength of the graphene/CNT composite film is observed and has evidently demonstrated that CNTs grew between graphene layers.

3.4.2 Conductivity measurement of graphene/CNT composite and **ReG-C_{12}-900** films

In order to further investigate the influence of the as-grown CNTs on the electrical properties of the composite films, the sheet resistances of the graphene/CNT composite and **Re-C_{12}-900** films are evaluated by means of four-probe resistance measurements. Their electrical properties are summarized in Table 3.1. It is remarkable that the conductivity of the graphene/CNT composite films is 535 S/cm, ~200 S/cm higher than that of **ReG-C_{12}-900** films, suggesting that the established CNT network between graphene layers can indeed improve the electron transport through the hybrids. We ascribe this enhanced conductivity to the close interaction between CNTs and graphene sheets. The graphene sheets cover the majority of the total surface area, while the CNTs act as wires connecting the large pads together, leading to a conductive percolated network, and thus exhibit a synergistic effect of both graphene and CNT components.[8]

Table 3.1 Sheet resistance and calculated conductivity of graphene/CNT composite and **ReG-C_{12}-900** films

Sample	*Square Resistance* (Ωsq^{-1})	*Thickness* (*μm*)	Conductivity ($S \cdot cm^{-1}$)
graphane/CNT composite films	0.21	20	535
ReG-C_{12}-900 films	0.23	30	314
GO/MWNT composite by *Song et al.*[13]	1.30×10^3	8	0.02
ReG/SWNT composite by *Yang et al.*[8]	636	~0.10	~34.69
ReG/CNT composite by *Su et al.*[41]	188×10^3	$\sim 3 \times 10^{-3}$	~3.91
ReG/CNT composite by *Min et al.*[42]	153×10^3	$\sim 3 \times 10^{-3}$	~4.81
graphane/CNT composite by *Li et al.*[43]	400	~0.03	~183.87

Such a synergetic effect was also widely reported in the literatures.[8,13,41-46] However, none of those works achieved as high electrical conductivity (or low sheet resistance) as our graphene/CNT composites film mainly due to two reasons. The first reason is the good quality of graphene oxide sheet. In the works of *Song et al.*[13] and *Yang et al*.[8], graphene oxide was only reduced in aqueous hydrazine solution. It is known that hydrazine is insufficient to reduce graphene oxide sheets completely.[47] Graphene with such poor quality usually exhibits very low conductivity.[13] Even though such graphene sheets still cover a large surface area, they have almost no contribution to electron transport in the graphene/CNT composites. In contrast, the graphene oxide sheets used in our work were not only chemically reduced by hydrazine but also thermally reduced with hydrogen. By this way, most of the oxygen on graphene oxide can be removed. Moreover, acetylene, as the carbon source for CNT growth, can repair the defects on graphene sheets during the thermolysis process. Hence, the resulting graphene sheets act as effective electrical conductor in the graphene/CNT composites (as proved by the good conductivity of **ReG-C_{12}-900** which is the graphene sheet produced in the same manner).

The second, yet more important reason is the close connection between graphene sheets and CNTs. To better illustrate its influence on the conductivity, the graphene/CNT composites produced by *Su et al.,*[41] *Min et al.,*[42] and *Li et al.*[43] were selected for comparison. In these works, graphene oxide was reduced by chemical as well as thermal approaches. Especially in the work of *Li et al*, the pristine graphene grown from Cu surface was applied in graphene/CNT composites. Such high quality graphene sheets should effectively contribute to the conductivity of the resulting graphene/CNT composites. However, all of these works mixed CNTs and graphene by physical methods (ultrasonication, layer-by-layer assembly or coating). Such methods can only promise a close contact, but not a direct connection between graphene sheets and CNTs. The electron transport at the graphene/CNT interface cannot be avoided. On the other hand, in our graphene/CNT composites, CNT was

directly raised from graphene sheets. In other words, the CNTs and graphene sheets are joined together by carbon networks, so that electrons can be transported within these 3-dimensional graphitic networks without crossing the interfaces. Hence, the rustling graphene/CNT composites illustrate a much higher electrical conductivity compared to others.

3.5 Conclusion

In conclusion, we have demonstrated a novel approach towards highly conductive free-standing graphene/CNT composite films via an in-situ thermolysis of functionalized graphene/organic cobalt complexes. By combining 1D-CNT and 2D-graphene, a synergistic effect was established for the hybrid materials. The conductivity of such graphene/CNT composite was 1.7 times higher than that of thermally reduced graphene oxide sheet. Moreover, both the stiffness and strength of graphene/CNT composite film are about 36 % and 218 % higher than that of thermally reduced graphene oxide sheet respectively. Such graphene/CNT composite materials are also expected to be promising electrode materials in various energy storage devices.[8,48-50]

Reference:

(1) Novoselov, K. S.; Geim, A. K.; Morozov, S. V.; Jiang, D.; Zhang, Y.; Dubonos, S. V.; Grigorieva, I. V.; Firsov, A. A. *Science* **2004**, *306*, 666.

(2) Novoselov, K. S.; Geim, A. K.; Morozov, S. V.; Jiang, D.; Katsnelson, M. I.; Grigorieva, I. V.; Dubonos, S. V.; Firsov, A. A. *Nature* **2005**, *438*, 197.

(3) Geim, A. K.; Novoselov, K. S. *Nature Materials* **2007**, *6*, 183.

(4) Castro Neto, A. H.; Guinea, F.; Peres, N. M. R.; Novoselov, K. S.; Geim, A. K. *Reviews of Modern Physics* **2009**, *81*, 109.

(5) Stankovich, S.; Dikin, D. A.; Dommett, G. H. B.; Kohlhaas, K. M.; Zimney, E. J.; Stach, E. A.; Piner, R. D.; Nguyen, S. T.; Ruoff, R. S. *Nature* **2006**, *442*, 282.

(6) Harris, P. J. F. *International Materials Reviews* **2004**, *49*, 31.

(7) Thostenson, E. T.; Ren, Z. F.; Chou, T. W. *Composites Science and Technology* **2001**, *61*, 1899.

(8) Tung, V. C.; Chen, L. M.; Allen, M. J.; Wassei, J. K.; Nelson, K.; Kaner, R. B.; Yang, Y. *Nano Letters* **2009**, *9*, 1949.

(9) Baughman, R. H.; Zakhidov, A. A.; de Heer, W. A. *Science* **2002**, *297*, 787.

(10) Popov, V. N. *Materials Science & Engineering R-Reports* **2004**, *43*, 61.

(11) Geim, A. K. *Science* **2009**, *324*, 1530.

(12) Lee, D. H.; Kim, J. E.; Han, T. H.; Hwang, J. W.; Jeon, S.; Choi, S. Y.; Hong, S. H.; Lee, W. J.; Ruoff, R. S.; Kim, S. O. *Adv. Mater.* **2010**, *22*, 1247.

(13) Cai, D. Y.; Song, M.; Xu, C. X. *Adv. Mater.* **2008**, *20*, 1706.

(14) Yu, A. P.; Ramesh, P.; Sun, X. B.; Bekyarova, E.; Itkis, M. E.; Haddon, R. C. *Adv. Mater.* **2008**, *20*, 4740.

(15) Hummers, W. S.; Offeman, R. E. *Journal of the American Chemical Society* **1958**, *80*, 1339.

(16) Bahr, J. L.; Yang, J. P.; Kosynkin, D. V.; Bronikowski, M. J.; Smalley, R. E.; Tour, J. M. *Journal of the American Chemical Society* **2001**, *123*, 6536.

(17) Bahr, J. L.; Tour, J. M. *Chem. Mat.* **2001**, *13*, 3823.

(18) Dyke, C. A.; Stewart, M. P.; Maya, F.; Tour, J. M. *Synlett* **2004**, 155.

(19) Sinitskii, A.; Dimiev, A.; Corley, D. A.; Fursina, A. A.; Kosynkin, D. V.; Tour, J. M. *ACS Nano* **2010**, *4*, 1949.

(20) Lomeda, J. R.; Doyle, C. D.; Kosynkin, D. V.; Hwang, W. F.; Tour, J. M. *Journal of the American Chemical Society* **2008**, *130*, 16201.

(21) Dyke, C. A.; Tour, J. M. *Journal of the American Chemical Society* **2003**, *125*, 1156.

(22) Li, D.; Muller, M. B.; Gilje, S.; Kaner, R. B.; Wallace, G. G. *Nature Nanotechnology* **2008**, *3*, 101.

(23) Xu, Y. X.; Bai, H.; Lu, G. W.; Li, C.; Shi, G. Q. *Journal of the American Chemical Society* **2008**, *130*, 5856.

(24) Hernandez, Y.; Nicolosi, V.; Lotya, M.; Blighe, F. M.; Sun, Z. Y.; De, S.; McGovern, I. T.; Holland, B.; Byrne, M.; Gun'ko, Y. K.; Boland, J. J.; Niraj, P.; Duesberg, G.; Krishnamurthy, S.; Goodhue, R.; Hutchison, J.; Scardaci, V.; Ferrari, A. C.; Coleman, J. N. *Nature Nanotechnology* **2008**, *3*, 563.

(25) Meyer, J. C.; Geim, A. K.; Katsnelson, M. I.; Novoselov, K. S.; Booth, T. J.; Roth, S. *Nature* **2007**, *446*, 60.

(26) El Hamaoui, B.; Zhi, L. J.; Wu, J. S.; Kolb, U.; Mullen, K. *Adv. Mater.* **2005**, *17*, 2957.

(27) Wang, X.; Zhi, L. J.; Mullen, K. *Nano Letters* **2008**, *8*, 323.

(28) Liang, Y. Y.; Frisch, J.; Zhi, L. J.; Norouzi-Arasi, H.; Feng, X. L.; Rabe, J. P.; Koch, N.; Mullen, K. *Nanotechnology* **2009**, *20*.

(29) Iyer, V. S.; Vollhardt, K. P. C.; Wilhelm, R. *Angewandte Chemie-International Edition* **2003**, *42*, 4379.

(30) Dosa, P. I.; Erben, C.; Iyer, V. S.; Vollhardt, K. P. C.; Wasser, I. M. *Journal of the American Chemical Society* **1999**, *121*, 10430.

(31) Stankovich, S.; Dikin, D. A.; Piner, R. D.; Kohlhaas, K. A.; Kleinhammes, A.; Jia, Y.; Wu, Y.; Nguyen, S. T.; Ruoff, R. S. *Carbon* **2007**, *45*, 1558.

(32) Chen, H.; Muller, M. B.; Gilmore, K. J.; Wallace, G. G.; Li, D. *Adv. Mater.* **2008**, *20*, 3557.

(33) Wu, S. D.; Jing, L.; Li, Q. X.; Shi, Q. W.; Chen, J.; Su, H. B.; Wang, X. P.; Yang, J. L. *Physical Review B* **2008**, *77*.

(34) Zhao, X. L.; Ando, Y.; Qin, L. C.; Kataura, H.; Maniwa, Y.; Saito, R. *Applied Physics Letters* **2002**, *81*, 2550.

(35) Dikin, D. A.; Stankovich, S.; Zimney, E. J.; Piner, R. D.; Dommett, G. H. B.; Evmenenko, G.; Nguyen, S. T.; Ruoff, R. S. *Nature* **2007**, *448*, 457.

(36) Compton, O. C.; Dikin, D. A.; Putz, K. W.; Brinson, L. C.; Nguyen, S. T. *Adv. Mater.* **2010**, *22*, 892.

(37) Whitten, P. G.; Spinks, G. M.; Wallace, G. G. *Carbon* **2005**, *43*, 1891.

(38) Coleman, J. N.; Khan, U.; Blau, W. J.; Gun'ko, Y. K. *Carbon* **2006**, *44*, 1624.

(39) Coleman, J. N.; Khan, U.; Gun'ko, Y. K. *Adv. Mater.* **2006**, *18*, 689.

(40) Cox, H. L. *British Journal of Applied Physics* **1952**, *3*, 72.

(41) Su, C. Y.; Xu, Y. P.; Zhang, W. J.; Zhao, J. W.; Tang, X. H.; Tsai, C. H.; Li, L. J. *Chem. Mat.* **2009**, *21*, 5674.

(42) Kim, Y. K.; Min, D. H. *Langmuir* **2009**, *25*, 11302.

(43) Li, C. Y.; Li, Z.; Zhu, H. W.; Wang, K. L.; Wei, J. Q.; Li, X. A.; Sun, P. Z.; Zhang, H.; Wu, D. H. *J. Phys. Chem. C* **2010**, *114*, 14008.

(44) Fan, Z. J.; Yan, J.; Zhi, L. J.; Zhang, Q.; Wei, T.; Feng, J.; Zhang, M. L.; Qian, W. Z.; Wei, F. *Adv. Mater.* **2010**, *22*, 3723.

(45) Cao, X. H.; He, Q. Y.; Shi, W. H.; Li, B.; Zeng, Z. Y.; Shi, Y. M.; Yan, Q. Y.; Zhang, H. *Small* **2011**, *7*, 1199.

(46) Hong, T. K.; Lee, D. W.; Choi, H. J.; Shin, H. S.; Kim, B. S. *ACS Nano* **2010**, *4*, 3861.

(47) Dreyer, D. R.; Park, S.; Bielawski, C. W.; Ruoff, R. S. *Chemical Society Reviews* **2010**, *39*, 228.

(48) Yoo, E.; Kim, J.; Hosono, E.; Zhou, H.; Kudo, T.; Honma, I. *Nano Letters* **2008**, *8*, 2277.

(49) Yang, S. B.; Cui, G. L.; Pang, S. P.; Cao, Q.; Kolb, U.; Feng, X. L.; Maier, J.; Mullen, K. *Chemsuschem* **2010**, *3*, 236.

(50) Yang, S. B.; Feng, X. L.; Wang, L.; Tang, K.; Maier, J.; Mullen, K. *Angewandte Chemie-International Edition* **2010**, *49*, 4795.

Chapter 4. Metal complexes of N-containing macrocycles as cathode materials for ORR

4.1 Introduction

As we have discussed in Chapter 1.2.2, the sluggish oxygen reduction at the cathode remains as the major source of losses in efficiency and power density in fuel cells. Therefore, developing catalytic materials for oxygen reduction reaction (ORR) at the cathode is the current bottleneck for the development of fuel cells.[1] In particular, the invention of an electrode material at which the rapid four-electron reduction of dioxygen to water proceeded at or near the reversible potential (+1.23 V vs. NHE) would constitute a major advance in fuel cell technology. Up to now, the most efficient catalysts for ORR have been still platinum-based materials.

A series of non-noble metal electrocatalysts were invented to replace platinum based materials, including transition metal alloys, transition metal chalcogenides, and transition metal macrocyclic compounds.[2-9] In designing possible macrocyclic transition metal complexes as oxygen reduction catalysts, favorite materials must be capable of delivering four electrons, more or less simultaneously, to the dioxygen substrate at a potential which is as positive as possible.

Numerous works have been devoted to developing a large number of macrocyclic transition metal complexes as oxygen reduction catalysts but most seem to function only at rather negative potentials and to effect only a two-electron reduction of dioxygen to hydrogen peroxide. By comparing the oxygen reduction activity of various metal macrocycles, it has been found that the nature of the ligand plays an important role. This has inspired the development of different porphyrin-like macrocycles. Contracted, expanded or isomeric macrocycles with

respect to porphyrin have been synthesized, in which one or more pyrrole units in the porphyrin core were replaced, giving the motivation to control and tune the properties of resulting complexes. For example, a modified porphyrin-like macrocycle by replacing pyrrole and pyrrolenine units by carbazole and pyridine was synthesized recently by our group and its Co complexes show a moderate oxygen reduction activity.[10]

On the other hand, it was also discovered that an additional heat treatment of metal-macrocycles in an inert atmosphere could significantly improve the ORR activity of such kind of electrocatalysts.[11] Before heat treatment, most transition metal macrocycles only catalyze ORR in a two-electron transfer manner. However After heat treatment in the range of 400 to 1000 ^{o}C, the number of electrons exchanged per O_2 is increased to 3.45 ~ 4, and the catalyzed ORR is better suited to a four-electron pathway.[7] Different theories have been proposed to explain the enhancement in activity. And this still remained as a controversial topic. It has been postulated that the nature of the catalytic sites of metal-macrocycles depend on the temperature of the heat treatment: After a heat treatment a low and medium temperature range (usually 200~700 ^{o}C), metal–N4 moieties (or their fragments) are supposed to be the active sites.[12,13] It was found that the metal–N4 moiety is no longer responsible for the activity at temperatures above 800°C. Other theories consider that the role of the metal atom was merely to catalyze the formation of C-N microsporous frameworks as catalytic active site.[14] Nevertheless, in some works, no electrocatalytic activity was detected anymore after removing the metal particles in the metal-N4 after heat treatment.

In this chapter, we set aside the controversy over the heat treatment of macrocycle, but aim to synthesizing a series of novel N-containing macrocycles (NHM) based on 1,10-phenanthroline and indole. Moreover, the cobalt complex of these macrocycles (Co-NHM) were created as cathodic catalyst for oxygen reduction

reaction. Its electrocatalytic properties were tested by rotating ring-disk electrode voltammetry (RRDE) in 0.1m KOH solution saturated with O_2 at a scan rate of 100 mVs^{-1}. This permits the quantitative measurement of (unwanted) H_2O_2 production and allows discrimination between the formation of such peroxide as an intermediate or merely as a minor side product. The on-set potential of Co-NHM was measured to be -0.45 V in alkali medium with an electron transfer number n= ~2.2 and a current density J_k= 2.35 mA/cm^2. These values are comparable with the average results achieved by Co-porphyrins, which represent an indirect pathway producing H_2O_2.

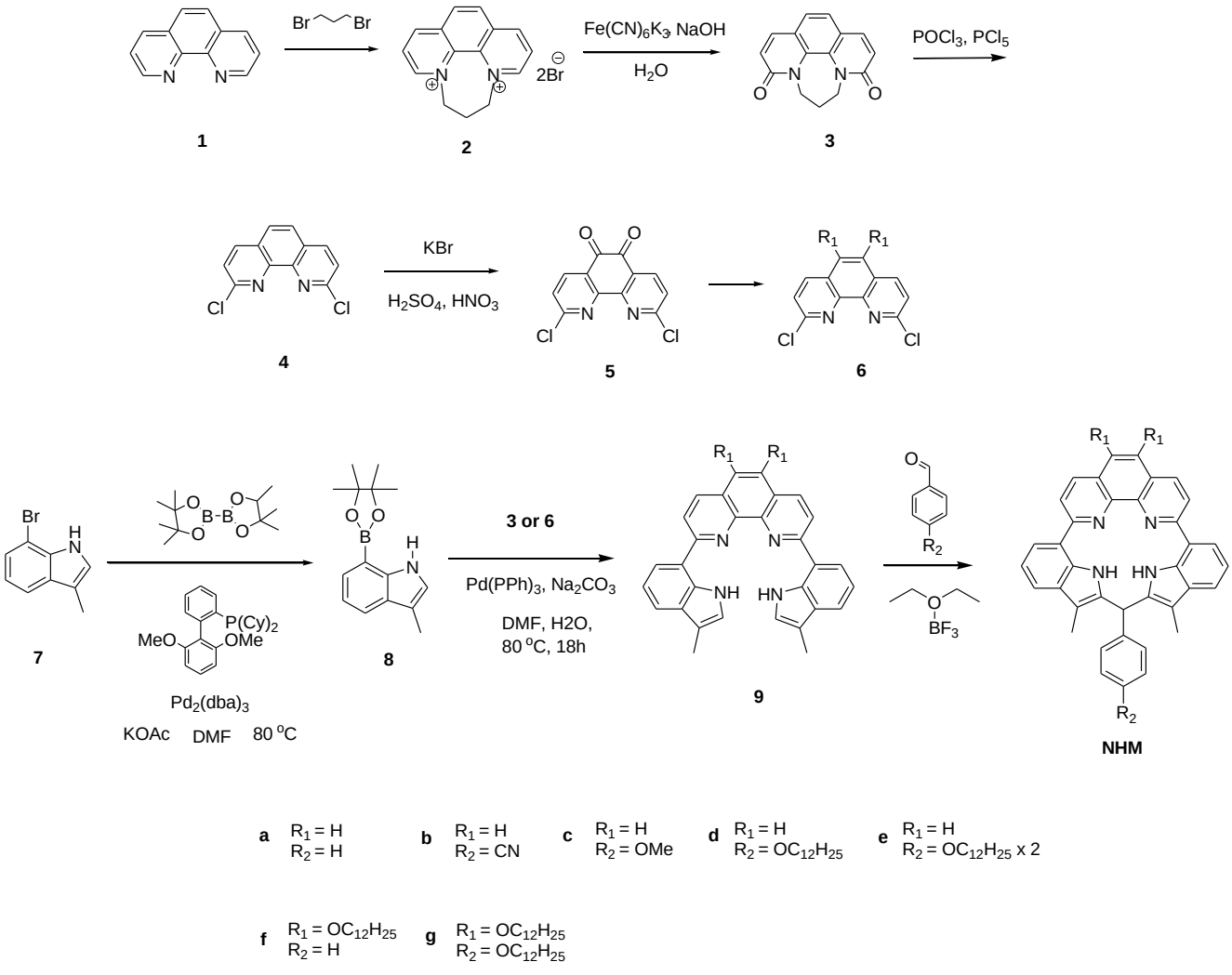

Figure 4.1 Synthetic route of NHM from 1,10-phenanthroline and 3-methyl-7-bromo-indole

To further increase the electrocatalytic properties of Co-NHM, a mild pyrolytic process was carried out in argon at 700 ^{o}C. As a result, the oxygen reduction activity after pyrolysis was greatly enhanced. The on-set potential is shifted to a more positive value at -0.38 V with electron transfer number ***n*** around 3.6 and a current density of 4.32 mA/cm^2.

4.2 Synthesis of N-containing macrocycles

To explore new structures of porphyrin-like N-containing macrocycles, as mentioned above, pyrrole has been replaced by 1,10-phenanthroline and indole. In executing the synthetic route illustrated in Figure 4.1, several distinct phases are involved: i) functionalization of the 2- and 9-positions of 1,10-phenanthroline, followed by ii) functionalization of 7-position of indole; iii) a open-ring structure via Suzuki–Miyaura cross-coupling reaction between 1,10-phenanthroline and indole; iv) ring closure via Friedel–Crafts condensation of benzaldehyde and α-C of indoles.

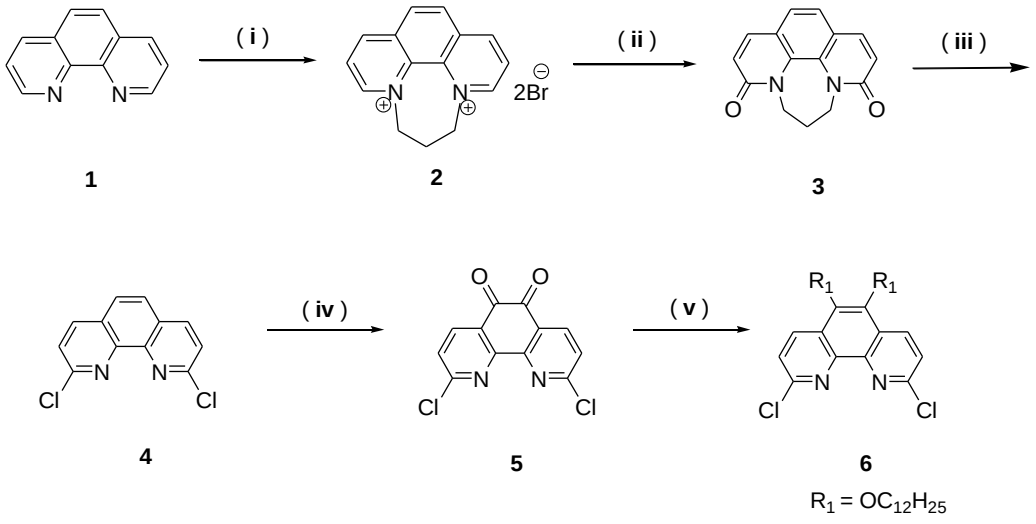

Figure 4.2 Synthesizing 2,9-dichloro-1,10-phenanthroline **4** and 2,9-dichloro-5,6-bis(dodecyloxy)-1,10-phenanthrolineobtained **6** from 1,10-phenanthroline **1** in five steps in an overall yield of 17 %. i) 1,3-dibromopropane, 120 °C, 4 h (90 %); ii) $[K_3Fe(CN)_6]$, NaOH, 2–5 °C, 8 h (40 %); iii) $POCl_3$, PCl_5, 110 °C, 8 h (90 %); iv) H_2SO_4, HNO_3, KBr, 80 °C, 5 h (75 %); v) Bu_4NBr, $Na_2S_2O_4$, KOH, $C_{12}H_{25}Br$ (65 %)

The sequence of reactions leading to **6** from 1,10-phenanthroline is indicated in Figure 4.2. To start the functionalization of the 2- and 9-positions of 1,10-phenanthroline, compound **2** was obtained according to literature with a revised procedure. Because 1,3-dibromopropane is a liquid with boiling point of 166 °C in which 1,10-phenanthroline can be dissolved, reaction (**i**) could be carried out at the desired temperature on a large scale without using any solvents. In comparison, nitrobenzene was used as solvent in literature. 100 g of 1,10-phenanthroline monohydrate afforded 160 g of $\mathbf{2}^{2+}\cdot 2\ Br^-$ as ochre crystals.

Compound $\mathbf{2}^{2+}\cdot 2\ Br^-$ was subsequently oxidized to the neutral species **3** using $[K_3Fe(CN)_6]$ in basic aqueous solution. Under reaction temperature at 2~5 °C, compound $\mathbf{2}^{2+}\cdot 2\ Br^-$ and $[K_3Fe(CN)_6]$ were not well dissolved in solvent, which led to an inhomogeneous reaction mixture with difficulty of stirring. Therefore, the scale of the reaction from compound $\mathbf{2}^{2+}\cdot 2\ Br^-$ to **3** was limited to 5 gram batches. 2,9-Dichloro-1,10-phenanthroline (**4**) was then prepared in high yield (85 %) by reacting **3** with PCl_5 and $POCl_3$ at 110 °C.

The α-dione **5** was prepared by oxidizing **4** with KBr and HNO_3 in concentrated sulfuric acid. After work-up and column chromatography, compound **5** was obtained as a fine yellow crystal. The dione function was subsequently reduced by sodium dithionite in basic condition and converted to dodecyloxy substituent by adding dodecylbromide in situ, and hence afforded 2,9-dichloro-5,6-bis(dodecyloxy)-1,10-phenanthroline **6** (chromatographic purification afforded **6** in 65 % yield as a pale crystal).

Besides 2,9-dichloro-1,10-phenanthroline, another building block of NHM is indole as an analogue of pyrrole. The borylation of 3-methyl-7-bromoindole was illustrated in Figure 4.3.

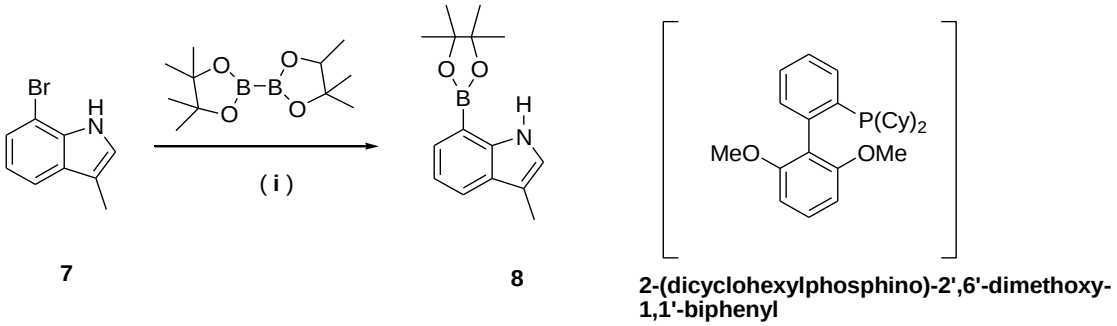

7 **8** **2-(dicyclohexylphosphino)-2',6'-dimethoxy-1,1'-biphenyl**

Figure 4.3 Miyaura borylation of 3-methyl-7-bromoindole **7** toward 3-methyl-7-(4,4,5,5-tetramethyl-1,3,2-dioxaborolan-2-yl)-1H-indole **8**: i) $[Pd_2(dba)_3]$, 2-(dicyclo- hexylphosphino)-2',6'-dimethoxy-1,1'-biphenyl, KOAc, DMF, 80 °C, 18 h (90 %).

In aim of functionalization of 7-position of indole, the Miyaura borylation reaction of 3-methyl-7-bromoindole **7** was carried out. The methyl substituent at 3-position is particularly important which will be explained in a later section. On the other hand, it is worth to notice that the classical conditions of the Miyaura borylation of **7** were chosen at first; none of them gave a better yield than 28 % as listed in table 4.1 (entries (ii) and (iii)). Since indole is one of the nitrogen heterocycles which often exhibit failures in aryl–aryl coupling reactions, a special condition, as described by Buchwald et al.,[15] involving tris(dibenzylideneacetone)-dipalladium(0) as the catalyst and 2-(dicyclohexylphosphino)-2',6'-dimethoxy-1,1'-biphenyl as the ligand. Only under this carefully chosen condition, the borylation of **7** was achieved in a good yield.

Table 4.1. reaction condition of Miyaura borylation toward compound **8**

Entry	Catalyst	Ligand	Salt	T (^{o}C)	Solvent	Yield
(i)	$Pd_2(dba)_3$	$C_{26}H_{35}O_2P$	KOAc	80	DMF	90%
(ii)	$PdCl_2(dppf)$	N/A	KOAc	80-100	DMF	17%
(iii)	$PdCl_2(PPh_3)_2$	N/A	KOPh	80-100	DMF	28%

The next step involved a double-side Suzuki-Miyaura coupling reaction between 2,9-dichloro-1,10-phenanthroline **4** (or its alkylated analogue **6**) and the boronic acid of indole **8**. As shown in Figure 4.4, compound **4** was subsequently reacted with **8** in DMF and aqueous Na_2CO_3 at 80 ^{o}C, with $Pd(PPh_3)_4$ as catalyst (10 % per chloro substituent). Usually chloro-substituent is thought to be inefficient in Suzuki coupling with boronic ester and the reaction must be heated up to 100 ^{o}C. However, the open cycle **9a** was obtained in almost quantitative yield (95 %) after column chromatography. It is believed that the halogen species on an electron-deficient system versus boronic ester on an electron-rich molecule is favorable for Suzuki coupling. This may explain the high yield of open cycle **9a** obtained at lower temperature.

When compound **6** was used as reactant in this twofold Suzuki coupling, toluene, except DMF and water, must be added as another co-solvent (PhMe/DMF/H_2O=1:1:1) Otherwise, oily beads appeared during the reaction which resulted in Suzuki reaction proceeding only on one side of phenanthroline. This was mainly caused by the bulky dodecyloxy substituent which is poorly soluble in polar solvents. By adding toluene, the reaction proceeded smoothly with high yield (93 %) after column chromatography.

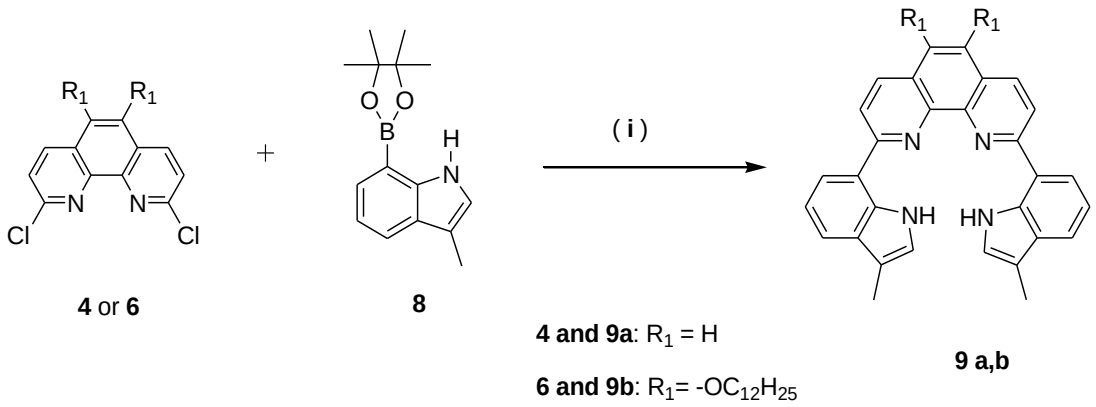

Figure 4.4 Suzuki-Miyaura coupling reaction between 2,9-dichloro- 1,10-phenanthroline **4** (or **6**) and the boronic acid of indole **8**: i) $Pd(PPh_3)_4$, Na_2CO_3, DMF:H_2O=2:1, 80 °C, 10 h (95 %).

After the open cycles have been made, the ring closure was carried out via Friedel-Crafts reaction with benzaldehyde. For the synthesis of porphyrin, ring formation of pyrrole is a routine step based on Lindsey synthesis in acidic conditions. Hence, the ring closure of **9** was firstly carried out in anhydrous chloroform refluxing with various Lewis acid. However, none of these attempts gave any desired products until the reaction was refluxed in 1,1,2,2-tetrachloroethane at 150 ^{o}C and boron trifluoride etherate was used as catalyst.

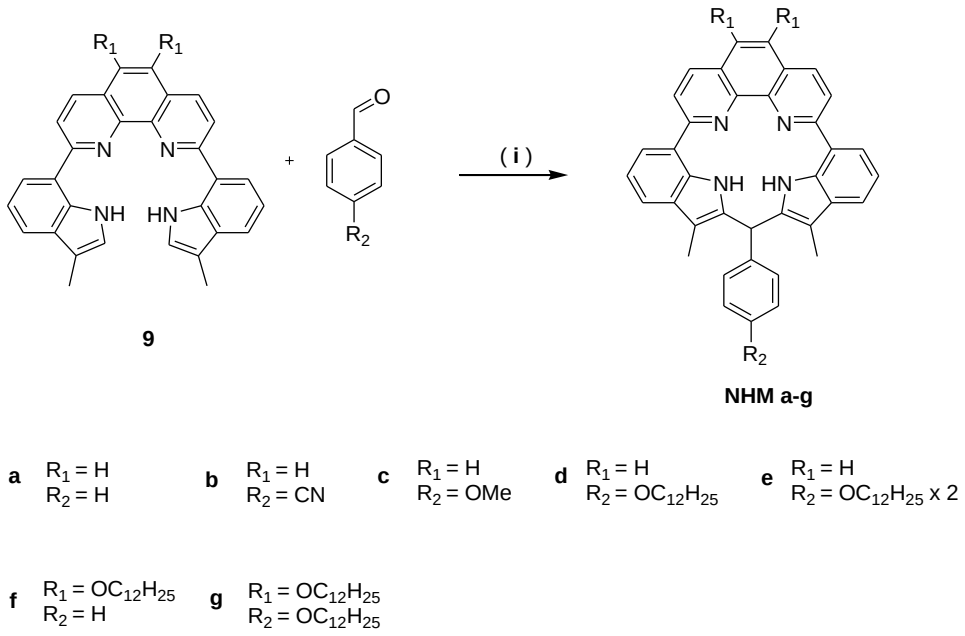

Figure 4.5 Ring closure reaction of **9** to NHM: i) $BF_3{\cdot}O(C_2H_5)_2$, $C_2H_4Cl_4$, 150°C, 10 h, (50~85%).

One of the most important factors that prevents the ring closure at moderate conditions is the lack of reactivity of 2-postion of indole. Usually, the most active site lies in the C-3 position of a pyrrolic ring in indole for an electrophilic aromatic substitution. To prove this, 7-bromoindole was coupled with benzaldehyde as model reaction. Catalyzed by any given Lewis acid, the reaction went smoothly under room temperature (as illustrated in Figure 4.5a). That is the reason why C-3 position was blocked by methyl group at the very beginning of the whole synthetic route. Otherwise, the Friedel-Crafts reaction could never lead to a ring formation. Nevertheless, the C-2 position is not as reactive as C-3 position, proven by the reaction between 3-methyl-7-bromoindole and benzaldehyde for which it was always necessary to reflux in chloroform (as illustrated in Figure 4.6b).

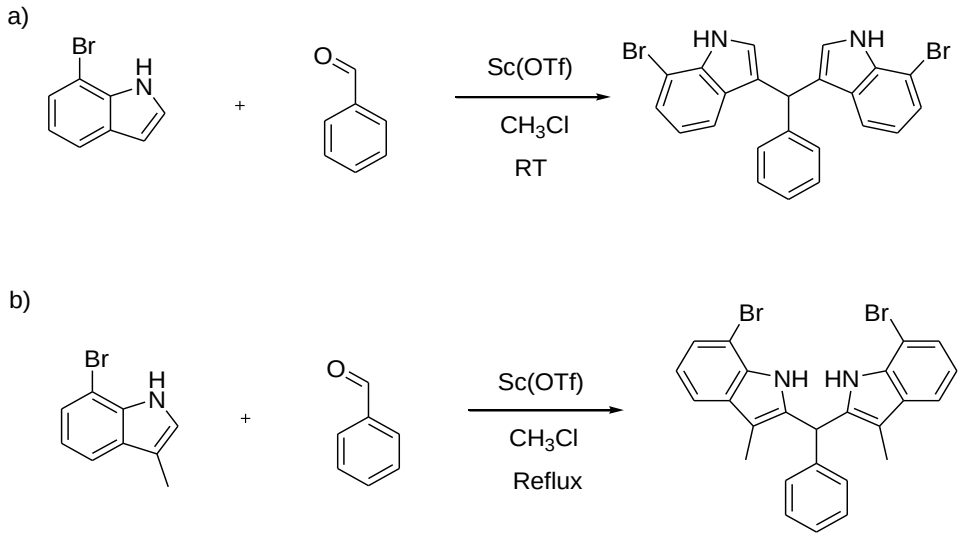

Figure 4.6 a) Lindsey reaction of 7-bromoindole with benzaldehyde: C-3 position reacts at room temperature giving a quantitive yield ; b) Lindsey reaction of 3-methyl-7-bromoindole with benzaldehyde: C-2 position reacts at 80 ^{o}C with yield of 96%.

Table 4.2. The yield of ring closure varied by the polar effect of substituent groups

Entry	Para-position	Polar effect	Yield
(a)	-H	N/A	72%
(b)	-OMe	donating	38%
(c)	-CN	withdrawing	82%
(d)	$-NO_2$	withdrawing	88%

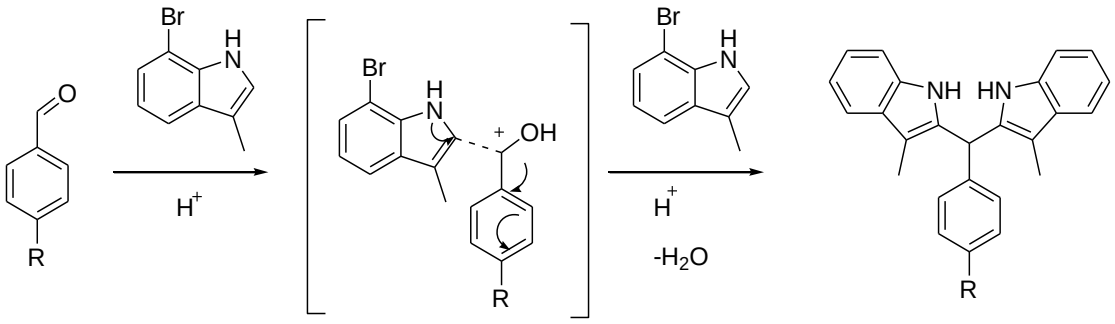

Figure 4.7 The mechanism of condensation reaction between indole and benzaldehyde

Beside the nature of the open cycle itself, the electrophilicity of the benzaldehyde also plays an important role in the ring closure reaction. When three substitutions with electron-donating or electron-withdrawing nature at the para-position of benzaldehyde (R_2 in Figure 4.5) were utilized, the yield of ring closure reaction varied from 38% to 88 % as listed in Table 4.2. It is interesting to notice that when electron-withdrawing groups located at the para-position of benzaldehyde, the reaction yield was dramatically higher than that for electron-donating groups. Given that the addition of α–C of benzaldehyde is an electrophilic reaction (as illustrated in Figure 4.7), the more electron-deficient character the benzaldehyde is, the easier the reaction can proceed. This may explain the increase of the reaction yield when 4-formylbenzonitrile or 4-nitrobenzaldehyde was used in reaction verses 4-methoxybenzaldehyde.

As soon as NHMs were synthesized, the oxidation of them was perused in a similar manner of porphyrin synthesis, aiming to achieve all- conjugated structures as porphyrin and phthalocyanine. Unfortunately, all these attempts failed with 2,3-dichloro-5,6-dicyano-1,4-benzoquinone (DDQ) as oxidant at temperatures from room temperature to 80 ^{o}C. Only starting material was identified by MALDTI-TOF mass spectra after reaction for 24 hours.

Since the oxidation of macrocycle NHMs was not successful, an all-aromatic structure of them could not be achieved so far.

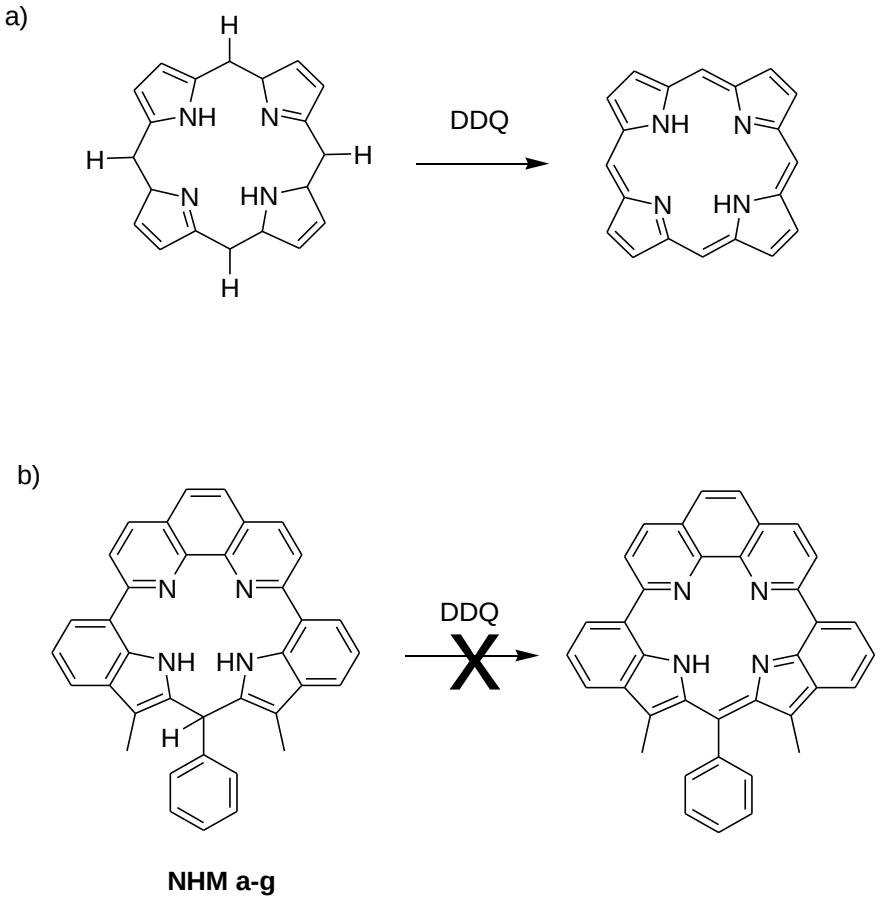

Figure 4.8 a) Porphyrin oxidation via DDQ; b) failed oxidation of NHM to all aromatic structures.

4.3 Metal complexes of NHM and their catalytic properties

Even without success of aromatization of NHM cycles, the ability of macrocycle NHM to act as a metal ligand was investigated by the insertion of zinc (II)-ion and cobalt (II)-ion into the ring cavity.

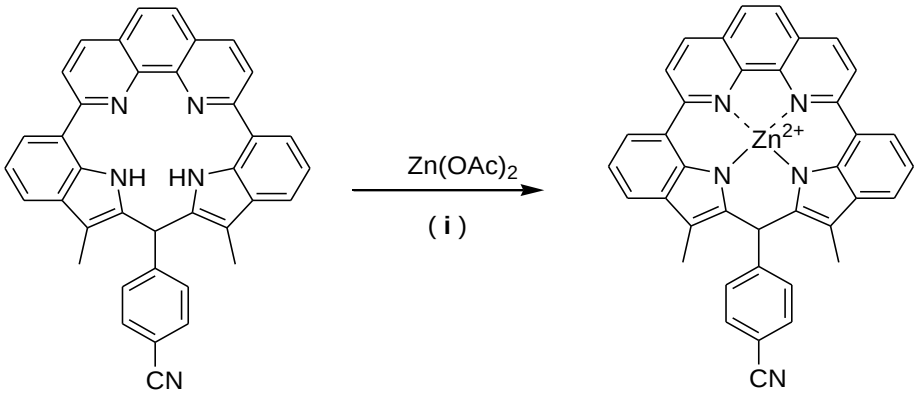

NHM-b **NHM-Zn-b**

Figure 4.9 Complexation of macrocycle NHM-b with Zn^{2+}: (**i**) anhydrous $Zn(OAc)_2$, anhydrous $CHCl_3$/MeOH (3:1), reflux, 8h.

The zinc complex NHM-Zn-b was obtained by refluxing macrocycle NHM-b with zinc(II)acetate in a mixture of chloroform and methanol in an anhydrous atmosphere (Figure 4.9). The success of zinc complexation could be easily recognized by the color change from light yellow to carmine during reaction.

Further evidence was provided by mass spectra. As illustrated in Figure 4.10, the solid state MALDIT-TOF mass spectrum of NHM-b from a TCNQ matrix is presented in Figure 4.10 with a clear peak at 551.10 g/mol. The calculated molecular weight of NHN-b is 551.64 g/mol, which is in agreement with the peak found in the mass spectrum. After zinc complexation, the peak at 551.10 g/mol disappeared while a new peak was found at 612.99 g/mol in Figure 4.1b, which indicated a complete complexation of zinc(II) into the ring cavity of macrocycle NHM-b .

The structure of NHM-Zn-b was further elucidated by comparison of ^{1}H-NMR of NHM-Zn-b with that of NHM- b (Figure 4.11). The signal at 11.92 ppm observed in ^{1}H-NMR spectrum (250 MHz, CD_2Cl_2, 298 K) of macrocycle NHM-b can be attributed

to the indole NH protons in the ring cavity of macrocycle (Figure 4.11a). This signal disappeared in ^{1}H-NMR spectrum (250 MHz, CD_2Cl_2, 298 K) of complex NHM-Zn-b. Even though most proton signals in the aromatic region were shifted during Zn complexation, the disappearance of the signal at 11.92 ppm evidently confirms the complete complexation of Zn(II) to indole NH protons.

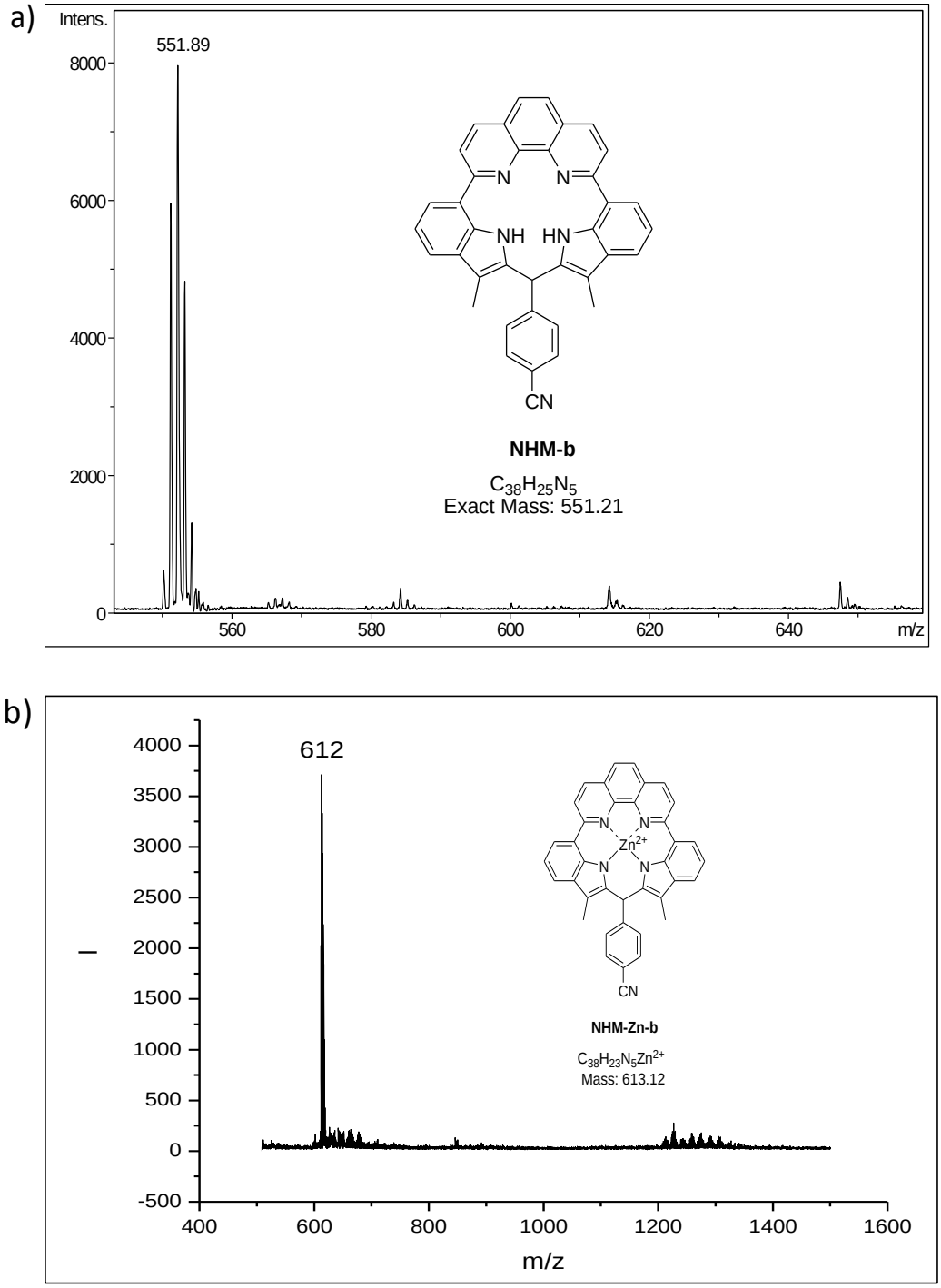

Figure 4.10 MALDI-Tof mass spectra of a) NHM-b and b) NHM-Zn-b

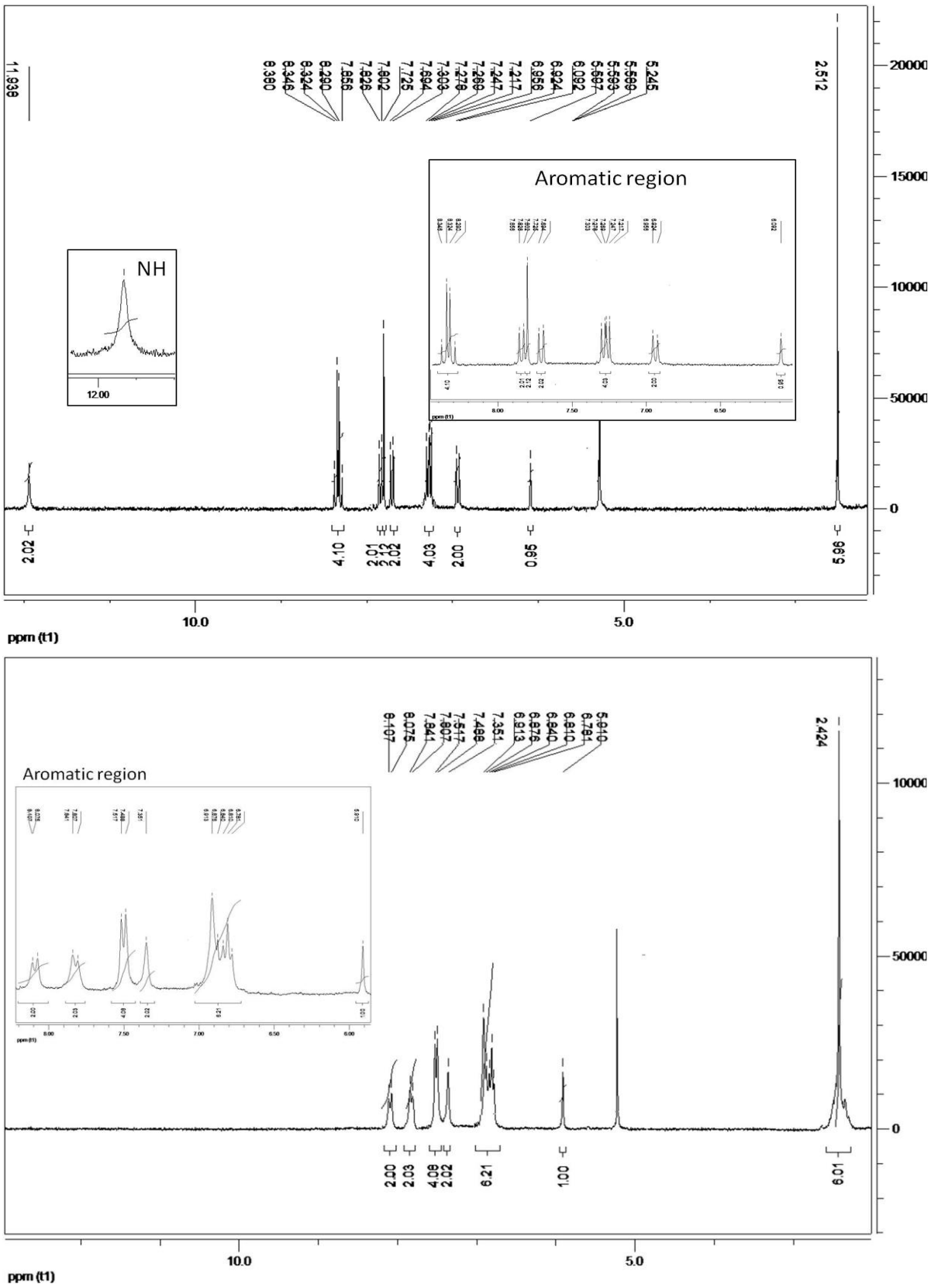

Figure 4.11 ^{1}H-NMR spectra of a) NHM-b and b) NHM-Zn-b

Since we could not oxidize macrocycle NHMs into all-annulene structure, no emission was observed at the excitation wave length of 366 nm. Therefore, the quenching of emission upon the metal insertion was neither observed.

The cobalt complexation with NHM-b was first attempted in the same manner as zinc complexation. However, refluxing NHM-b with cobalt(II)acetate in chloroform/methanol did not provide a complete metal insertion. To further increase the reaction energy, the reaction was carried out by microwave heating, at 150 ^{o}C, with a power of 300 W in anhydrous DMF as the solvent in a sealed tube. Heating using microwave radiation allows the direct heating of the substrates, not the solvents. Therefore, even the reactant did not totally dissolve in DMF at the room temperature, the metal complexation proceeded completely.

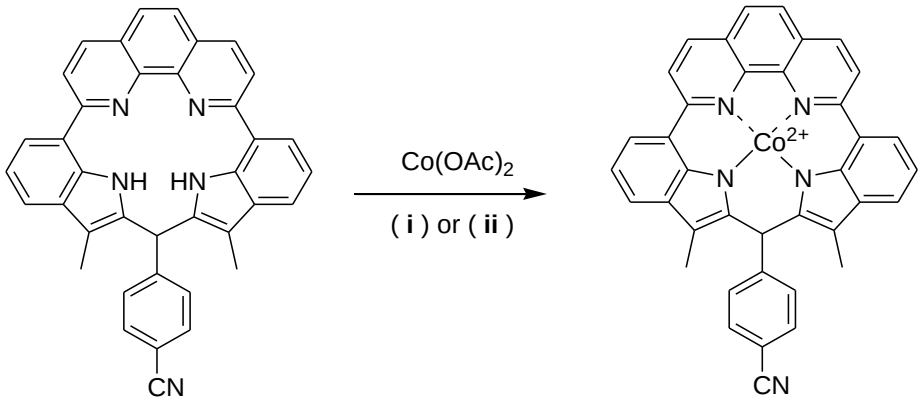

NHM-b **NHM-Co-b**

Figure 4.12 Complexation of macrocycle NHM-b with Co^{2+}: (**i**) anhydrous $Co(OAc)_2$, anhydrous $CHCl_3$/MeOH (3:1), reflux, 8h; (**ii**) anhydrous $Co(OAc)_2$, anhydrous DMF, Microwave radiation at 150 ^{o}C, 300 W for 4h.

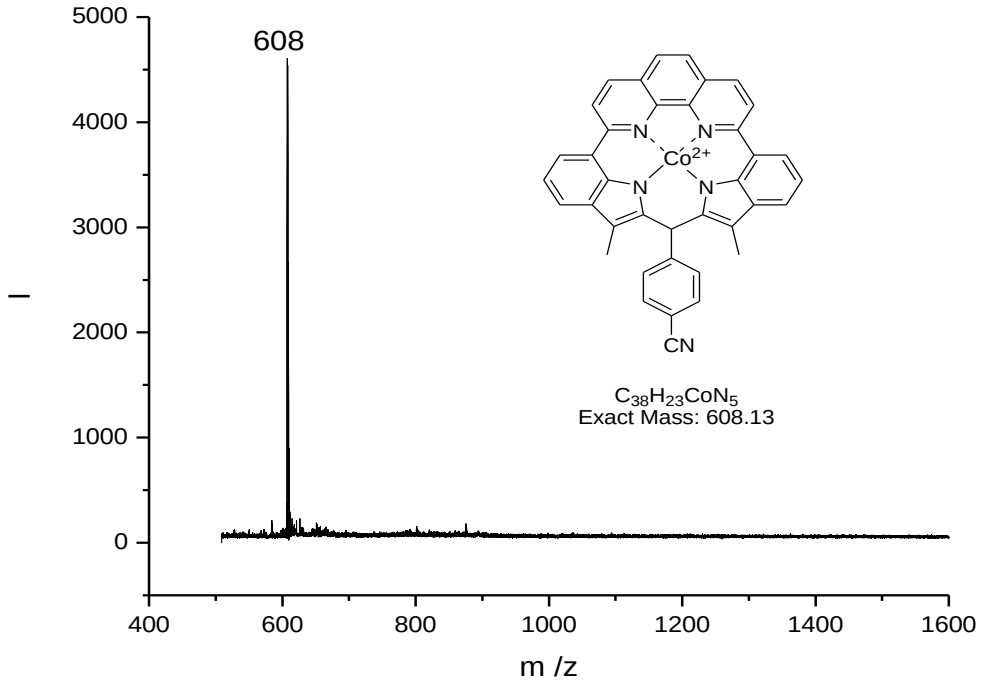

Figure 4.13 MALDI-Tof mass spectrum of NHM-Co-b

The completion of Co insertion can be confirmed by MALDI-TOF mass spectra. As illustrated in Figure 4.13, the peak at 551.10 g/mol of NHM-b can not be observed after cobalt complexation. And the appearance of a new peak at 607.89 g/mol indicates a complete complexation of cobalt (II) into the ring cavity of macrocycle NHM-b.

Unfortunately, the NMR measurement of NHM-Co-b reveals no assignable peak which is due to the high-spin Co(II) species in magnetic field.

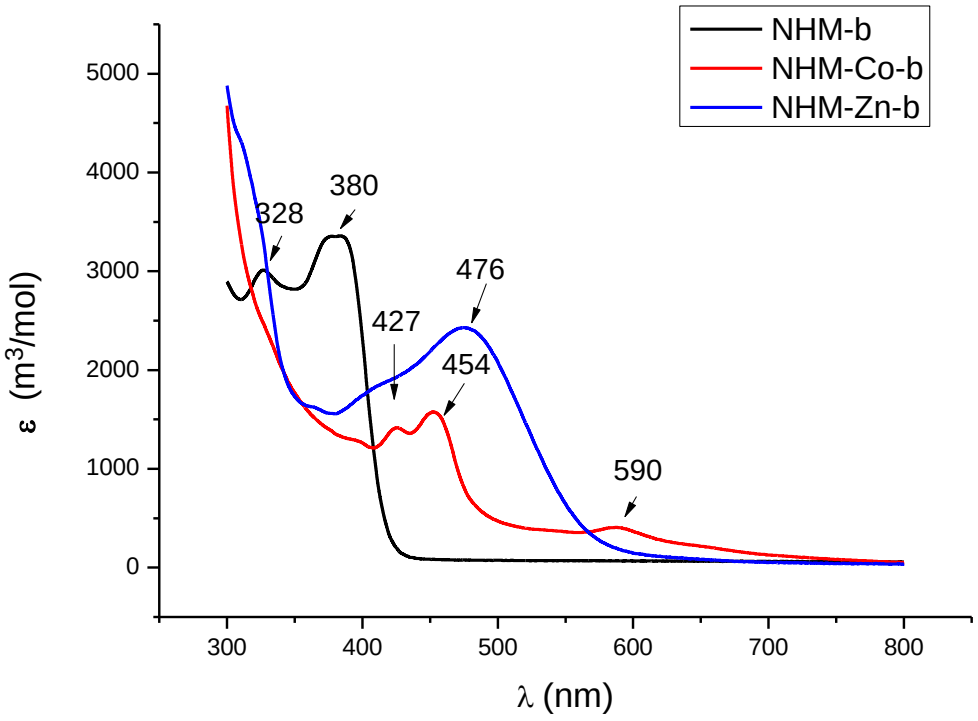

Figure 4.14 Electronic absorption spectra in CH_2Cl_2 of NHM-b (black, 1.8×10^{-5} M) and its cobalt complex NHM-Co-b (red, 1.2×10^{-4} M) and its zinc complex NHM-Zn-b (blue, 1.5×10^{-4} M)

The absorption spectra of NHMs show two absorption maxima at 328 nm and 380 nm (CH_2Cl_2, RT, Figure 4.14). For unsubstituted 1,10-phenathroline and 3-methyindole, the absorption bands are at about 220 and 230 nm respectively.[16,17] For macrocycle NHMs, this band is bathochromically shifted to 328 nm. Therefore, the absorption maximum at 380 nm is assigned to a weak intramolecular charge transfer from the donor to the acceptor units, indole and pyridine respectively.

Compared to the absorption spectra of NHMs, the absorption maxima for the zinc(II) complex NHM-Zn-b were bathochromically shifted to 427 nm and 476 nm, while the absorption maxima for the cobalt(II) complex NHM-Co-b were

bathochromically shifted to 427 nm and 454 nm. As demonstrated in literature, bands in the region of 427 nm are often assigned to metal-to-ligand charge transfer.[18] Therefore, the absorption spectra of NHMs evidently confirm the success of metal insertion of NHM-Zn-b and NHM-Co-b.

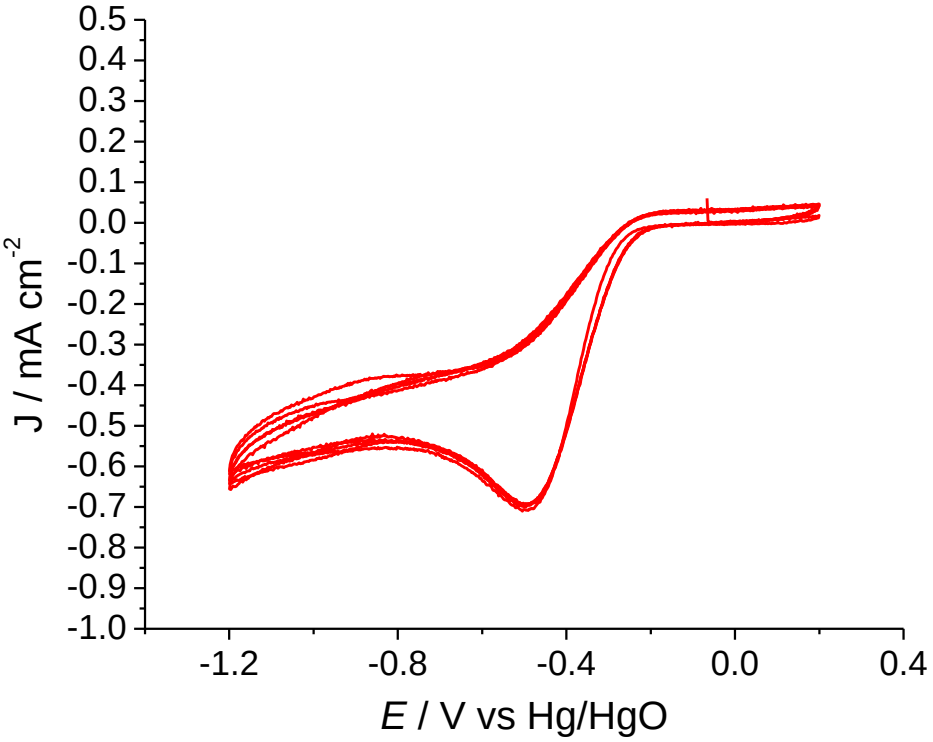

Figure 4.15 Cyclic voltammograms of NHM-Co/GC

As we have discussed previously, a large number of macrocyclic transition metal complexes have been developed as oxygen reduction catalysts.[3,19] To investigate how NHM-Co-b would act as cathodic electrocatalyst, we have prepared glass carbon rotating disk electrode (3 mm in diameter, from Autolab) based on a 20 wt% NHM-Co-b on Vulcan XC-72R for cyclic voltammograms measurement. The catalyst was loaded onto a glassy-carbon (GC) rotating-disk electrode (RDE) to give NHM-Co /GC with load of 25 $\mu g cm^{-2}$. Figure 4.15 presents cyclic voltammogram (CV) curves of

NHM-Co/GC in 0.1M H_2SO_4 solution saturated with O_2 at a scan rate of 100 mVs^{-1}. The reduction current appeared as a reduction peak at −0.5 V.

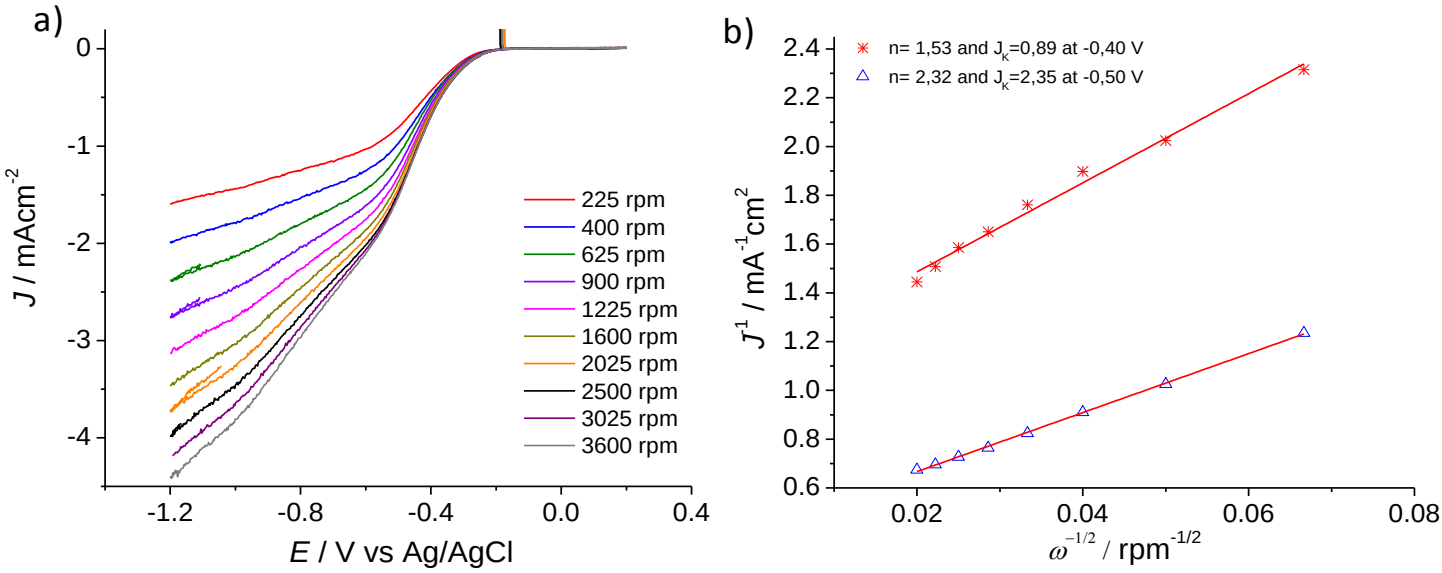

Figure 4.16 (a) Rotating-disk voltammogram curves measured at different rotation speeds and (b) Koutecky-Levich plots of NHG-Co/GC at the potential sweep rate of 10 mV/s. 0.1M KOH solution saturated by oxygen is used as electrolyte.

The further kinetics study by rotating-disk voltammetry provides more understanding of the role of NHM-Co/GC during the ORR electrochemical process. The voltammetric profiles in O_2-saturated 0.1M KOH as the electrolyte showed that the current density was enhanced by an increase in the rotation rate (from 400 to 3600 rpm; Figure 4.16a). The onset potential of NHM-Co/GC for ORR was at approximately −0.5 V, same to the value identified from CV measurements.

The corresponding Koutecky–Levich plots (J^{-1} vs $\omega^{-1/2}$) at various electrode potentials exhibited a feature of linearity (Figure 4.16b). However, the slopes change dramatically over the potentials from −0.40 to −0.50 V, which suggests that the

electron transfer numbers for oxygen reduction at different electrode potentials are quite different. Usually the linearity and parallelism of the Koutecky–Levich plots are taken as an evidence of first-order reaction kinetics with respect to the concentration of dissolved O_2.[20] Therefore, the dramatic change of the slopes of NHM-Co/GC indicates an indirect pathway of oxygen reduction that involves two-electron reduction.

The kinetic parameters can be further analyzed on the basis of the Koutecky–Levich equations:

$$\frac{1}{J} = \frac{1}{J_L} + \frac{1}{J_k} = \frac{1}{B\omega^{1/2}} + \frac{1}{J_k} \qquad \ldots\ldots (1)$$

$$B = 0.62\, nFC_0(D_0)^{2/3}v^{-1/6} \qquad \ldots\ldots (2)$$

$$J_k = nFkC_0 \qquad \ldots\ldots (3)$$

in which J is the measured current density, J_K and J_L are the kinetic- and diffusion-limiting current densities, ω is the angular velocity of the disk ($\omega=2\pi N$, N is the linear rotation speed), n is the overall number of electrons transferred in oxygen reduction, F is the Faraday constant (F=96485 C mol^{-1}), C_0 is the bulk concentration of O_2, v is the kinematic viscosity of the electrolyte, and k is the electron-transfer rate constant. According to Equations (1) and (2), the number of electrons transferred (n) and J_K can be obtained from the slope and intercept of the Koutecky–Levich plots, respectively.[20] By using the values C_0=1.2×10^{-3} molL^{-1}, D_o=1.9×10^{-5} cm s^{-1}, and v=0.1 m^2 s^{-1} in 0.1 M KOH,[21] n was calculated at different potential as illustrated in Figure 4.16b. At potential of -0.5 V, the total electron transfer number (n) of NHM-Co/GC is 2.32 with current density of 2.35 mA cm^{-2}. This result suggests that NHM-Co leads mainly to a two-electron transfer in oxygen

reduction. The calculated J_K value of 2.35 mA cm^{-2} at −0.5 V is about half as high as that of commercially available Pt/C/GC (4.44 mA cm^{-2} at −0.35 V).

The above results are in accordance with observations in literature that Co macrocycles generally give rise to a two-electron reduction pathway.[22,23] However, it was found that high temperature treatment of macrocycles leading to carbonaceous materials under an inert atmosphere could be an effective way to significantly increase their activity for ORR.[3,19,23] Van Veen *et al*[24] discussed four models in an effort to explain this phenomenon: (1) improving the dispersion of the supported chelate; (2) catalyzing the formation of a special type of carbon, which is actually the active phase; (3) generating the M–N species; and (4) promoting a reaction between chelate and subjacent carbon in such a way as to modify the electronic structure of the central metal ion with retention of its N4 coordinated environment. Although there is still controversy on which model is the right explanation, there is a general agreement in the literature that a heat-treatment step has positive effects on both the activity and the stability of these M-N4 macrocycle catalysts.

In order to find out the proper temperature for the heat treatment of NHM-Co, the thermogravimetric analysis (TGA) under nitrogen atmosphere was conducted. As can be seen from Figure 4.17, five stages are found during the heating process. This is in agreement with the well established process discovered by literature: [3]

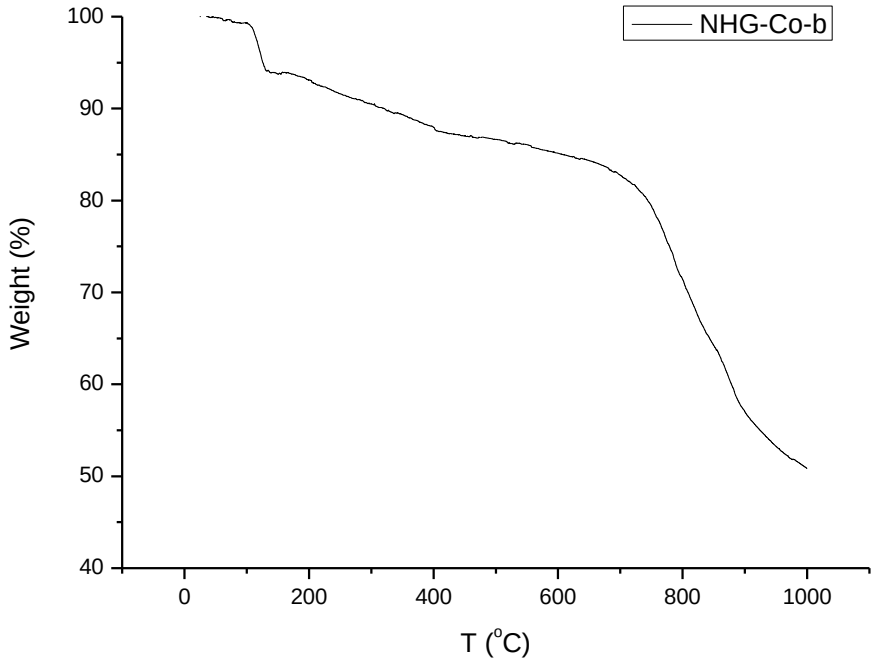

Figure 4.17 thermogravimetric analysis of NHM-Co

(1) <200 °C: dehydration;

(2) 200–400 °C: lose of substituent groups of aromatic core;

(3) 400–600 °C: Co-macrocycle stars to polymerize and is stable up to this temperature range;

(4) ~700 °C: pyrolysis of the polymer to produce fragments containing Co bound to C and N on the catalyst surface.

(5) >700 °C: only inorganic Co (Co^o and CoO) is found on the support;

As for the structure change above 400 °C, many works observed that the metal–N4 moiety can be maintained at lower temperatures and gradually disappeared partially or completely, at medium to high temperatures from 400 - 600 °C.[14,16,25-34] According to these observations, the final catalyst seems to have two types of active sites: the first one is a metal center coordinated by four N atoms, and

the other is one metal coordinated by two N atoms, to form MN4/C and MN2/C, respectively.[3] The MN4/C moiety is more abundant at pyrolysis temperatures below 700 ^{o}C and it favors the reduction of the 2e^{-} pathway mechanism, while the MN2/C moiety can be formed at temperatures around 700 ^{o}C and has the catalytic activity towards the 4e^{-} pathway mechanism to produce water. When the temperature goes higher than 700 ^{o}C, metal particles can be formed inside the graphite shell, showing insignificant ORR catalytic activity.[29-31,33]

In order to achieve the best catalytic activity of C-N matrices impregnated with Co, 20 wt % of NHG-Co-700 was loaded on a carbon support (Vulcan XC-72R). The pyrolysis was carried out at 700 ^{o}C for 1 h in Argon to produce NHG-Co-700. Electrode was prepared by loading NHG-Co-700 onto same glassy-carbon rotating-disk electrode to give NHG-Co-700/GC.

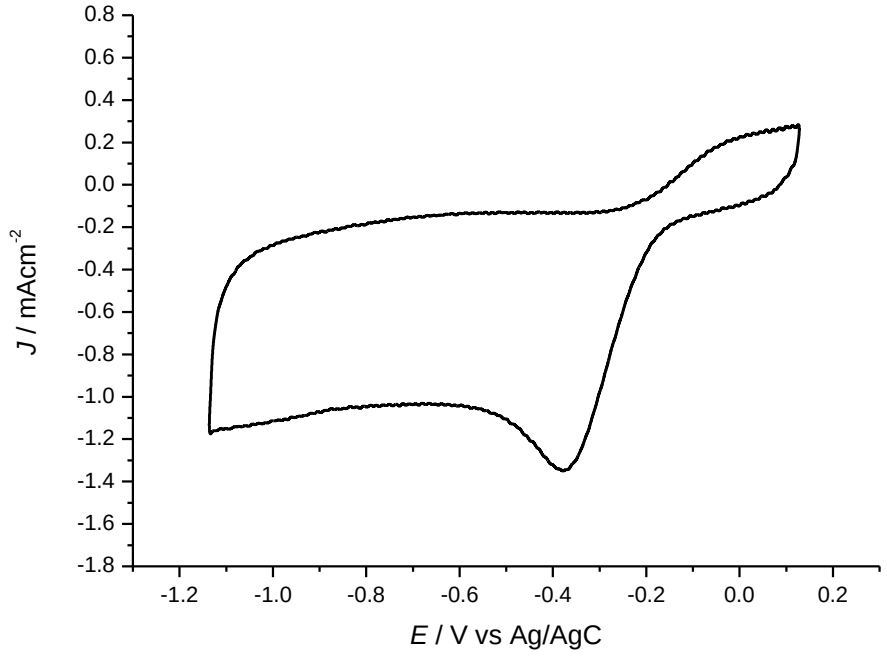

Figure 4.18 Cyclic voltammograms of NHG-Co-700/GC on a glassy-carbon RDE electrode in an O_2-saturated 0.1 M solution of KOH

Figure 4.18 presents CV curves of NHG-Co-700/GC in 0.1 M KOH solution saturated with O_2 at a scan rate of 100 mV s^{-1}. The reduction current appeared as a well-defined cathodic peak at −0.36 V, which suggests pronounced electrocatalytic activity of NHG-Co-700/GC for oxygen reduction with respect to NHG-Co.

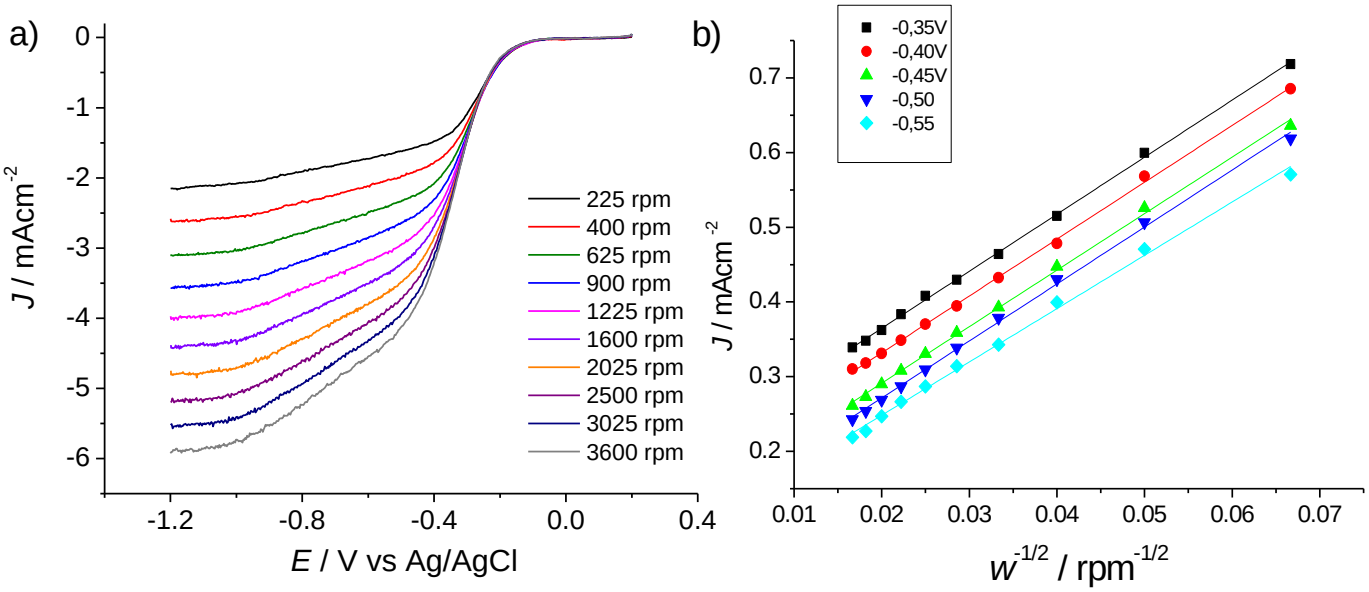

Figure 4.19 (a) Rotating-disk voltammogram curves measured at different rotation speeds and (b) Koutecky-Levich plots of NHG-Co-700/GC at the potential sweep rate of 10 mV/s. 0.1M KOH solution saturated by oxygen is used as electrolyte.

Table 4.3. The kinetic parameters of NHG-Co-700/GC at different Voltage

Voltage (V)	Intercept	J_k (mA /cm^2)	*k*	*n*	slope
-0.35	0.212	4.71698	0.00938	3.67374	7.638
-0.4	0.1797	5.56483	0.01192	3.68774	7.609
-0.45	0.13964	7.16127	0.01695	3.70527	7.573
-0.5	0.11892	8.40901	0.01897	3.82878	7.32871
-0.55	0.10555	9.47418	0.02125	3.93153	7.13717

Figure 4.19a shows the rotating-disk voltammogram curves of NHG-Co-700/GC measured at different rotating speeds and the corresponding Koutecky-Levich plots. According to Equations (1) and (2), the number of electrons transferred (*n*) and J_K can be calculated from the slope and intercept of Koutecky–Levich plots in Figure 4.19b, respectively.[20] The variation of *n* and J_K with different reductive potential in ORR are illustrated in Table 4.3 and Figure 4.19b respectively. With the decrease of the reductive potential from -0.35 to -0.55, NHG-Co-700/GC shows an increase of the electron transfer number from 3.6 to 3.9 and of J_K from 4.7 to 9.5, which suggests a dominant kinetic of 4-electron pathway.

Table 4.4. The kinetic parameters of different pyrolyzed Co-macrocycles

Catalysts	Pyrolysis Temperature (^oC)	Operation Voltage (V)	***n***	J_k (mA /cm^2)
NHG-Co-700	700	-0.35	3.6	4.7
Co-tetraphenylporphyrines	600~900	-0.4~-0.7	2.8~3.9	2.0~3.9
Co-phthalocyanines	600~800	-0.4~-0.7	3.0~3.9	3.0~5.1
Pt/C	**-**	**-0.35**	**3.9**	**4.4**

In terms of both n and J_k values, NHG-Co-700/GC shows a better electrocatalytic ability than NHM-Co/GC. These results evidently demonstrate that a thermal treatment led to a dramatic enhancement of the electron-transfer kinetics of NMGCAs for oxygen reduction as cathode for ORR in fuel cell. Compared to pyrolyzed Co-porphyrines and Co-phthalocyanines, which are two classes of the most common Co macrocycles, NHG-Co-700 exhibits similar oxygen reduction kinetics (four-electron pathway) and comparable catalytic activity (Table 4.4).[3,19] These results indicate that whether the macrocyclic ligand of a transition metal macrocycle is fully

aromatized / conjugated is not important as long as the resulting complexes have good stability. Even though the NHM macrocycle is not fully aromatized, it exhibits fairly good chelate ability. Meanwhile, its Co complex presents comparable thermal stability as other Co-macrocycles. Therefore, its catalytic activity for ORR after pyrolysis is among the best of Co-macrocycles, and almost as good as commercial Pt/C electroncatalysts

4.4 Conclusion

In this chapter, we have synthesized a series of novel N-containing macrocycles (NHM) base on 1,10-phenanthroline and indole. Even it is unable to aromatize them into fully conjugated structure, we still successfully complexed Zn and Co into these macrocycles. The Co complexes of NHM (NHM-Co) were applied as transition metal catalyst for ORR in fuel cell which exhibited a 2-eletron kinetic reduction of oxygen. To further improve the electrocatalytic activity, NHM-Co was pyrolyzed at 700 ^{o}C in argon. As a consequence, the oxygen reduction activity of NHM-Co after pyrolysis was greatly enhanced. The on-set potential is shifted to a more positive value at -0.38 V with electron transfer number ***n*** around 3.6 and a current density of 4.32 mA/cm^2.

Reference:

(1) Jaouen, F.; Proietti, E.; Lefevre, M.; Chenitz, R.; Dodelet, J.-P.; Wu, G.; Chung, H. T.; Johnston, C. M.; Zelenay, P. *Energy & Environmental Science* **2011**, *4*, 114.

(2) Jaouen, F.; Herranz, J.; Lefevre, M.; Dodelet, J. P.; Kramm, U. I.; Herrmann, I.; Bogdanoff, P.; Maruyama, J.; Nagaoka, T.; Garsuch, A.; Dahn, J. R.; Olson, T.; Pylypenko, S.; Atanassov, P.; Ustinov, E. A. *Acs Applied Materials & Interfaces* **2009**, *1*, 1623.

(3) Bezerra, C. W. B.; Zhang, L.; Lee, K. C.; Liu, H. S.; Marques, A. L. B.; Marques, E. P.; Wang, H. J.; Zhang, J. J. *Electrochimica Acta* **2008**, *53*, 4937.

(4) Lefevre, M.; Proietti, E.; Jaouen, F.; Dodelet, J. P. *Science* **2009**, *324*, 71.

(5) Bashyam, R.; Zelenay, P. *Nature* **2006**, *443*, 63.

(6) Jasinski, R. *Nature* **1964**, *201*, 1212.

(7) Wang, B. *Journal of Power Sources* **2005**, *152*, 1.

(8) Cheng, X.; Shi, Z.; Glass, N.; Zhang, L.; Zhang, J. J.; Song, D. T.; Liu, Z. S.; Wang, H. J.; Shen, J. *Journal of Power Sources* **2007**, *165*, 739.

(9) Zhang, L.; Zhang, Y.; Zhou, X. G.; Li, R. X.; Li, X. J.; Tin, K. C.; Wong, N. B. *Journal of Molecular Catalysis a-Chemical* **2006**, *256*, 171.

(10) Arnold, L.; Norouzi-Arasi, H.; Wagner, M.; Enkelmann, V.; Mullen, K. *Chemical Communications* **2011**, *47*, 970.

(11) Alt, H.; Binder, H.; Sandsted.G *Journal of Catalysis* **1973**, *28*, 8.

(12) Lalande, G.; Cote, R.; Guay, D.; Dodelet, J. P.; Weng, L. T.; Bertrand, P. *Electrochimica Acta* **1997**, *42*, 1379.

(13) Bouwkamp-Wijnoltz, A. L.; Visscher, W.; van Veen, J. A. R.; Tang, S. C. *Electrochimica Acta* **1999**, *45*, 379.

(14) Wiesener, K. *Electrochimica Acta* **1986**, *31*, 1073.

(15) Billingsley, K. L.; Anderson, K. W.; Buchwald, S. L. *Angewandte Chemie-International Edition* **2006**, *45*, 3484.

(16) Mesaric, S. *Fresenius Zeitschrift Fur Analytische Chemie* **1972**, *258*, 193.

(17) Carney, J. R.; Zwier, T. S. *Journal of Physical Chemistry A* **1999**, *103*, 9943.

(18) Mudadu, M. S.; Singh, A. N.; Thummel, R. P. *Journal of Organic Chemistry* **2008**, *73*, 6513.

(19) Vasudevan, P.; Santosh; Mann, N.; Tyagi, S. *Transition Metal Chemistry* **1990**, *15*, 81.

(20) Liu, R. L.; Wu, D. Q.; Feng, X. L.; Mullen, K. *Angewandte Chemie-International Edition* **2010**, *49*, 2565.

(21) Chen, W.; Chen, S. W. *Angewandte Chemie-International Edition* **2009**, *48*, 4386.

(22) Collman, J. P.; Denisevich, P.; Konai, Y.; Marrocco, M.; Koval, C.; Anson, F. C. *Journal of the American Chemical Society* **1980**, *102*, 6027.

(23) Biloul, A.; Coowar, F.; Contamin, O.; Scarbeck, G.; Savy, M.; Vandenham, D.; Riga, J.; Verbist, J. J. *Journal of Electroanalytical Chemistry* **1993**, *350*, 189.

(24) Vanveen, J. A. R.; Colijn, H. A.; Vanbaar, J. F. *Electrochimica Acta* **1988**, *33*, 801.

Chapter 5. N-doped graphitic Carbon derived from N-containing polyaromatic cations as cathode materials for ORR

5.1 Introduction

As we have discussed in chapter 1 and 4, the search for non-precious metal electrocatalysts that are efficient, low-cost, and stable for ORR is the bottle-neck for the large-scale practical application of fuel cells.[1] Transition metal macrocycles, as we have investigated in chapter 4, are considered to be one of the good candidates. Recently, another type of non-precious metal materials, namely metal-free catalysts, are already known to exhibit electrocatalytic activity for ORR.[1-12]

In general, nitrogen-doped carbon materials are prepared by two methods. The first is the pyrolysis of transition-metal macrocyclic compounds or mixtures of metal salts and nitrogen-containing precursors. [7,12-18] In these processes, the transition metals play an important role not only in the formation of graphitic frameworks, but also in the introduction of nitrogen active sites.[11,19-21] However, an extra step is necessary to remove metal species after pyrolysis. Yet, metal particles encapsulated in the framework can hardly be completely removed after a tedious removal process. Hence, there is still a controversy if the activity of nitrogen-doped carbon materials produced in this way comes from the metal or from the carbon materials themselves.[17,22]

In contrast, in-situ doping of carbons using metal-free precursors can realize a homogeneous incorporation of nitrogen into the carbon material without any interference of metal species. As we discussed in chapter 1, several nitrogen-doped carbons have been prepared using this method. As graphene has recently become a rising a star, N-doped graphene has also been synthesized via a modified CVD process on a thin layer of nickel. Ammonia in this case was used as nitrogen source, and the resulting N-doped graphene

showed a superb catalytic property as cathode materials for ORR.[23-26]

It was found that the ORR performance of nitrogen-doped carbon materials crucially depends on the local structure of the integrated nitrogen and the amount of nitrogen in the carbon host, as well as the accessibility of active sites to fuel.

There are mainly three types of nitrogen integrated in the carbon host: graphitic, pyridinic and pyrrole/pyridine type nitrogen. It was well accepted that either pyridinic or pyrrole/pyridone type nitrogen was responsible for the ORR activity of carbon.[27] However there are still controversies over this topic. Ozkan et al.[18] believed that, even though a significantly higher amount of pyridinic nitrogen results in a better activity of catalyst, pyridinic nitrogen itself may not be the active site for ORR, but an activator for edge plane exposure (the plane in which pyridinic nitrogen is found), on which many electrocatalytic reactions show increased kinetics. It has been shown that the final product of ORR (H_2O versus H_2O_2) is influenced by the plane where oxygen reacted. Oxygen could only be reduced to peroxide when it reacted on the basal plane of nitrogen-doped carbon,[28,29] but could potentially be reduced further to H_2O when it reacted at the edge.[28-31] Furthermore, the samples that had higher edge plane exposure were found to be more selective towards 4-electron reduction of oxygen directly to water. Modeling simulations could, to some extent, explain this observation that higher nitrogen content and edge plane exposure lead to more active N-doped graphitic nanostructures.[30,32] On the other hand, some experimental results demonstrated that the graphitic nitrogen could also be responsible for ORR activity.[21]

Besides the local structure, the amount of nitrogen in the carbon host is crucial for the ORR catalytic activity of nitrogen-doped carbon materials. In principle, the higher nitrogen content a nitrogen-doped carbon material has, the better performance it shows in ORR.[33] Therefore, synthesizing nitrogen-doped carbon materials via heat treatment requires high molecular weight precursors to avoid evaporation or sublimation of the C-N source during

heat treatment. For this reason, often polymers, such as polyvinylpyrrolidone,[34] polyacrylonitrile,[35] polypyrrole,[36] or others,[37] have been used as precursors, which were either immersed into the pores from solutions or directly polymerized in the porous template. Ionic liquids, as a class of materials that are liquid at room temperature but exhibit practically no vapor pressure, were also used as precursors and heated under the help of hard templates without evaporation.[38] Other suitable molecules applied for metal-free thermolysis synthesis of nitrogen-doped carbons are large N-containing polyaromatic molecules which have good thermal stability, and in which the nitrogen could be integrated into carbon host via graphitization under heat treatment.[21] Nevertheless, this kind of molecules (such as perylene diimides or phthalocyanines) always involves great synthetic complexity, and thus limits its practical application in large scale.

The last yet equally important issue is the accessibility of active sites of nitrogen-doped carbon materials to the electrochemical surface. For most nitrogen-doped carbon materials, one of the biggest limitations for improving their catalytic activity is the low surface density of the catalytic sites.[2,7,39] It is believed that creating large surface area during the synthesis of nitrogen-doped carbon materials is a potential solution to overcome the low accessibility of active sites.[39] Except N-doped CNTs and N-doped graphene which have large surface area intrinsically, a large number of N-doped carbons derived from metal-free precursors are synthesized via nanocasting technology which requires ordered nanoporous materials such as hard templates (e.q. porous alumina membranes or porous silica). In general, it is a three-step procedure as illustrated in Figure 5.1. The first step is the casting of precursors into templates for direct replication of the porous structure, which is preferentially done from a melt or a liquid solution of precursors. For example, by infiltrating a solution through a porous template and evaporating the solvent, the precursor in the solution could be incorporated into a porous structure. The next step is to pyrolyze this precursor-template composite at an elevated temperature that leads to a polymerization and carbonizatoin of the precursor in the

pores. In this way, the porous structure of N-doped carbons forms by directly replicating the porous structure of the template. After removing the template as the last step, an N-doped carbon material with nanoporous structure and high surface area could be achieved. If such a material possesses a vast number of catalytically active sites that can be easily accessible to oxygen, it promises a high totally efficiency for ORR in fuel cells.

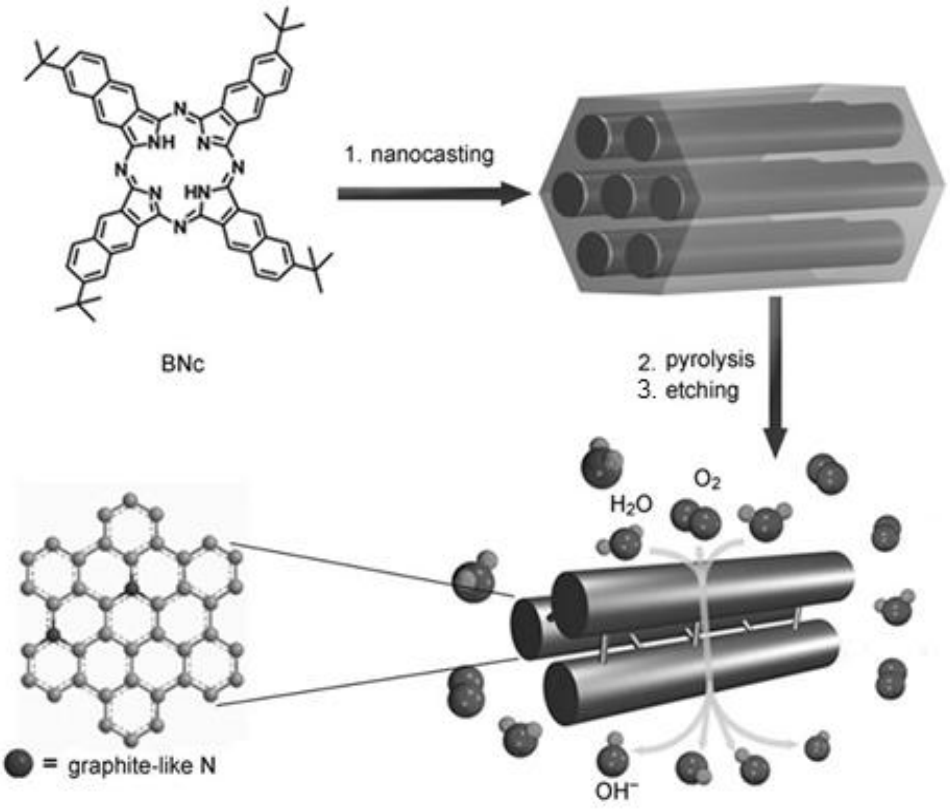

Figure 5.1 Preparation of nitrogen-doped carbon materials as metal-free catalysts for the ORR: 1) casing precursor into template; 2) pyrolysis; 3) removing template.[21]

Thus, the present contribution to the development of metal-free electrocatalysts as high performance cathode for ORR lies in the careful combination between solution processable precursors with good thermal stability and microscopic structure control by nanocasting. The aim is to have a rational control over the nitrogen content, the structure

of nitrogen and the porosity of the resulting nitrogen-containing carbons. It would not only promise good candidates for ORR catalysts but would aid attempts to elucidate the correlation between the structure, composition, and electrochemical activity of nitrogen-doped carbon materials.

In this chapter, we have investigated the fabrication of novel nitrogen-doped ordered mesoporous graphitic carbon arrays (NMGCAs) on the basis of a metal-free nanocasting technology. Ordered mesoporous silica SBA-15 was used as a template, and a series of N-containing polyaromatic cations as precursors. By a straightforward synthetic route, small aromatic molecules such as bipyridine and 1,10-phenanthroline were modified into cations with different aromatic structures. By ionization, their thermal stability was greatly enhanced. This enables the following heat treatment up to 900 ^{o}C with graphitization in template and minimum loss of nitrogen content. Therefore, the resulting NMGCAs possess unique features including high surface area and a graphitic framework with high nitrogen content. Such features led to high electric conductivity and electrocatalytic activity for the ORR.

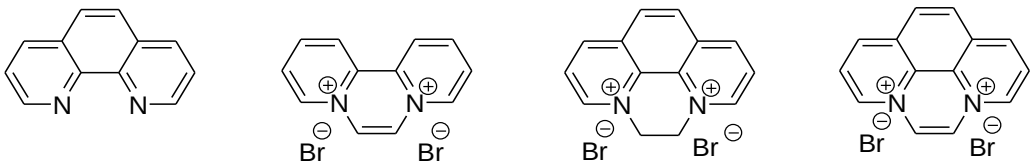

Figure 5.2 The molecular structure of N-containing polyaromatic cationic precursors.

Moreover, we have investigated the relation between the structure of NMGCAs and the structure of precursors by carefully evaluating the nitrogen content and local structure of nitrogen in NMGCAs versus various precursors pyrolyzed at different pyrolysis temperatures, in attempts to build up a fabrication route that is able to control over the electrocatalytic activity of N-doped carbons in ORR via rational design of precursors.

5.2 Experimental part

5.2.1 Synthesis of N-containing polyaromatic cations

To assure a high nitrogen content in the carbon host after heat treatment, starting materials for fabricating nitrogen-doped carbon materials must contain a certain amount of nitrogen atoms which also need to be thermally stable to avoid evaporation or sublimation of the C-N source during heat treatment. Other than polymers, ionic liquids and large N-containing polyaromatic molecules, there are still a lot of small aromatic molecules that have a high N/C ratio. The advantage for small molecules is their simplicity and low cost of synthesis. But their volatility and poor stability under high temperature limits them from being as precursors for thermal treatment. Two methods have been used so far to overcome such a problem. One must incorporate small nitrogen containing aromatic molecules with metal particles via a preheating treatment and generate M-N4 structures. The drawback of this method is the difficulty of removing metal species completely and the complicated mechanism of such a metal/metal-free system. The other method is to dissolve N-containing aromatic molecules in an ionic liquid in which the small molecules act only as addends to further increase the N-content. Most of the nitrogen remaining after pyrolysis comes actually from ionic liquids, which are usually expensive materials that limit the massive application of such method.

On the other hand, ionizing an N-containing aromatic molecule to an organic salt can turn it from molecular crystal into ionic crystal. The latter usually exhibits a far better thermal stability and higher melting/boiling point than the former, in that the electrostatic force is stronger than the London force (as well as dipole-dipole attraction). For instance, quaternary ammonium salts are often found to be more stable than their amines.[40] Considering this fact, we have modified the N-containing small aromatic molecules into N-containing polyaromatic quaternary ammonium cations (NPCs), which exhibited good thermal stability and thus were applied as a novel type of precursors for fabricating

nitrogen-doped carbon materials for ORR.

As illustrated in Figure 5.3, the synthesis of dipyrido[1.2-a :2'.1'-c]pyrazinium dibromide (**NPC-1**) from 2,2'-bipyridyl was accomplished by modifying the method developed by Calder *et. al* with a total yield of 67 %.[41] Bipyridine was firstly converted to the quaternary salt **3** as an orange crystal by reaction with bromoacetaldehyde 2,4-dinitrophenylhydrazone in toluene. The salt **3** was cyclized in concentrated aqueous hydrobromic acid to 9-hydroxy-9,10-hydro-8a,10a- diazoniaphenanthrene dibromide (**4**) as a yellow crystal. Salt **4** was dehydrated by thionyl chloride to a fully aromatized cyclic salt **NPC-1** which was obtained as pale crystal from a mixture of acetone and aqueous hydrobromic acid, the structure of which was confirmed by ^{1}H-NMR spectrum.

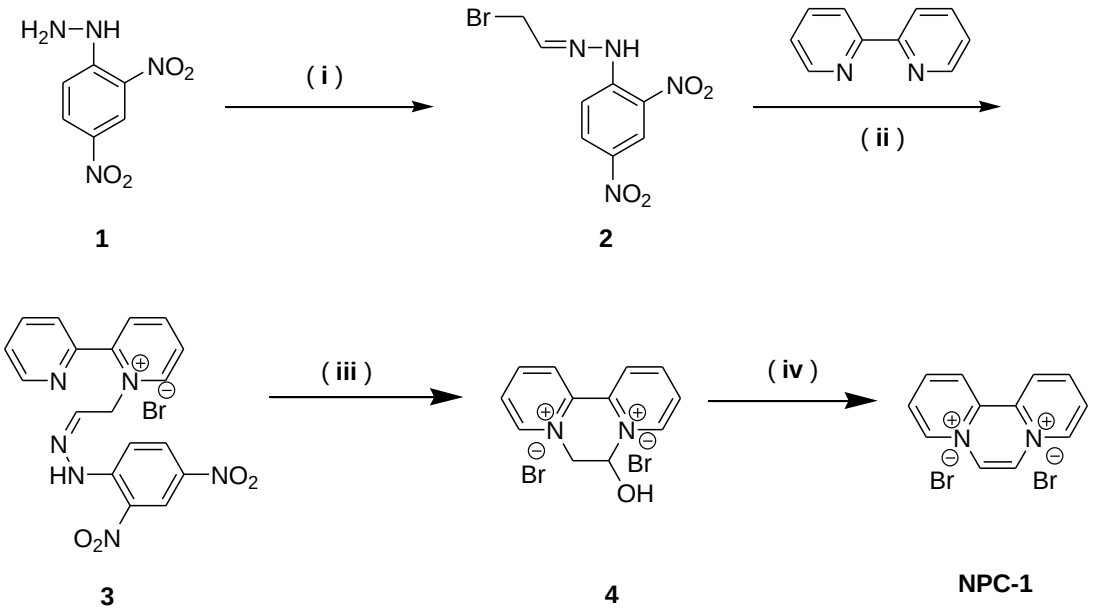

Figure 5.3 Synthetic scheme of dipyrido[1.2-a :2'.1'-c]pyrazinium dibromide from bipyridine (**NPC-1**): (i) bromoacetaldehyde diethylacetal, 12N HCl, 70 %; (ii) bipyridine, C_6H_5Me, reflux overnight, 98 %; (iii) 48 % HBr, 90 ^{o}C, 1h, 85 %, (iv) $SOCl_2$, reflux, 2h, 80 %.

The synthesis of 2,3-dihydropyrazine[1,2,3,4-lmn] 1,10-phenanthrolinium dibromide (**NPC-2**) was even simpler than that of **NPC-1**. A one-step reaction of commercially

available 1,10-phenanthroline and 1,2-dibromoethane produced **NPC-2** in a yield of 96 % as a light yellow crystal (Figure 5.4).

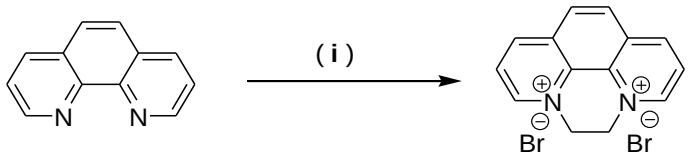

NPC-2

Figure 5.4 Synthetic scheme of 2,3-dihydropyrazine[1,2,3,4-lmn] 1,10-phenanthrolinium dibromide (**NPC-2**): (i) 1,2-dibromoethane, reflux, 4h, 96 %.

Pyrazino[1,2,3,4-lmn] 1,10-phenanthrolinium dibromide (**NPC-3**) was derived from 1,10-phenanthroline according to the method developed by Black *et. al* [42] with a total yield of 33 %.[41] The synthesis of salt **5** was done in the same manner as salt **3** and a yellow powder was achieved in a crude yield of 95 %. The cyclization of salt **5** in HBr to 5,6-dihydro-5-hydroxypyrazino[1,2,3,4-lmn]1,10-phenanthrolinium dibromide (**6**) and the following dehydration of **6** to pyrazino[1,2,3,4-lmn] 1,10-phenanthrolinium dibromide (**NPC-3**) were not as straightforward as that of salt **4** and **NPC-1**, in that the diquaternary salts **6** and **NPC-3** are reactive compounds and are much less easily handled than the corresponding compounds **4** and **NPC-1** prepared from 2,2'- bipyridine; they are difficult to purify and readily deteriorate in hot hydroxylic solvents to give highly colored solutions. If **6** and **NPC-3** are pure, they are stable in aqueous solution or other alcoholic solution, but decompose in strong alkali.

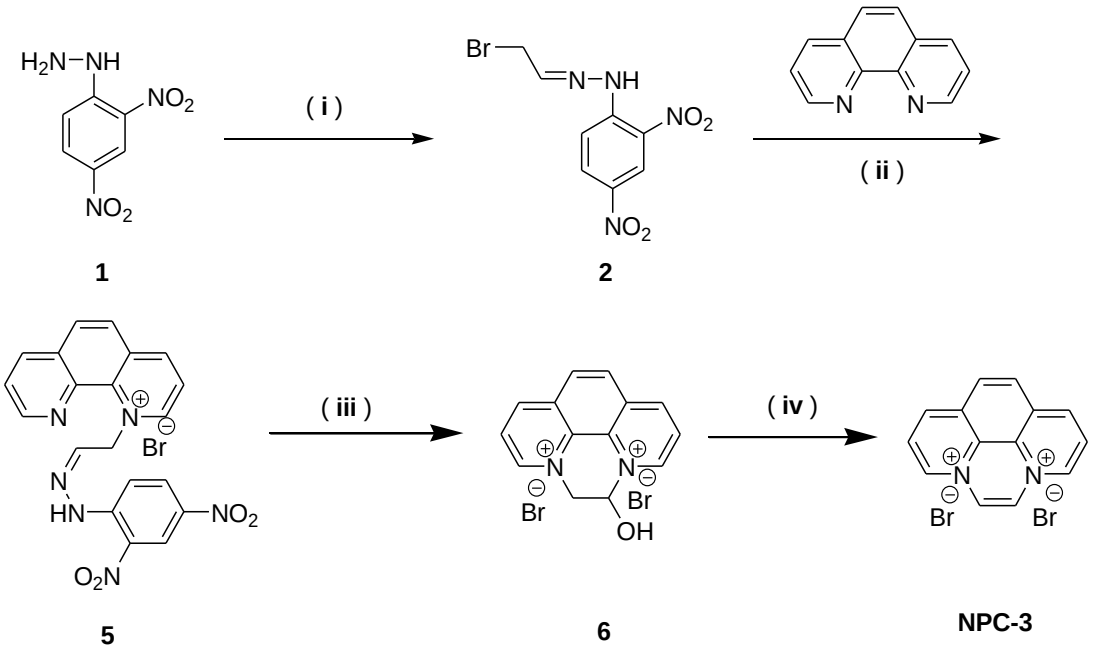

Figure 5.5 Synthetic scheme of pyrazino[1,2,3,4-lmn] 1,10-phenanthrolinium dibromide (**NPC-3**): (i) bromoacetaldehyde diethylacetal, 12N HCl, 70 %; (ii) 1,10-phenanthroline, C_6H_5Me, reflux overnight, 95 %; (iii) 48 % HBr, 90 ^{o}C, 1h, 70 %, (iv) $SOCl_2$, reflux, 2h, 50 %.

5.2.2 Fabrication of novel nitrogen-doped ordered mesoporous graphitic carbon arrays (NMGCAs)

As soon as NPC precursors are available, NMGCAs catalysts were ready to be prepared based on a metal-free nanocasting technology. Commercially available mesoporous silica SBA-15 was used here as hard template, which was prepared under hydrothermal conditions according to the established procedures. The carbon replica was then prepared from different precursors (**NPC-1**, **NPC-2**, **NPC-3**) in the same manner.

To determine the pyrolysis temperature, thermogravimetric analysis of NPC precursors was performed under inert atmosphere. As shown in Figure 5.6, severe weight loss can be observed for NPCs between 300 and 500 ^{o}C, followed by a gradual loss from 500 ^{o}C to 900 ^{o}C. In order to investigate the structure change occurred during these

steps, 300 °C, 500 °C, 750 °C and 900 °C was selected as pyrolysis temperatures respectively.

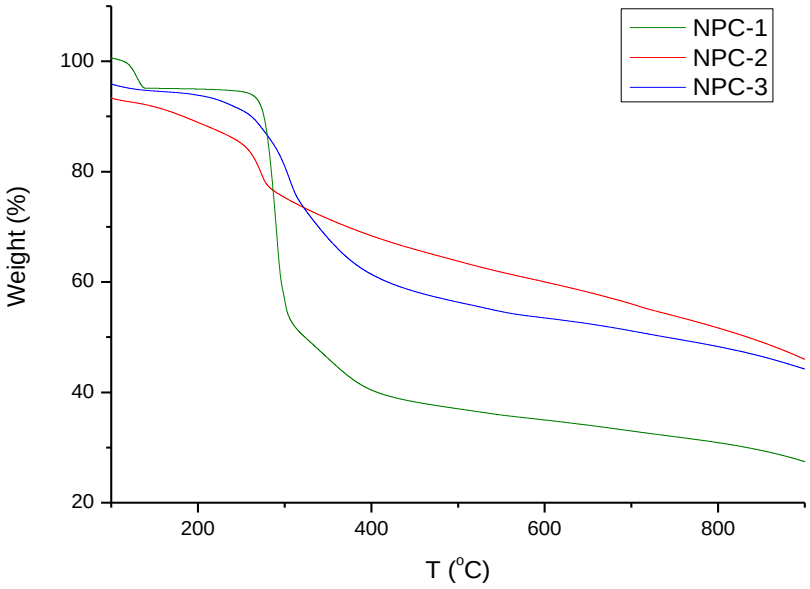

Figure 5.6 Thermogravimetric analysis of **NPC-1**, **NPC-2** and **NPC-3**

A typical procedure for NPC-1, as an example, was described as follows: 500 mg SBA-15 was mixed with 750 mg NPC-1 in 30 ml methanol at room temperature under stirring in an open crucible. After evaporation of MeOH, the obtained NPC/SBA-15 composites were dried overnight at 60 °C in an oven and subsequently calcined at 300 °C, 500 °C, 750 °C and 900 °C for 5 h, respectively. After etching silica by 2M NaOH for 1 day, nitrogen-doped ordered mesoporous graphitic carbon arrays (NMGCAs) were obtained as black solid.

When NPC-2 and NPC-3 were used as carbon precursors, the same procedure was followed.

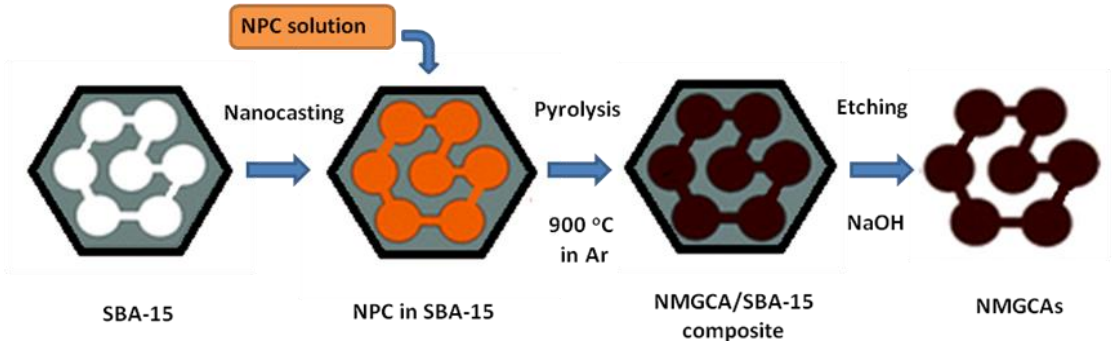

Figure 5.7 Schematic illustration of fabricating NMGCAs form NPCs with the aid of ordered mesoporous template

5.2.3 Fabrication of rotating disk electrode based on novel nitrogen-doped ordered mesoporous graphitic carbon arrays (NMGCAs/GC)

The procedure of preparing glass carbon rotating disk electrode (3 mm in diameter, from Autolab) is described as follows: prior to use, the working electrode was polished mechanically with 0.5 µm diamond down to 0.05 µm alumina slurry to obtain a mirror-like surface and then washed with Mill-Q water followed by acetone, then allowed to dry in oven. 1 mg NMGCAs was dissolved in 1 ml solvent mixture of Nafion (5%) and EtOH (V: V ratio = 1:9) by sonication. For comparison, a commercially available catalyst of 20 wt.% Pt supported on black carbon (from Sigma, fuel cell grade) was used and 1 mg/ml Pt/C suspension was also prepared as the same procedure described above. 1.8 µL NMGCAs or Pt/C suspension was pipetted on the glassy carbon electrode surface. The electrode was allowed to dry at RT and heated at 50 ^{o}C for 30 min before measurement. This led to a catalyst (NMGCAs or Pt-C) loading of 25.5 µg/cm^2

5.3 Results and discussion

5.3.1 The influence of the porous structure on the electrocatalytic activity of NMGCAs

As we described in the chapter 5.2, **NPC** precursors can be detained by ionizing 1,10-phenanthroline via standard synthetic procedures with good yields. It promises a gram-scale production of NMGCAs. Moreover, **NPC** precursors show very good solubility in most common alcoholic solvents at room temperature. Meanwhile, as charged molecules, their solutions exhibit strong interactions with inorganic surfaces. Therefore, they are ideal precursors for a nanocasting approach in which they can be easily incorporated into porous templates and subsequently heat-treated to generate high-surface-area nitrogen-doped carbons without using any high-pressure treatment.

Conventional SBA-15 silica, which has been widely used to generate mesoporous carbon, was applied in our case as a template. For example, a SBA-15 template was immersed in one of the NPC solutions (**NPC-3** in methanol was used here as example) for several minutes, long enough that complete pore-filling could be assumed. The solvents were subsequently evaporated by constant stirring at room temperature. The white solid residue was then calcined in an oven to 900 ^{o}C. Removal of the silica with HF yielded a black powder, which was analyzed by means of TEM, nitrogen sorption measurements, Raman spectroscopy, X-ray photoelectron spectroscopy (XPS) and wide angle X-ray spectroscopy (WAXS).

The ordered mesoporous structure of SBA-15 template can be identified clearly from its TEM image (Figure 5.8a). TEM image of **NPC-3-900** (Figure 5.8b) shows a good replication of the pore structure of SBA-15 template in the nitrogen-doped carbon.

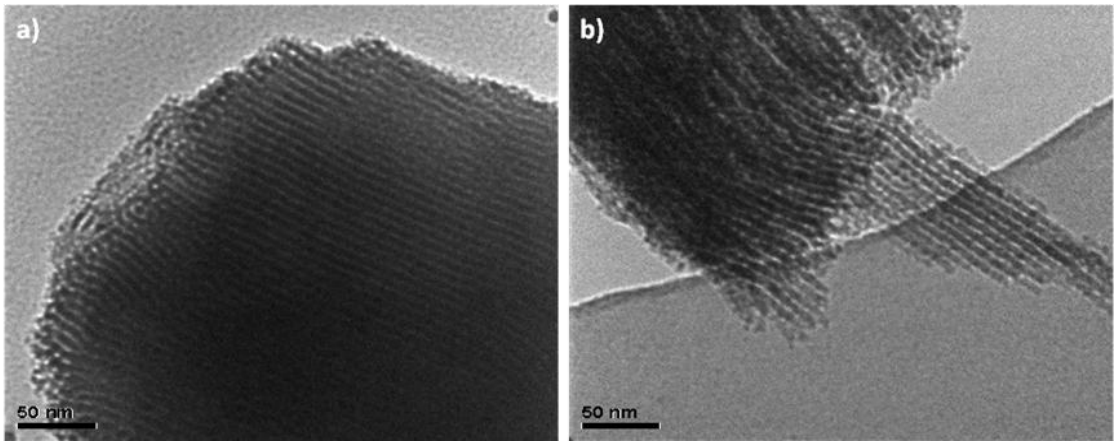

Figure 5.8TEM image of a) SBA-15 and b) the obtained porous N-doped carbon material using SBA-15 as template.

For comparison, a reference sample (**NPC-3-900N**) was prepared by directly pyrolyzing **NPC-3** at 900^{o}C without using the SBA-15 template. From the nitrogen sorption measurements of **NPC-3-900N**, no porous structure could be identified in it which demonstrated that the porosity of **NPC-3-900** comes from the usage of the SBA-15 template. In contrast, the nitrogen sorption measurements of **NPC-3-900** reveal that this replica is indeed mesoporous, with a maximum pore size of 3.8 nm and a specific surface area of 580 m^2 g^{-1} (compared to 20 m^2g^{-1} for **NPC-3-900N**).

For a better understanding of the effect of using SBA-15 upon the microstructure of NMGCAs, Wide angle X-ray scattering (WAXS) and Raman spectra of **NPC-3-900** and **NPC-3-900N** were investigated and compared.

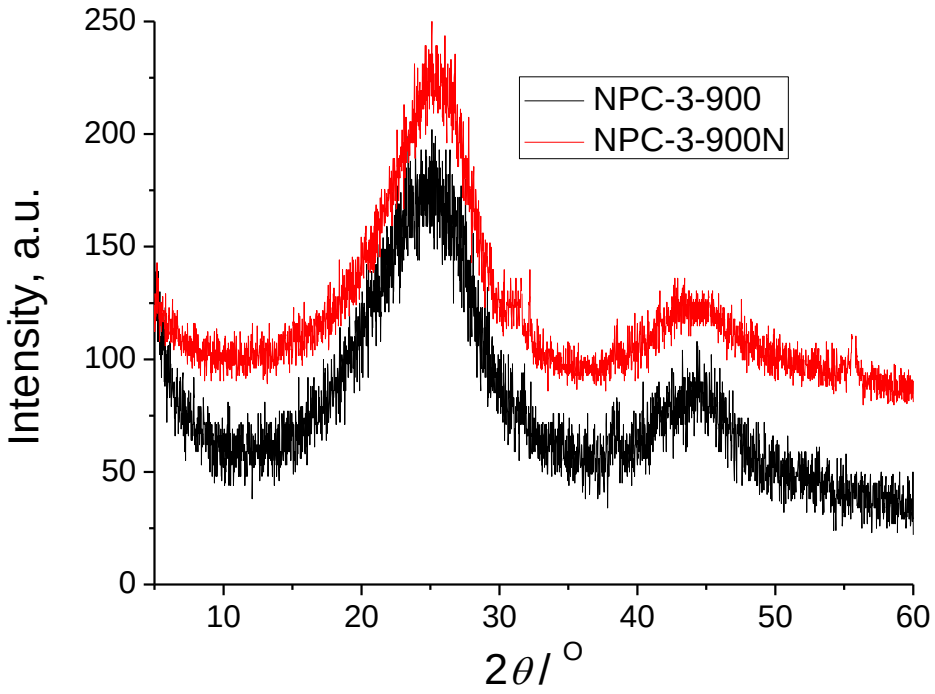

Figure 5.9 WAXS of **NPC-3-900** and **NPC-3-900N**

WAXS measurements (Figure 5.9) illustrate a well-developed graphitic stacking peak at 25.2 ^{o} for both **NPC-3-900** and **NPC-3-900N**. The width of the peak stays constant or even slightly narrower when template is applied. The more pronounced peak at 44.5^{o}, however, indicates the formation of a better intralayer condensation for **NPC-3-900N**. The less interlayer condensation of **NPC-3-900** may be caused by the interference of mesoporous SBA-15 during the carbonization of **NPC-3**, which hampered the intralayer crosslink. As a result, a WAXS measurement indicates that the mesoporous template has no obvious effect on local graphitic structure of NMGCAs but may intervene in the formation of interlayer graphitic structure s in a higher order.

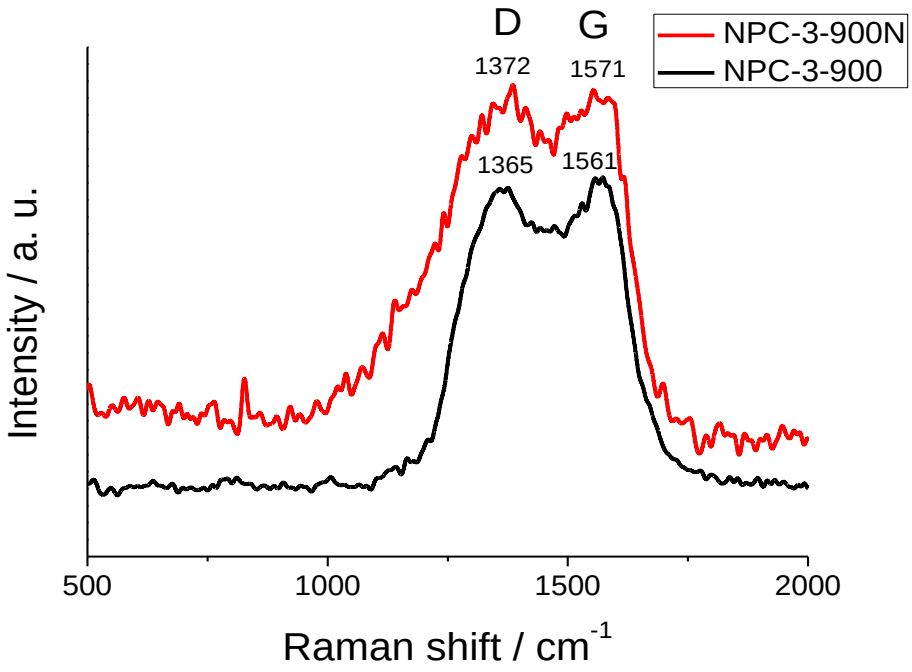

Figure 5.10 Raman spectra of **NPC-3-900** and **NPC-3-900N**

Same conclusions can be drawn from the Raman spectra of **NPC-3-900** and **NPC-3-900N** as illustrated in Figure 5.10. The two peaks in the Raman spectrum of **NPC-3-900** are attributed to the G band at 1561 cm^{-1} and D band at 1365 cm^{-1}, respectively, while the G band of **NPC-3-900N** is at 1562 cm^{-1}, the D band 1372 cm^{-1}. The G band denotes the in-plane bond-stretcshing motion of pairs of sp^2-C atoms. The D band (''disordered'' band) is the breathing mode of the aromatic rings of the graphene domains that is related to a series of defects: bond-angle disorder, bond-length disorder, and hybridization which are caused by heteroatom (nitrogen/oxygen) doping. [43-46] It can be found that the G/D ratio of **NPC-3-900** is slightly higher than that of **NPC-3-900N**, which indicates that **NPC-3-900** contains a similar, if not slightly better, local graphitic structure compared to **NPC-3-900N**. In other words, using SBA-15 template only has a minor effect on the local graphitic structure of NMGCAs.

It is also interesting to notice that the G bands and D bands are not so pronouncedly separated from each other if we compare the Raman spectra of **NPC-3-900** and **NPC-3-900N** to that of graphene samples illustrated in chapter 2 and 3. This is due to the dramatic increase of intensity of D bands of **NPC-3-900**, suggesting that a severe nitrogen doping, i.e. a high nitrogen content was preserved after pyrolysis at 900 ^{o}C leading to the disordered graphitic structures.

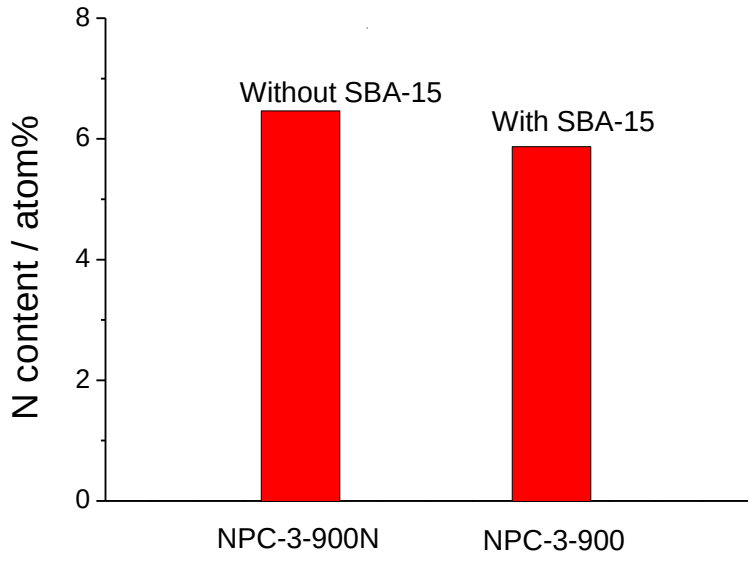

Figure 5.11 Nitrogen content of **NPC-3-900** and **NPC-3-900N**

This assumption was confirmed by the elemental analysis of **NPC-3-900** and **NPC-3-900N**. As can be calculated from the ionic formula of the **NPC-3** cation, the molar ratio of N/C is 17%. After pyrolysis at 900 ^{o}C, the nitrogen content decreases to 6.4 % and 6.0 % for **NPC-3-900N** and **NPC-3-900**, respectively as shown in Figure 5.11. These are remarkably high nitrogen contents remaining in the final carbonized structures even at those temperatures, which can be important for the electrochemical applications. Because **NPC-3-900** has a higher surface area than **NPC-3-900N** which forms more "escaping" pathways for nitrogen at high temperature, a slightly lower nitrogen content was observed for **NPC-3-900** compared to **NPC-3-900N.**

By comparing TEM images, porosity, Raman spectra, WAXS and N content of **NPC-3-900** and **NPC-3-900N**, it can be concluded that using a SBA-15 template leads to a higher surface area but has not much influenced the local structure of **NPC-3-900**. Based on this discovery, the electrocatalytic properties of **NPC-3-900** in ORR were investigated to disclose the relationship between the porosity and the catalytic activity of NMGCAs.

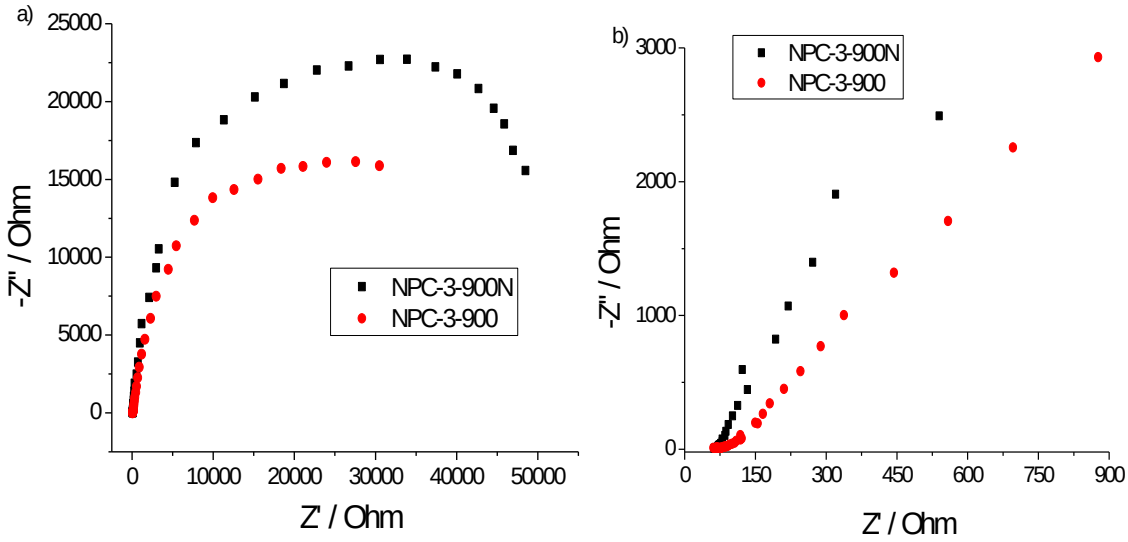

Figure 5.12 (a) The EI spectra (Nyquist plots) of **NPC-3-900** and **NPC-3-900N** in oxygen-saturated 0.1M KOH solution in the frequency range of 0.01Hz-100kHz; (b) Magnification of the EI spectra in oxygen-saturated 0.1M KOH solution at high frequency range.

Figure 5.12 shows the electrochemical impedance (EI) spectra of **NPC-3-900** and **NPC-3-900N** presented via Nyquist plots in oxygen-saturated 0.1M KOH solution in the frequency range of 0.01 Hz-100 kHz. The Ohmic resistance of the electrode can be read from the diameters of the semicircles on the abscissa (real axes). As illustrated in Figure 5.12a, less diameter of **NPC-3-900** indicates its smaller resistance during the electron transfer process. As for the oxygen reduction reaction, the electron transfer process refers to two steps: the oxygen absorption on the surface of the electrode and the electron-gain step of oxygen from the catalysts. The electron transfer process during oxygen reduction

reaction on the surface of **NPC-3-900** is supposed to proceed more smoothly owing to its smaller diameters of the semicircle in Nyquist plot compared with that of **NPC-3-900N**.

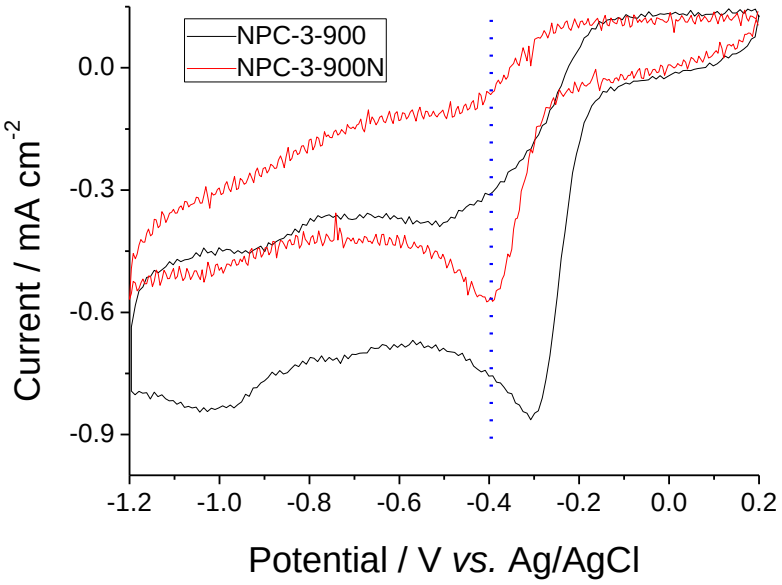

Figure 5.13 The cyclic voltamogramms of **NPC-3-900/GC** and **NPC-3-900N/GC** in O_2-saturated 0.1M KOH solution.

To evaluate the influence of porosity on the catalytic activity of NMGCAs in a real ORR process, the glassy carbon rotating disk electrodes based on **NPC-3-900** and **NPC-3-900N** were prepared as **NPC-3-900/GC** and **NPC-3-900N/GC,** respectively, according to the fabrication techniques described in chapter 5.2.3.. Their cyclic voltamogramms are shown in Figure 5.13. The oxygen reduction peak of **NPC-3-900/GC** appears at -0.29 V. This potential is much higher than that of **NPC-3-900N/GC** (-0.40V). A more positive peak potential of **NPC-3-900/GC** suggests a lower over potential and a more facile electrochemical kinetics of oxygen reduction reaction compared with that of **NPC-3-900N/GC**. In addition, the peak current density of **NPC-3-900/GC** is higher than that of **NPC-3-900N/GC**, indicating more electrocatalytic sites for the reduction of oxygen.

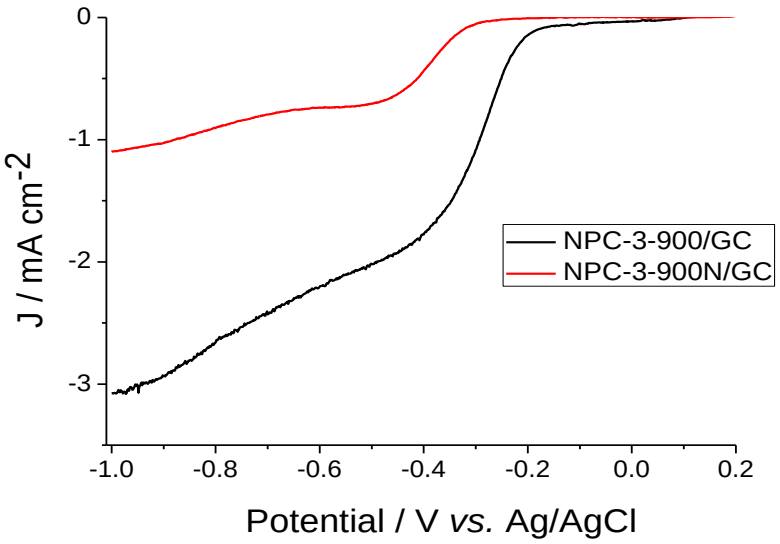

Figure 5.14 Linear scanning voltamogramms of **NPC-3-900/GC** and **NPC-3-900N/GC** in O_2-saturated 0.1M KOH solution. The rotating speed is 900rpm.

Figure 5.14 shows the linear scanning voltamogramms (LSV) of **NPC-3-900/GC** and **NPC-3-900N/GC**. It can be seen that the onset potential of **NPC-3-900/GC** prepared with the SBA-15 template is close to -0.2 V, much higher than that of **NPC-3-900N/GC** (-0.35 V). The higher current density of the NMGCAs electrode with mesopores compared to that of the bulk one clearly demonstrates that porosity of NMGCAs enables more electrocatalytic sites for the reduction of oxygen.

The rotating-disk voltammograms for the glassy carbon supported NMGCAs electrodes prepared from **NPC-3-900** and **NPC-3-900N** are presented in Figure 5.15a and b. As the rotating speed increases, the measured current density ascends gradually owing to the enhanced diffusion rate of O_2. It should be noted that an obvious plateau appears at the potential of ca. -0.5 V for **NPC-3-900N/GC** (Figure 5.15b), while the porous **NPC-3-900/GC** shows no plateau in this potential region (Figure 5.15a). Considering that the pre-plateau often indicates a two-electron reduction pathway owe to the formation of H_2O_2, the different shapes of the rotating-disk voltammograms suggest that **NPC-3-900**,

the N-doped carbon with porosity must exhibit a higher electron-transfer number for ORR than that of bulk carbon.

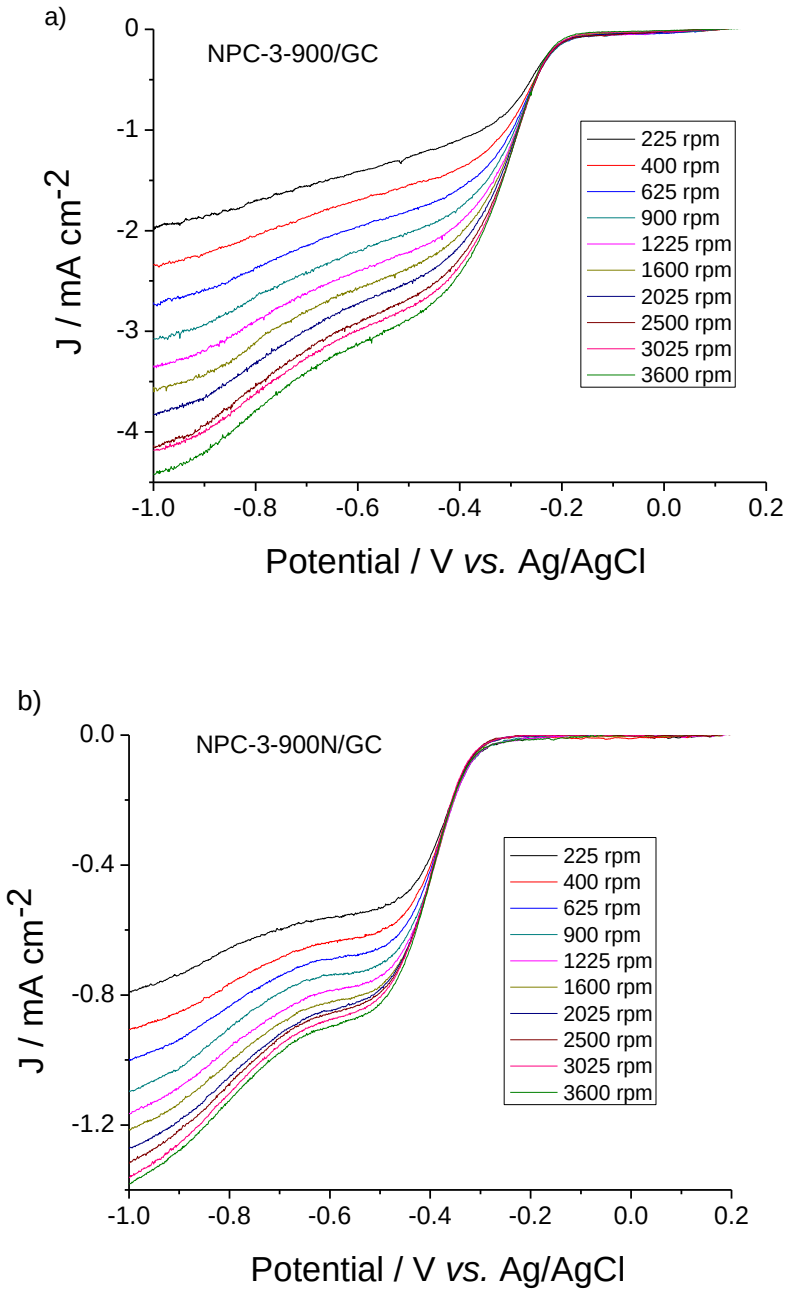

Figure 5.15 Rotating-disk voltammograms recorded for (a) **NPC-3-900/GC** and (b) **NPC-3-900N/GC** at different rotation speeds at the potential sweep rate of 10 mV/s. 0.1M KOH solution saturated by oxygen is used as electrolyte.

The corresponding Koutecky-Levich plots (J^{-1} versus $w^{-1/2}$) of **NPC-3-900/GC** and **NPC-3-900N/GC** are illustrated in Figure 5.16, which are extracted from the current density at different rotating speed and potentials. A good linearity can be observed at various reduction potentials. The kinetic parameters can be analyzed on the basis of the Koutecky–Levich equations as described in Chapter 4 with details:

$$\frac{1}{J} = \frac{1}{J_L} + \frac{1}{J_k} = \frac{1}{B\omega^{1/2}} + \frac{1}{J_k} \qquad \text{..... (1)}$$

$$B = 0.62\, nFC_0(D_0)^{2/3}v^{-1/6} \qquad \text{..... (2)}$$

$$J_k = nFkC_0 \qquad \text{..... (3)}$$

According to equations (1) and (2), the number of electrons transferred (n) and J_K can be obtained from the slope and intercept of the Koutecky–Levich plots in Figure 5.16, respectively.[21] By using the values C_0=1.2×10^{-3} molL^{-1}, D_o=1.9×10^{-5} cms^{-1}, and v=0.1 m^{2}s^{-1} in 0.1M KOH,[47] n was calculated at different potential and illustrated in Figure 5.16a. With the decrease of reductive potentials, **NPC-3-900/GC** shows an increase of electron transfer number from 3.1 to 4, which suggests a semi-4-electron transfer kinetic which is dominated by 4-electron transfer pathway that directly reduce O_2 to H_2O combined with a two-electron transfer pathway involving H_2O_2. For comparison, **NPC-3-900N/GC** exhibits relatively constant electron transfer numbers around 2 against all ORR potentials that illustrates a total two-electron transfer mechanism for cathodic reduction in fuel cell. The calculated kinetic current densities J_K at different potential are also shown in Figure 5.16b. The J_K value of **NPC-3-900/GC** is dramatically increased from 3.9 to 6.5 mA cm^{-2}, higher than *that* of a commercial Pt/C electrode (4.2 mA cm^{-2} as measured), while that of **NPC-3-900N/GC** always remains at a low value around 1.2 mA cm^{-2} which indicates a very slow reduction speed during ORR.

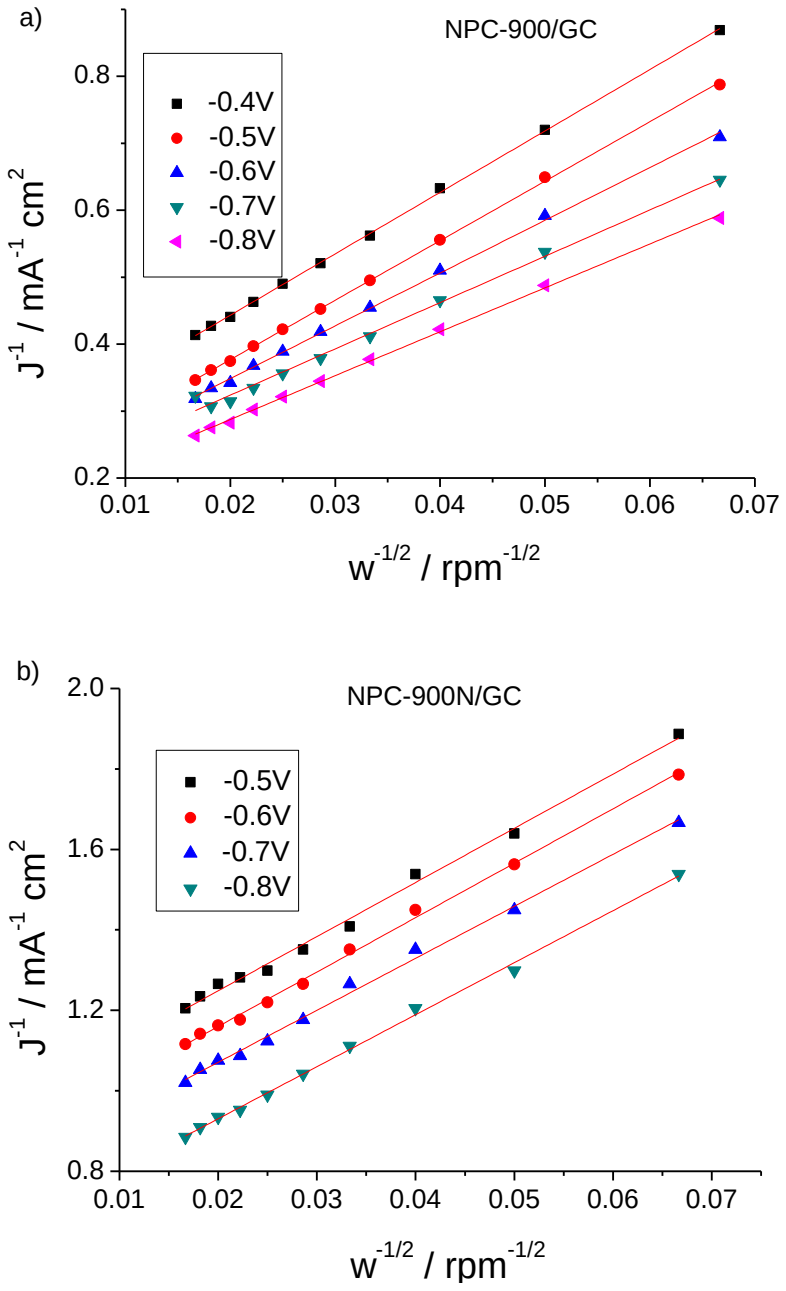

Figure 5.16 Koutecky-Levich plots (a) **NPC-3-900/GC** and (B) **NPC-3-900N/GC.**

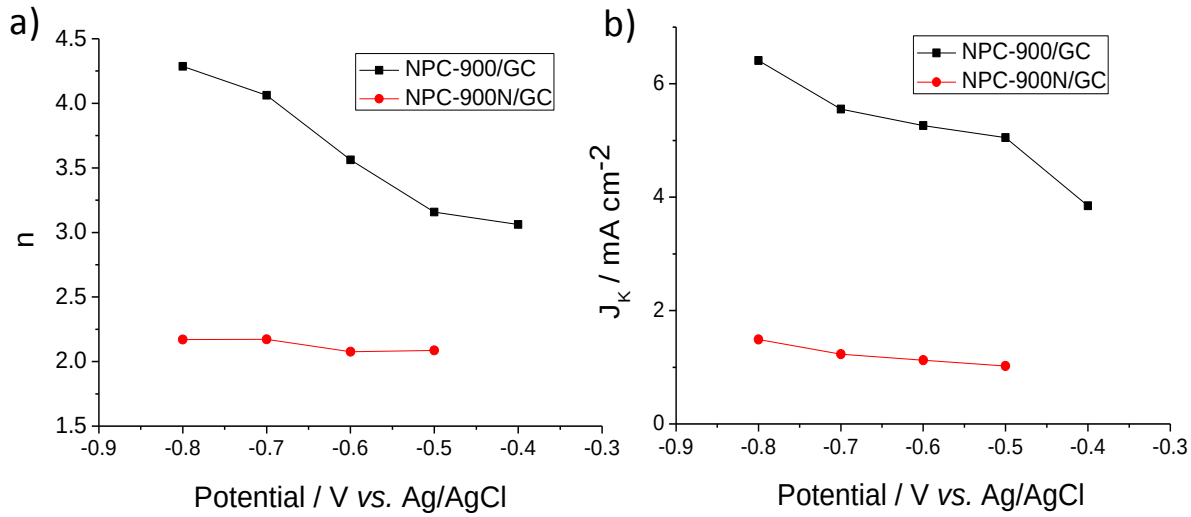

Figure 5.17 a) The electron transfer numbers and b) Kinetic current density (J_k) of **NPC-3-900/GC** and **NPC-3-900N/GC** at different potentials**.**

As previously illustrated, the structures of **NPC-3-900** to **NPC-3-900N** are very similar except that **NPC-3-900** exhibits a much higher porosity and higher surface area than **NPC-3-900N**. Even though **NPC-3-900N** has a higher nitrogen content than **NPC-3-900**, the electrocatalytic performance of **NPC-3-900/GC** is apparently superior to that of **NPC-3-900N/GC** for all parameters (electron transfer number, current density). The combination of these facts has demonstrated that a better porosity and higher surface area can indeed enhance the electrocatalytic properties of NMGCAs for ORR. Therefore, nanocasting by using hard template such as SBA-15 leads us an effective way to improve the performance of NMGCAs as cathodic catalyst in fuel cells.

5.3.2 The influence of pyrolysis temperature on the electrocatalytic activity of NMGCAs

The molar ratios N/C of **NPC** precursors are 0.19 for **NPC-1** and 0.17 for **NPC-2** and **NPC-3**, which are comparable to the N/C ratio of phenanthroline (0.19). Nevertheless, as

soon as this aromatic molecule was converted into its quaternary ammonium salts, the thermal stability is supposed to be dramatically enhanced as we discussed in chapter 5.1. Accordingly, **NPC-1**, **NPC-2** and **NPC-3** are expected to possess a higher nitrogen and carbon yield than phenanthroline after thermal treatment.

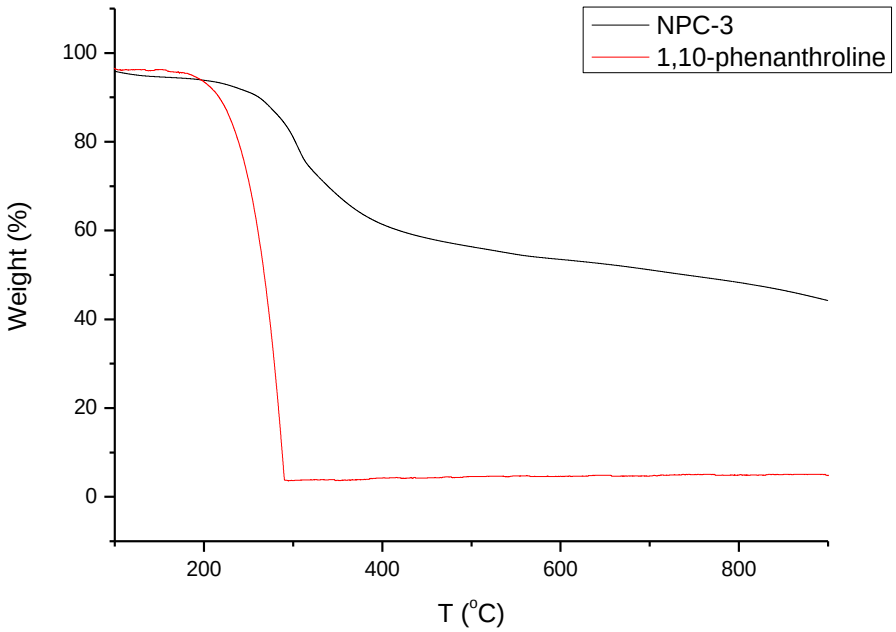

Figure 5.18 TGA measurement of phenanthroline and **NPC-3**

To confirm this assumption carbonization of phenanthroline and **NPC** precursors were firstly analyzed by thermogravimetric analysis (TGA) of bulk samples. As illustrated in Figure 5.18, no weight loss of phenanthroline is observed up to a temperature of 200 ^{o}C before decomposition occurs. The total mass loss of phenanthroline at 900 ^{o}C is 97 %. This result is coherent with the experimental phenomenon that almost no solid product remained after pyrolysis of phenanthroline in a CVD chamber at 900 ^{o}C under an argon flow. In contrast, the aromatic core of **NPC** precursors exhibit far better thermal stability. Here **NPC-3** is again taken as an example. In Figure 5.18, the upper limit of thermal stability of **NPC-3** lies at 300 ^{o}C. Decomposition was generally observed in two steps. The

first decomposition step can be found between 300 and 400 °C with mass loss of 40 %. Taking into account that **NPC-3** is an organic salt with bromide as the counterion which has a wt% of 43 %. These counterions are known to form HBr or Br_2 gas at 300 to 400 °C. This leads to the assumption that the first decomposition step is caused by the elimination of Br anions, maintaining the nitrogen elements. This is indeed confirmed by XPS measurements (Figure 5.19) of pyrolyzing **NPC-3** at elevated temperatures from 300 °C to 500 °C in which the signal of Br3p dramatically decreased at 400 °C and faded away at 500 °C.

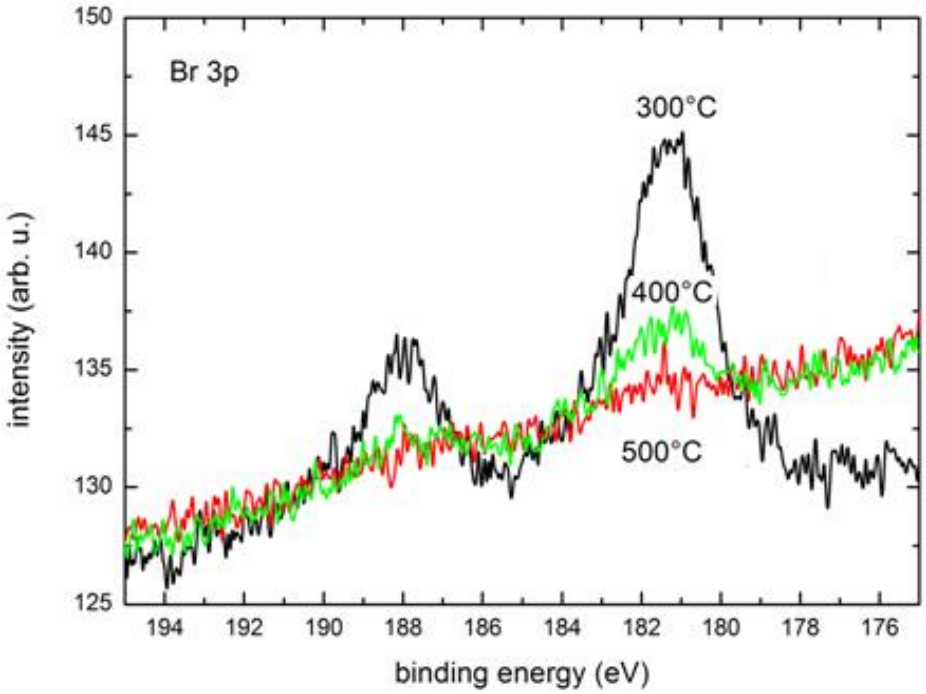

Figure 5.19 XPS of **NPC-3** pyrolyzed at 300 °C, 400°C and 500°C.

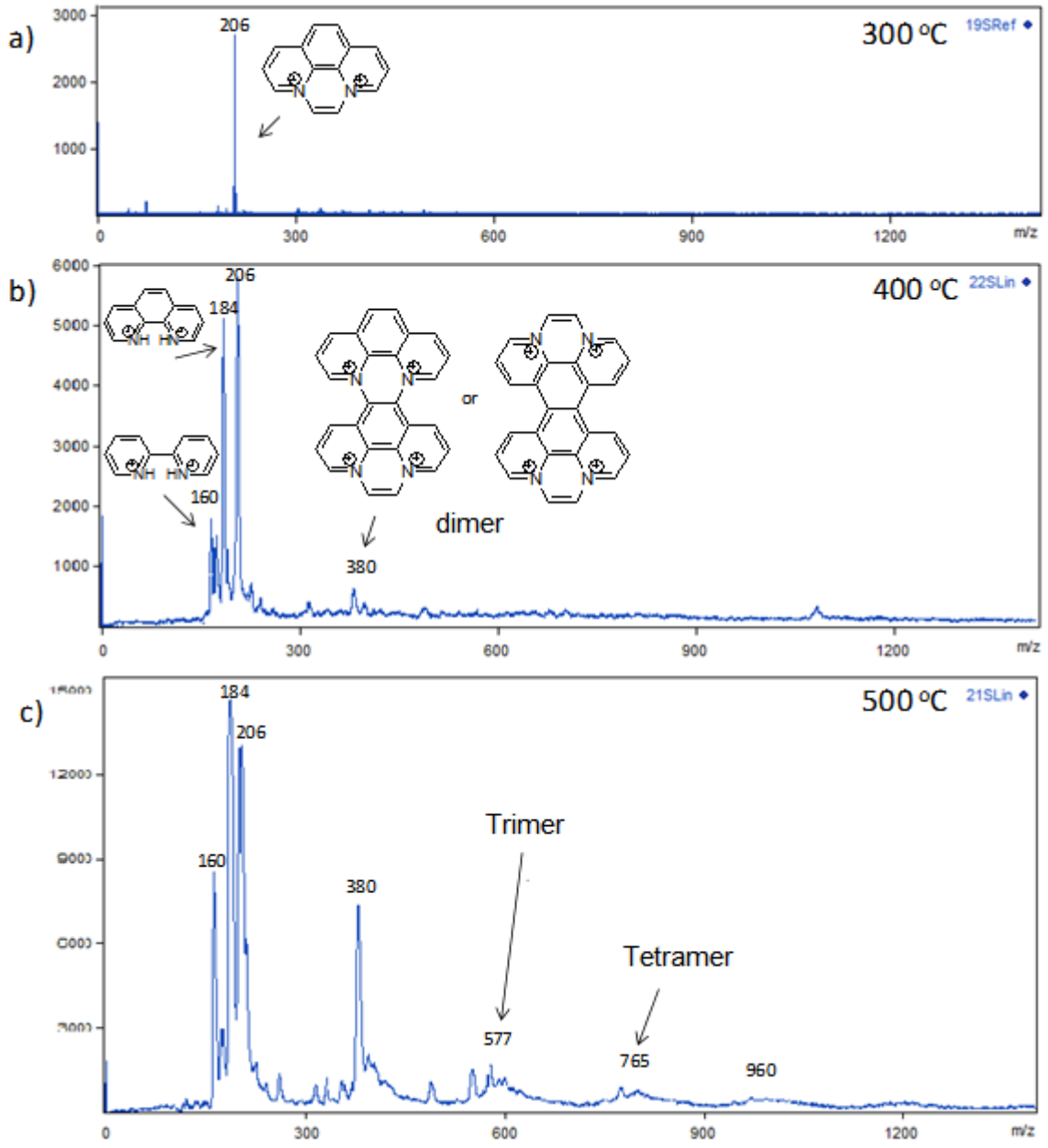

Figure 5.20 MALDIT-TOF mass spectra of **NPC-3** pyrolyzed at 300 °C, 400°C and 500°C

To look into the details of the thermal process of **NPC-3** between 300 °C to 500 °C, the MALDI-TOF mass spectra were measured for NPC-3 pyrolyzed under 300, 400 and 500 °C for 1h in Argon respectively. As shown in Figure 20a, after heat treatment at 300 °C, only the cations of **NPC-3** are identified in the mass spectra, which correlated to results achieved from XPS that the main thermal reaction occurring at 300 °C is releasing Br^-

counter ions. The aromatic core of **NPC-3** remains intact in this stage. Further increasing pyrolysis temperature to 400 ^{o}C led to a minor decomposition and polymerization of **NPC-3** which is illustrated in Figure 20b. Under 400 ^{o}C, in addition to further elimination of Br^{-}, the α–carbon of pyrazine and 5,6-carbon of **NPC-3** start to fall off from the aromatic core, and hence, leave bipyridinic and phenanthrolinic cations. Meanwhile, polymerization occurred at this phase as a peak at 380 g/mol was found in the mass spectra. When the temperature further goes up to 500 ^{o}C, more decomposition and further polymerization of **NPC-3** were observed. In this stage, the polymers of **NPC-3** with increasing number of repeating units were generated as can be identified in Figure 20c.

The second step, as shown in TGA analysis (Figure 18) is found to stay more-or-less constant up to a temperature of 900 ^{o}C. Accompanied by the loss of carbon and hydrogen above 500 ^{o}C, polymerization and graphitization generates a nitrogen-doped ordered graphitic carbon structures.

For a better understanding of the effect of pyrolyzing the NPC precursor at different temperature, **NPC-3-500, NPC-3-750** and **NPC-3-900** were prepared according to the same nanocasting technique described in chapter 5.3 by using SBA-15 as hard template and pyrolyzed at temperate of 500 ^{o}C, 750 ^{o}C and 900 ^{o}C, respectively. WAXS, Raman spectra, XPS and elemental analysis were measured and compared in order to investigate the influence of the pyrolysis temperature on the electrocatalytic activity of NMGCAs.

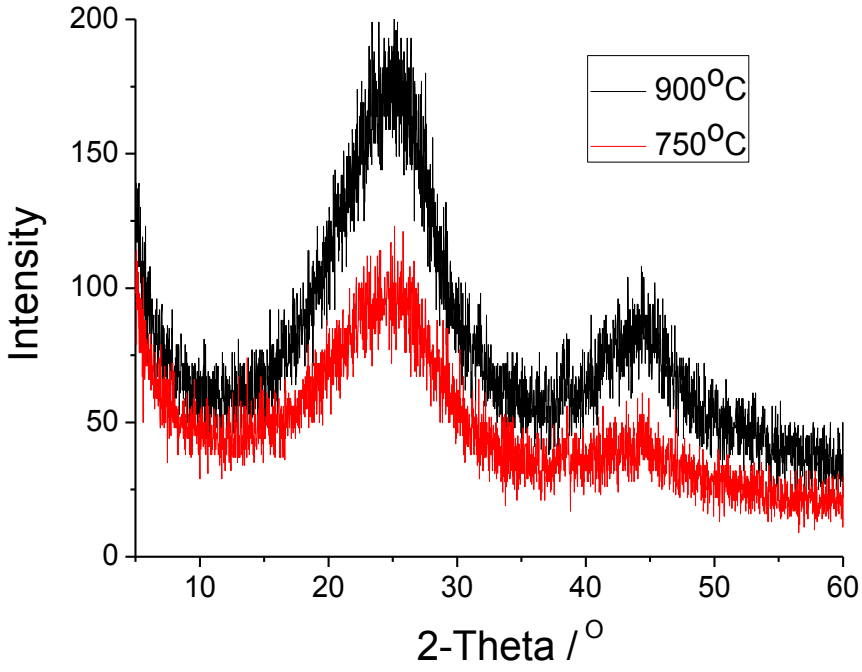

Figure 5.21 WAXS of **NPC-3-750** and **NPC-3-900**

In Figure 5.21, WAXS measurements present a well-developed graphitic stacking peak at 25.2 ^{o} for both **NPC-3-750** and **NPC-3-900**. However, the intensity of this peak increases dramatically when a higher pyrolyzing temperature was applied. This observation holds true for the peaks found at 44.5 ^{o}, which implies a higher degree of intralayer condensation for **NPC-3-900**. The observation is in agreement with the well accepted theory that a higher pyrolysis temperature could lead to a better graphitization of carbon materials. Meanwhile, more nitrogen and hydrogen would be eliminated by further increasing the temperature, leaving a better organized carbon matrix without so much heteroatom doping according to the TGA measurement. Therefore, the WAXS measurement indicates that at a higher temperature the pyrolysis is carried out, a better graphitization and lower nitrogen content of NMGCAs could be achieved.

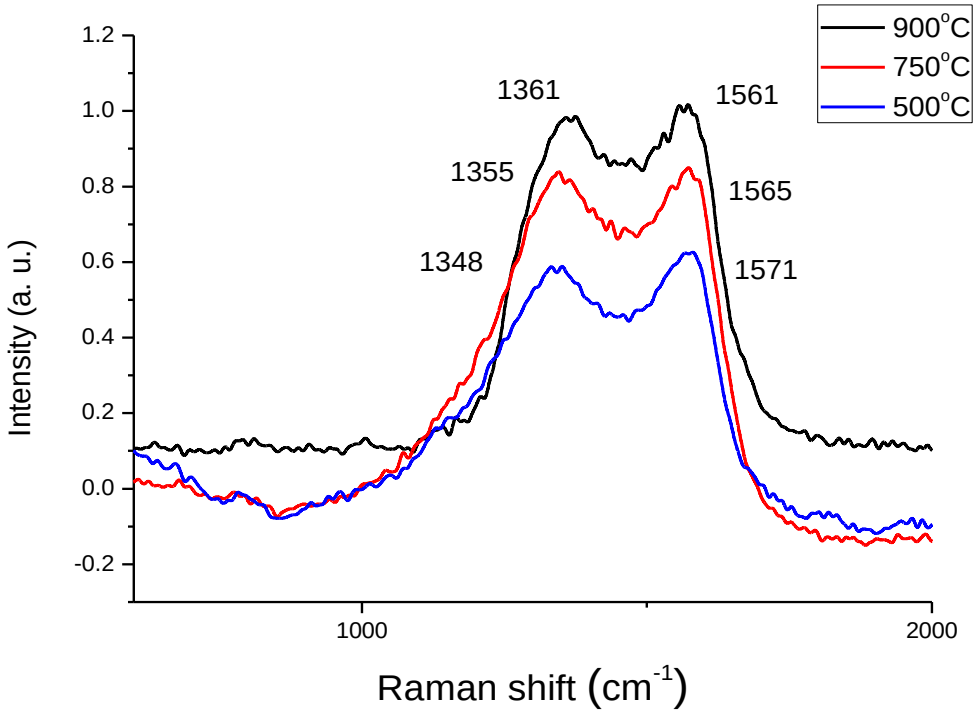

Figure 5.22 Raman spectra of **NPC-3-500**, **NPC-3-750** and **NPC-3-900**.

On the contrary, the comparison of the Raman spectra of **NPC-3-500**, **NPC-3-750** and **NPC-3-900** in Figure 5.22 fails to reveal dramatic changes of G/D ratios. The two peaks in the Raman spectrum of **NPC-3-750** are attributed to the G band at 1565 cm^{-1} and the D band at 1355 cm^{-1}, respectively, while the G band of **NPC-3-750** is at 1571 cm^{-1}, the D band 1348 cm^{-1}. A slight increase of G/D ratios observed for **NPC-3-500** to **NPC-3-900** indicates the improvement of graphitic network with an elevating pyrolyzing temperature. However, since all **NPC-3-500**, **NPC-3-750** and **NPC-3-900** are nitrogen doped, a strong interruption of the sp^2-C network is always observed even with a thermal treatment at 900 °C. This may be the reason that a strong D band is pronounced for all **NPC-3-500**, **NPC-3-750** and **NPC-3-900**, and thus a dramatic change of G/D ratios cannot be revealed in Raman spectra of NMGCAs.

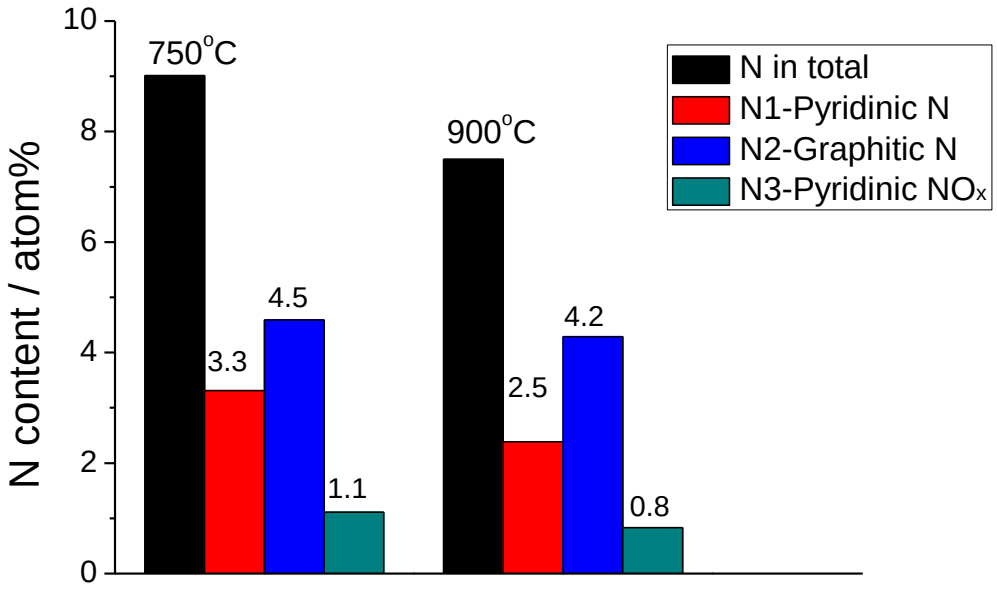

Figure 5.23 Nitrogen content of **NPC-3-750** and **NPC-3-900**

The strong nitrogen doping that interrupts the sp^2-C **NPC-3-750** and **NPC-3-900** is further confirmed by the elemental analysis of **NPC-3-750** and **NPC-3-900**. The calculated molar ratios N/C of **NPC-3** cation is 14 %. As shown by the black columns in Figure 5.23 the nitrogen content decreases to 9.0 % and 7.5 % for **NPC-3-750** and **NPC-3-900**, respectively. Both samples exhibit remarkably high nitrogen content bound in the carbonized structures at high temperature. Because **NPC-3-900** was pyrolyzed at a higher temperature, its nitrogen content was 1.5 % lower than that of **NPC-3-750**, which is in agreement with the conclusion drawn from TGA measurement.

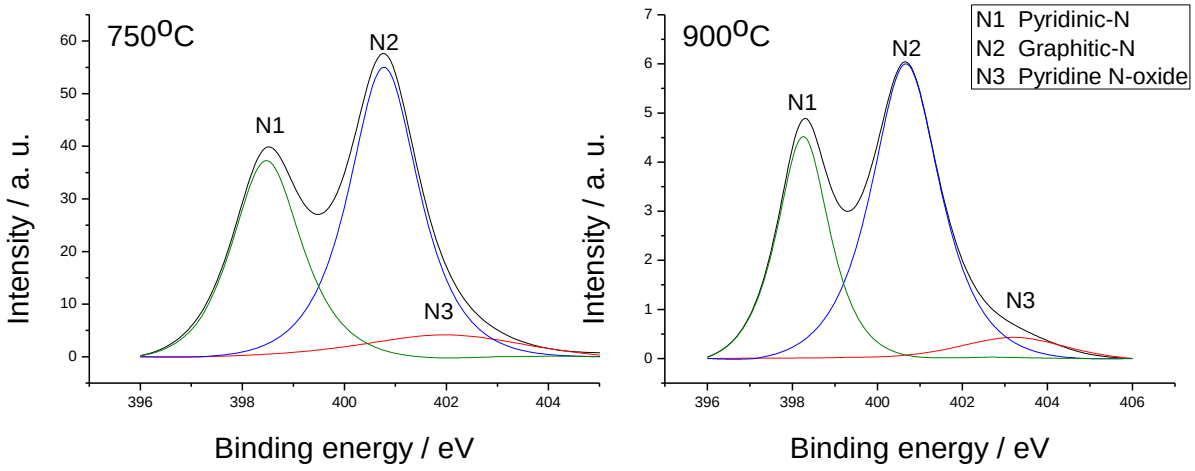

Figure 5.24 N1s XPS and deconvolution of **NPC-3-750** and **NPC-3-900**.

The XPS measurement enables a closer examination of the different types of the nitrogen contents of **NPC-3-750** and **NPC-3-900**. The high resolution XPS spectra of the N1s for the two materials are demonstrated in Figure 5.24. The split peaks at binding energy of 398.3±0.2 (N1), 400.9±0.2 (N2), and 403.0±0.2 (N3) eV are characteristic for pyridinic-N, graphitic-N and pyrrolic N-oxide, respectively. It can be found in Figure 5.24 that the signal of pyridinic-N is more pronounced for **NPC-3-900** compared to **NPC-3-750**. The calculated peak area ratios of N1/N2 of **NPC-3-750** and **NPC-3-900** are 1.51 and 1.70, respectively. This suggests a higher ratio of graphitic-N/pyridinic-N (N2/N2) in **NPC-3-900** than that of **NPC-3-750**. The pyridine-like nitrogen atoms can be transformed into graphite-N atoms at higher pyrolysis temperatures. Considering that the total N content of **NPC-3-900** is less than that of **NPC-3-750**, the content of different types of nitrogen were calculated as shown in Figure 5.23.

The ratio between N2/N1 is not only related to the local structure of NMGCAs, but also impacts on their electrocatalytic properties for ORR. It is well accepted that pyridinic N-oxide is inactive for oxygen reduction, while either pyridinic or graphitic type nitrogen is responsible for the ORR activity of carbon.[27] The controversies mainly focus on which one is exactly the active specie. Therefore, determining the N2/N1 ratio is very important to

clarify the catalytic mechanism of NMGCAs in ORR, i.e. which nitrogen is the real active species.

The Nyquist plots of the EI spectra of NPC-**3-750** and **NPC-3-900** (Figure 5.25a) exhibit similar diameters of the two semicircles, suggesting comparable electrochemical kinetic processes for **NPC-3-750** and **NPC-3-900** in the oxygen reduction reaction, or in other words, a similar kinetic speed of the oxygen absorption on the surface of the electrode and the electrons that oxygen obtains from the catalysts. It indicates that similar porous structures from SBA-15 result in the same electron transfer process for NMGCAs in ORR. The electrochemical impedance spectra of **NPC-3-750** and **NPC-3-900** are shown in Figure 5.24b. The intercepts of **NPC-3-900** and **NPC-3-750** at the real axis are 60Ω and 90Ω, respectively. These results demonstrate that **NPC-3-900** has a higher electrical conductivity than **NPC-3-750** which is a consequence of a better crystallization for the carbon pyrolyzed at higher temperature.

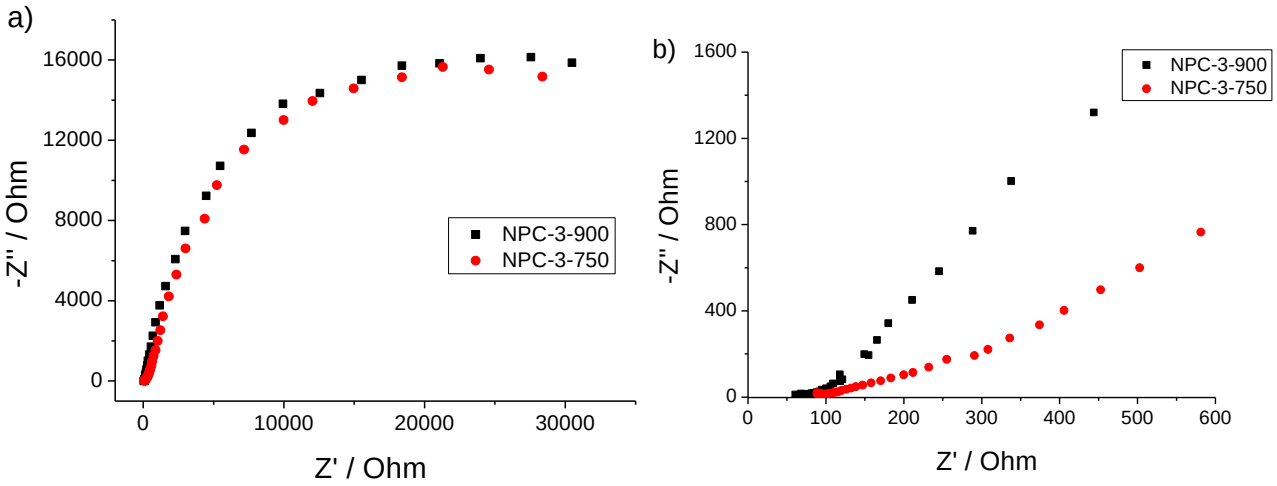

Figure 5.25 a) The EI spectra (Nyquist plots) of **NPC-3-750** and **NPC-3-900**, the frequency range of 0.01Hz-100kHz; b) Magnification of the EI spectra of **NPC-3-750** and **NPC-3-900** in oxygen-saturated 0.1M KOH solution at high frequency.

In order to investigate the effect of pyrolysis temperature on the electrocatalytic activity, rotating disk NMGCAs/GC (**NPC-3-900/GC** or **NPC-3-750/GC**) electrodes were prepared by loading of **NPC-3-900** or **NPC-3-750** on glassy carbon as described in chapter 5.2.3, respectively.

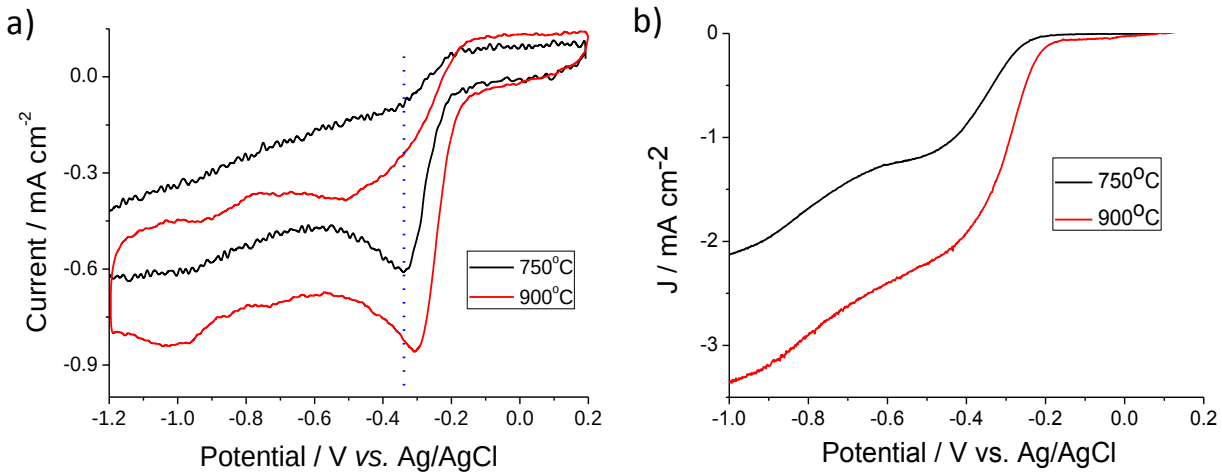

Figure 5.26 (a) The cyclic voltamogramms and (b) LSV curves of **NPC-3-750/GC** and **NPC-3-900/GC**.

It can be seen from the cyclic voltamogramms of **NPC-3-900/GC** and **NPC-3-750/GC** (Figure 5.26a) that the onset potential of **NPC-3-900/GC** in ORR is 0.27 eV, 0.08 eV more positive than that of **NPC-3-750/GC**. The current density of **NPC-3-900/GC** observed in LSV curves (Figure 5.26b) is also higher than that of **NPC-3-900/GC**, indicating a better electrocatalytic performance of **NPC-3-900/GC**. Moreover, LSV curve of **NPC-3-750/GC** reveals a distinct pre-plateau at the potential of ca. -0.47 V, which implies the tendency of two-electron reduction pathway accompanied by the formation of H_2O_2.

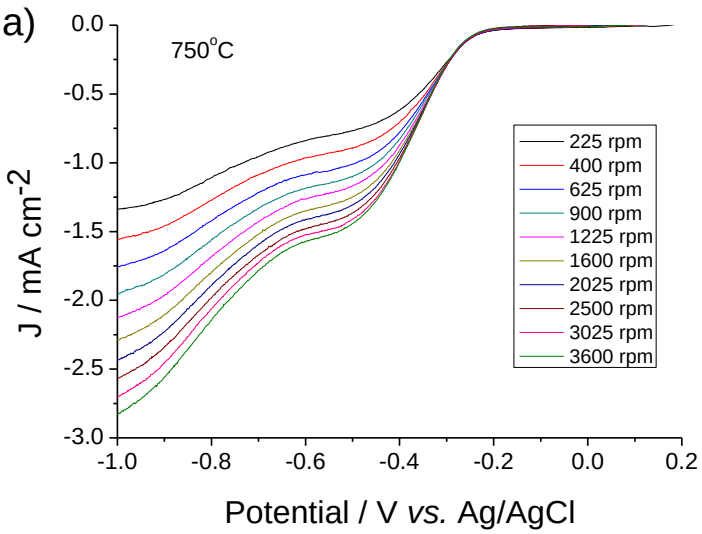

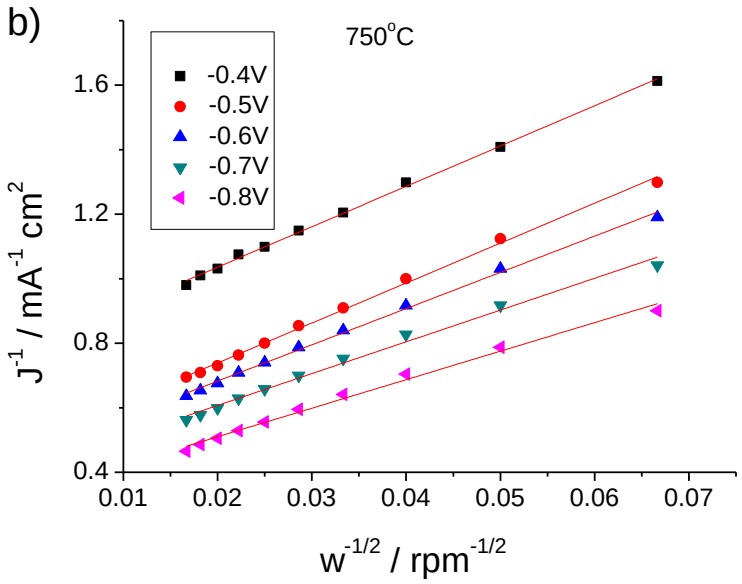

Figure 5.27 (a) Rotating-disk voltammograms recorded at different rotation speeds and (b) Koutecky-Levich plots of **NPC-3-750/GC** at the potential sweep rate of 10 mV/s. 0.1M KOH solution saturated by oxygen is used as electrolyte.

Figure 5.27 shows rotating-disk voltammogram curves of **NPC-3-750/GC** measured at different rotating speeds and the corresponding Koutecky-Levich plots. According to equations (1) and (2) described in chapter 5.3.1, the number of electrons transferred (*n*) and J_K can be obtained from the slope and intercept of Koutecky–Levich plots in Figure 5.27b, respectively.[21] The comparisons of *n* and J_K of **NPC-3-750/GC** and **NPC-3-900/GC** in ORR are illustrated in Figure 5.28a and 5.28b respectively. With the decrease of the reduction potentials, **NPC-3-750/GC** shows an increase of the electron transfer number from 2.2 to 3.2 and of J_K from 1.7 to 3.0, which suggests a combined two-electron and four-electron transfer kinetics in which 2e pathway plays a major role. In terms of both n and J_k values, **NPC-3-900/GC** shows better electrocatalytic ability than **NPC-3-750/GC**. These results evidently demonstrate that higher pyrolysis temperatures lead to a clear enhancement of the electron-transfer kinetics of NMGCAs for oxygen reduction as cathode for ORR in fuel cell.

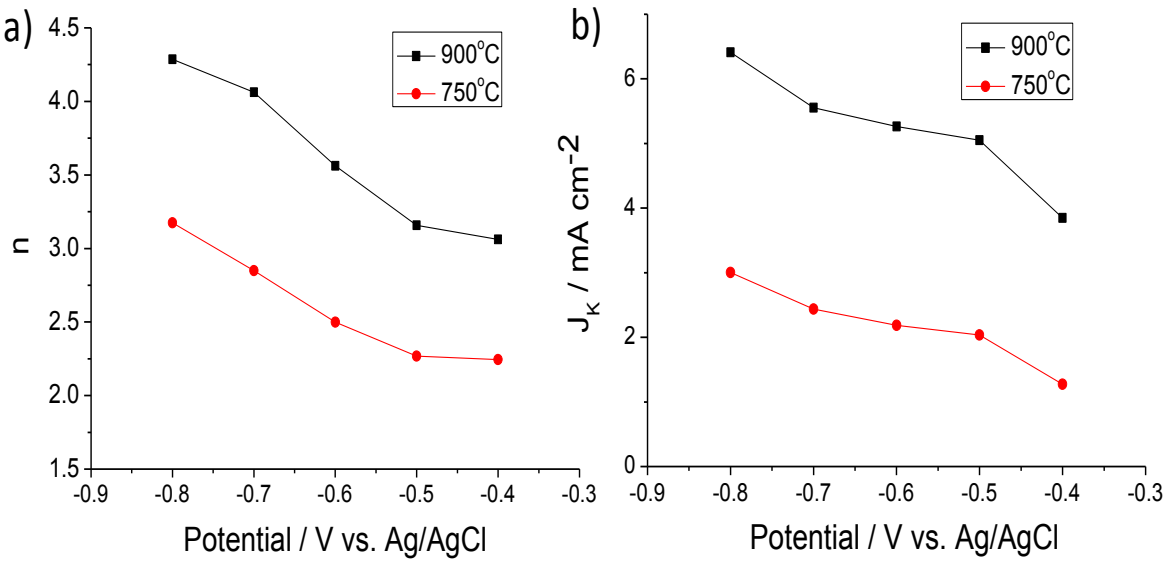

Figure 5.28 (a) The electron transfer numbers and (b) current density (J_k) of **NPC-3-900/GC** and **NPC-3-750/GC** for oxygen reduction reaction at different reductive potentials.

As previously illustrated, the structures of **NPC-3-900** to **NPC-3-750** at different pyrolysis temperatures are the replica of SBA-15 which has almost identical mesostructures. On the other hand, although **NPC-3-900/GC** has a higher content of graphite-N than **NPC-3-750/GC**, the total N content of **NPC-3-750/GC** is actually higher than that of **NPC-3-900/GC**. Therefore, one is not able to draw a clear conclusion from the better selectivity and catalytic activity of **NPC-3-900/GC** on whether the graphitic nitrogen or the pyridinic nitrogen determine the electrochemical performance of NMGCAs in ORR. On the other hand, **NPC-3-900/GC** shows a better graphitic degree and higher electron conductivity than **NPC-3-750/GC**. Therefore, the significantly enhanced activity of **NPC-3-900/GC** must be attributed to the better graphitization of **NPC-3-900** at a higher pyrolysis temperature. In other words, a higher pyrolysis temperature, as a condition for better graphitization, increases the conductivity of cathodes, and thus improves the electrochemical performance of NMGCAs in ORR.

5.3.3 The influence of the precursors on the electrocatalytic activity of NMGCAs

By varying the pyrolysis temperature, it has been found that both graphitic degree and local structures of nitrogen in graphitic network have great effects on the electrocatalytic activity of NMGCAs for ORR.

Besides the pyrolysis temperature the nature of precursors also plays a very important role in controlling the local structure and the electrocatalytic activity of NMGCAs for ORR as discussed in chapter 1.2 and 5.1. By carefully introducing quaternary ammonium cations into polyaromatic molecules, it has been proved that the thermal stability of precursor and the consequential nitrogen content of NMGCAs were greatly enhanced. Furthermore, we have investigated the structure relation between NMGCAs and precursors by carefully evaluating the nitrogen content and local structure of nitrogen in NMGCAs versus various precursors, namely **NPC-1**, **NPC-2** and **NPC-3**, in attempts to build up a fabrication route that is able to tune the electrocatalytic activity of N-doped carbons in ORR via rational design of precursors.

As previously mentioned, the molar ratios N/C of **NPC** are comparable with the ratio of phenanthroline. On the other hand as soon as this aromatic molecule was converted into its quaternary ammonium salts, the thermal stability was supposed to be dramatically enhanced. To illustrate this assumption, TGA measurement of phenanthroline, **NPC-1**, **NPC-2** and **NPC-3** was carried out with elevating temperature from 150 ^{o}C to 900 ^{o}C (10 ^{o}C/min) under Argon.

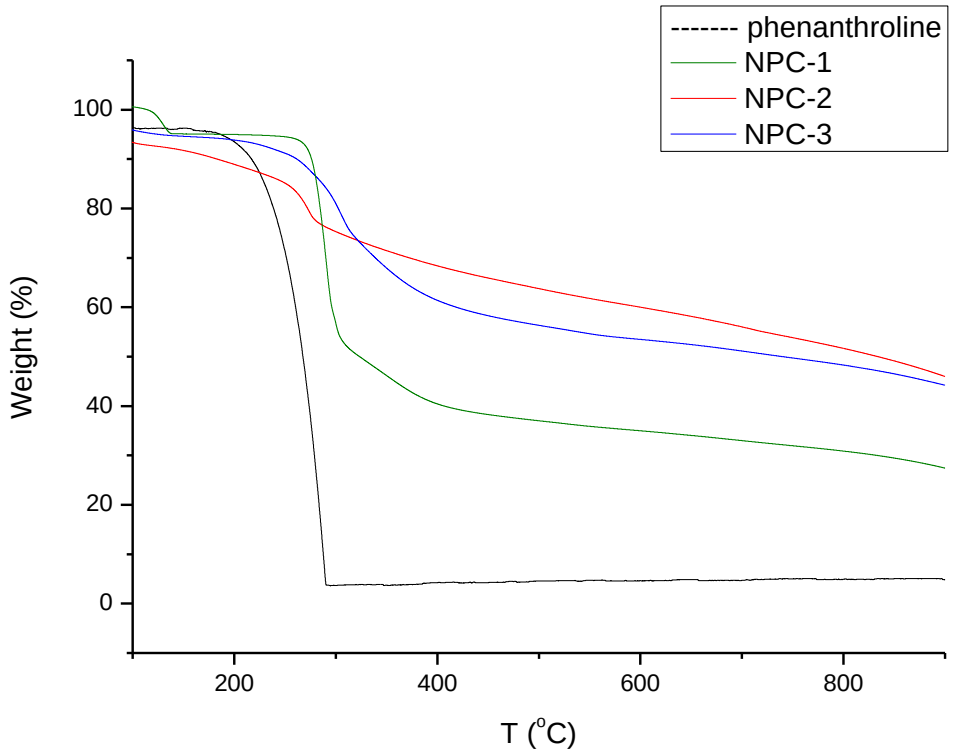

Figure 5.29 TGA measurement of phenanthroline **NPC-1**, **NPC-2** and **NPC-3**

As illustrated in Figure 5.29, two different thermal decomposition steps are observed for **NPC-1**, **NPC-2** and **NPC-3**. The first step lies around 300 ^{o}C, which is 50 ^{o}C higher than that of phenanthroline. This exhibits a better thermal stability of **NPC-1**, **NPC-2** and **NPC-3** than phenanthroline. The second step is from 400 to 900 ^{o}C after which the weight loss of **NPC-1**, **NPC-2** and **NPC-3** is 54 %, 62 % and 56 % respectively. At this stage **NPC-1** and **NPC-3** demonstrate a similar slope (or rate of weight loss against temperature increase), and a smaller slope compared to **NPC-2**. These results indicate that **NPC-1** and **NPC-3** have better thermal stability than **NPC-2**.

To better understand how the structures of NPC precursors affect the structure and electrocatalytic properties of NMGCAs, the methanol solutions of **NPC-1**, **NPC-2** and **NPC-3** were casted into the SBA-15 template, respectively, and pyrolyzed at 900 ^{o}C under argon as described in chapter 5.2.2. The structures of resulting NMGCAs (**NPC-1-900**,

NPC-2-900 and **NPC-3-900**) were examined by WAXS, Raman spectroscopy, elemental analysis, XPS and resistance measurement.

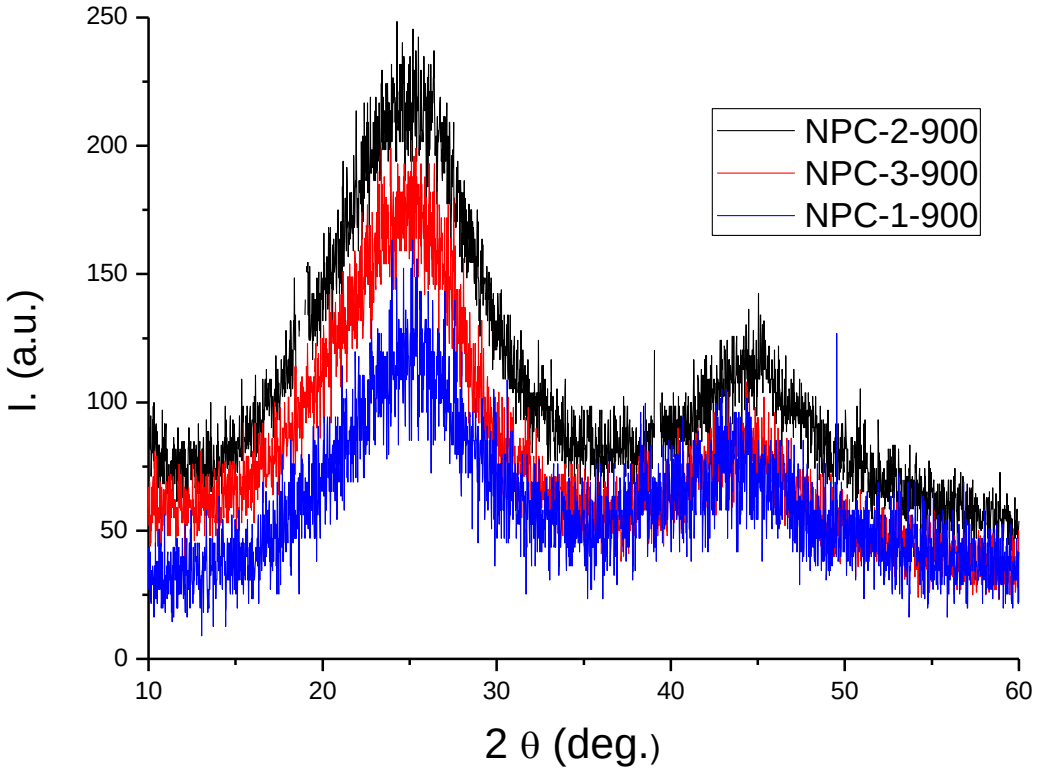

Figure 5.30 WAXS of **NPC-1-900**, **NPC-2-900** and **NPC-3-900**

No obvious difference can be identified in the XRD patterns of **NPC-1-900**, **NPC-2-900** and **NPC-3-900** shown in Figure 5.30. All three samples exhibit pronounced peaks at 25.2 ^{o} for graphitic stacking, and at 44.5 ^{o} for a higher degree of intralayer condensation. Only the full width of the peaks of **NPC-1-900** is a bit broader than those of **NPC-2-900** and **NPC-3-900**. These results suggest a similar crystallite structure of carbon matrices of **NPC-2-900** and **NPC-3-900**, and a slightly lower graphitization degree of **NPC-1-900**.

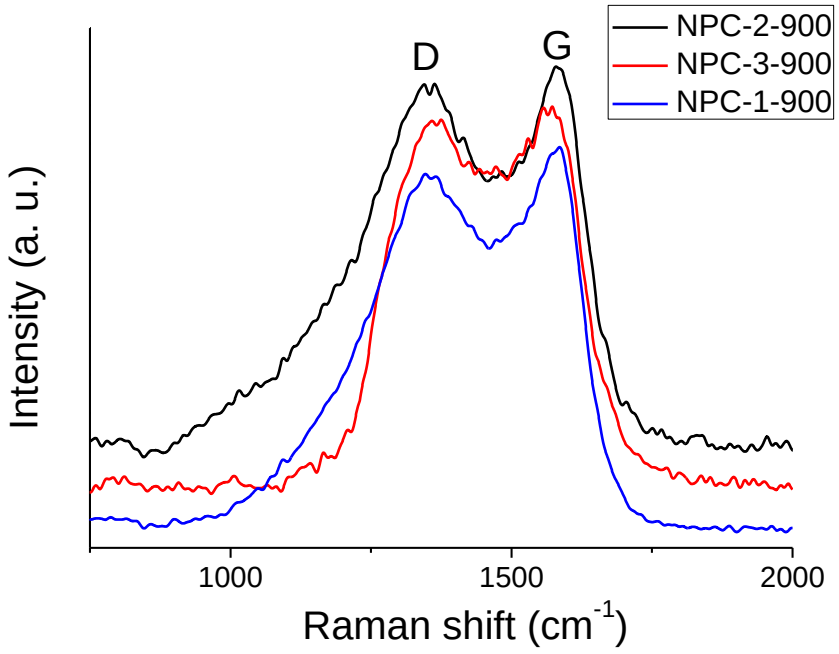

Figure 5.31 Raman spectra of **NPC-1-900**, **NPC-2-900** and **NPC-3-900**

A similar conclusion can be confirmed by Raman spectra of **NPC-1-900**, **NPC-2-900** and **NPC-3-900** illustrated in Figure 5.31. To clarify the reason why **NPC-1-900** has a lower graphitization degree, we compare carefully the precursor structures of **NPC-1**, **NPC-2** and **NPC**-3. As a result, **NPC-2** and **NPC-3** have a similar aromatic core as phenanthroline which is larger than bipyridinic core of **NPC-1**. Even though **NPC-2** is not fully aromatized as **NPC-1**, a larger aromatic core and a higher C/N ratio of **NPC-2** than those of **NPC-1** may enable a better crystallization of carbon of **NPC-2-900**. Therefore, it is reasonable to assume that a large aromatic core of the N-containing precursor will improve the graphitization of NMGCAs.

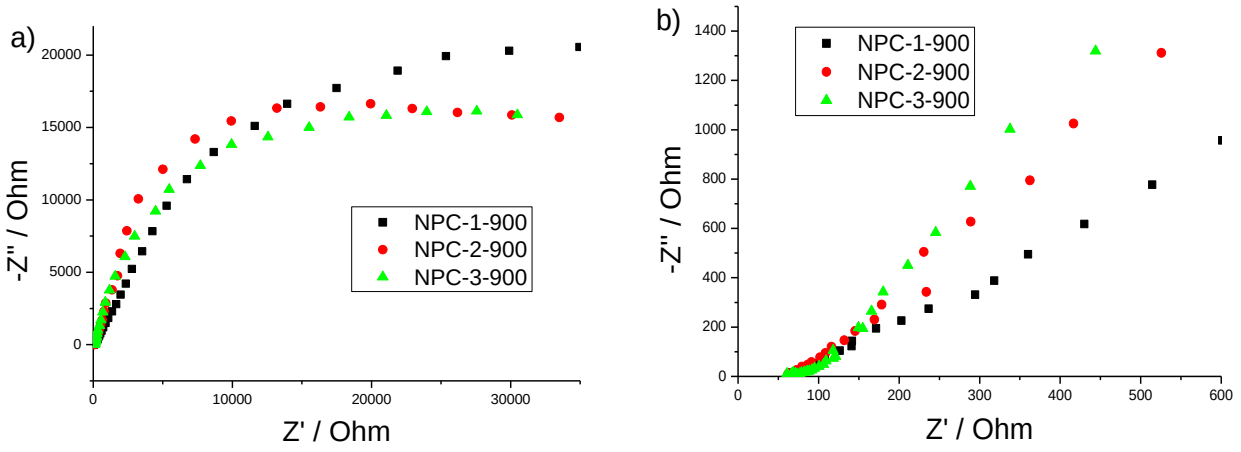

Figure 5.32 a) The EI spectra (Nyquist plots) of **NPC-1-900**, **NPC-2-900** and **NPC-3-900** in the frequency range of 0.01Hz-100kHz and (b) the magnification at high frequency.

To further characterize the graphitic structures of the three NMGCAs, their electrical conductivity was evaluated via electrochemical impedance spectra (Figure 5.32). All three samples show a similar conductivity around 60 Ω, where **NPC-1-900** has a little higher resistance (~66 Ω compared to 61 Ω and 60 Ω of **NPC-2-900** and **NPC-3-900** respectively). This again demonstrates a similar graphitic structure of **NPC-2-900** and **NPC-3-900** and a slightly lower graphitic degree of **NPC-1-900**. Nevertheless, it should be noticed that the difference of the resistance of **NPC-1-900**, **NPC-2-900** and **NPC-3-900** is not as distinctive as that of **NPC-3-750** and **NPC-3-900**, suggesting that pyrolysis temperature has a stronger impact on graphitization and conductivity for synthesizing NMGCAs compared to the molecular size of precursors.

Not only graphitization degree of NMGCAs, but the amount of nitrogen in the carbon host and the local structure of nitrogen atoms are crucial for the ORR catalytic activity of nitrogen-doped carbon materials. For this reason, elemental analysis and N1 XPS of **NPC-1-900**, **NPC-2-900** and **NPC-3-900** were also carried out to measure the N content and the type of N in these NMGCAs.

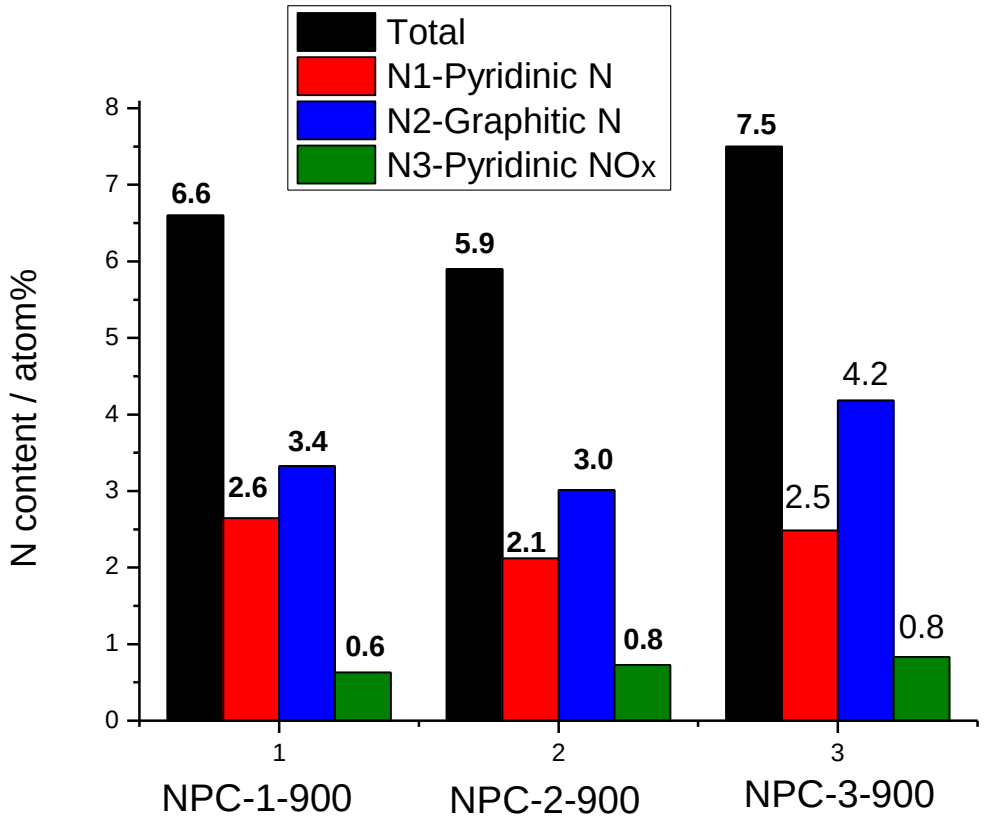

Figure 5.33 Nitrogen content of **NPC-1-900**, **NPC-2-900** and **NPC-3-900**

Based on the elemental analysis and N1s XPS spectra, the total N content after pyrolysis was determined to be 6.6 %, 5.9 % and 7.5 % for **NPC-1-900**, **NPC-2-900** and **NPC-3-900**, respectively (Figure 5.33). In contrast to graphitic degree of NMGCAs, **NPC-2-900** has the lowest N content, while **NPC-3-900** contains more nitrogen than the remaining two. The higher N content of **NPC-1-900** and **NPC-3-900** could be attributed to their pure aromatic structure where nitrogen atoms are embedded in the aromatic core. When compared to **NPC-2-900**, the higher N content of **NPC-1-900** indicates the assumption that an aromatic local structure of nitrogen atoms in precursor the molecules is more important for stabilizing nitrogen during thermal treatment than the size of aromatic molecules.

Figure 5.34 shows the high resolution XPS spectra of N1s of **NPC-1-900** and **NPC-2-900** (N1s XPS of **NPC-3-900** is given in Figure 5.24b). After deconvolution and integration of the

N1s peaks, the ratio between graphitic N (N2) and pyridinic N (N1) is 1.26 : 1, 1.42 : 1 and 1.69: 1 for **NPC-1-900**, **NPC-2-900** and **NPC-3-900**, respectively. It is noticeable that **NPC-3-900** contains more graphitic-N than **NPC-1-900** and **NPC-2-900**, while **NPC-1-900** has the highest content of pyridinic N compared to the others.

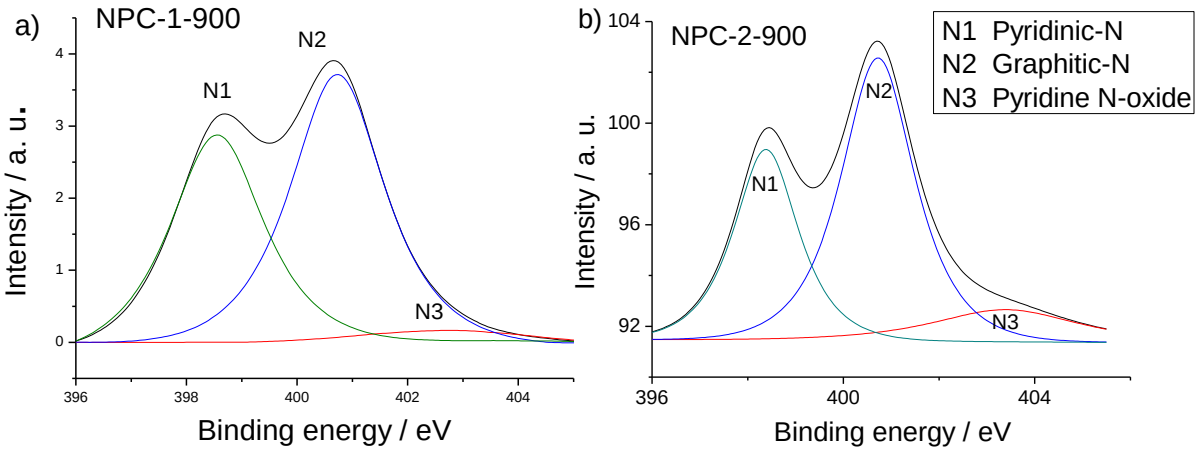

Figure 5.34 N1s XPS and the deconvolution of **NPC-1-900** and **NPC-2-900**.

Based on the structure elucidation, it is appropriate to measure the electrocatalytic activity of the cathodes based on **NPC-1-900**, **NPC-2-900** and **NPC-3-900**, in order to investigate which type of nitrogen of NMGCAs is the key active species for a better performance of ORR in fuel cell. For this purpose, rotating disk NMGCAs/GC electrodes were prepared by loading of **NPC-1-900**, **NPC-2-900** or **NPC-3-900** on glassy carbon respectively.

Consequently, Figure 5.35 shows the CV and LSV curves of the glassy carbon electrodes **NPC-1-900/GC**, **NPC-2-900/GC** and **NPC-3-900/GC**. It can be found in CV curves that the onset potential of **NPC-1-900/GC**, **NPC-2-900/GC** and **NPC-3-900/GC** is -0.30, -0.33 and -0.27 V respectively. Moreover, the current density of **NPC-1-900/GC** and **NPC-3-900/GC** is similar, while **NPC-2-900/GC** exhibits the worst catalytic activity. Its pre-plateau in the LSV curves obviously indicates the formation of H_2O_2 during ORR.

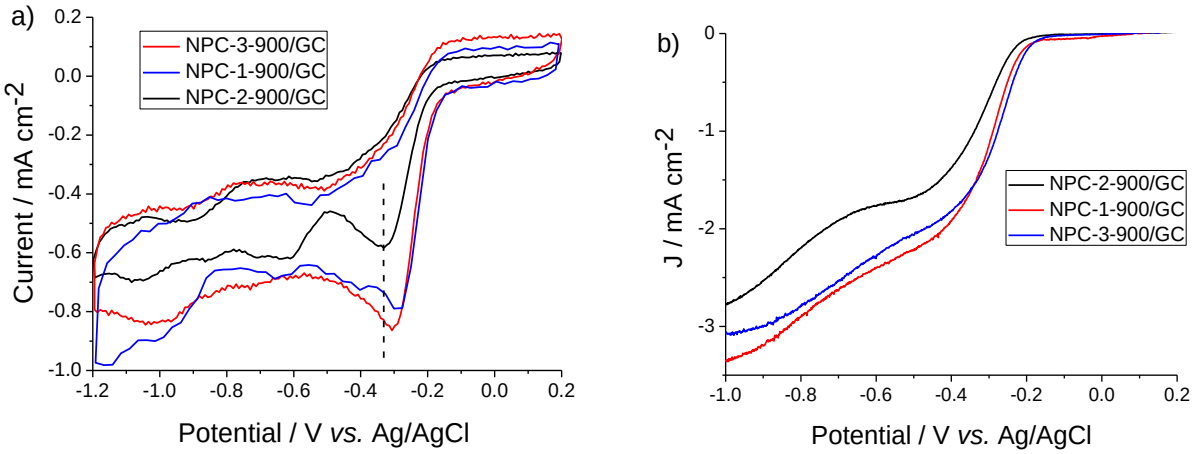

Figure 5.35 (a) The cyclic voltamogramms and (b) Linear scanning voltamogramms curves of **NPC-1-900/GC**, **NPC-2-900/GC** and **NPC-3-900/GC**

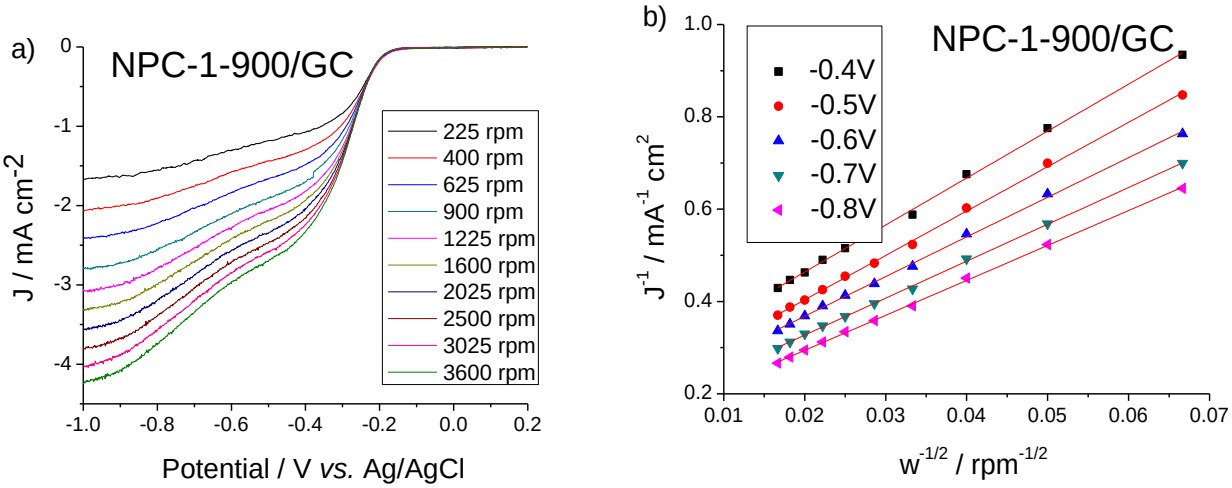

Figure 5.36 (a) Rotating-disk voltammogram curves measured at different rotation speeds and (b) Koutecky-Levich plots of **NPC-1-900/GC** at the potential sweep rate of 10 mV/s. 0.1M KOH solution saturated by oxygen is used as electrolyte.

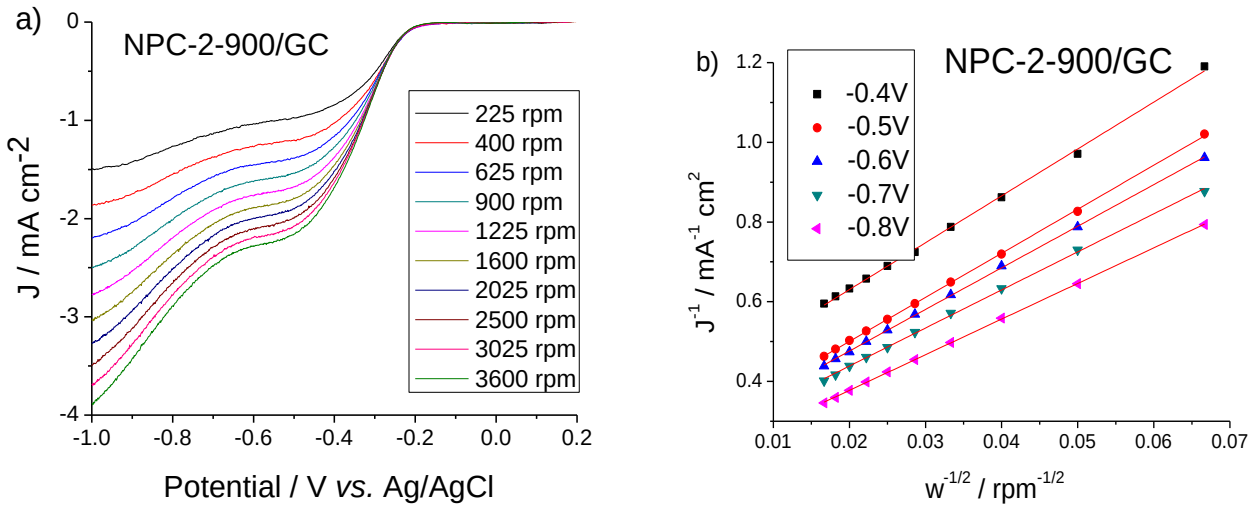

Figure 5.37 (a) Rotating-disk voltammograms measured at different rotation speeds and (b) Koutecky-Levich plots of **NPC-2-900/GC** at the potential sweep rate of 10 mV/s. 0.1M KOH solution saturated by oxygen is used as electrolyte.

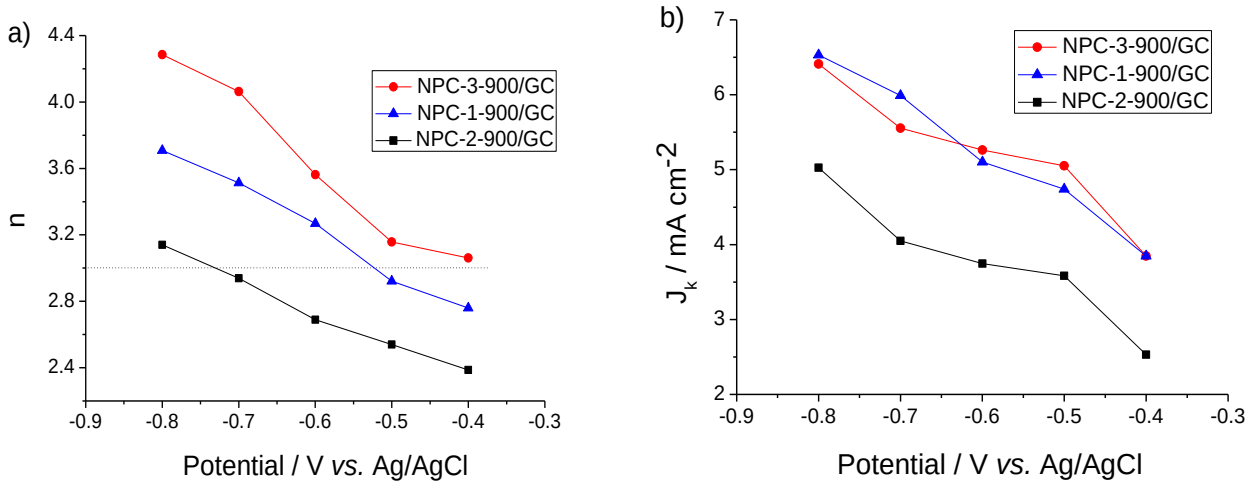

Figure 5.38 (a) The electron transfer numbers and (B) kinetic current density (J_k) of **NPC-1-900/GC**, **NPC-2-900/GC** and **NPC-3-900/GC** for ORR at different potentials.

The rotating-disk voltammograms of **NPC-1-900/GC**, **NPC-2-900/GC** and **NPC-3-900/GC** measured at different rotating speeds are illustrated in Figure 5.36a, Figure

5.37a and Figure 5.15a respectively. The corresponding Koutecky-Levich plots (J^{-1} versus $w^{-1/2}$) are shown in Figure 5.36b, Figure 5.37b and Figure 5.16a, which are extracted from the current density at different rotating speed and potentials in rotating-disk voltammograms. The kinetic parameters (number of electron transfer and kinetic current density) were calculated on the basis of the Koutecky–Levich equations, and summarized in Figure 5.38. First of all, with an increasing reduction potential, all three NMGCAs/GC cathodes exhibit a better ORR performance in term of the electron transfer numbers and current density. Moreover, it is evident that **NPC-1-900/GC** and **NPC-3-900/GC** exhibit higher electron transfer numbers as well as current densities than **NPC-2-900/GC** at all reduction potential. At potential of -0.6 V, the electron transfer number of **NPC-1-900/GC**, **NPC-2-900/GC** and **NPC-3-900/GC** are 3.3, 2.7 and 3.6 respectively. This means that all three NMGCAs/GC illustrate a hybridized oxygen reduction pathway which involves four-electron transfer and two-electron transfer kinetics. Yet **NPC-1-900/GC** and **NPC-3-900/GC** is more prone to four-electron transfer pathway, as **NPC-2-900/GC** mainly goes through a two-electron transfer pathway. As a consequence, **NPC-3-900/GC** presents the best electrocatalytic activity as ORR cathodes, while **NPC-1-900/GC** is proved to be more active than **NPC-2-900/GC**. Similar conclusions can be drawn when we compare their current density. As illustrated in Figure 5.37b, **NPC-1-900/GC** and **NPC-3-900/GC** always exhibit far better current density than **NPC-2-900/GC** at all reduction potentials. To sum up, **NPC-3-900/GC** is the most active electrocatalytic cathodes of all, while **NPC-2-900/GC** shows the lowest oxygen reduction activity compared to the others.

As we have elucidated, **NPC-2-900/GC** and **NPC-3-900/GC** exhibit similar graphitization degree and conductivity, whereas **NPC-1-900/GC**, due to its smaller precursor size, have a slightly lower conductivity. From the discoveries of chapter 5.3.2 we have learned that a higher conductivity of NMGCAs/GC electrodes leads to a better electrocatalytic activity for ORR. However, since the conductivity of **NPC-1-900**, **NPC-2-900** and **NPC-3-900** are quite similar, it must be the nitrogen content and the local structure of nitrogen but not the conductivity or graphitization degree that account for the better

activity of **NPC-1-900/GC** and **NPC-3-900/GC**. Furthermore, as measured by elemental analysis and N1s XPS, the sequence of the total nitrogen content and the content of graphitic nitrogen is **NPC-3-900** > **NPC-1-900** > **NPC-2-900**, and the sequence of the amount of pyridinic nitrogen is **NPC-1-900** > **NPC-3-900** > **NPC-2-900**. Because **NPC-3-900/GC** shows the best ORR performance among all the three NMGCAs/GC, and better than **NPC-1-900**, it can be confirmed that it is the graphitic nitrogen, rather than pyridinic nitrogen, which is likely the key active species of NMGCAs to reduce oxygen in fuel cell. In addition, if we compare the molecular structure of precursor **NPC-1**, **NPC-2** and **NPC-3**, it can be found that the nitrogen atoms of **NPC-1** and **NPC-3** are embedded in a fully aromatic core as graphitic nitrogen. So for a defined precursor design, it is reasonable to conclude that a nitrogen containing precursor molecule, given that it is thermally stable, should contain more graphitic nitrogen in its aromatic core which generates more graphitic nitrogen after thermal pyrolysis. By this way, the performance of such NMGCAs/GC for ORR can be improved.

On the other hand, a better graphitization and higher conductivity of a NMGCA/GC could also enhance its activity and selectivity for ORR as we learned from chapter 5.2.3. When **NPC-1** was compared to **NPC-2** and **NPC-3**, we found that a smaller aromatic core of precursor molecules has led to a lower graphitization degree. This suggests that a larger aromatic structure is another critical qualification for precursor design, besides a higher content of graphitic N, to generate NMGCAs/GC with a higher conductivity and to further increase the electrocatalytic performance for ORR.

In conclusion, by comparing the structure of 1,10-phenanthroline, **NPC-1, NPC-2** and **NPC-3** and the electrocatalytic activity of the resulting in oxygen reduction reaction **NPC-1-900/GC**, **NPC-2-900/GC** and **NPC-3-900/GC**, three criteria of molecular design have been revealed for producing highly active NMGCAs cathode materials for ORR via precursor defined thermolysis: *i*) the polyaromatic molecules must contain as much graphitic nitrogen as possible to increase the final graphitic N content after pyrolysis; *ii*) a

reasonably large aromatic core is necessary to enable high graphitization and conductivity; *iii*) the nitrogen embedded in the aromatic core should be present as quaternary ammonium salt to increase the local stability during heat treatment.

5.4 Conclusion

In this chapter, we have demonstrated the fabrication of novel nitrogen-doped ordered mesoporous graphitic carbon arrays (NMGCAs) by a simple, cost-effective, and readily reproducible approach. This approach involves a metal-free nanocasting technology based on a series of N-containing polyaromatic cations as precursors and ordered mesoporous silica SBA-15 as template. The resulting nitrogen-doped carbon materials serve as true metal-free catalysts that exhibit good electrocatalytic activity for ORR (electron transfer number is 3.6 with J_k of 5.3 mA cm^{-2}).

More importantly, we have compared the electrocatalytic performance of NMGCA electrodes produced via different casting procedures, at various pyrolysis temperatures and from different precursors to investigate how these parameters influence the final catalytic activity. As a result, the mesoporous structure of NMGCAs has been proved to be critical for improving the catalytic activity, since it ensures large surface area and good accessibility of active sites. Moreover, we found that a higher pyrolysis temperature leads to a better graphitization and higher conductivity of NMGCA electrodes, which could help to further increase the electrocatalytic property for ORR. Last but not least, the structures of precursor molecules also play a very important role to control the nanostructure of NMGCAs and their catalytic performance. First of all, the polyaromatic molecules, as structure defined precursors, must contain as much nitrogens as possible to increase the final graphitic N content in NMGCAs after pyrolysis, because the graphitic N of NMGCA electrode catalyzes the oxygen reduction. Secondly, such polyaromatic molecules must have a large aromatic core which is necessary for high graphitization and conductivity after

pyrolysis. And, of course, the nitrogen embedded in the aromatic core is better to be quaternary ammonium salt that increases the local thermal stability during heat treatment. These are the three principles to design nitrogen containing polyaromatic cations for precursor defined pyrolysis to produce N-doped mesoporous graphitic carbon arrays as high performance cathode materials for oxygen reduction reaction in fuel cell.

Reference:

(1) Gong, K. P.; Du, F.; Xia, Z. H.; Durstock, M.; Dai, L. M. *Science* **2009**, *323*, 760.

(2) Jaouen, F.; Herranz, J.; Lefevre, M.; Dodelet, J. P.; Kramm, U. I.; Herrmann, I.; Bogdanoff, P.; Maruyama, J.; Nagaoka, T.; Garsuch, A.; Dahn, J. R.; Olson, T.; Pylypenko, S.; Atanassov, P.; Ustinov, E. A. *Acs Applied Materials & Interfaces* **2009**, *1*, 1623.

(3) Matter, P. H.; Ozkan, U. S. *Catalysis Letters* **2006**, *109*, 115.

(4) Ozaki, J.; Anahara, T.; Kimura, N.; Oya, A. *Carbon* **2006**, *44*, 3358.

(5) Nallathambi, V.; Lee, J. W.; Kumaraguru, S. P.; Wu, G.; Popov, B. N. *Journal of Power Sources* **2008**, *183*, 34.

(6) Cote, R.; Lalande, G.; Guay, D.; Dodelet, J. P.; Denes, G. *Journal of the Electrochemical Society* **1998**, *145*, 2411.

(7) Zhang, L.; Lee, K.; Bezerra, C. W. B.; Zhang, J. L.; Zhang, J. J. *Electrochimica Acta* **2009**, *54*, 6631.

(8) Su, D. S.; Zhang, J.; Frank, B.; Thomas, A.; Wang, X. C.; Paraknowitsch, J.; Schlogl, R. *Chemsuschem* **2010**, *3*, 169.

(9) Tang, Y.; Allen, B. L.; Kauffman, D. R.; Star, A. *Journal of the American Chemical Society* **2009**, *131*, 13200.

(10) Zhu, C.; Higgins, D.; Haisheng, T.; Hsu, R. S.; Zhongwei, C. *Journal of Physical Chemistry C* **2009**, 21008.

(11) Maldonado, S.; Stevenson, K. J. *Journal of Physical Chemistry B* **2005**, *109*, 4707.

(12) Lefevre, M.; Proietti, E.; Jaouen, F.; Dodelet, J. P. *Science* **2009**, *324*, 71.

(13) Biddinger, E. J.; von Deak, D.; Ozkan, U. S. *Topics in Catalysis* **2009**, *52*, 1566.

(14) Iwazaki, T.; Obinata, R.; Sugimoto, W.; Takasu, Y. *Electrochemistry Communications* **2009**, *11*, 376.

(15) Niwa, H.; Horiba, K.; Harada, Y.; Oshima, M.; Ikeda, T.; Terakura, K.; Ozaki, J.; Miyata, S. *Journal of Power Sources* **2009**, *187*, 93.

(16) Tang, Y. F.; Allen, B. L.; Kauffman, D. R.; Star, A. *Journal of the American Chemical Society* **2009**, *131*, 13200.

(17) Shao, Y. Y.; Sui, J. H.; Yin, G. P.; Gao, Y. Z. *Applied Catalysis B-Environmental* **2008**, *79*, 89.

(18) Matter, P. H.; Zhang, L.; Ozkan, U. S. *Journal of Catalysis* **2006**, *239*, 83.

(19) Wiesener, K. *Electrochimica Acta* **1986**, *31*, 1073.

(20) Yeager, E. *Electrochimica Acta* **1984**, *29*, 1527.

(21) Liu, R. L.; Wu, D. Q.; Feng, X. L.; Mullen, K. *Angewandte Chemie-International Edition* **2010**, *49*, 2565.

(22) Jaouen, F.; Lefevre, M.; Dodelet, J. P.; Cai, M. *Journal of Physical Chemistry B* **2006**, *110*, 5553.

(23) Shao, Y. Y.; Zhang, S.; Engelhard, M. H.; Li, G. S.; Shao, G. C.; Wang, Y.; Liu, J.; Aksay, I. A.; Lin, Y. H. *Journal of Materials Chemistry* **2010**, *20*, 7491.

(24) Wang, Y.; Shao, Y. Y.; Matson, D. W.; Li, J. H.; Lin, Y. H. *Acs Nano* **2010**, *4*, 1790.

(25) Jafri, R. I.; Rajalakshmi, N.; Ramaprabhu, S. *Journal of Materials Chemistry* **2010**, *20*, 7114.

(26) Qu, L. T.; Liu, Y.; Baek, J. B.; Dai, L. M. *Acs Nano* **2010**, *4*, 1321.

(27) Ozaki, J. I.; Tanifuji, S. I.; Kimura, N.; Furuichi, A.; Oya, A. *Carbon* **2006**, *44*, 1324.

(28) Strelko, V. V.; Kuts, V. S.; Thrower, P. A. *Carbon* **2000**, *38*, 1499.

(29) Strelko, V. V.; Kartel, N. T.; Dukhno, I. N.; Kuts, V. S.; Clarkson, R. B.; Odintsov, B. M. *Surface Science* **2004**, *548*, 281.

(30) Sidik, R. A.; Anderson, A. B.; Subramanian, N. P.; Kumaraguru, S. P.; Popov, B. N. *Journal of Physical Chemistry B* **2006**, *110*, 1787.

(31) Khomenko, V. G.; Barsukov, V. Z.; Katashinskii, A. S. *Electrochimica Acta* **2005**, *50*, 1675.

(32) Zhong, H. X.; Zhang, H. M.; Liu, G.; Liang, Y. M.; Hu, J. W.; Yi, B. L. *Electrochemistry Communications* **2006**, *8*, 707.

(33) Maruyama, J.; Fukui, N.; Kawaguchi, M.; Abe, I. *Journal of Power Sources* **2009**, *194*, 655.

(34) Maiyalagan, T.; Viswanathan, B. *Materials Chemistry and Physics* **2005**, *93*, 291.

(35) Parthasarathy, R. V.; Phani, K. L. N.; Martin, C. L. R. *Advanced Materials* **1995**, *7*, 896.

(36) Jang, J.; Oh, J. H. *Chemical Communications* **2004**, 882.

(37) Vinu, A.; Ariga, K.; Mori, T.; Nakanishi, T.; Hishita, S.; Golberg, D.; Bando, Y. *Advanced Materials* **2005**, *17*, 1648.

(38) Paraknowitsch, J. P.; Zhang, J.; Su, D. S.; Thomas, A.; Antonietti, M. *Advanced Materials* **2010**, *22*, 87.

(39) Yang, W.; Fellinger, T. P.; Antonietti, M. *Journal of the American Chemical Society* **2011**, *133*, 206.

(40) D. R. Linde, C. H. o. C. a. P., 90th ed. (CRC, 2009).

(41) Calder, I. C.; Sasse, W. H. F. *Tetrahedron Letters* **1965**, 1465.

(42) Black, A. L.; Summers, L. A. *Tetrahedron* **1968**, *24*, 6453.

(43) Casiraghi, C.; Pisana, S.; Novoselov, K. S.; Geim, A. K.; Ferrari, A. C. *Applied Physics Letters* **2007**, *91*.

(44) Kudin, K. N.; Ozbas, B.; Schniepp, H. C.; Prud'homme, R. K.; Aksay, I. A.; Car, R. *Nano Letters* **2008**, *8*, 36.

(45) Ferrari, A. C. *Solid State Communications* **2007**, *143*, 47.

(46) Ferrari, A. C.; Meyer, J. C.; Scardaci, V.; Casiraghi, C.; Lazzeri, M.; Mauri, F.; Piscanec, S.; Jiang, D.; Novoselov, K. S.; Roth, S.; Geim, A. K. *Physical Review Letters* **2006**, *97*.

(47) Chen, W.; Chen, S. W. *Angewandte Chemie-International Edition* **2009**, *48*, 4386.

Chapter 6. General Conclusions

This work has explored many unprecedented synthetic approaches towards novel graphene composites and nitrogen containing graphitic materials.

In chapter 2, large aromatic donor/accepter molecules (PyS/PDI) were composited with reduced graphene oxide (ReG) and effectively repaired the defects of ReG via heat treatment. The resulting transparent films exhibited a conductivity higher than 1000 S/cm, and delivered a power converting efficiency (η = 1.12) as good as ITO and pristine graphene in an organic heterojunction solar cell.

In chapter 3, carbon nanotubes (CNTs) were grown directly from a graphene-cobalt complex (**ReG-Co**) via an acetylene-assisted thermolysis. The resulting composite electrode film presented an enhanced mechanical strength (σ = 31.50 MPa, Y = 30.14 GPa) and an increased electrical conductivity (535 S/cm).

Chapter 4 has presented the synthesis of novel N-containing macrocycles (NHMs) based on 1,10-phenanthroline and indole. Their Co complexes were applied as transition metal catalyst for ORR in fuel cells which exhibited only a two-electron kinetic reduction of oxygen. A further pyrolysis at 700 ^{o}C converted the NHM-Co complexes to a MNx/C network, and thus, successfully promoted its ORR to a four-electron kinetic reduction with a comparable current density (4.7 mA/cm^2) with the Pt/C catalyst.

In Chapter 5, nitrogen-doped ordered mesoporous graphitic carbon arrays (NMGCAs) were fabricated based on N-containing polyaromatic cations (NPCs). They exhibited a great ORR catalytic activity (four-electron transfer with a current density of 5.6 mA/cm^2). Moreover, graphitic nitrogen was identified as active nitrogen in NMGCAs for oxygen reduction.

All these results have clearly demonstrated the great potential of graphene based materials and nitrogen containing graphitic carbons as novel electrode materials for new energy devices such as solar cells and fuel cells.

Chapter 7. Synthetic procedures

7.1 Equipments of characterization

UV-vis spectra were measured using a Perkin-Elmer Lambda 9 spectrometer at room temperature. FTIR spectra were recorded using a Nicolet 730 FT-IR spectrometer. The morphology and microstructure of the samples were investigated by SEM (LEO 1530), TEM (Philips EM 420) and HRTEM (Philips Tecnai F20). Raman spectra were performed from 500 to 2000 cm^{-1} using a Raman spectrometer (Bruker, RFs 100/S) employing a 15798.3 nm He–Ne laser beam. Electrical conductivity measurements were conducted on a Jandel microposition probe equipped with a Keithley data acquisition system (2700). Atomic force microscopic (AFM) microscopy was conducted on a Veeco **Dimension 3100** AFM operated in tapping mode at room temperature. X-ray diffraction was measured by a Siemens D500 Kristalloflex diffractometer with a graphite-monochromized Cu-Kα X-ray beam. The diffraction patterns were recorded in the 2θ range from 1^{o} to 35^{o} at a wavelength of λ = 0.154 nm. XPS was measured by an ESCALAB MkII (VG instruments), equipped with 150 mm hemispherical analyzer and Twin anode X-ray source for Al-Kα and Mg-kα radiation. The overall resolution was set to 250 meV. The detection angle of the photoelectrons was 45° with respect to the sample surface. Chamber with a base pressure of 10^{-10} mbar Pressure during measurement is better than 10^{-9} mbar.

7.2 Synthesis of graphene/aromatic molecules nanocomposites

Graphite flakes were purchased from Sigma-aldrich. All the chemicals were of analytical reagent grade and received without further purification.

Graphene oxide:

Graphite oxide (GO) was produced from natural graphite flakes (Sigma Aldrich) by a modified Hummer's method.[1] Graphite flake (10 g) was put into a solution of concentrated H_2SO_4 (300 mL) and $NaNO_3$ (7.5 g). KMnO4 (40 g) was slowly added into the reaction mixture over 1 h. The mixture was stirred at room temperature for 3 days. Afterwards, 1 L of H_2O_2 solution (1 % in water) was slowly added into the dark brown paste. Then, the mixture was filtered and washed with Ultrapure Milli-Q (MQ) water. The resulting black cake was re-suspended in MQ water to give a dark brown dispersion, which was subjected to dialysis for 2 weeks to remove residual salts and acids. The dark brown residue was then collected via ultracentrifugation under a rotation speed of 5000 rpm for 30 min. The exfoliation of graphene oxide was then carried out in a mild bath sonication and the unexfoliated bulk graphite was eliminated via further ultracentrifugation under a rotation speed of 3000 rpm for 20 min. The resulting homogeneous golden brown dispersion was tested to be stable at a concentration around 10 mg/ml for several months and ready for reduction without further work-up.

ReG (reduced graphene oxide):

5.0 mL of the resulting homogeneous GO dispersion (0.2 mg/ml) was mixed with 5.0 ml of water, 5.0 µl of hydrazine solution (35 wt% in water, Aldrich) and 35.0 µl of ammonia solution (28 wt% in water, Crown Scientific) in a 20-ml glass tube. After being vigorously shaken or stirred for a few minutes, the vial was kept at 90 °C for 1 h. After the reaction mixture cooled down to room temperature, excess of hydrazine in the resulting dispersions was removed by dialysis against a ~0.5% ammonia solution. The resulting dispersion after filtration through a paste of glass wool was kept stable for max. 3 days.

ReG-PDI/ReG-PyS nanocomposite dispersion:

20 mg (0.020 mmol) of PDI, 20 mg (0.5 mmol) of sodium hydroxide and 125 mL (2.5 mmol) of hydrazine monohydrate (35.5 wt% aqueous solution) were added to 20 mL of GO aqueous dispersion (0.25 mg/ml). After vigorous shaking and a mild bath-sonication for 10 min, the mixture was kept at 90 ^{o}C for 24 h. After cooling down to room temperature, there was no aggregate observed in this carmine dispersion (as shown in Figure 2.3b).

The preparation of a ReG-PyS composite dispersion was same as the procedure to produce ReG-PDI composite dispersion except that sodium pyrene-1-sulfonate was used as dispersant. After keeping reaction mixture at 90 ^{o}C for 24 h, there was no aggregate observed in this blue-black dispersion (as shown in Figure 2.3c). The ReG-PDI and ReG-PyS dispersions with concentration of 0.25 mg/mL ReG in water were kept stable for more than 15 days under ambient condition.

7.3 Synthesis of 1-(dodec-1-ynyl)-graphene and its Cobalt complex

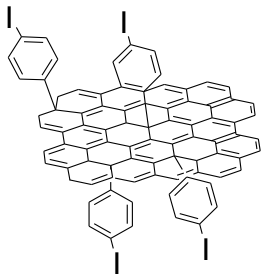

ReG-PhI:

ReG (50 mg) and 4-iodoaniline (4 equiv/mol of carbon) were added to a 25 mL Schlenk flask. The flask was degassed and backfilled with argon three times. The mixture was stirred and heated to 65 °C to allow 4-iodoaniline to completely melt

and mix well with ReG. Subsequently, isoamyl nitrite (4 equiv/mol of carbon) was added slowly via a syringe. The mixture was then stirred vigorously at 60 °C overnight. The resulting paste was diluted with DMF and filtered through a PTFE (200 nm pore diameter) membrane. The collected solid was then dispersed in DMF (100 mL) and sonicated for 20 min, followed by filtration and washing with DMF (100 mL) for 3 times until the filtrate was colorless. The solid was finally washed with acetone (100 mL), and dried in a vacuum oven (70 °C) overnight to afford 46 mg black solid (92 % yield by weight calculated as : Yield = weight of product / weight of starting material, sic passim in Chapter 6.2).

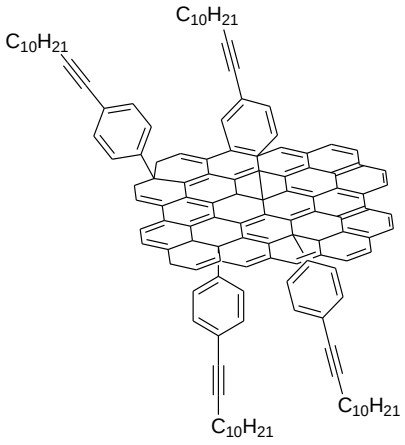

ReG-C_{12}:

ReG-PhI (40 mg) and DMF (10 mL) were added in a 250 mL Schlenck flask charged with condenser. After sonicating for 5 min at room temperature, a black suspension was formed. Then, $Pd(PPh_3)_4$ (38 mg, 0.01 equiv/mol of carbon), CuI (19 mg, 0.03 equiv/mol of carbon) and 1-dodecyne (1.5 mL, 2 equiv/mol of carbon) in THF (50 mL) and triethylamine (20 mL) were added to the reaction mixture. This mixture was then degassed and backfilled with argon three times. The reaction mixture was carried out at 70 °C under argon overnight. After cooling to room temperature, the reaction mixture was diluted with 200 mL THF, sonicated for 5 min, and filtered through a 200 nm PTFE membrane. The product was washed thoroughly

with THF, methanol, water, methanol, and THF (100 mL of each) and then dried under vacuum overnight to afford 36 mg **ReG-C_{12}** as a black solid (90 % yield by weight).

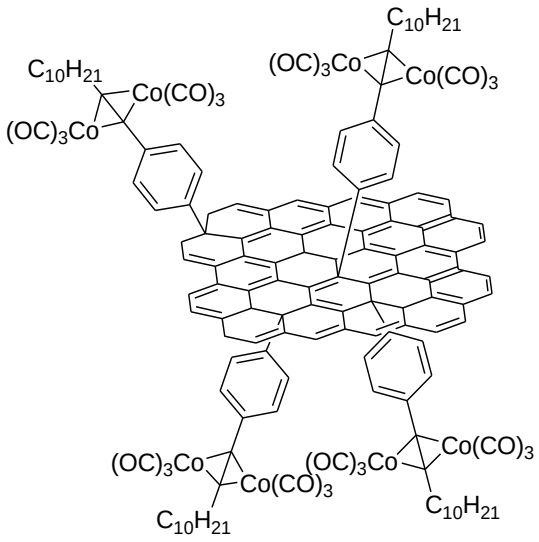

ReG-Co:

ReG-C_{12} (50 mg) and $Co_2(CO)_8$ were dissolved in 50 mL anhydrous THF in an oven-dried Schlenck flask. The solution was stirred at room temperature for 6 h under argon. The resulting solution was filtrated through a 200 nm PTFE membrane. The resulting paste was further washed by THF (100 mL) for three times to give **ReG-Co** as a black free-standing film (48 mg, 95% yield by weight).

7.4 Synthesis of N-containing macrocycles and the metal complexes

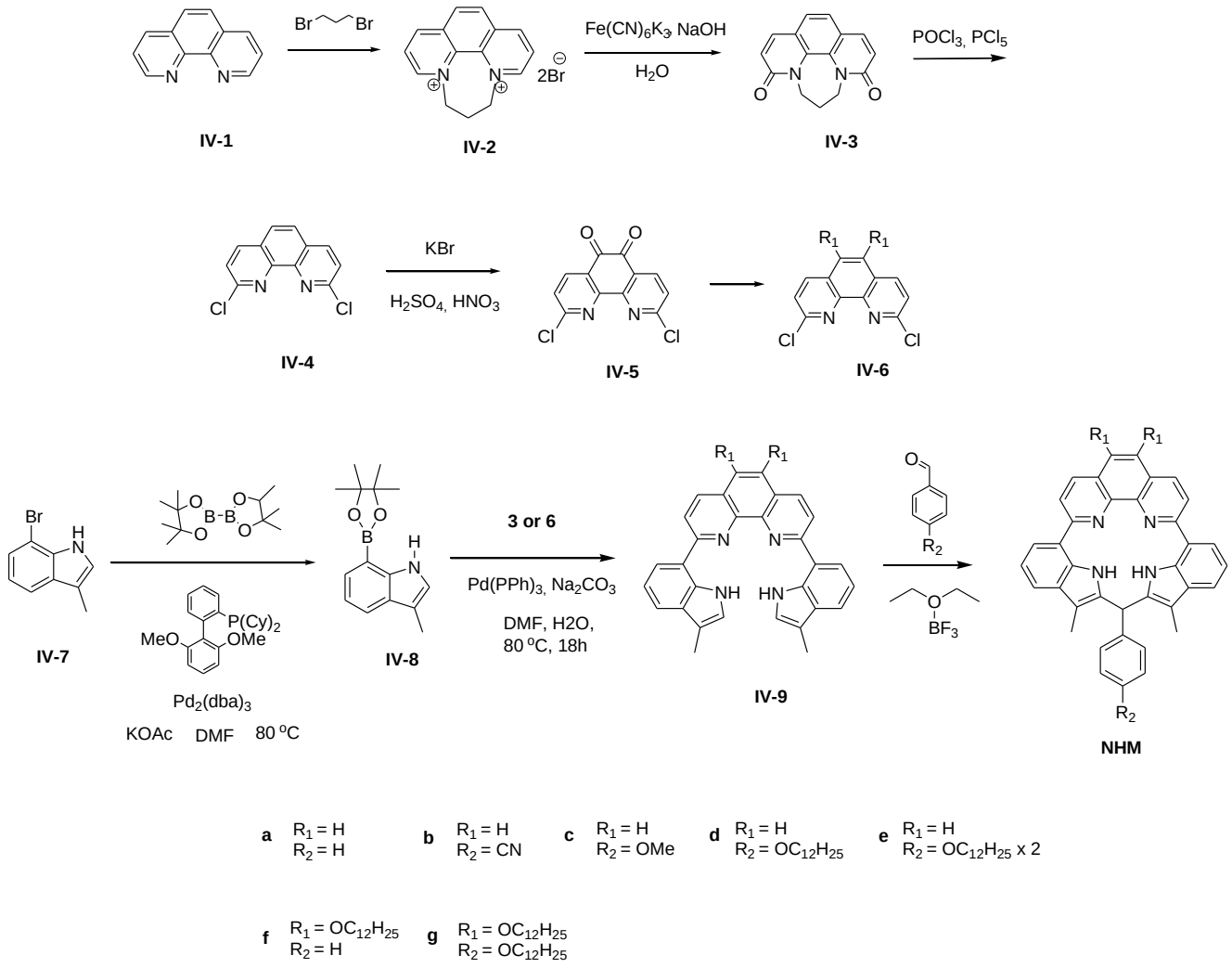

Figure 7.1 Synthetic route of NHM from 1,10-phenanthroline and 3-methyl-7-bromo-indole

The synthesis of **IV-2** ~ **IV-6** was described in the work of Frey *et al.*[2] and **IV-7** was described in the work of Batroli *et al*.[3]

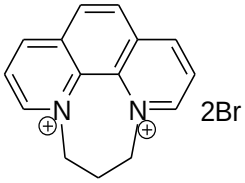

IV-2

6,7-Dihydro-5H-[1,4]Diazepino[1,2,3,4-lmn][1,10]phenanthrolinediium dibromide (IV-2):

Phenanthroline (50 g, 277.46 mmol) was dissolved in bromopropane (140.8 mL 1.387 mol). The mixture was heated up to 120 ^{o}C for overnight. After cooling to room temperature, the yellow precipitate was filterated and washed with dichloromethane. Afterwards, the residue was recrystllized in ethanol/water (v:v=5:1) at 100 ^{o}C. The needle crystal (135 g, 90 % Yield) was washed by ethanol and collected by filtration. [^{1}H NMR (250 MHz, D_2O):=9.75 (d, 2 H), 9.51 (d, 2 H), 8.69 (s, 2 H), 8.55 (dd, 2 H), 5.19 (t, 4 H), 3.47 (q, 2 H).]

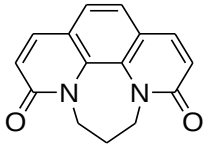

IV-3

6,7-Dihydro-5H-[1,4]Diazepino[1,2,3,4-lmn][1,10]phenanthroline-3,9-dione (IV-3):

To a aqueous solution of [$K_3Fe(CN)_6$] (430.84 g, 1.308 mol) was added sodium hydroxide solution at -10 ^{o}C. Then the aqueous solution of the quaternary ammonia salt was added into the reaction dropwise via a drifting funnel at -20 ^{o}C. The mixture was slowly warmed up to RT and kept overnight. The resulting mixture was neutralized via insulating Con. HCl with simultaneous COOLING!! After the solvent was evaporated, the brown residue was further extracted by Soxhlet extraction with chloroform. The combined organic phase was dried over $NaSO_4$, then adsorbed on silica and subjected to chromatography (elution from CH_2Cl_2 to CH_2Cl_2/2% MeOH) which gave **2** (14.02 g, 40 %). [FD-MS: m/z = 452.6 (calcd. 452.26). ^{1}H NMR (250 MHz, D_2O): δ =7, 57 (d, 2H), 7,13 (s, 2H), 6,54 (d, 2H), 4,03 (t, 4H), 2,38 (m, 2H,)]

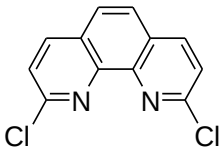

IV-4

2,9-Dichloro-1,10-phenanthroline (IV-4):

Compound **IV-3** (5.00 g, 19.82 mmol) was suspended in $POCl_3$ (60 mL, 654.07 mmol) and PCl_5 (8.26 g, 39.64 mmol) was added. The mixture was degassed and refluxed under argon for 8 h. The excess $POCl_3$ was then distilled off under reduced pressure. The resulting suspension was neutralized with aqueous ammonia solution (30 %) with simultaneous cooling. The brown precipitate was collected and dried under vacuum. The resulting crude product was then purified by chromatography. Elution with CH_2Cl_2 gave **3** (4.48 g, 90 %). [FD-MS: m/z = 250.6 (calcd. 249.095). ^{1}H-NMR (CD_2Cl_2): δ=8.76 (d, 2H), 8.60 (s, 2H), 8.08 (d, 2H)].

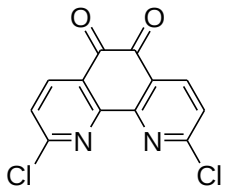

IV-5

2,9-Dichlorophenanthrolin-5,6-dione (IV-5):

Solid KBr (14.35 g, 120.5 mmol) was placed in a two-necked flask equipped with a condenser. The flask was immersed in a large ice/water bath, and then concentrated H_2SO_4 (98 %, 20 mL) was added dropwise with stirring followed by concentrated HNO_3 (68 %, 30 mL). A solution of compound **IV-4** (3.00 g, 12.04 mmol) in concentrated H_2SO_4 (98 %, 30 mL) was added dropwise to the pre-cooled mixture. The resulting mixture was stirred for 20 min at room temperature and then for 3 h at 80 °C. After cooling to RT the reaction mixture was poured into 500 ml of ice/water and stirred for overnight at RT. The yellow-orange precipitate formed was collected and washed with water. Compound **IV-5** was directly used for the next step without further purification.

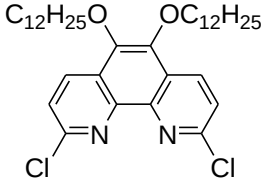

IV-6

2,9-Dichloro-5,6-bis(dodecyloxy)-1,10-phenanthroline (IV-6):

To a mixed solution of H_2O (40 ml) and THF (40 ml) 2,9-dichlorophenanthrolin-5,6-dione (IV-5, 2,0 g, 7.17 mmol), tetrabutylammonium bromide (1.50 g, (4.66 mmol) and $Na_2S_2O_4$ (7.54 g, 43.32 mmol) were added. Then dodecyl bromide (6.0 g, 24.04 mmol) were added to the mixture. A solution of KOH (6.0 g, 108.3 mmol) in 40 ml H_2O was subsequently added slowly. The reaction mixture turned black immediately and was stirred for 2 days at 40°C. After dilution with H_2O the crude compound was extracted with ethyl acetate (3 x 50 ml). The organic phase was washed with H_2O, dried with Na_2SO_4 and evaporated. The crude product was purified by column chromatography (DCM) to yield Compound **IV-6 (**3.0 g, yield 67%). [FD-MS: m/z = 618.6 (calcd. 617.73), ^{1}H-NMR (250 MHz, $CDCl_3$): δ =8.47 (d, 2H), 7.98 (d, 2H), 4.17(t, 4H), 1.79 (q, 4H), 1.19 (m, 32H), 1.51 (t, 6H), ^{13}C-NMR (250 MHz, $CDCl_3$): δ =156.6, 146.34, 137.05, 131.13, 121.30, 119.15, 67.10, 29.25, 26.25, 23.62, 21.12, 13.72 ppm].

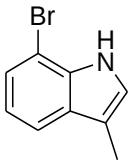

IV-7

7-Bromo-3-methyl-1H-indole (IV-7):[3]

1-Bromo-2-nitrobenzene (1.01g, 5 mmol) was placed in a two-necked round-bottomed flask fitted with a gas inlet (argon) and rubber septum. The flask was purged several times with argon before adding dry THF (35-40 mL) and cooling to between -40 and -45 °C. The Grignard reagent (30 mL, 15 mmol) was then added rapidly in one portion to the THF solution and stirring continued for a further 1 h. Saturated ammonium chloride solution was added to the reaction mixture (at ca. -40 °C) before allowing the mixture to warm to room temperature. The mixture was thoroughly extracted with diethyl ether (2 x200 mL), the ether extracts combined

and thoroughly washed with further ammonium chloride (300 mL), water (300 mL), and brine (300 mL) before drying (MgSO4) and concentrating in vacuo to give a dark brown gum, which was purified by flash column chromatography (hexane/ethyl acetate 9:1) to give a light yellow crystal (500 mg, 47% yield). [FD-MS: m/z = 210.6 (calcd. 210.07), ^{1}H-NMR (250 MHz, $CDCl_3$): δ =10.57 (s, 1H), 7.68 (d, 1H), 7.37(d, 1H), 7.09 (t, 1H), 6.79 (s, 1H), 2.21 (s, 3H), ^{13}C-NMR (250 MHz, $CDCl_3$): δ =135.78, 129.67, 124.43, 122.83, 121.30, 118.15, 11.10, 100.25, 16.25ppm].

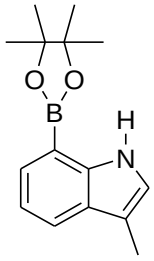

IV-8

3-Methyl-7-(4,4,5,5-tetramethyl-1,3,2-dioxaborolan-2-yl)-1H-indole (IV-8):

An oven-dried 25-mL round bottom flask was charged with 7-bromo-3-methyl-1H-indole (**IV-7,** 100 mg, 0.47 mmol), tris(dibenzylideneacetone)-dipalladium(0) (5 mg, 0.005 mmol), 2-(dicyclo-hexylphosphino)-2',6'-dimethoxy -1,1'-biphenyl (15 mg, 0.04 mmol), bis(pinacolato)diboron (120 mg, 0.47 mmol) and KOAc (94 mg, 0.95 mmol). The flask was capped and then evacuated and backfilled with argon (this was repeated two additional times). DMF was added via syringe, through the septum and the mixture was treated via freeze-pump-thaw for three times. The reaction mixture was heated to 80 °C overnight. After cooling to room temperature, the reaction mixture was diluted by dichloromethane and extracted with water for 3 times. The organic residue was further purified by flash column chromatography (hexane/DCM 2:1) to give a colorless crystal (100 mg, 81% yield). [FD-MS: m/z = 258.1 (calcd. 257.14), ^{1}H-NMR (250 MHz, $CDCl_3$): δ =12.11 (s, 1H), 8.68 (m, 3H), 7.17(s, 1H), 2.51 (s, 3H), 1.45 (s, 12H), ^{13}C-NMR (250 MHz, $CDCl_3$): δ =137.78, 127.21, 122.93, 122.22, 120.30, 119.19, 111.20, 111.05, 83.25, 21.20, 16.05ppm].

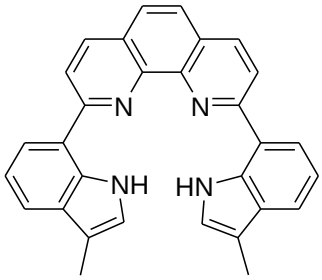

IV-9a

2,9-Bis(3-methyl-1H-indol-7-yl)-1,10-phenanthroline (IV-9a):

2,9-Dichloro-1,10-phenanthroline (**IV-4**, 50 mg, 0.2 mmol) and 3-methyl-7-(4,4,5,5-tetramethyl-1,3,2-dioxaborolan-2-yl)-1H-indole (**IV-8**, 134 mg, 0.521 mmol) were dissolved in 6 mL DMF and mixed with 2 mL of 2M aqueous solution of Na_2CO_3. Then, tetrakis(triphenylphosphine)palladium(0) (11 mg, 0.01 mmol) was rapidly added under a flow of argon, the mixture was degassed via freeze-pump-thaw for 3 times. The mixture was heated at 80 ^{o}C with vigorous stirring overnight. It was then allowed to cool to room temperature and CH_2Cl_2 was added. The organic layer was washed with water and concentrated to dryness. The resulting brown solid was purified by flash chromatography (elution with CH_2Cl_2:PE =1:2) to afford a pale crystal (84 mg, 95%). [Maldi-Tof: m/z = 438.1 (calcd. 438.52), ^{1}H-NMR (250 MHz, CD_2Cl_2): δ = 12.12 (s, 2 H), 8.12(d, 2 H), 7.88 (d, 2 H), 7.72 (s, 2 H), 7.37 (d, 2 H), 7.18 (m, 4 H), 6.83 (s, 2 H), 2.33 (s, 6 H), ^{13}C-NMR (250 MHz, $CDCl_3$): δ =156.41, 147.57, 144.80, 137.60, 128.00, 127.60, 126.20, 122.90, 122.69, 122.20, 119.40, 117.60, 116.70, 111.19, 16.05ppm; Elemental Analysis: Cal.= C, 82.17; H, 5.06; N, 12.78, Found= C, 82.25; H, 5.10; N, 12.65].

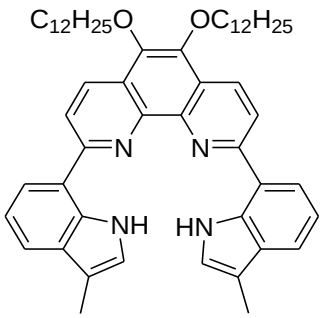

IV-9f

5,6-Bis(dodecyloxy)-2,9-bis(3-methyl-1H-indol-7-yl)-1,10-phenanthroline (IV-9f):

2,9-Dichloro-5,6-bis(dodecyloxy)-1,10-phenanthroline (**IV-6**, 100 mg, 0.16 mmol) and 3-methyl-7-(4,4,5,5- tetramethyl-1,3,2-dioxaborolan-2-yl)-1H-indole (**IV-8**, 500 mg, 1.94 mmol) were dissolved in a mixture of 5 mL DMF and 4 mL toluene, and mixed with 5 mL of 2M aqueous solution of Na_2CO_3. After tetrakis(triphenylphosphine)palladium(0) (43 mg, 0.037 mmol) was rapidly added under a flow of argon, the mixture was degassed via freeze-pump-thaw for 3 times. The mixture was heated at 80 ^{o}C with vigorous stirring overnight. It was then allowed to cool to room temperature and CH_2Cl_2 was added. The organic layer was washed with water and concentrated to dryness. The resulting brown-greenish solid was purified by flash chromatography (elution with CH_2Cl_2) to afford a colorless crystal (55 mg, 91%). [Maldi-Tof: m/z = 808.1 (calcd. 807.16), ^{1}H-NMR (250 MHz, CD_2Cl_2): δ = 11.43 (s, 2 H), 8.37(m, 4 H), 7.73 (d, 2 H), 7.18 (m, 4 H), 6.78 (s, 2 H), 4.03 (m, 4 H), 2.43 (s, 6 H), 1.86 (m, 4 H), 1.36 (m, 36 H), 1.01 (t, 6 H); ^{13}C-NMR (250 MHz, CD_2Cl_2): δ =155.77, 155.57, 149.49, 139.66, 128.66, 127.64, 126.09, 122.85, 122.63, 122.27, 119.43, 117.55, 116.68, 111.19, 69.89, 31.77, 29.65, 29.37, 26.00, 22.77, 16.03, 14.31ppm; Elemental Analysis: Cal.= C, 80.35; H, 8.74; N, 6.94; Found= C, 80.25; H, 8.81; N, 6.85].

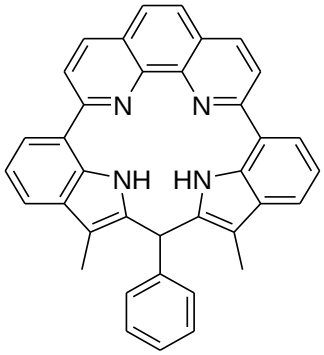

NHM-a

NHM-a:

In a flame-dried 50 mL Schlenk's tube charged with a reflux condenser was added 2,9-bis(3-methyl-1H-indol-7-yl)-1,10-phenanthroline (**IV-9a**, 50 mg, 0.114 mmol) and benzaldehyde (13 mg, 0.125 mmol). After evacuating and backfilling the tube with argon, 10 mL tetrachloroethane (dried over CaH) was insulated followed by adding BF_3-complexed with ethoxyethane (5 eq. 0.07 mL). The reaction was heated up and kept at 128 °C overnight and quenched by adding concentrated NH_4Cl solution. After washed with water the residue was columned via DCM:PE=3:1 to afford colorless solid (43 mg, 72 % yield) [Maldi-Tof mass= 526.7 (calcd. 526.63); ^{1}H NMR (250 MHz, CD_2Cl_2):=11.88 (bs, 2 H), 8.33 (dd, 4 H), 7.82 (t, 4 H), 7.70 (d, 2 H), 7.26 (m, 5 H), 6.90 (d, 2 H), 6.09 (s, 1 H), 2.51 (s, 6 H); ^{13}C-NMR (250 MHz, $CDCl_3$): δ =156.41, 149.47, 144.80, 138.12, 137.60, 135.33, 129.10, 128.71, 127.80, 127.65, 126.10, 125.85, 122.69, 122.20, 119.40, 117.60, 116.70, 107.19, 34.55, 10.73ppm; Elemental Analysis: Cal.= C, 84.38; H, 4.98; N, 10.64; Found= C, 84.22; H, 4.90; N, 10.88].

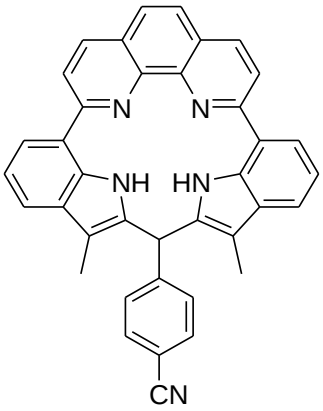

NHM-b

NHM-b:

The reaction procedure was carried out in the same manner with the **NHM-a,** except 4-formylbenzonitrile (16.5 mg, 0.125 mmol) was applied. The crude residue was purified via column chromatography (eluted by DCM:PE=1:1) to afford light yellow crystal (52 mg, 82 % yield) [Maldi-Tof mass= 551.89 (calcd. 551.63); ^{1}H NMR (250 MHz, CD_2Cl_2):=11.94 (s, 2 H), 8.32 (m, 4 H), 7.82 (d, 2 H), 7.69 (s, 2 H), 7.30 (d, 2 H), 7.24 (dd, 4 H), 6.99 (d, 2 H), 6.09 (s, 1 H), 2.51 (s, 6 H); ^{13}C-NMR (250 MHz, $CDCl_3$): δ =156.52, 149.43, 144.77, 142.52, 137.56, 135.53, 132.11, 129.82, 127.85, 127.69, 126.12, 122.63, 122.21, 119.41, 117.62, 116.73, 115.83, 109.19, 107.07, 34.59, 10.77ppm; Elemental Analysis: Cal.= C, 82.74; H, 4.57; N, 12.70; Found= C, 82.72; H, 4.60; N, 12.68].

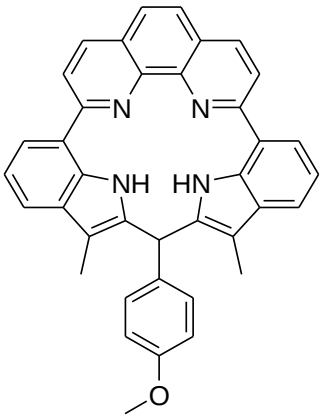

NHM-c

NHM-c:

The reaction procedure was carried out in the same manner with the **NHM-a**, except para-methoxyl-benzaldehyde (17 mg, 0.125 mmol) was applied. The crude residue was purified via column chromatography (eluted by DCM:PE=1:2) to afford light colorless crystal (24 mg, 38 % yield) [Maldi-Tof mass= 557.0 (calcd. 556.63);. ^{1}H NMR (250 MHz, CD_2Cl_2):=11.72 (s, 2 H), 8.36 (dd, 4 H), 7.67 (t, 4 H), 7.40 (d, 2 H), 7.06 (m, 4 H), 6.63 (d, 2 H), 5.94 (s, 1 H), 3.51 (s, 3H). 2.51 (s, 6 H); ^{13}C-NMR (250 MHz, $CDCl_3$): δ =157.70, 156.52, 149.43, 144.77, 137.56, 135.53, 130.55, 130.01, 127.85, 127.69, 126.12, 122.63, 122.21, 119.41, 117.62, 116.73, 114.25, 107.07, 55.96, 34.59, 10.77ppm; Elemental Analysis: Cal.= C, 81.99; H, 5.07; N, 10.06; O, 2.87; Found= C, 82.12; H, 5.20; N, 10.08].

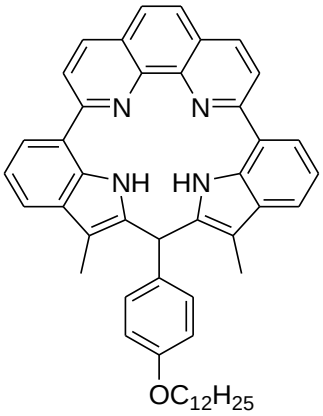

NHM-d

NHM-d:

The reaction procedure was carried out in the same manner with the **NHM-a**, except 4-(dodecyloxy)benzaldehyde (37 mg, 0.125 mmol) was applied. The crude residue was purified via column chromatography (eluted by DCM:PE=1:2) to afford light colorless crystal (44 mg, 54 % yield) [Maldi-Tof mass= 711.1 (calcd. 710.90);. ^{1}H NMR (250 MHz, CD_2Cl_2):=10.92 (s, 2 H), 8.13 (dd, 4 H), 7.67 (s, 2 H), 7.59 (d, 2 H), 7.06 (m, 4 H), 6.70 (d, 2 H), 6.63 (d, 2 H), 5.74 (s, 1 H), 3.98 (t, 2H). 2.51 (s, 6 H), 1.80 (m, 2 H), 1.41 (m, 18 H), 1.01 (t, 3 H); ^{13}C-NMR (250 MHz, $CDCl_3$): δ =156.52, 154.43, 149.47, 144.80, 137.60, 135.57, 129.79, 129.74 127.83, 127.69, 126.18, 122.69, 122.24, 119.40, 117.60, 116.70, 114.21, 107.76, 68.96, 34.59, 31.91, 29.71, 29.43, 26.07,

22.81, 14.16, 10.70ppm; Elemental Analysis: Cal.= C, 82.78; H, 7.09; N, 7.88; O, 2.25; Found= C, 82.72; H, 7.10; N, 7.90].

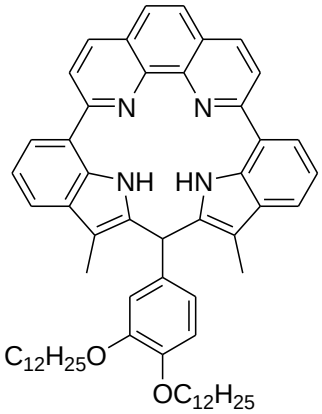

NHM-e

NHM-e:

The reaction procedure was carried out in the same manner with the **NHM-a**, except 3,4-bis(dodecyloxy)benzaldehyde (60 mg, 0.125 mmol) was applied. The crude residue was purified via column chromatography (eluted by DCM:PE=1:2) to afford light colorless crystal (24 mg, 24 % yield) [Maldi-Tof mass= 895.9 (calcd. 895.26);. ^{1}H NMR (250 MHz, CD_2Cl_2):=12.12 (s, 2 H), 8.41 (dd, 4 H), 7.87 (s, 2 H), 7.69 (d, 2 H), 7.16 (m, 4 H), 6.83 (m, 3 H), 5.94 (s, 1 H), 4.09 (t, 4H). 2.57 (s, 6 H), 1.82 (m, 4 H), 1.47 (m, 36 H), 1.09 (t, 6 H); ^{13}C-NMR (250 MHz, $CDCl_3$): δ =156.46, 149.41, 146.32, 144.80, 143.74, 137.60, 135.57, 130.29, 127.83, 127.69, 126.18, 122.69, 122.24, 121.33 119.40, 117.60, 116.70, 114.91, 107.70, 69.06, 34.51, 31.91, 29.71, 29.43, 26.10, 22.80, 14.16, 10.72ppm; Elemental Analysis: Cal.= C, 81.84; H, 8.33; N, 6.26; O, 3.57; Found= C, 81.92; H, 8.40; N, 8.00].

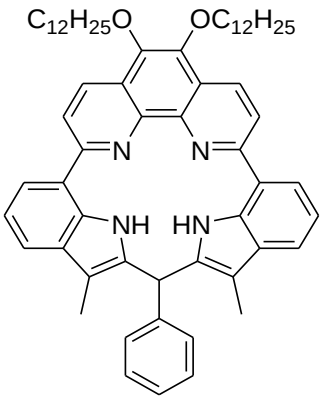

NHM-f

NHM-f:

The reaction procedure was carried out in the same manner with the **NHM-a**, except 5,6-bis(dodecyloxy)-2,9-bis(3-methyl-1H-indol-7-yl)-1,10-phenanthroline (**9f**, 50 mg, 0.61 mmol) was applied. The crude residue was purified via column chromatography (eluted by DCM:PE=1:2) to afford colorless crystal (42 mg, 75 % yield) [Maldi-Tof mass= 896.0 (calcd. 895.26); ^{1}H NMR (250 MHz, CD_2Cl_2):= 10.02 (bs, 2 H), 8.25 (dd, 4 H), 7.72 (t, 4 H), 7.65(m, 3 H), 7.37(d, 2 H), 6.50 (s, 1 H), 4.05 (m, 4 H), 2.56 (s, 6 H), 1.75(m, 4 H), 1.34(m, 36 H), 0.96 (t, 6 H); ^{13}C-NMR (250 MHz, $CDCl_3$): δ =159.91, 155.42, 149.41, 139.94, 138.10, 135.31, 133.88, 129.10, 128.67, 127.86, 125.82, 122.69, 122.20, 119.20, 117.60, 117.45, 116.70, 107.69, 69.64, 34.55, 31.91, 29.70, 29.41, 26. 01, 22.80, 14.10, 10.69ppm; Elemental Analysis: Cal.= C, 81.84; H, 8.33; N, 6.26; O, 3.57; Found= C, 81.88; H, 8.33; N, 6.30].

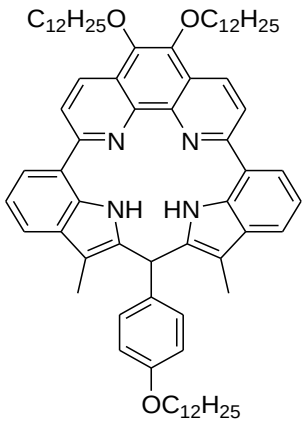

NHM-g

NHM-g:

The reaction procedure was carried out in the same manner with the **NHM-f**, except 4-(dodecyloxy)benzaldehyde (20 mg, 0.068 mmol) was applied. The crude residue was purified via column chromatography (eluted by DCM:PE=1:1) to afford colorless wax (25 mg, 37 % yield) [Maldi-Tof mass= 1080.0 (calcd. 1079.584); ^{1}H-NMR (250 MHz, CD_2Cl_2): d=12.12 (s, 2 H), 9.87 (dd, 4 H), 9.55 (d, 2 H), 9.03 (d, 2 H), 8.86 (m, 4 H), 8.34 (d, 2 H), 6.72 (s, 1 H), 5.05 (t, 6 H), 2.84 (s, 6 H), 1.81 (m, 60 H). 1.01 (t, 9 H); ^{13}C-NMR (250 MHz, $CDCl_3$): δ =155.42, 154.50, 149.41, 139.94, 135.31, 133.88, 129.70, 127.86, 122.69, 122.20, 119.20, 117.60, 117.55, 116.70, 114.30, 107.69, 68.90, 69.64, 34.55, 31.91, 29.70, 29.41, 26. 01, 22.80, 14.10, 10.69ppm; Elemental Analysis: Cal.= C, 81.21; H, 9.15; N, 5.19; O, 4.45; Found= C, 81.38; H, 9.33; N, 5.10].

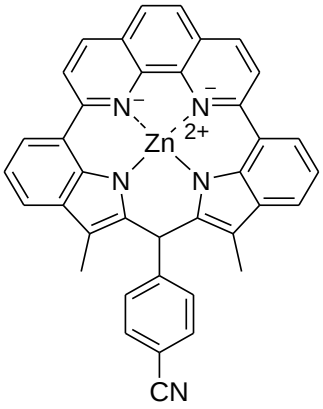

NHM-Zn-b

Zinc complex NHM-Zn-b:

NHM-b (100 mg, 0.18 mmol) and $Zn(OAc)_2$ (50 mg, 0.27 mmol) were put in a oven dried flask with condenser filled with argon and reflux in chloroform/methanol (2:1) overnight. The mixture was cooled, and the solvent was removed under reduced pressure. The product was redissolved in CH_2Cl_2 washed extensively with water. Evaporating solvent affords dark red solid (101 mg, 91 % yield). [Maldi-Tof mass= 612.1 (calcd. 613.13); ^{1}H NMR (250 MHz, CD_2Cl_2):= 8.10 (d, 2 H), 7.62 (d, 2 H), 7.51(d, 4 H), 6.84 (m, 6 H), 5.91 (s, 1 H), 2.42 (s, 6 H); ^{13}C-NMR (250 MHz, $CDCl_3$): δ =156.52,

144.70, 142.52, 137.56, 135.54, 132.15, 129.83, 127.85, 127.72, 126.17, 122.61, 122.22, 119.45, 117.68, 116.72, 115.84, 109.19, 107.01, 30.94, 10.72ppm].

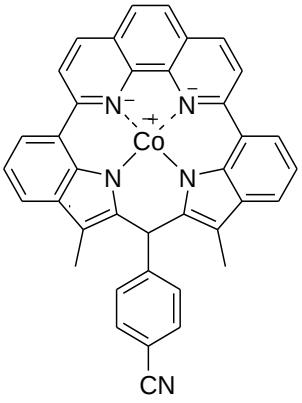

NHM-Co-b

Cobalt complex NHM-Co-b:

NHM-b (50 mg, 0.09 mmol) and $Co(OAc)_2$ (24 mg, 0.136 mmol) were dispersed in 10 mL DMF in a oven dried microwave tube and bubbled with argon for 15 min. The tube was heated in a microwave reaction at 300 W for 8 h. Afterwards, the solvent was removed under reduced pressure. The product was extensively washed with water to afford dark green solid (42 mg, 76 % yield). [Maldi-Tof mass= 608.2 (calcd. 608.5].

7.5 Synthesis of N-containing polyaromatic hydrocarbon precursors

The synthesis and characterization of **V-2, V-3, V-4** and **NPC-1** was described in the work of Calder *et al.*[4]

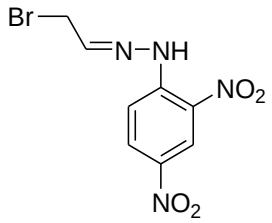

V-2

Bromoacetaldehyde 2,4-dinitrophenylhydrazone (V-2):

A solution of 2,4-dinitrophenylhydrazine (5.00 g, 0.0255 mol) in 600 mL of 12N hydrochloric acid was slowly added to a rapidly stirred mixture of bromoacetaldehyde diethylacetal (5.05g, 0.0255 mol) in 100 mL of the same solvent at room temperature. The yellow solid which separated was vacuum-filtered and washed with petroleum ether. The crude product was washed with methanol recrystallized from anhydrous ether to afford orange-yellow crystals (6.1 g, 64.2% yield) [FD-mass = 303.7 (calculated 303.1); m.p. 155.8-157.0^{o}; [^{1}H-NMR (250 MHz, CD_3OD): δ=8.75 (s, 1 H), 8.21 (d, 1 H), 7.39 (t, 1 H), 6.85 (t, 3 H), 3.19 (d, 2 H); ^{13}C-NMR (250 MHz, CD_3OD): δ=154.65, 147.90, 139.33, 135.85, 128.06, 119.55, 118.12, 22.72 ppm].

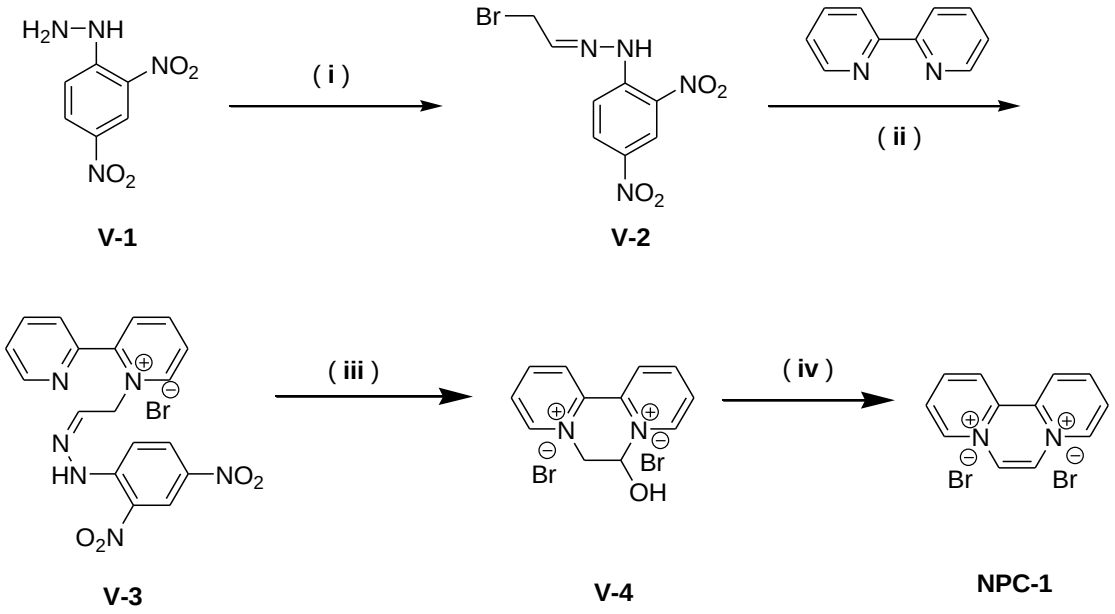

Figure 7.2 Synthetic scheme of dipyrido[1.2-a :2'.1'-c]pyrazinium dibromide from bipyridine (**NPC-1**): (i) bromoacetaldehyde diethylacetal, 12N HCl, 70 %; (ii) bipyridine, C_6H_5Me, reflux overnight, 98 %; (iii) 48% HBr, 90 ^oC, 1h, 85%, (iv) $SOCl_2$, reflux, 2h, 80 %.

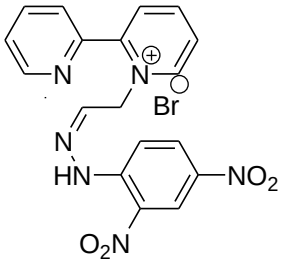

V-3

1-(ß-2,4-Dinitrophenylhydrazono)ethy-2,2'-bipyridyl bromide (V-3):

In 10 mL acetonitrile were added 2,2'-bipyridyl (100.00 mg, 0.640 mmol) and bromoacetaldehyde 2,4-dinitrophenyl-hydrazone (**2**, 194.00 mg, 0.640 mmol). The mixture was heated at 90^o for 3 h with vigorous agitation. After cooled down to room temperature, the yellow salt was precipitated out and collected by filtration (289.40 mg, 98% yield). The crude product was used in the next stage of the synthesis without further purification.

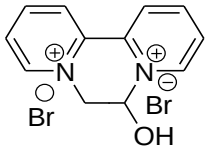

V-4

9-Hydroxy-9,10-hydro-8a,10a- diazoniaphenanthrene dibromide (V-4)

1-(ß-2,4-Dinitrophenylhydrazono)ethy-2,2'-bipyridyl bromide (**V-3**, 1 g, 2.17 mmol) was dissolved in concentrated aqueous solution of HBr (5 ml) at 90 ^{o}C for 3 h. The dark mixture was filtered and washed with acetone to give a yellow crude product which crystallized from cold mixture of water/acetone (v:v=1:10) as light yellow crystals (670 mg, 85% yield). [Maldi-Tof Mass= 200.4 (Calcd= 200.24 (cationic part); m.p.~273-275^{o}C, ^{1}H-NMR (250 MHz, D_2O): δ=10.75 (m, 2 H), 9.71 (d, 2 H), 8.89 (m, 4 H), 7.55 (t, 1 H), 5.89 (d, 2 H); ^{13}C-NMR (250 MHz, D_2O): δ=146.05, 142.50, 141.84, 128.55, 128.46, 123.35, 100.10, 62.32 ppm]

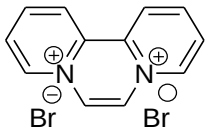

NPC-1

8a,10a-Diazoniaphenanthrene dibromide (NPC-1)

9-Hydroxy-9,10-hydro-8a,10a-diazoniaphenanthrene dibromide (**V-4**, 100 mg, 0.28 mmol) was refluxed in $SOCl_2$ (5 ml) under for 2 hr. The $SOCl_2$ was removed in vacuo and the crude product was crystallized from a mixture of acetone and aqueous HBr to give the product as pale crystals (81 mg, 85% yield) [Maldi-Tof Mass= 182.4 (Calcd= 182.22 (cationic part); m.p~271-273^{o}C; ^{1}H-NMR (250 MHz, D_2O): δ=9.65 (t, 2H), 9.33 (d, 2H), 9.08 (s, 2H), 8.75 (m, 2H), 8.59 (d, 2H); ^{13}C-NMR (250 MHz, D_2O): δ=146.25, 145.00, 142.47, 142.51, 124.21ppm]

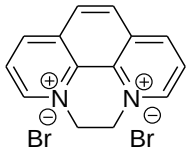

NPC-2

2,3-Dihydropyrazine[1,2,3,4-lmn] 1,10-phenanthrolinium dibromide (NPC-2)

1,10-Phenanthroline (100.00 mg, 0.56 mol) was reflux in 1,2-dibromoethane for 4h with vigorous agitation. After cooled down to room temperature, the yellow salt was precipitated out to afford a yellow powder (197 mg, 96% yield). Further recrystalisation in methanol affords orange crystal (110 mg, 51% yield). [Maldi-Tof Mass= 208.1 (Calcd= 208.24 (cationic part); m.p.>360^{o}; ^{1}H-NMR (250 MHz, d-DMSO): δ=9.75 (m, 2 H), 8.71 (d, 2 H), 7.89 (m, 4 H), 5.69 (m, 4 H); ^{13}C-NMR (250 MHz, d-DMSO): δ=146.05, 142.50, 141.84, 128.55, 128.46, 123.35, 62.32 ppm]

The synthesis and characterization of **V-5**, **V-6,** and **NPC-3** was described in the work of Black *et al.*[5]

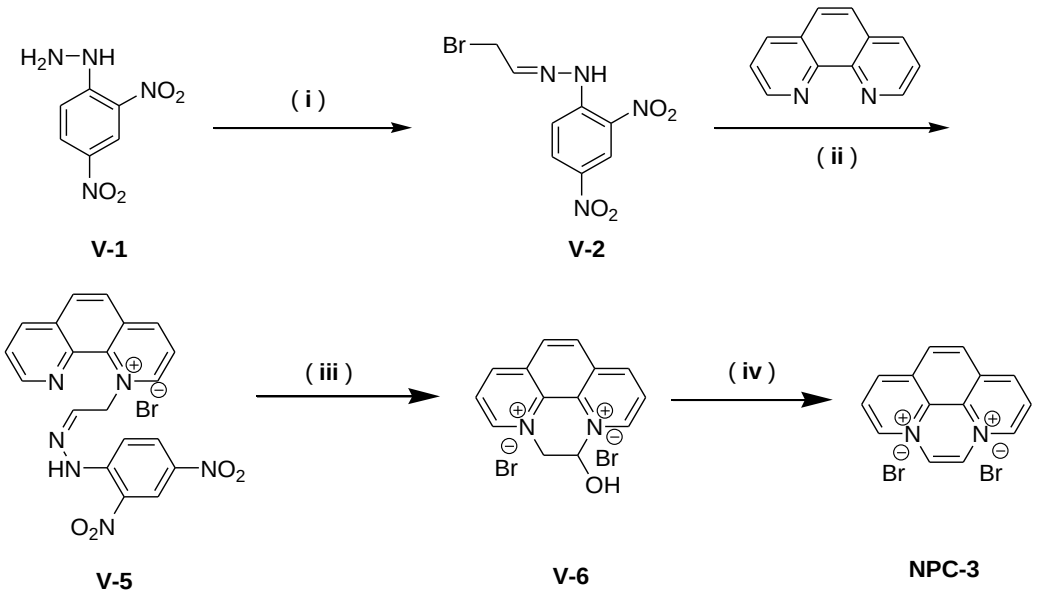

Figure 7.3 Synthetic scheme of pyrazino[1,2,3,4-lmn] 1,10-phenanthrolinium dibromide (**NPC-3**): (i) bromoacetaldehyde diethylacetal, 12N HCl, 70 %; (ii) 1,10-phenanthroline, C_6H_5Me, reflux overnight, 95 %; (iii) 48 % HBr, 90 ^{o}C, 1h, 70 %, (iv) $SOCl_2$, reflux, 2h, 50 %.

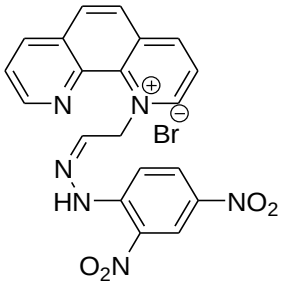

V-5

1-(ß-2,4-Dinitrophenylhydrazono)ethy-1,10-phenanthrolinium bromide (V-5):

In 10 mL toluene were added 1,10-phenanthroline (100.00 mg, 0.56 mol) and bromoacetaldehyde 2,4-dinitrophenyl-hydrazone (**V-2**, 168.76 mg, 0.56 mol). The mixture was heated at 90^{o} for 3 h with vigorous agitation. After cooled down to room temperature, the yellow salt was precipitated out and collected by filtration (77.40 mg 95% yield). The crude product was used in the next stage of the synthesis without further purification.

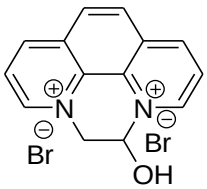

V-6

5,6-Dihydro-5-hydroxypyrazino[1,2,3,4-lmn]1,10-phenanthrolinium dibromide (V-6)

1-(ß-2,4-Dinitrophenylhydrazono)ethy-1,10-phenanthrolinium bromide (**V-5**, 1 g, 2.10 mmol) was dissolved in concentrated aqueous solution of HBr (5 ml) at 90 ^{o}C for 3 h. The dark mixture was filtered and the cold filtrate was diluted with acetone to give a brownish crude product which crystallized from cold mixture of water/acetone (v:v=1:10) as brown crystals (564 mg, 70% yield). [Maldi-Tof Mass= 224.4 (Calcd= 224.26 (cationic part); m.p.>360^{o}, ^{1}H-NMR (250 MHz, D_2O): δ=10.75 (m, 2 H), 9.71 (d, 2 H), 8.89 (m, 4 H), 7.55 (t, 1 H), 5.89 (d, 2 H); ^{13}C-NMR (250 MHz, D_2O): δ=146.05, 142.50, 141.84, 128.55, 128.46, 123.35, 100.10, 62.32 ppm]

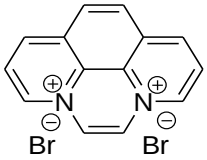

NPC-3

Pyrazino[1,2,3,4-lmn]1,10-phenanthrolinium dibromide (NPC-3):

5,6-Dihydro-5-hydroxypyrazino[1,2,3,4-lmn]1,10-phenanthrolinium dibromide (**6**, 100 mg) was refluxed in $SOCl_2$ (5 ml) for 2 hr. The $SOCl_2$ was removed in vacuo and the crude product was crystallized from a mixture of acetone and aqueous HBr to give the product as brown crystals, 45% yield [Maldi-Tof Mass= 206.6 (Calcd= 206.24 (cationic part); m.p.>360^{o}; ^{1}H-NMR (250 MHz, D_2O): δ=10.25 (d, 2H), 9.83 (d, 2H), 9.41 (s, 2H), 9.01 (s, 2H), 8.95 (m, 2H); ^{13}C-NMR (250 MHz, D_2O): δ=145.15, 145.00, 142.50, 141.91, 128.51, 128.42, 123.31ppm]

Reference:

(1) Hummers, W. S.; Offeman, R. E. *Journal of the American Chemical Society* **1958**, *80*, 1339.

(2) Frey, J.; Kraus, T.; Heitz, V.; Sauvage, J. P. *Chemistry-a European Journal* **2007**, *13*, 7584.

(3) Bartoli, G.; Palmieri, G.; Bosco, M.; Dalpozzo, R. *Tetrahedron Letters* **1989**, *30*, 2129.

(4) Calder, I. C.; Sasse, W. H. F. *Tetrahedron Letters* **1965**, 1465.

(5) Black, A. L.; Summers, L. A. *Tetrahedron* **1968**, *24*, 6453.